NASA TECHNICAL NOTE

NASA TN D-7795

NASA TN D-7795

EXPERIMENTAL STUDY OF THE EFFECTIVENESS OF CYLINDRICAL PLUME SIMULATORS FOR PREDICTING JET-ON BOATTAIL DRAG AT MACH NUMBERS UP TO 1.30

by David E. Reubush

Langley Research Center
Hampton, Va. 23665

NATIONAL AERONAUTICS AND SPACE ADMINISTRATION • WASHINGTON, D. C. • NOVEMBER 1974

1. Report No. NASA TN D-7795	2. Government Accession No.	3. Recipient's Catalog No.
4. Title and Subtitle EXPERIMENTAL STUDY OF THE EFFECTIVENESS OF CYLINDRICAL PLUME SIMULATORS FOR PREDICTING JET-ON BOATTAIL DRAG AT MACH NUMBERS UP TO 1.30		5. Report Date November 1974 6. Performing Organization Code
7. Author(s) David E. Reubush		8. Performing Organization Report No. L-9746 10. Work Unit No. 501-24-06-01
9. Performing Organization Name and Address NASA Langley Research Center Hampton, Va. 23665		11. Contract or Grant No. 13. Type of Report and Period Covered Technical Note
12. Sponsoring Agency Name and Address National Aeronautics and Space Administration Washington, D.C. 20546		14. Sponsoring Agency Code

15. Supplementary Notes

16. Abstract

An investigation has been conducted in the Langley 16-foot transonic tunnel to determine the effectiveness of utilizing solid circular cylinders to simulate the jet exhaust plume for a series of eight nacelle-mounted isolated circular-arc afterbodies. This investigation was conducted at Mach numbers from 0.40 to 1.30 at an angle of attack of 0°. Plume simulators with simulator diameter to nozzle-exit diameter ratios of 0.82, 0.88, 0.98, and 1.00 were investigated. Results of this investigation indicate that use of one of the larger diameter simulators at all Mach numbers would generally result in pressure-coefficient distributions and drag coefficients useful for preliminary design work.

17. Key Words (Suggested by Author(s))	18. Distribution Statement
Jet-exhaust simulation Boattail drag	Unclassified – Unlimited STAR Category 01

19. Security Classif. (of this report)	20. Security Classif. (of this page)	21. No. of Pages	22. Price*
Unclassified	Unclassified	156	$6.25

*For sale by the National Technical Information Service, Springfield, Virginia 22151

EXPERIMENTAL STUDY OF THE EFFECTIVENESS OF CYLINDRICAL PLUME SIMULATORS FOR PREDICTING JET-ON BOATTAIL DRAG AT MACH NUMBERS UP TO 1.30

By David E. Reubush
Langley Research Center

SUMMARY

An investigation has been conducted in the Langley 16-foot transonic tunnel to determine the effectiveness of utilizing solid circular cylinders to simulate the jet exhaust plume for a series of eight nacelle-mounted isolated circular-arc afterbodies. This investigation was conducted at Mach numbers from 0.40 to 1.30 at an angle of attack of 0^{o}. Plume simulators with ratios of simulator diameter to nozzle-exit diameter of 0.82, 0.88, 0.98, and 1.00 were investigated. Reynolds number based on maximum model diameter varied from approximately 1.50×10^{6} to 2.14×10^{6}.

Results of this investigation generally indicate that, for jet total-pressure ratios near 2, jet-on boattail pressure-coefficient distributions and pressure-drag coefficients for any of the configurations are closely approximated at the low subsonic Mach numbers by one of the smaller diameter simulators. At the higher subsonic and transonic Mach numbers, however, the use of one of the larger diameter simulators resulted in good approximations of the jet-on pressure-coefficient distributions and drag coefficients. The use of one of the larger diameter simulators at all Mach numbers would generally result in pressure-coefficient distributions and drag coefficients that would be useful for preliminary design work. The two theoretical methods of boattail pressure-coefficient distribution prediction evaluated as a part of this investigation usually gave reasonably good approximations to the jet-on (again, jet total-pressure ratios near 2) boattail pressure-coefficient distributions for the configurations with little or no flow separation.

INTRODUCTION

Insofar as the requirement for a low drag configuration is concerned, one of the critical areas in the design of an aircraft is in the area of the afterbody and nozzles. The flow in this region is extremely complex with upstream disturbances interacting with the expansion and succeeding recompression on the boattail surface; all three of these

phenomena interact with the jet exhaust plume. Therefore it is important to obtain knowledge of the afterbody and nozzle flow field and resultant drag as early as possible in the design procedure to insure that the afterbody-nozzle design is the best possible. Unfortunately, wind-tunnel models which include means to simulate the jet exhaust for afterbody-nozzle investigations are extremely complex and costly, conditions which work to the disadvantage of the designer in his attempt to obtain data early in the design procedure. The complexity associated with the internal plumbing required for the jet simulation medium and the cost of this type of model deters the construction of the model until the configuration lines are finalized to be sure that the model will correctly represent the final selected configuration.

It would therefore be extremely advantageous to devise a method whereby the afterbody-nozzle pressure distributions, and hence the drag of a configuration, could be reasonably predicted early in the design process either analytically or by use of a relatively inexpensive wind-tunnel model. An attempt at a low cost simple substitute for jet simulation has been used by Lewis Research Center and others. (See refs. 1 to 14.) This simple substitute method involves the use of a sting-mounted model with a jet boundary simulator (also known as a "sting" or "plume" simulator) hereafter referred to as a simulator. These simulators normally are a circular cylinder mounted on the model support sting whose diameter is equal to that of the nozzle exit. This configuration simulates the on-design jet plume shape when external flow effects on the plume are neglected. (See refs. 14 to 17.) On-design means that the exit static pressure of the jet equals the free-stream static pressure. For convergent nozzles, like those of this investigation, the on-design condition occurs at a jet total-pressure ratio $p_{t,j}/p_\infty$ of about 1.9. Although the simulator method has been used a number of times, most of the previous work done to assess the validity of the method has used for comparison models of two different scales, or even a model and the full-scale flight vehicle. As a result these comparisons could be affected by other factors such as Reynolds number differences, model support system differences, or variations in instrumentation location and accuracy between tests.

In order to assess the validity of the simulator technique, an investigation utilizing simulators of various diameters was conducted in the Langley 16-foot transonic tunnel in conjunction with the air-powered model investigation of several circular-arc afterbodies (refs. 18 and 19). The investigation was conducted at Mach numbers from 0.40 to 1.30 at an angle of attack of 0°. (The investigation in references 18 and 19 covered the same Mach number range with jet total-pressure ratios varying from jet-off to about 6 depending on Mach number.) In addition to evaluating the usefulness of the simulators, two theoretical techniques for the prediction of afterbody pressure distributions for afterbodies with attached flow (refs. 20 and 21) were evaluated. In addition, one of these inviscid solutions has been modified by the addition of the boundary-layer solution from reference 22. It must be noted that some of the simulator data presented in this report has been previously

presented in reference 23. An appendix is included which provides boattail pressure-coefficient data for the eight afterbodies of this report with the circular-arc contours extended to a point.

SYMBOLS

A	cross-sectional area, m^2
A_{max}	maximum cross-sectional area, m^2
A_β	incremental area assigned to a boattail static-pressure orifice for drag integration, m^2
$C_{D,\beta}$	boattail-pressure-drag coefficient, $\frac{D_\beta}{q_\infty A_{max}}$
$C_{p,\beta}$	boattail pressure coefficient, $\frac{p_\beta - p_\infty}{q_\infty}$
D_β	pressure drag on boattail, N
d_b	base diameter of afterbody, m
d_e	exit diameter of nozzle, m
d_m	maximum diameter of model, m
d_s	diameter of plume simulator, m
l	length of boattail, m
M	free-stream Mach number
N_{Re}	Reynolds number
$p_{t,j}$	jet total pressure, N/m^2
$p_{t,\infty}$	free-stream total pressure, N/m^2
p_∞	free-stream static pressure, N/m^2
p_β	boattail static pressure, N/m^2

q_∞ free-stream dynamic pressure, N/m^2

R boattail circular-arc radius, m

r radial distance from center line of model, m

S nozzle covergence length, m

s axial coordinate in nozzle convergence section, m

$T_{DP,\infty}$ free-stream dewpoint temperature, K

$T_{t,\infty}$ free-stream stagnation temperature, K

t nozzle throat length, m

X axial distance aft from model nose, m

x axial distance aft from start of boattail, m

β terminal boattail angle, deg

β_c boattail chord angle, deg

ϕ meridional angle about model axis, positive clockwise when viewed from rear, 0^o at top of model, deg

EXPERIMENTAL APPARATUS AND PROCEDURE

Wind Tunnel

This investigation was conducted in the Langley 16-foot transonic tunnel, which is a single-return, continuous-flow, atmospheric tunnel. The test section is a regular octagon in cross section with slots at the corners of the octagon. The tunnel speed is continuously variable from Mach 0.20 to 1.30. Further description of the Langley 16-foot transonic tunnel can be found in references 24 to 26.

Model and Support System

A sketch of the single-engine nacelle model used in the air-powered portion of this investigation (refs. 18 and 19) is shown in figure 1 with a typical circular-arc boattail

configuration attached. This figure shows the typical complexity associated with any powered model. Figure 2 is a photograph of the nacelle model installed in the Langley 16-foot transonic tunnel. The cone-cylinder nacelle has a rounded shoulder at the junction of the conical nose and cylindrical section.

For the simulator investigation, the cone-cylinder single-engine nacelle model was modified by the addition of an internal sting arrangement to provide for the various simulators. A sketch of the modified model is shown in figure 3 with a typical circular-arc boattail configuration attached. Figure 4 is a photograph of the nacelle model installed in the Langley 16-foot transonic tunnel with a typical afterbody configuration and $d_s/d_e = 1.00$ simulator attached.

The model was supported in the tunnel by a sting-strut support system, the swept strut being attached to the nose of the model as shown in figures 1 to 5. The center line of the model was located on the wind-tunnel center line, with the center line of the sting 55.88 cm below that level. The sting was 5.08 cm by 10.16 cm in cross section with the top and bottom capped by half-cylinders of 2.54-cm radius. The strut blade was 5 percent thick with a 50.8-cm chord in the streamwise direction and with the leading and trailing edges swept 45°.

A sketch of the model and support system, with corresponding cross-sectional area distributions, is shown in figure 5. The model blockage was 0.099 percent of the test-section cross section, and the maximum blockage cross section of the model and support system was 0.148 percent.

Afterbody Models and Simulators

A detailed sketch of a typical afterbody model and a table of dimensions for the eight configurations are presented in figure 6. Simulators of various ratios of simulator diameter to nozzle-exit diameter were tested with each afterbody configuration. Simulators with d_s/d_e of 1.00, 0.98, 0.88, and 0.82 were available for each of the three nozzle-exit sizes. All simulators were 27.94 cm long. It was felt that this length was sufficient to insure that the results were not affected by the simulator base (ref. 1). Not all simulator-exit diameter ratios were tested with all afterbodies because of the limited test time.

Instrumentation and Tests

The eight afterbody models were equipped with static-pressure orifices distributed longitudinally on an equal annular area basis at the locations given in table I. These orifices were connected to individual, remotely located, electrical strain-gage-pressure transducers. The simulators were each instrumented with 16 static-pressure orifices at the locations given in table II. These orifices were connected to a pressure scanning valve installed in the model.

All tests were conducted in the Langley 16-foot transonic tunnel at Mach numbers from 0.40 to 1.30 at an angle of attack of 0°. Model attitude was set to account for tunnel upflow (about 0.1° through the Mach number range), but no account was taken of a possible sting deflection which was found to be extremely small. Boundary-layer transition on the model was fixed by a 0.254-cm strip of No. 100 grit, located 2.54 cm from the nose in accordance with the techniques described in references 27 and 28.

Since the Langley 16-foot transonic tunnel is an atmospheric tunnel, the tunnel free-stream conditions will vary according to the ambient conditions. The range of the free-stream conditions plotted against Mach number is shown in figure 7.

Data Reduction

Pressure drag coefficients were computed from the measured pressures on each boattail. These coefficients are based on the maximum cross-sectional area of the model and were obtained from the pressure data by assigning an equal annular area to each orifice in the top row and computing the coefficients from the equation:

$$C_{D,\beta} = \frac{1}{q_\infty A_{max}} \sum_{i=1}^{n} (p_\infty - p_{\beta,i}) A_{\beta,i}$$

The top row of orifices was used exclusively because of the possibility of support-strut interference. In references 18 and 19, it was reported that the data from the $\phi = 0^{\circ}$ row of orifices could be assumed to be interference free. Unpublished data from the present investigation, which compared pressures on these boattails mounted on the sting-strut with pressures on the same boattails mounted on a sting, support this assumption. No attempt was made to include the forces on the small rim at the nozzle exit between d_b and d_e. (See fig. 6.)

PRESENTATION OF RESULTS

The results obtained in this investigation are presented in the following figures.

	Figure
Comparison of pressure-coefficient distributions obtained through the use of plume simulators with those obtained from jet operation at $p_{t,j}/p_\infty = 2$	8 to 15
Comparison of pressure-coefficient distributions obtained by the use of the theoretical techniques of references 20 and 21 with those obtained from jet operation at $p_{t,j}/p_\infty = 2$ and for the use of the $d_s/d_e = 1.00$ simulator . . .	16 to 23
Comparison of integrated boattail pressure-drag coefficients obtained through the use of the simulators with jet-on values	24 to 31

DISCUSSION

Pressure Distributions

The jet exhaust plume affects the afterbody boattail pressures in two ways: by the entrainment of external air flowing over the boattail and by the blockage or shape effect of a body downstream of the boattail. These two phenomena result in opposite effects on the boattail pressure distributions. The entrainment of the external flow causes a reduction in the afterbody pressure coefficients, whereas the blockage effect causes a rise in the afterbody pressure coefficients. In trying to model the effects of the jet exhaust on the afterbody, both of these phenomena should be taken into account. However, at the present time no known methods exist to predict the entrainment of any given jet. Therefore, the use of circular cylinder simulators is, at best, a compromise, since the jet entrainment effects will not be simulated, and only the plume shape of a nozzle operating at its design point will be matched (holds true only at static conditions). Fortunately, this compromise is not unusable since most subsonic transport aircraft and fighters operating at subsonic cruise utilize convergent nozzles and turbofan engines; these engines operate in a range of jet total-pressure ratios near the convergent nozzle design point of about 2. (See fig. 32.) Also, the data of references 18 and 19 show that generally there are no significant variations in afterbody boattail drag levels (for jet-on conditions) with jet total-pressure ratio until the ratio passes 3. Therefore, simulating the design point jet total-pressure ratio $\left(p_{t,j}/p_\infty \approx 2\right)$ with the solid cylinder simulator should result in an error in drag caused only by the missing entrainment effect.

Shown in figures 8 to 15 are comparisons of the afterbody pressure-coefficient distributions for the eight configurations discussed in this paper. These comparisons are of pressure distributions obtained through the use of simulators of varying diameters and pressure distributions which were obtained with high-pressure air $\left(\text{at } p_{t,j}/p_\infty = 2\right)$ as the exhaust medium (refs. 18 and 19). (It must be noted that the blockage and mixing could be different for real engine exhaust because of different gas properties and temperature.)

Simulators of a smaller diameter than the nozzle-exit diameter were utilized in an attempt to lessen the blockage effects, and, as a result, these simulators have the potential to produce the desired combination of blockage and entrainment effects. The pressure-coefficient distributions on the simulators themselves are shown for information in the figures.

Figure 8 presents the simulator—jet-on comparisons for configuration 1. At all Mach numbers there are only very small differences between the pressure-coefficient distributions obtained with all four simulator diameters. The jet-on pressure coefficients are slightly more negative (especially at Mach numbers above 0.90) than any simulator-produced pressure-coefficient distributions. The lack of difference between the various simulators is caused by the fact that the flow over this boattail is substantially separated at all Mach numbers. (Separation occurs somewhat upstream of where the pressure distribution curve flattens out.) As a result, there is probably little pressurization of the boattail caused by the plume or simulator blockage effect, and this small effect does not vary substantially with simulator diameter. The reason the jet-on pressure-coefficient distributions are lower than the simulator-produced distributions is that the entrainment effect is missing when the simulators are used. However, any of the simulators produce a pressure-coefficient distribution which is a reasonably good approximation to the jet-on distribution (especially below $M = 0.92$). The same general comments also apply to the data for configuration 2 as shown in figure 9, because the flow over this boattail is also substantially separated for most Mach numbers investigated.

Figure 10 presents the simulator—jet-on comparisons for configuration 3. Since this configuration generally has unseparated flow (except for shock-induced separation at supersonic speeds), the differences between the pressure-coefficient distributions obtained with the various simulators are greater than those for configurations 1 and 2. At the lower Mach numbers (e.g., $M = 0.40$ and 0.60), entrainment probably has a larger effect on the afterbody pressure-coefficient distribution than it does at the higher subsonic Mach numbers where the exhaust and free stream have close to the same velocity (e.g., $M = 0.85$ to 0.96). As a result, the jet-on pressure-coefficient distributions at the low Mach numbers are more closely represented by one of the smaller diameter simulators (e.g., $d_s/d_e = 0.82$ or 0.88) than by the $d_s/d_e = 1.00$ simulator. Those at the higher subsonic Mach numbers are most closely represented by the $d_s/d_e = 0.98$ simulator. At the supersonic Mach numbers investigated, the boattail pressure coefficients upstream of the shock (shock located at approximately $x/d_m = 1.45$ for this configuration) are about the same for all the simulators and for jet-on. Downstream of the shock in the separated region (shock-induced separation), the jet-on pressure coefficients generally fall between the pressure coefficients for the $d_s/d_e = 0.98$ and $d_s/d_e = 0.88$ simulators. However, the use of one of the larger diameter simulators at all Mach numbers would generally

result in pressure-coefficient distributions with the correct shape and minimum pressure coefficient satisfactory for preliminary design work.

The same general comments are valid for the configurations 4 to 8 (figs. 11 to 15) which have no separation or only small regions of separated flow. Also, by examining the various pressure-coefficient distributions at any given subsonic Mach number, it becomes apparent that as the boattail angle and the resultant inflow into the plume are reduced, so is the effect of the entrainment. As a result, the pressure-coefficient distributions obtained with the smaller diameter simulators $\left(\text{e.g., } d_s/d_e = 0.82 \text{ and } 0.88\right)$ are further from the jet-on $\left(p_{t,j}/p_\infty = 2\right)$ data for the nonseparated flow configurations since they do not match the plume blockage effect.

Comparison With Theory

There are several theoretical techniques available with which to predict afterbody pressure distributions. One of the most widely used and one of the most recent are given in references 20 and 21, respectively. These methods both assume inviscid flow but utilize different solution techniques. The method of reference 20, which is a relatively inexpensive method in terms of computer time and cost, utilizes distributed sources and sinks on the body surface to calculate the flow field and resulting body pressure distribution. In order to simulate jet effects with this method, the jet plume shape must be specified for input as a solid body downstream of the nozzle exit. The method of reference 21 utilizes a stream tube curvature analysis in which an initial grid of streamlines and orthogonals is set up and then refined in an iterative solution (relatively expensive in computer time and cost). This method has the capability of calculating its own plume shape for low jet total-pressure ratio exhaust flows so that only jet total pressure, total temperature, and exit Mach number need be specified in order to simulate a jet exhaust. (Plumes resulting from this calculation are very close to cylindrical.) Since these methods are inviscid solutions, they have no provision for computing the boundary-layer development on the afterbody. The boundary-layer effects are often substantial and this condition can result in the neglect of a significant contribution to the resultant pressure distribution. In an attempt to account for the contributions caused by boundary-layer development, the method of reference 20 has been modified by the addition of an iterative boundary-layer solution which was adapted from reference 22 (modified Reshotko-Tucker solution). Also, since they are inviscid solutions, a concave corner, such as between the boattail and the assumed cylindrical plume, results in the theory predicting a stagnation point. The result is that all pressure coefficients near the end of the boattail are too high.

Figures 16 to 23 present comparisons of the afterbody pressure-coefficient distributions for the eight configurations discussed in this paper. These comparisons of distributions were obtained with jet-on (at a jet total-pressure ratio of two) and with the $d_s/d_e = 1.00$ simulator at various Mach numbers at which the pressure-coefficient

distributions were predicted by the theoretical methods. In all cases, the solid body used to simulate the jet plume shape for the method of reference 20 was a circular cylinder with the diameter of the cylinder equal to the exit diameter of the nozzle (same as $d_s/d_e = 1.00$ simulator).

Figures 16 and 17 present the pressure-coefficient distribution comparisons for configurations 1 and 2 at six subsonic Mach numbers from 0.40 to 0.90. As expected, since both of these configurations have steep boattails which result in large regions of separated flow, the predicted pressure-coefficient distributions are very much in error when compared with the experimental, jet-on results. Configuration 1 is so steep that the computer program solution from reference 21 would not converge, and the boundary-layer addition to the program from reference 20 would not iterate when it reached the separated region for either configuration. Therefore, it is recommended that prediction of pressure-coefficient distributions for configurations with large boattail angles and highly separated flow not be attempted with these programs.

For configuration 3 (fig. 18) the method of reference 20 approximately predicts the minimum pressure coefficient on the boattail except for $M = 0.90$. The general shape of the curve is reasonably predicted. The addition of the boundary-layer solution to this method virtually eliminates the problem of the stagnation point at the trailing edge; however, it does result in the predicted boattail pressure coefficients being too high. (It must be noted that the program would not run for this configuration at Mach numbers of 0.80, 0.85, and 0.90. As a result, no boundary-layer curves are shown for those conditions.)

The method of reference 21 produces varied results: at some Mach numbers the predicted pressure coefficients are lower than those obtained with the jet operating or with the plume simulators; at other Mach numbers it predicts pressure coefficients that are too high. The reason for this situation is that the program sets up a grid of streamlines and orthogonals at a given Mach number and refines it until certain convergence criteria are met. At that point it produces answers and proceeds to the next Mach number. At the next Mach number the program starts with the already developed grid and accomplishes any further refinement necessary, produces answers, and starts the process over again. However, in most instances, the refinement criteria are not sufficiently stringent and thus the same grid will satisfy the equations of motion for more than one Mach number. When this condition occurs, the predicted pressure-coefficient distributions will be essentially the same for both Mach numbers. It is at the Mach numbers where the grid has changed that the program predicts pressure coefficients lower than the data. An increase in Mach number above this change, but before the next grid refinement, will result in a decrease in the measured pressure coefficients, the predicted coefficients remaining the same and thus changing the relationship of the two curves. This problem can be alleviated in some cases (but only with a large increase in computer time and cost) by running the program for each Mach number individually rather than going from one Mach number to the next. However,

this method results in the predicted minimum pressure coefficient being too low for all Mach numbers. (See fig. 21.) In addition, this theory predicts pressure coefficients that are too high in the region near the boattail trailing edge, but which are not as high as those predicted by the method of reference 20.

Similar statements can be made for the comparisons for configurations 5, 7, and 8 (figs. 20, 22, and 23), which again are configurations with little or no flow separation. For those boattails with unseparated flow, both theoretical techniques do a reasonably good job of predicting the afterbody pressure-coefficient distributions, but not as accurately as the $d_s/d_e = 1.00$ simulators. In addition, the integrated boattail pressure-drag values, which would be calculated from these theoretical pressure distributions, would, in general, predict afterbody drags much lower than the jet-on $\left(p_{t,j}/p_\infty = 2\right)$ drag for all configurations. These values would therefore be unsatisfactory for drag estimation because of the stagnation point at the trailing edge and, if the boundary layer solution is added, because all the pressure coefficients are too high.

The comparisons for configuration 4 and configuration 6 are shown in figures 19 and 21, respectively. Although the simulator results for these two configurations are similar to the results for the configurations with unseparated flow (e.g., configurations 3, 5, 7, and 8), these boattails are relatively steep. Therefore, the pressure-coefficient distribution predictions are reasonably good at the lower Mach numbers ($M = 0.40$ to about $M = 0.70$) where there is little or no separation. At the higher Mach numbers (above about $M = 0.70$), the predictions are not very good. Even where there is good agreement, in both programs there is the ever-present problem of the stagnation point at the trailing edge. Figure 21 also illustrates the differences obtained when the program for the method of reference 21 is run with Mach numbers both sequentially and individually. Sequentially, the predicted minimum pressure coefficients vary from below the experimental data to above them; whereas individually, the predicted minimum pressure coefficients are always below the experimental data. (Note that the solution would not converge for Mach numbers of 0.85 and 0.90 when run individually for this configuration.)

Boattail Drag

Figures 24 to 31 show curves of boattail drag coefficients as a function of jet total-pressure ratio $\left(p_{t,j}/p_\infty\right)$ from references 18 and 19, as well as some unpublished data with the pressure-drag coefficients obtained by using the simulators superimposed on them. As mentioned before, not all ratios of simulator diameter to nozzle-exit diameter were tested with every afterbody configuration.

The results for configuration 1 are as expected based on the pressure-coefficient distribution comparisons for this highly separated flow afterbody. Since all the simulator-produced pressure-coefficient distributions were higher than the jet-on $p_{t,j}/p_\infty = 2$

distributions, the resultant simulator-produced drag coefficients are too low when compared with the jet-on data for this configuration. It would seem that entrainment plays a very significant part in determining the drag characteristics of a configuration such as this, and even by using small-diameter simulators, the phenomena cannot be adequately simulated. Although the simulator-produced drag coefficients are in error for most jet-on conditions for this afterbody, the jet-on drag predicted by the use of one of the larger diameter simulators (e.g., $d_s/d_e = 0.98$ or 1.00) generally falls reasonably close to the drag values for most Mach numbers in the unchoked range of jet total-pressure ratios 1 to about 1.9.

Configuration 2 is also a configuration with substantial amounts of flow separation. However, for most subsonic Mach numbers, the simulators produce boattail drag coefficients which are close to jet-on values in the range of jet total-pressure ratios between 2 and 4. For Mach numbers of 0.70 and below, the $d_s/d_e = 0.88$ simulator generally gives a boattail drag coefficient closer to jet-on values than does any of the other simulators. Between $M = 0.70$ and 0.90, one of the two larger diameter simulators usually gives better results. At the subsonic speeds investigated above $M = 0.90$ where the curves of $C_{D,\beta}$ plotted against $p_{t,j}/p_\infty$ begin to resemble those of configuration 1 (because of the large amount of separation), one of the smaller diameter simulators again gives slightly better matching. At supersonic speeds the results are similar for both configuration 1 and configuration 2, the simulator-produced drag coefficients falling across the jet-on drag coefficient curves in the range of jet total-pressure ratios between 4 and 6. At most Mach numbers the simulators produce drag coefficients which are closer to the jet-on than to the jet-off coefficients. Therefore, using simulators would be preferable to running a configuration with no jet simulation.

The results for the remaining six configurations are similar since all have little or no flow separation. With a few exceptions (configuration 4 at supersonic speeds and configuration 5 at $M = 0.40$), the drag coefficients obtained with the $d_s/d_e = 0.82$ simulators were always higher than any jet-on drag coefficients obtained for the corresponding configuration at any Mach number. Also, with the exception of $M = 0.40$ and 0.60 for configuration 3, the drag coefficients obtained with the $d_s/d_e = 0.88$ simulators were at least slightly higher than any jet-on drag coefficients. For subsonic Mach numbers above 0.60, the drag coefficients produced through the use of the $d_s/d_e = 0.98$ and 1.00 simulators, generally fall on the curves of $C_{D,\beta}$ plotted against $p_{t,j}/p_\infty$ somewhere in the range of jet total-pressure ratios from 1.5 to 3 for all six configurations (configurations 3 to 8). At Mach numbers below 0.60, the drag values obtained by using these two simulators are too low. At supersonic Mach numbers, the drag values fall on the curves of $C_{D,\beta}$ plotted against $p_{t,j}/p_\infty$ at slightly higher values of jet total-pressure ratio.

The drag coefficient results are, for the most part, as expected based on the pressure distributions. The smaller diameter simulators ($d_s/d_e = 0.82$ and 0.88) more closely

match the drag coefficient levels (although slightly high) at the low Mach numbers where the entrainment effects are large. These entrainment effects reduce the beneficial blockage effect of the full jet plume. The large-diameter simulators (d_s/d_e = 1.00 and 0.98) more closely match the drag coefficients at the higher Mach numbers where the entrainment effects are not as great. However, the use of the d_s/d_e = 1.00 simulators often results in drag coefficient values corresponding to jet total-pressure ratios in the range of 2 to 4. Fortuitously, this is the typical operating range for subsonic transport aircraft and for fighter-type aircraft at subsonic cruise conditions. This is evidenced by the two typical curves of operating jet total-pressure ratio as a function of Mach number as shown in figure 32. Therefore, the drag coefficient data obtained by the use of a model with the simulators would provide useful information for early design (particularly for boattails with little or no flow separation) pertaining to the jet-on operation of the aircraft configuration. The drag coefficient data are especially useful when compared with a dependence on drag data obtained at jet-off conditions.

The capability of the simulators to provide reasonable approximations of the drag coefficients for an afterbody configuration with jet operation can be further illustrated by examining the boattail drag coefficients obtained with the simulators which have been plotted as a function of Mach number and compared with jet-on $\left(p_{t,j}/p_\infty = 2\right)$ drag coefficient data from references 18 and 19 in figure 33.

As concluded from the previously presented data, it is evident that the larger diameter (d_s/d_e = 0.98 and 1.00) simulators match more closely the jet-on drag coefficients for all six configurations with little or no flow separation for a greater range of Mach numbers than do the smaller diameter simulators (d_s/d_e = 0.82 and 0.88). To be able to choose one simulator diameter for general use in order to reach a compromise between plume blockage and entrainment effects would require additional tests with both the d_s/d_e = 1.00 and 0.98 simulators and simulators of slightly smaller diameter (down to possibly d_s/d_e = 0.95) with a greater number of configurations. However, the present results do indicate that the simulators can be an effective tool to gain information about the jet-on drag characteristics of an afterbody configuration with less time and expense.

Figure 34 shows cross-plots of the jet-on drag coefficient data from references 18 and 19 for the eight configurations discussed in this paper at the transport jet total-pressure ratio schedule of figure 32, compared with the drag coefficient data obtained using the various simulators with those configurations. Again, the larger diameter simulators (d_s/d_e = 0.98 and 1.00) more closely match the jet-on drag coefficients for all six configurations (with little or no separation for a larger range of Mach numbers) than do the smaller diameter (d_s/d_e = 0.82 and 0.88) simulators. This similarity to the $p_{t,j}/p_\infty = 2$ comparisons is due to the fact that the jet total-pressure ratio schedule of figure 32 does not significantly vary from a $p_{t,j}/p_\infty$ of 2 for the range of subsonic Mach numbers tested, and the jet-on drag coefficient curves for these afterbodies are relatively flat in this range.

CONCLUDING REMARKS

An investigation at an angle of attack of 0° has been conducted in the Langley 16-foot transonic tunnel at Mach numbers from 0.40 to 1.30 in order to determine the effectiveness of utilizing solid circular cylinders to simulate the jet exhaust plume effects on a series of eight nacelle-mounted isolated circular-arc afterbodies. The results of this investigation indicate three primary conclusions:

1. The use of the jet plume simulators resulted in boattail pressure-coefficient distributions close to jet-on $\left(p_{t,j}/p_{\infty} = 2\right)$ pressure-coefficient distributions for all configurations at all Mach numbers. The smaller diameter simulators (d_s/d_e = 0.82 and 0.88) usually produced pressure-coefficient distributions which more closely matched the jet-on distributions at low subsonic Mach numbers (e.g., M = 0.40 and 0.60) where entrainment effects are large. The larger diameter simulators (d_s/d_e = 0.98 and 1.00) often matched more closely the jet-on pressure-coefficient distributions at the higher subsonic Mach numbers (e.g., M = 0.80 to 0.96) and transonic Mach numbers where the blockage effect predominates. However, the use of one of the larger diameter simulators at all Mach numbers would generally result in pressure-coefficient distributions with the correct shape and minimum pressure coefficient satisfactory for preliminary design work.

2. Comparisons of the integrated pressure-drag values obtained through the use of the simulators with those jet-on values obtained from the references follow the same trends as the pressure-coefficient distribution comparisons. At the lower Mach numbers the small-diameter simulators (d_s/d_e = 0.82 and 0.88) usually match drag coefficients more closely, whereas at the higher Mach numbers the larger diameter simulators (d_s/d_e = 0.98 and 1.00) are somewhat better. Again, the use of the large-diameter simulators for all Mach numbers would probably result in integrated drag coefficients which would be of value in the early design stages of an aircraft configuration. The choice of a simulator-exit diameter ratio that would most accurately simulate the dual plume effects of blockage and entrainment for general use would require further testing with a number of simulators and additional afterbodies.

3. Both of the theoretical techniques used to predict boattail pressure distributions evaluated as a part of this investigation gave reasonably good approximations to the correct pressure-coefficient distributions (for the configurations with little or no flow separation) when compared with the jet-on distributions from the references. Although both

predict a stagnation point at the boattail trailing edge, the method of Hess and Smith would probably be preferred for its consistency in predicting the peak negative pressure coefficients reached on each boattail for most Mach numbers.

Langley Research Center,
National Aeronautics and Space Administration,
Hampton, Va., September 26, 1974.

APPENDIX

POINTED BODY OF REVOLUTION PRESSURE DISTRIBUTION

Boattail pressure-coefficient distributions for the various configurations of this investigation with their circular-arc contours continued to a point are presented in figures 35 to 37. The geometric characteristics of these configurations are given in table III. These pressure-coefficient distribution curves are presented as a body of data for comparison with theoretical techniques which do not have an internal method of simulating a jet plume and for which a cylinder downstream of the exit is not acceptable.

REFERENCES

1. Cahn, Maurice S.: An Experimental Investigation of Sting-Support Effects on Drag and a Comparison With Jet Effects at Transonic Speeds. NACA Rep. 1353, 1958. (Supersedes NACA RM L56F18a.)

2. Shrewsbury, George D.: Effect of Boattail Juncture Shape on Pressure Drag Coefficients of Isolated Afterbodies. NASA TM X-1517, 1968.

3. Shrewsbury, George D.: Effect of a Simulated Wing on the Pressure-Drag Coefficients of Various 15° Boattails at Mach Numbers From 0.56 to 1.00. NASA TM X-1662, 1968.

4. Blaha, Bernard J.; and Mikkelson, Daniel C.: Wind Tunnel Investigation of Airframe Installation Effects on Underwing Engine Nacelles at Mach Numbers From 0.56 to 1.46. NASA TM X-1683, 1968.

5. Blaha, Bernard J.; and Bresnahan, Donald L.: Wind Tunnel Installation Effects on Isolated Afterbodies at Mach Numbers From 0.56 to 1.5. NASA TM X-52581, 1969.

6. Harrington, Douglas E.: Jet Effects on Boattail Pressure Drag of Isolated Ejector Nozzles at Mach Numbers From 0.60 to 1.47. NASA TM X-1785, 1969.

7. Wilcox, Fred A.; Samanich, Nick E.; and Blaha, Bernard J.: Flight and Wind Tunnel Investigation of Installation Effects on Supersonic Cruise Exhaust Nozzles at Transonic Speeds. AIAA Paper No. 69-427, June 1969.

8. Blaha, Bernard J.: Effect of Underwing Engine Nacelle Shape and Location on Boattail Drag and Wing Pressures at Mach Numbers From 0.56 to 1.46. NASA TM X-1979, 1970.

9. Mikkelson, Daniel C.; and Blaha, Bernard J.: Flight and Wind Tunnel Investigation of Installation Effects on Underwing Supersonic Cruise Exhaust Nozzles at Transonic Speeds. NASA TM X-52827, 1970.

10. Bergman, Dave: Implementing the Design of Airplane Engine Exhaust Systems. AIAA Paper No. 72-1112, Nov.-Dec. 1972.

11. Chamberlin, Roger; and Blaha, Bernard J.: Flight and Wind Tunnel Investigation of the Effects of Reynolds Number on Installed Boattail Drag at Subsonic Speeds. NASA TM X-68162, [1973].

12. Glasgow, Edsel R.; Santman, Don M.; Miller, Leonard D., et al.: Integrated Airframe – Nozzle Performance for Designing Twin-Engine Fighters. AFFDL-TR-73-71, Vol. I, U.S. Air Force, June 30, 1973.

13. Bergman, Dave: Unique Characteristics of Exhaust-Plume Interference. J. Aircraft, vol. 10, no. 8, Aug. 1973, pp. 508-511.

14. Grund, E.; Presz, W., Jr.; and Konarski, M.: Predicting Airframe/Exhaust Nozzle Interactions at Transonic Mach Numbers. AIAA Paper No. 71-720, June 1971.

15. Hill, Philip G.; and Peterson, Carl R.: Mechanics and Thermodynamics of Propulsion. Addison-Wesley Pub. Co., Inc., c.1965.

16. Englert, Gerald W.: Operational Method of Determining Initial Contour of and Pressure Field About a Supersonic Jet. NASA TN D-279, 1960.

17. Nagamatsu, H. T.; Sheer, R. E., Jr.; and Gill, M. S.: Flow and Acoustic Characteristics of Subsonic and Supersonic Jets From Convergent Nozzle. NASA CR-1693, 1970.

18. Reubush, David E.: Effects of Fineness and Closure Ratios on Boattail Drag of Circular-Arc Afterbody Models With Jet Exhaust at Mach Numbers up to 1.30. NASA TN D-7163, 1973.

19. Reubush, David E.; and Runckel, Jack F.: Effect of Fineness Ratio on the Boattail Drag of Circular-Arc Afterbodies Having Closure Ratios of 0.50 With Jet Exhaust at Mach Numbers up to 1.30. NASA TN D-7192, 1973.

20. Hess, J. L.; and Smith, A. M. O.: Calculation of Potential Flow About Arbitrary Bodies. Progress in Aeronautical Sciences, Vol. 8, D. Kuchemann, ed., Pergamon Press, Ltd., c.1967, pp. 1-138.

21. Keith, J. S.; Ferguson, D. R.; Merkle, C. L.; Heck, P. H.; and Lahti, D. J.: Analytical Method for Predicting the Pressure Distribution About a Nacelle at Transonic Speeds. NASA CR-2217, 1973.

22. Anon.: Users Manual for the External Drag and Internal Nozzle Performance Deck (Deck XI) – Supersonic Flow Analysis (Applicable to Deck VI). PWA-3465, Suppl. F, Pt. I (Contract No. AF33(615)-3128), Pratt & Whitney Aircraft, Sept. 1, 1968.

23. Reubush, David E.: An Experimental Investigation of Jet Plume Simulation With Solid Circular Cylinders. NASA TM X-71963, 1974.

24. Ward, Vernon G.; Whitcomb, Charles F.; and Pearson, Merwin D.: Air-Flow and Power Characteristics of the Langley 16-Foot Transonic Tunnel With Slotted Test Section. NACA RM L52E01, 1952.

25. Schaefer, William T., Jr.: Characteristics of Major Active Wind Tunnels at the Langley Research Center. NASA TM X-1130, 1965.

26. Corson, Blake W., Jr.; Runckel, Jack F.; and Igoe, William B.: Calibration of the Langley 16-Foot Transonic Tunnel With Test Section Air Removal. NASA TR R-423, 1974.

27. Braslow, Albert L.; and Knox, Eugene C.: Simplified Method for Determination of Critical Height of Distributed Roughness Particles for Boundary-Layer Transition at Mach Numbers From 0 to 5. NACA TN 4363, 1958.

28. Braslow, Albert L.; Hicks, Raymond M.; and Harris, Roy V., Jr.: Use of Grit-Type Boundary-Layer-Transition Trips on Wind-Tunnel Models. NASA TN D-3579, 1966.

TABLE I.- AFTERBODY-SURFACE ORIFICE LOCATIONS

x/l	x/d_m	Orifice located at ϕ, deg, of –									
		0	30	60	90	120	135	150	180	225	315
Configuration 1											
0	0	x		x	x			x	x	x	x
.2165	.1732	x	x		x	x			x		
.3775	.3020	x		x	x			x	x		
.4913	.3930	x	x	x	x	x		x	x	x	x
.5863	.4690	x	x	x	x	x		x	x		
.6710	.5368	x	x	x	x	x		x	x		
.7498	.5998	x	x	x	x	x		x	x	x	x
.8248	.6598	x	x	x	x	x		x	x		
.8981	.7185	x	x	x	x	x		x	x		
.9717	.7773	x	x	x	x	x		x	x	x	x
Configuration 2											
0	0	x		x	x			x	x	x	x
.2132	.2132	x	x		x	x			x		
.3723	.3723	x		x	x			x	x		
.4852	.4852	x	x	x	x	x		x	x	x	x
.5800	.5800	x	x	x	x	x		x	x		
.6648	.6648	x	x	x	x	x		x	x		
.7442	.7442	x	x	x	x	x		x	x	x	x
.8202	.8202	x	x	x	x	x		x	x		
.8950	.8950	x	x	x	x	x		x	x		
.9707	.9707	x	x	x	x	x		x	x	x	x
Configuration 3											
0	0	x		x	x			x	x	x	x
.2092	.3698	x	x		x	x			x		
.3661	.6472	x		x	x			x	x		
.4778	.8447	x	x	x	x	x		x	x	x	x
.5722	1.0115	x	x	x	x	x		x	x		
.6573	1.1620	x	x	x	x	x		x	x		
.7373	1.3033	x	x	x	x	x		x	x	x	x
.8146	1.4400	x	x	x	x	x		x	x		
.8912	1.5755	x	x	x	x	x		x	x		
.9694	1.7137	x	x	x	x	x		x	x	x	x
Configuration 4											
0	0	x	x	x	x	x		x	x	x	x
.2365	.2365	x	x	x	x	x		x	x		
.4133	.4133	x	x	x	x	x		x	x		
.5388	.5388	x	x	x	x	x		x	x	x	x
.6443	.6443	x	x	x	x	x		x	x		
.7392	.7392	x	x	x	x	x		x	x		
.8278	.8278	x	x	x	x	x		x	x	x	x
.9130	.9130	x	x	x	x	x		x	x		
.9667	.9667	x	x	x	x	x		x	x		

TABLE I.- AFTERBODY-SURFACE ORIFICE LOCATIONS – Concluded

x/l	x/d_m	Orifice located at ϕ, deg, of –									
		0	30	60	90	120	135	150	180	225	315
Configuration 5											
0	0	x	x	x	x		x		x	x	x
.2343	.3513	x	x	x	x		x		x		
.4098	.6147	x	x	x	x		x		x		
.5349	.8023	x	x	x	x		x		x	x	x
.6404	.9607	x	x	x	x		x		x		
.7357	1.1035	x	x	x	x		x		x		
.8250	1.2375	x	x	x	x		x		x	x	x
.9113	1.3670	x	x	x	x		x		x		
.9722	1.4583	x	x	x	x		x		x		
Configuration 6											
0	0	x	x	x	x		x		x	x	x
.2720	.2620	x	x	x	x		x		x		
.4758	.4758	x	x	x	x		x		x		
.6205	.6205	x	x	x	x		x		x	x	x
.7425	.7425	x	x	x	x		x		x		
.8523	.8523	x	x	x	x		x		x		
.9550	.9550	x	x	x	x		x		x	x	x
Configuration 7											
0	0	x	x	x	x		x		x	x	x
.2706	.4058	x	x	x	x		x		x		
.4737	.7105	x	x	x	x		x		x		
.6183	.9275	x	x	x	x		x		x	x	x
.7406	1.1108	x	x	x	x		x		x		
.8509	1.2763	x	x	x	x		x		x		
.9546	1.4318	x	x	x	x		x		x	x	x
Configuration 8											
0	0	x	x	x	x		x		x	x	x
.2701	.5402	x	x	x	x		x		x		
.4729	.9458	x	x	x	x		x		x		
.6176	1.2352	x	x	x	x		x		x	x	x
.7399	1.4798	x	x	x	x		x		x		
.8504	1.7008	x	x	x	x		x		x		
.9544	1.9088	x	x	x	x		x		x	x	x

TABLE II.- SIMULATOR-SURFACE ORIFICE LOCATIONS

Orifice locations for –									
Configuration 1		Configurations 2, 4, and 6		Configuration 3		Configurations 5 and 7		Configuration 8	
x/l	x/d_m	x/l	x/d_m	x/l	x/d_m	x/l	x/d_m	x/l	x/d_m
1.104	0.883	1.083	1.083	1.047	1.851	1.056	1.583	1.042	2.083
1.208	.967	1.167	1.167	1.094	1.935	1.111	1.667	1.083	2.167
1.313	1.050	1.250	1.250	1.141	2.018	1.167	1.750	1.125	2.250
1.417	1.133	1.333	1.333	1.189	2.101	1.222	1.833	1.167	2.333
1.521	1.217	1.417	1.417	1.236	2.185	1.278	1.917	1.208	2.417
1.625	1.300	1.500	1.500	1.283	2.268	1.333	2.000	1.250	2.500
1.729	1.383	1.583	1.583	1.330	2.351	1.389	2.083	1.292	2.583
1.833	1.467	1.667	1.667	1.377	2.435	1.444	2.167	1.333	2.667
1.938	1.550	1.750	1.750	1.424	2.518	1.500	2.250	1.375	2.750
2.042	1.633	1.833	1.833	1.471	2.601	1.556	2.333	1.417	2.833
2.146	1.717	1.917	1.917	1.519	2.685	1.611	2.417	1.458	2.917
2.250	1.800	2.000	2.000	1.566	2.768	1.667	2.500	1.500	3.000
2.458	1.967	2.167	2.167	1.660	2.935	1.778	2.667	1.583	3.167
2.667	2.133	2.333	2.333	1.754	3.101	1.889	2.833	1.667	3.333
2.875	2.300	2.500	2.500	1.848	3.268	2.000	3.000	1.750	3.500
3.083	2.467	2.667	2.667	1.943	3.435	2.111	3.167	1.833	3.667

TABLE III.- CLOSED BODY GEOMETRIC DATA

Configuration	l/d_m	β	β_c
1	1.0856	49.4575	24.7287
2	1.3832	39.7472	19.8736
3	2.5000	22.6199	11.3099
4	1.5529	35.6941	17.8471
5	2.3700	23.8264	11.9132
6	1.8085	30.9088	15.4544
7	2.7534	20.5849	10.2925
8	3.6899	15.4336	7.7168

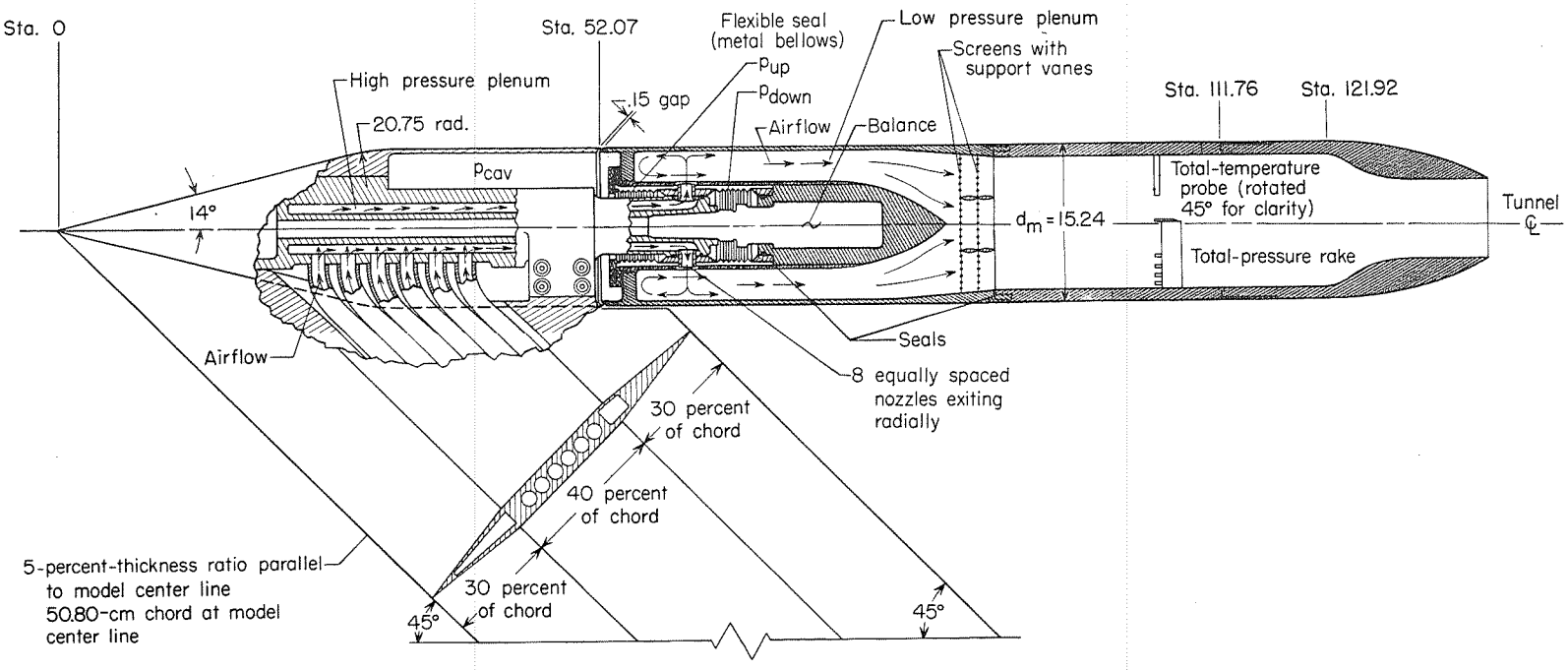

Figure 1.- Sketch of air-powered cone-cylinder model with a typical circular-arc convergent nozzle installed. All dimensions are in centimeters unless otherwise noted.

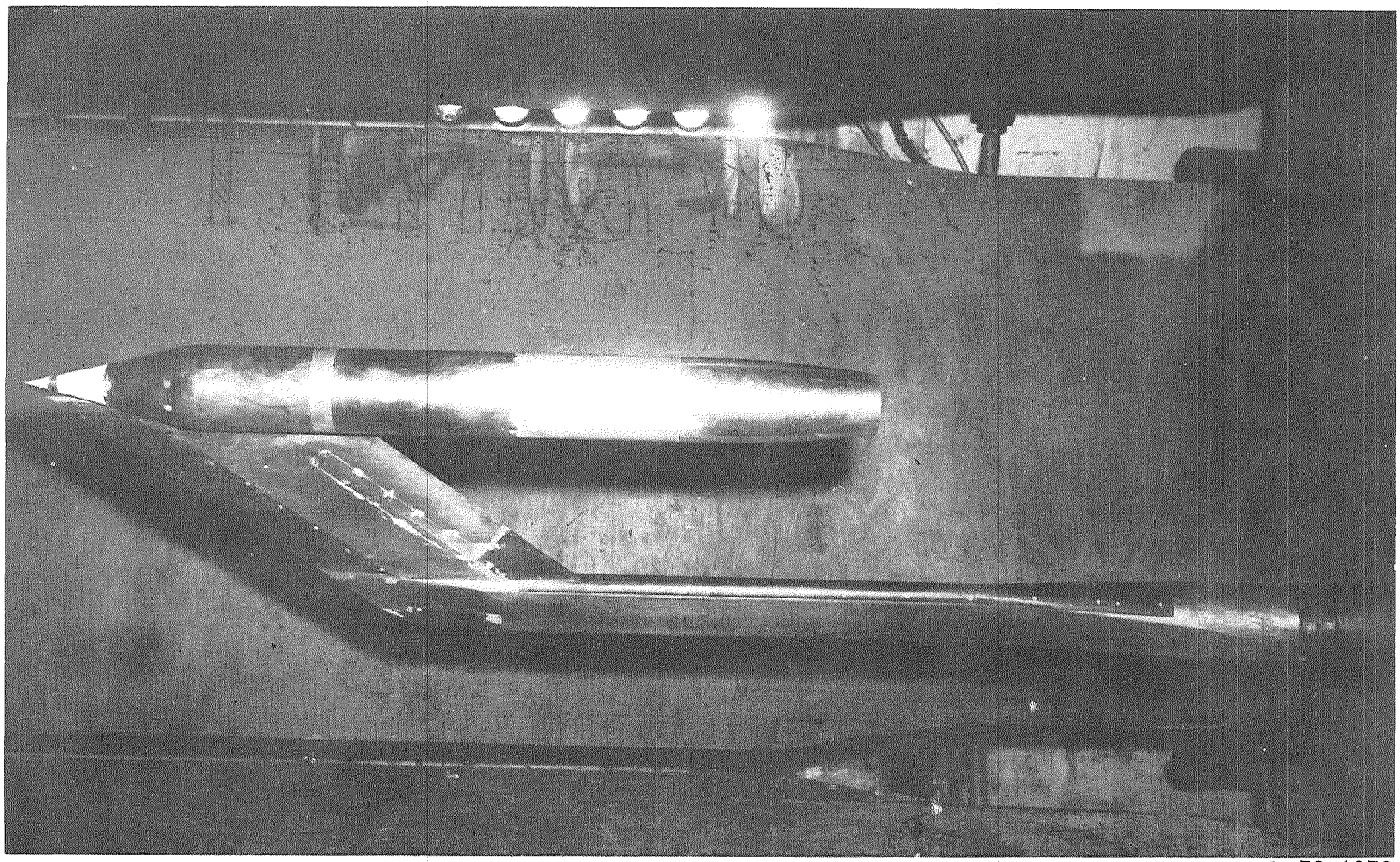

L-72-1872

Figure 2.- Air-powered model with configuration 8 attached, installed in the Langley 16-foot transonic tunnel.

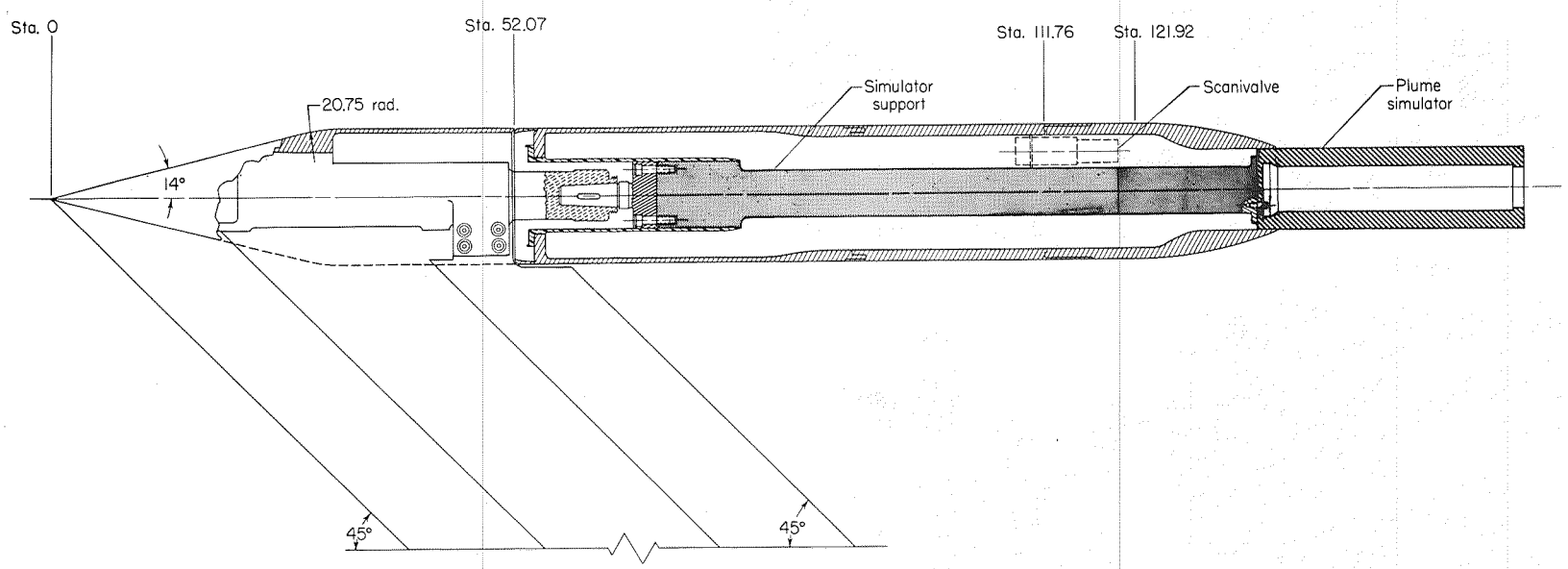

Figure 3.- Sketch of cone-cylinder nacelle model showing internal sting arrangement for support of simulators.

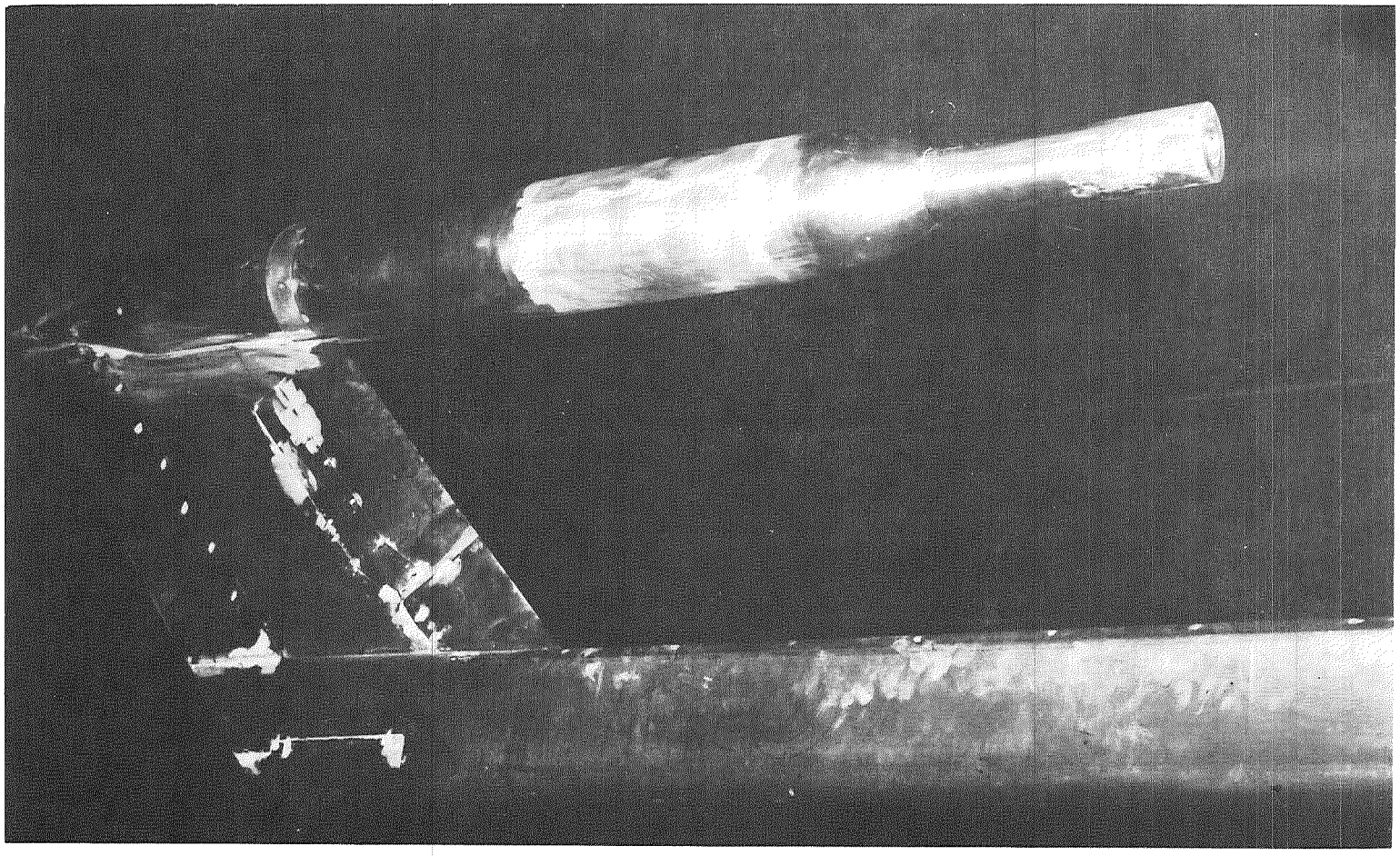

L-73-9559

Figure 4.- Nacelle model installed in the Langley 16-foot transonic tunnel with typical circular-arc afterbody and $d_s/d_e = 1.00$ simulator attached.

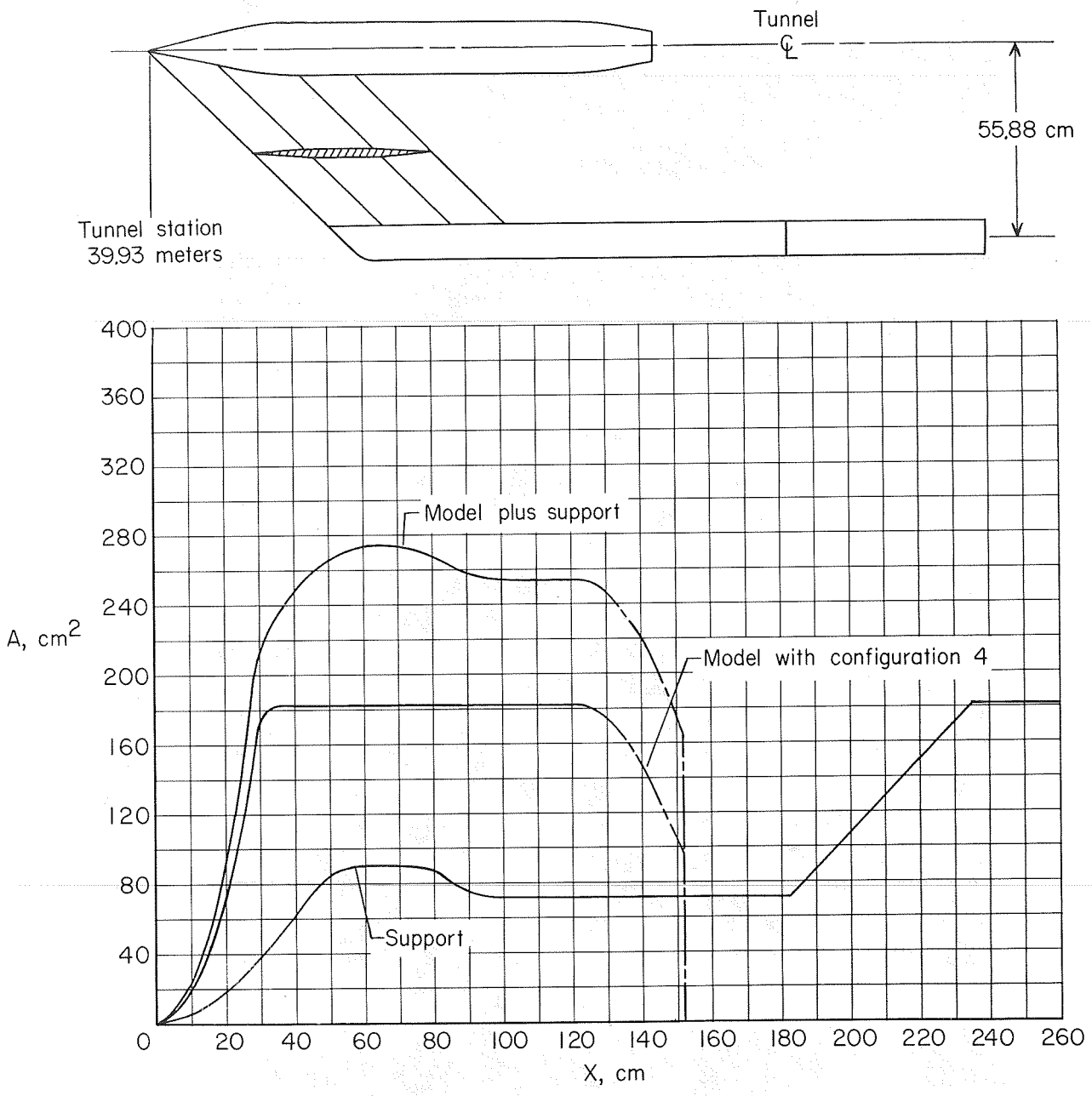

Figure 5.- Sketch of model and support system with corresponding cross-sectional area distributions.

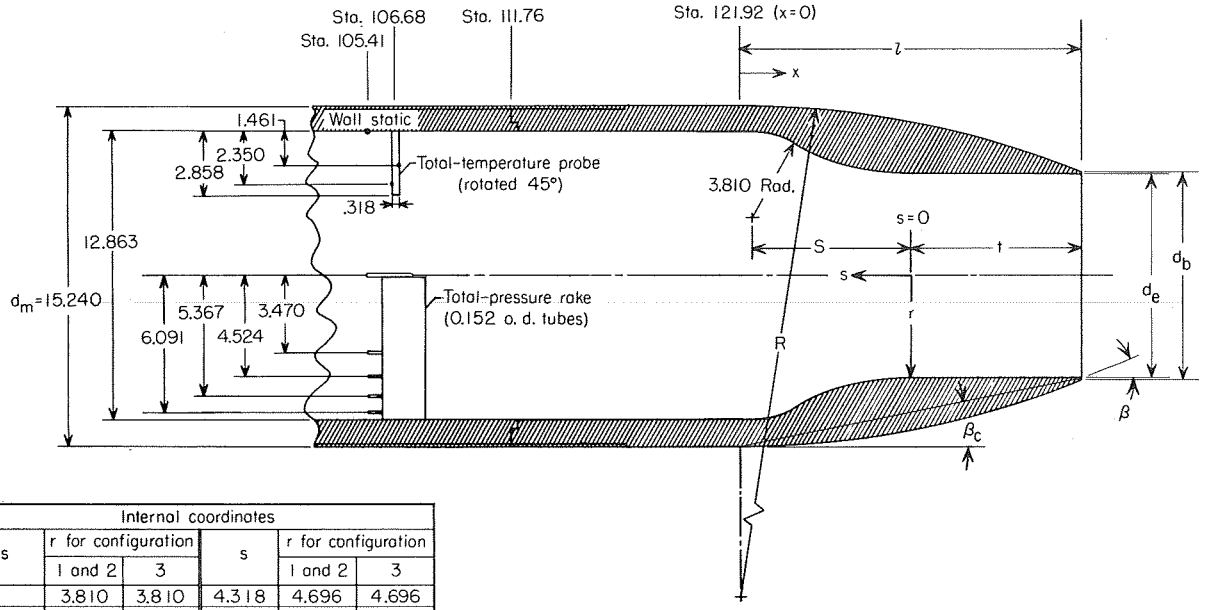

Internal coordinates					
s	r for configuration		s	r for configuration	
	1 and 2	3		1 and 2	3
0	3.810	3.810	4.318	4.696	4.696
.254	3.813	3.813	4.445	4.755	4.755
.508	3.820	3.820	4.572	4.816	4.816
.762	3.835	3.835	4.699	4.882	4.882
1.016	3.856	3.856	4.826	4.948	4.948
1.270	3.881	3.881	4.953	5.019	5.019
1.524	3.912	3.912	5.080	5.090	5.090
1.778	3.950	3.950	5.207	5.169	5.169
2.032	3.993	3.993	5.334	5.248	5.248
2.286	4.041	4.041	5.461	5.334	5.334
2.540	4.097	4.097	5.588	5.420	5.420
2.794	4.161	4.161	5.715	5.514	5.514
3.048	4.229	4.229	5.842	5.611	5.611
3.302	4.308	4.308	5.969	5.715	5.715
3.556	4.392	4.392	6.096	5.822	5.822
3.810	4.483	4.483	6.223	5.939	——
3.937	4.534	4.534	6.350	6.060	——
4.064	4.585	4.585	6.477	6.190	——
4.191	4.641	4.641			

Geometric parameters								
Configuration	l/d_m	d_e/d_m	d_b/d_m	R/d_m	t/d_m	S/d_m	β, deg	β_c, deg
1	0.800	0.50	0.51	1.429	0.50	0.533	34.054	17.027
2	1.000	.50	.51	2.163	.50	.533	27.533	13.766
3	1.768	.50	.51	6.500	.50	.458	15.781	7.891

(a) Configurations 1 to 3.

Figure 6.- Detailed sketch of typical configuration with tables of geometric parameters and internal coordinates. All dimensions are in centimeters unless otherwise noted.

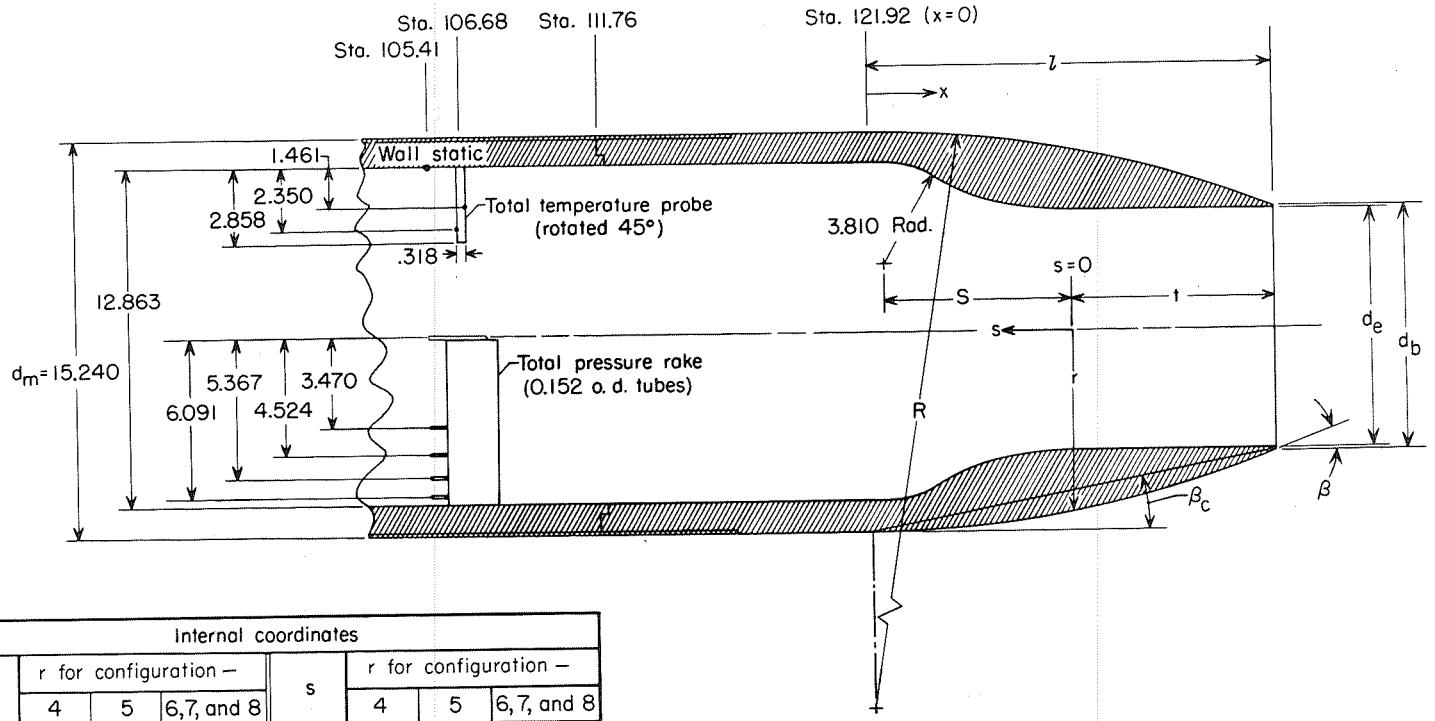

Internal coordinates							
s	r for configuration —			s	r for configuration —		
	4	5	6, 7, and 8		4	5	6, 7, and 8
0	4.572	4.572	5.334	4.318	5.458	5.052	5.618
.254	4.575	4.575	5.337	4.445	5.517	—	—
.508	4.582	4.577	5.339	4.572	5.578	5.123	5.659
.762	4.597	4.585	5.342	4.699	5.644	—	—
1.016	4.618	4.595	5.349	4.826	5.710	5.202	5.705
1.270	4.643	4.608	5.357	4.953	5.781	5.245	—
1.524	4.674	4.625	5.364	5.080	5.852	5.291	5.758
1.778	4.712	4.646	5.377	5.207	5.931	5.339	5.786
2.032	4.755	4.669	5.390	5.334	6.010	5.392	5.819
2.286	4.803	4.694	5.405	5.461	6.096	5.448	5.852
2.540	4.859	4.722	5.423	5.588	6.182	5.512	5.888
2.794	4.923	4.757	5.443	5.715	6.276	5.578	5.928
3.048	4.991	4.793	5.466	5.842	6.373	5.654	5.972
3.302	5.070	4.836	5.489	5.969	6.477	5.738	6.022
3.556	5.154	4.882	5.517	6.096	6.584	5.839	6.081
3.810	5.245	4.933	5.547	6.223	6.701	5.961	6.154
3.937	5.296	—	—	6.350	6.822	6.137	6.259
4.064	5.347	4.991	5.580	6.431	—	6.431	6.431
4.191	5.403	—	—				

Geometric parameters								
Configuration	l/d_m	d_e/d_m	d_b/d_m	R/d_m	l/d_m	S/d_m	β, deg	β_c, deg
4	1.00	0.60	0.61	2.662	0.500	0.462	22.068	11.034
5	1.50	.60	.61	5.867	.592	.536	14.814	7.407
6	1.00	.70	.71	3.521	.367	.507	16.507	8.250
7	1.50	.70	.71	7.831	.667	.507	11.043	5.521
8	2.00	.70	.71	13.866	.833	.507	8.293	4.147

(b) Configurations 4 to 8.

Figure 6.- Concluded.

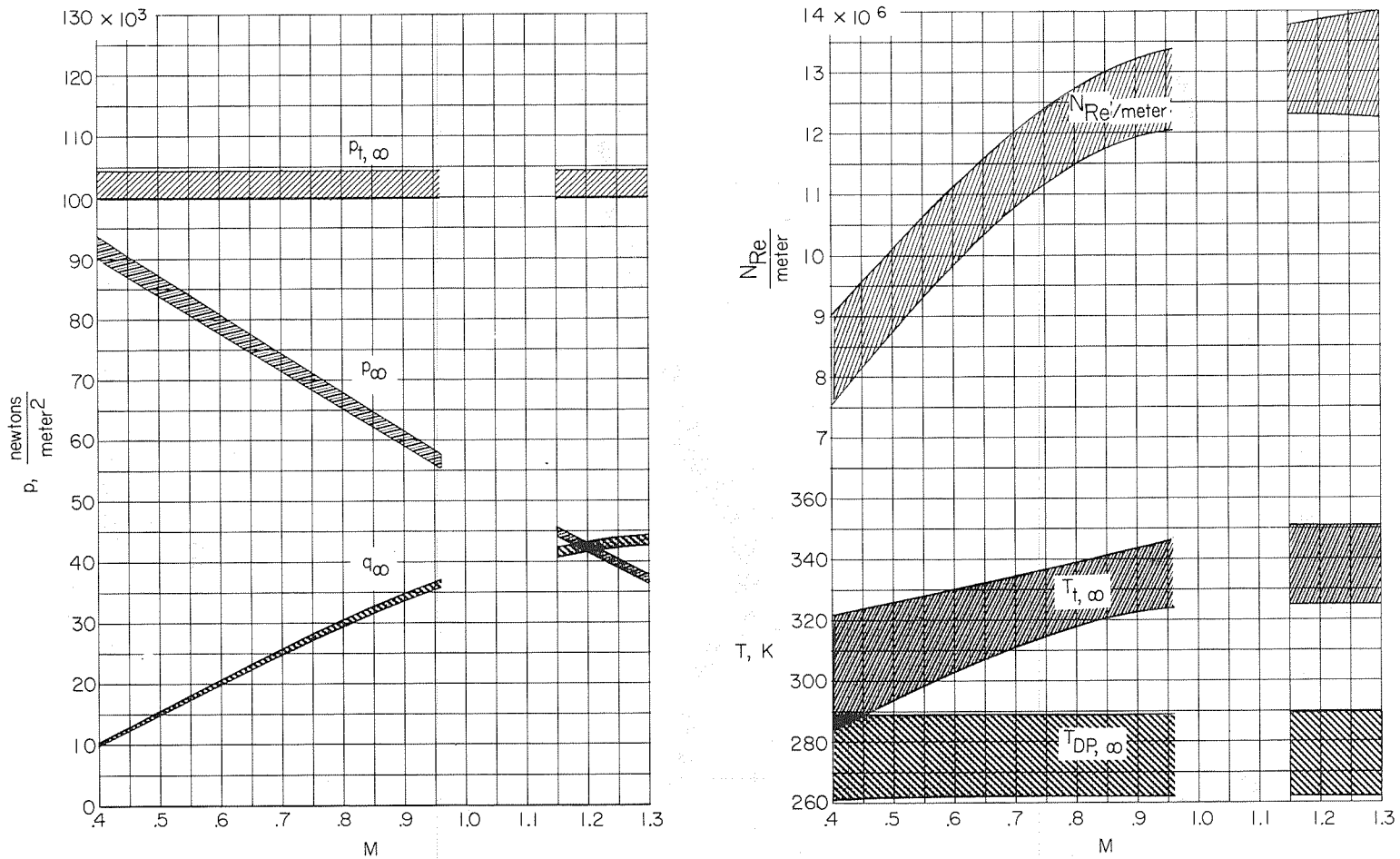

Figure 7.- Band of the free-stream parameters encountered during the investigation.

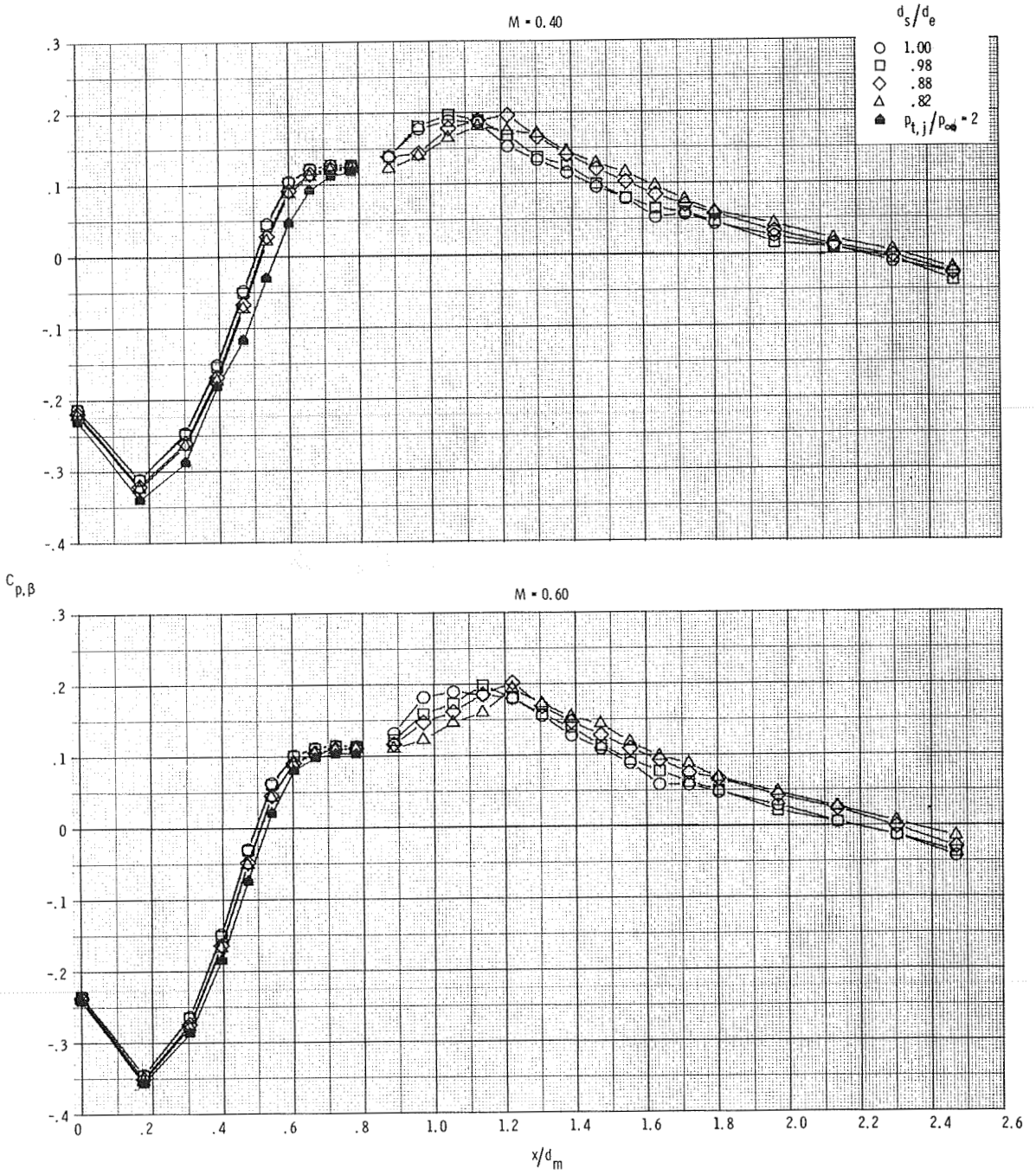

(a) M = 0.40 and 0.60.

Figure 8.- Comparison of pressure-coefficient distributions obtained through use of plume simulators with those obtained from jet operation at $p_{t,j}/p_\infty = 2$ for configuration 1 ($\ell/d_m = 0.80$, $d_e/d_m = 0.50$).

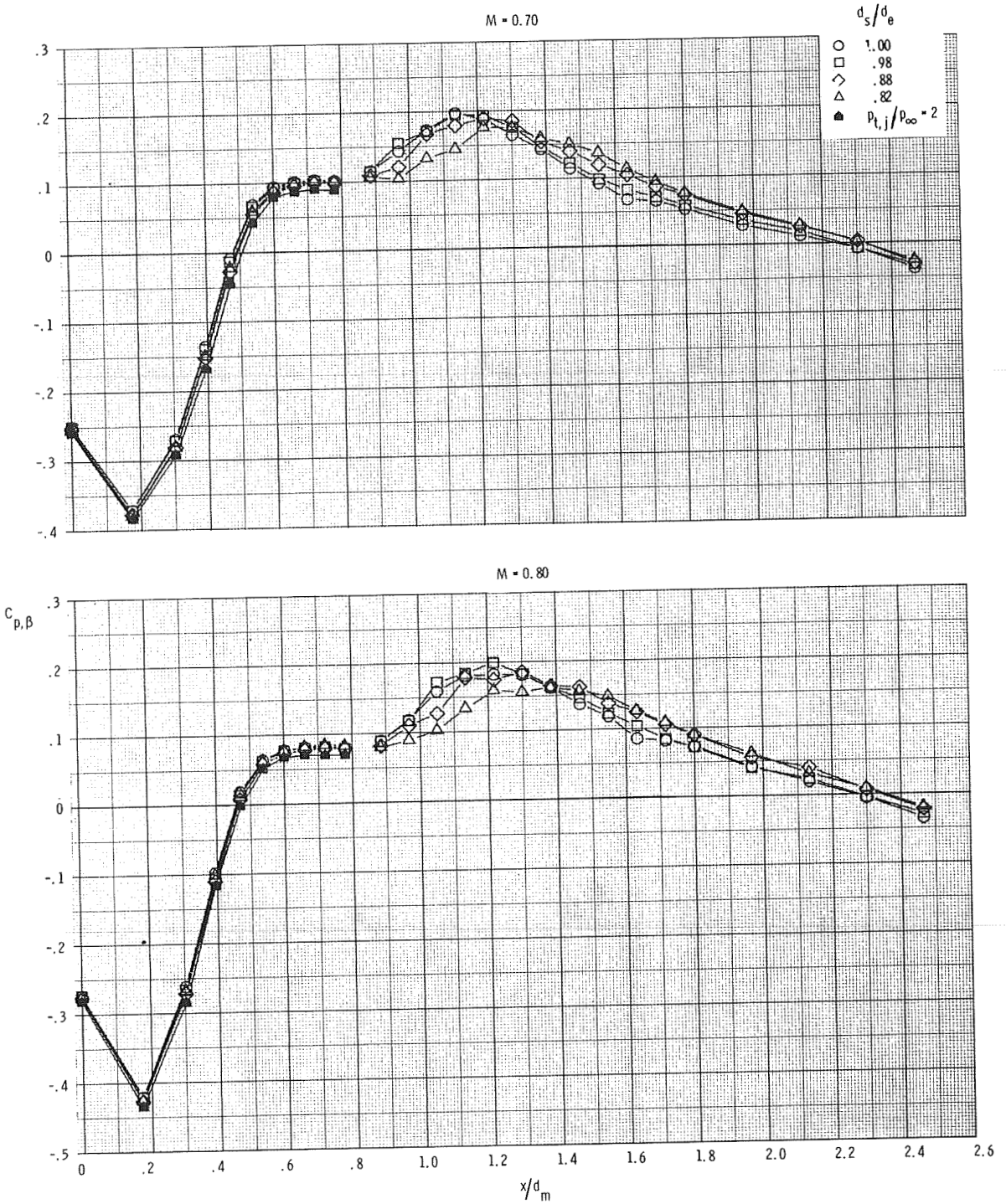

(b) M = 0.70 and 0.80.

Figure 8.- Continued.

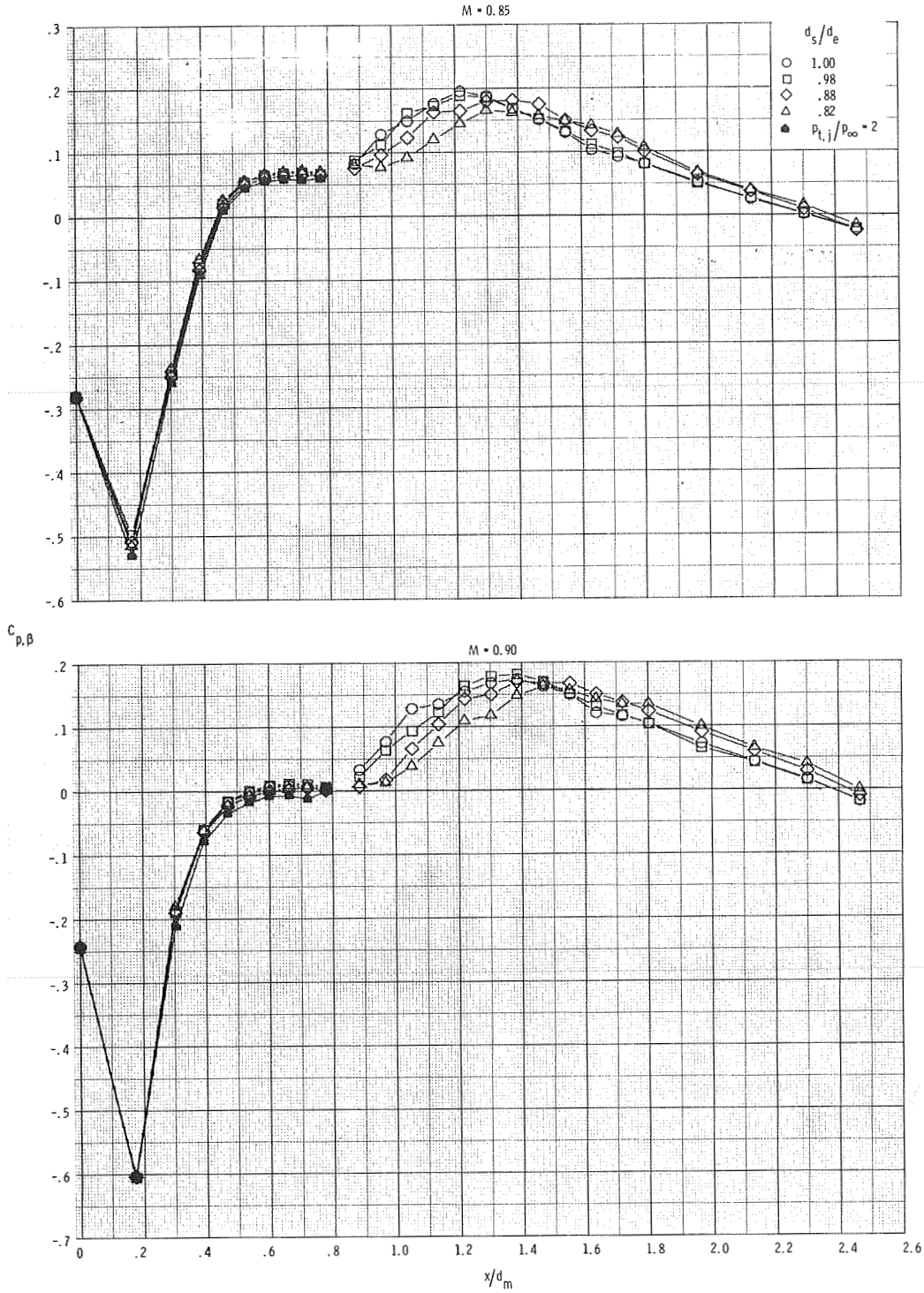

(c) M = 0.85 and 0.90.

Figure 8.- Continued.

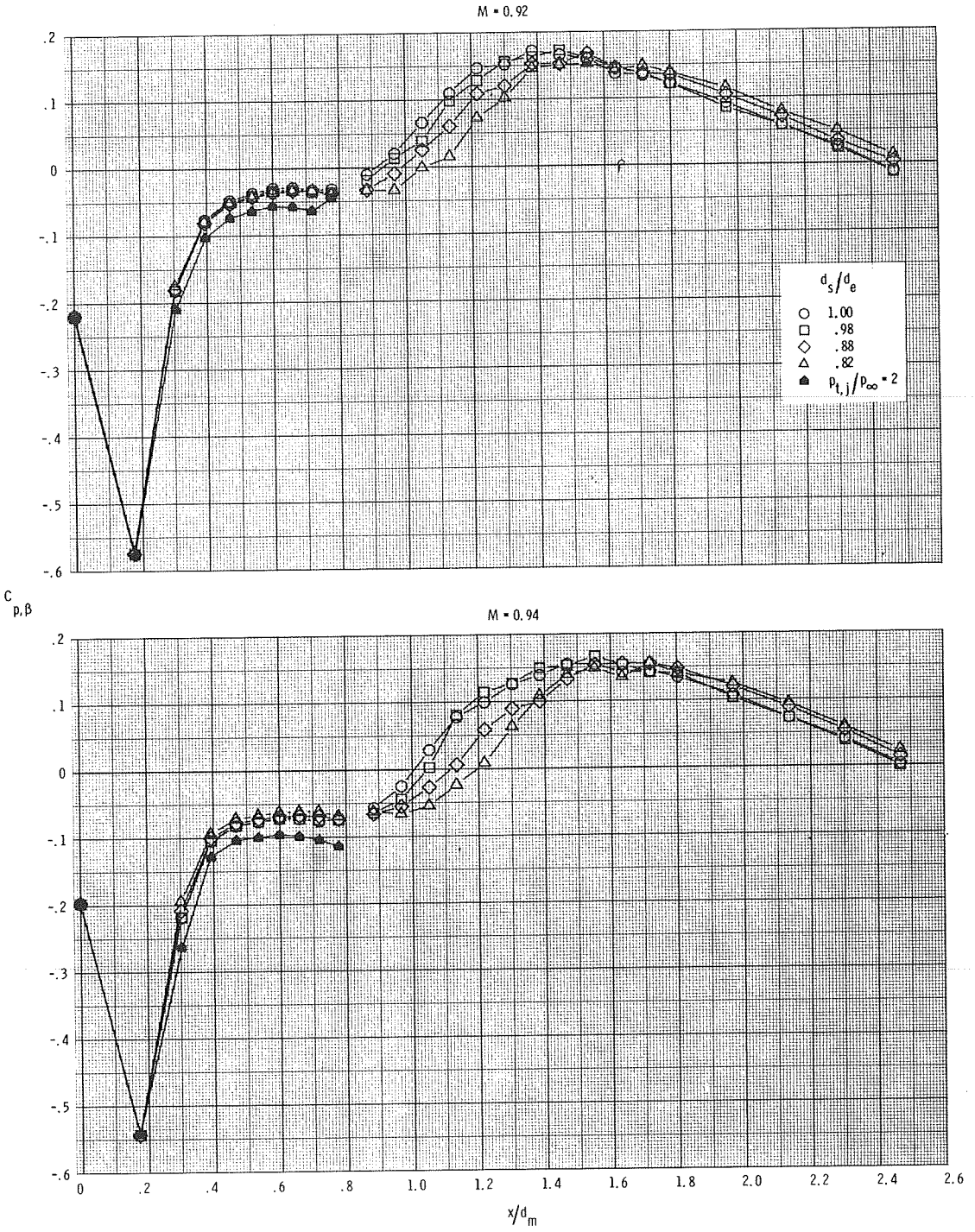

(d) M = 0.92 and 0.94.

Figure 8.- Continued.

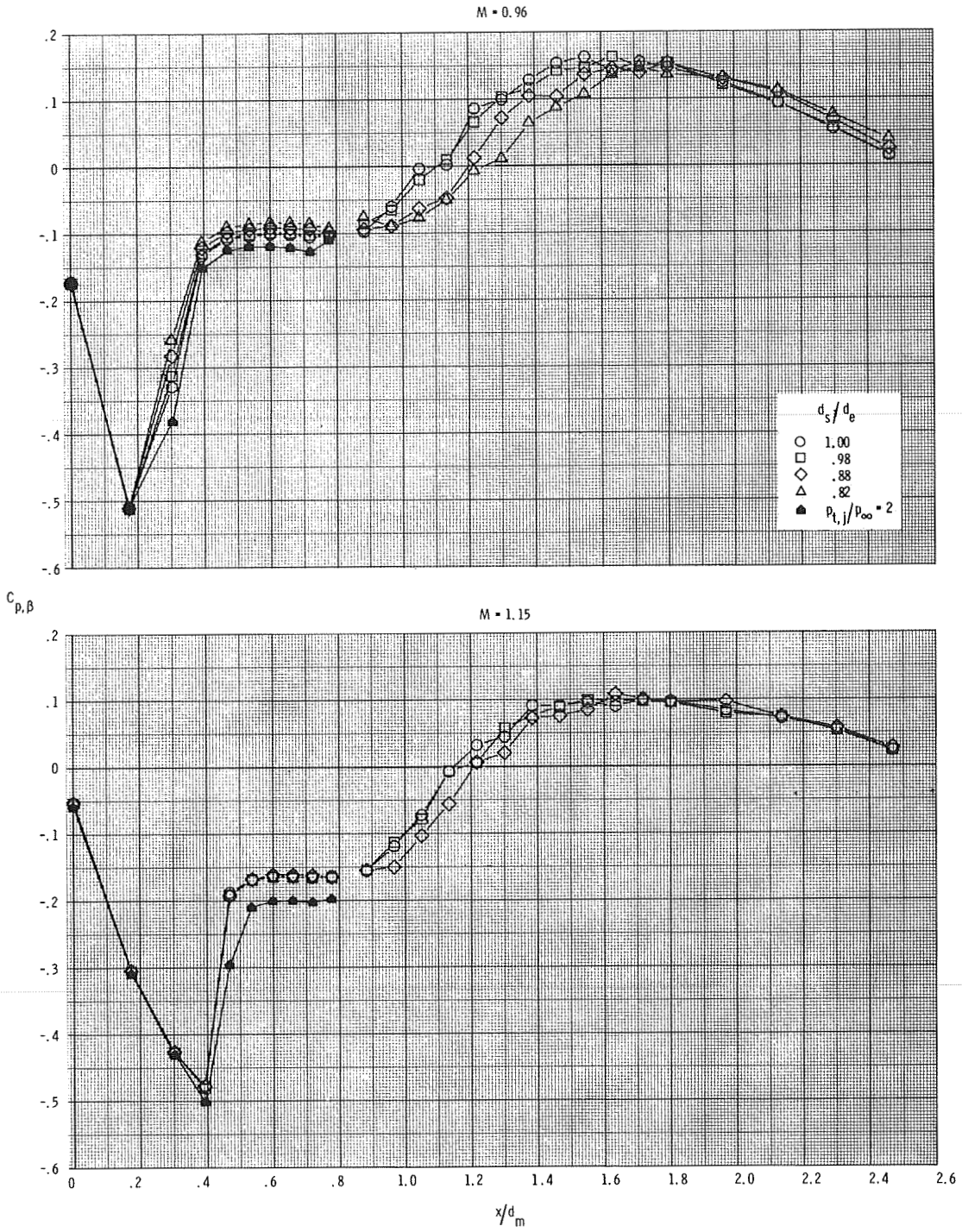

(e) M = 0.96 and 1.15.

Figure 8.- Continued.

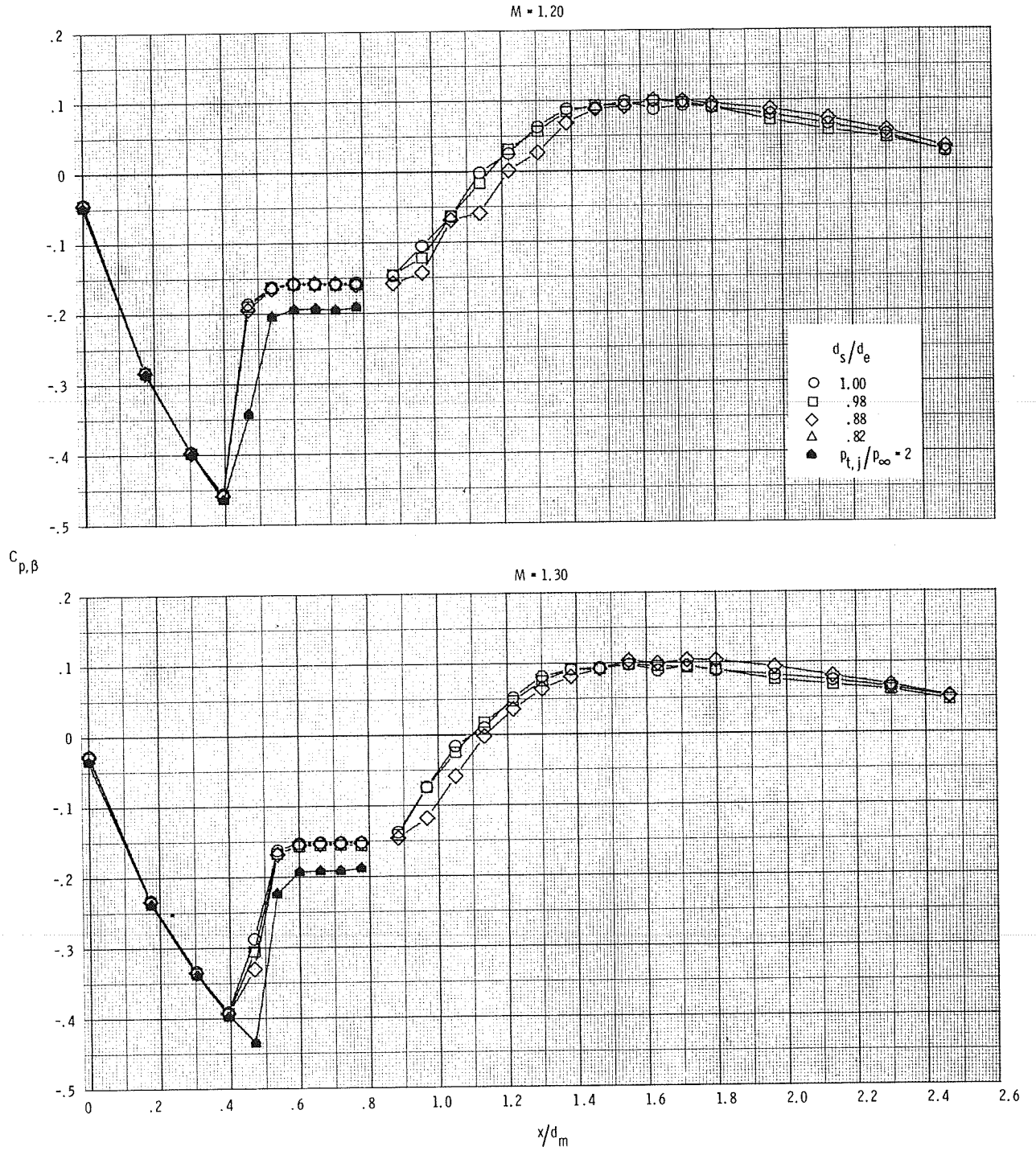

(f) M = 1.20 and 1.30.

Figure 8.- Concluded.

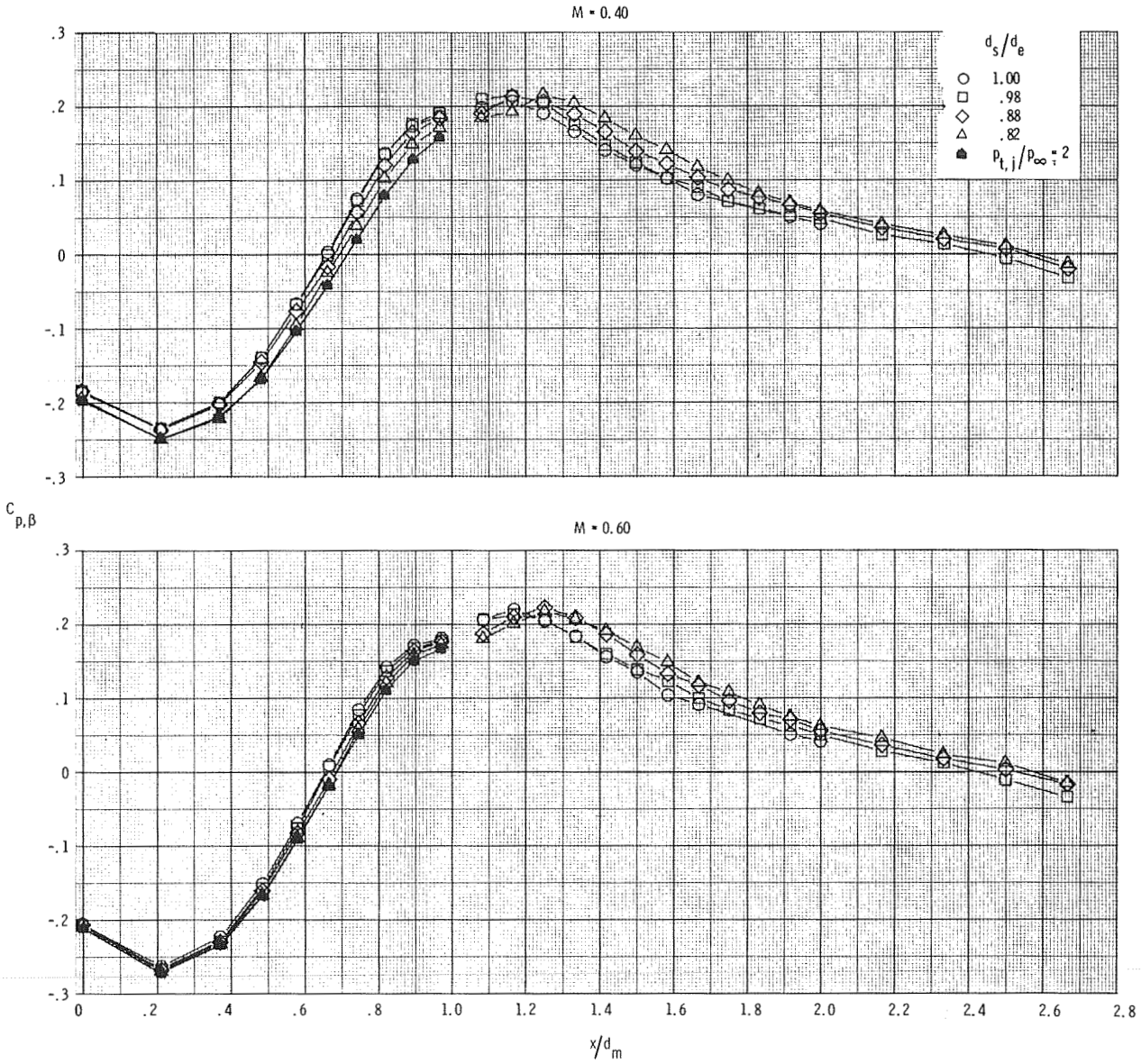

(a) M = 0.40 and 0.60.

Figure 9.- Comparison of pressure-coefficient distributions obtained through use of plume simulators with those obtained from jet operation at $p_{t,j}/p_\infty = 2$ for configuration 2 ($\ell/d_m = 1.00$, $d_e/d_m = 0.50$).

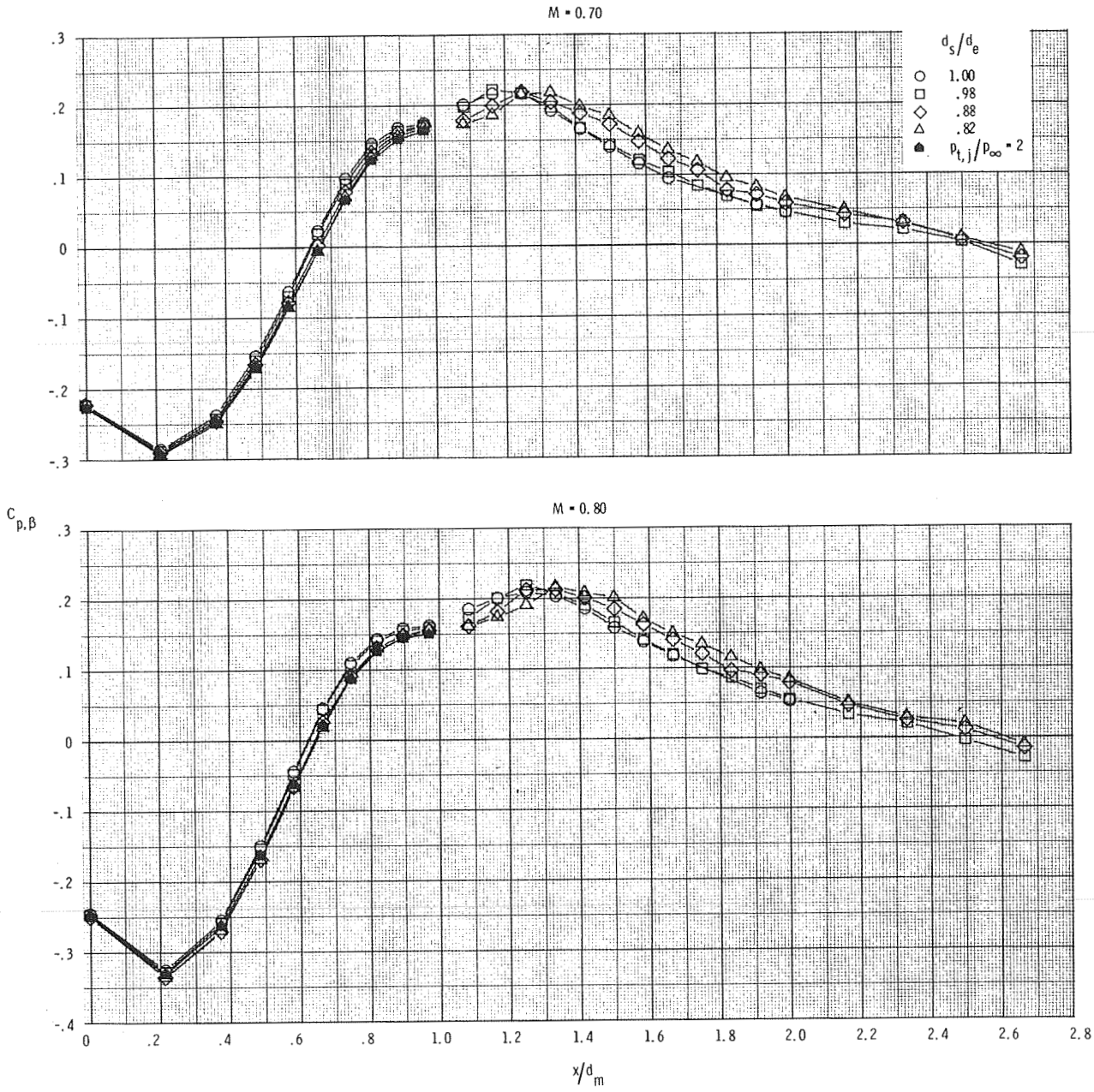

(b) M = 0.70 and 0.80.

Figure 9.- Continued.

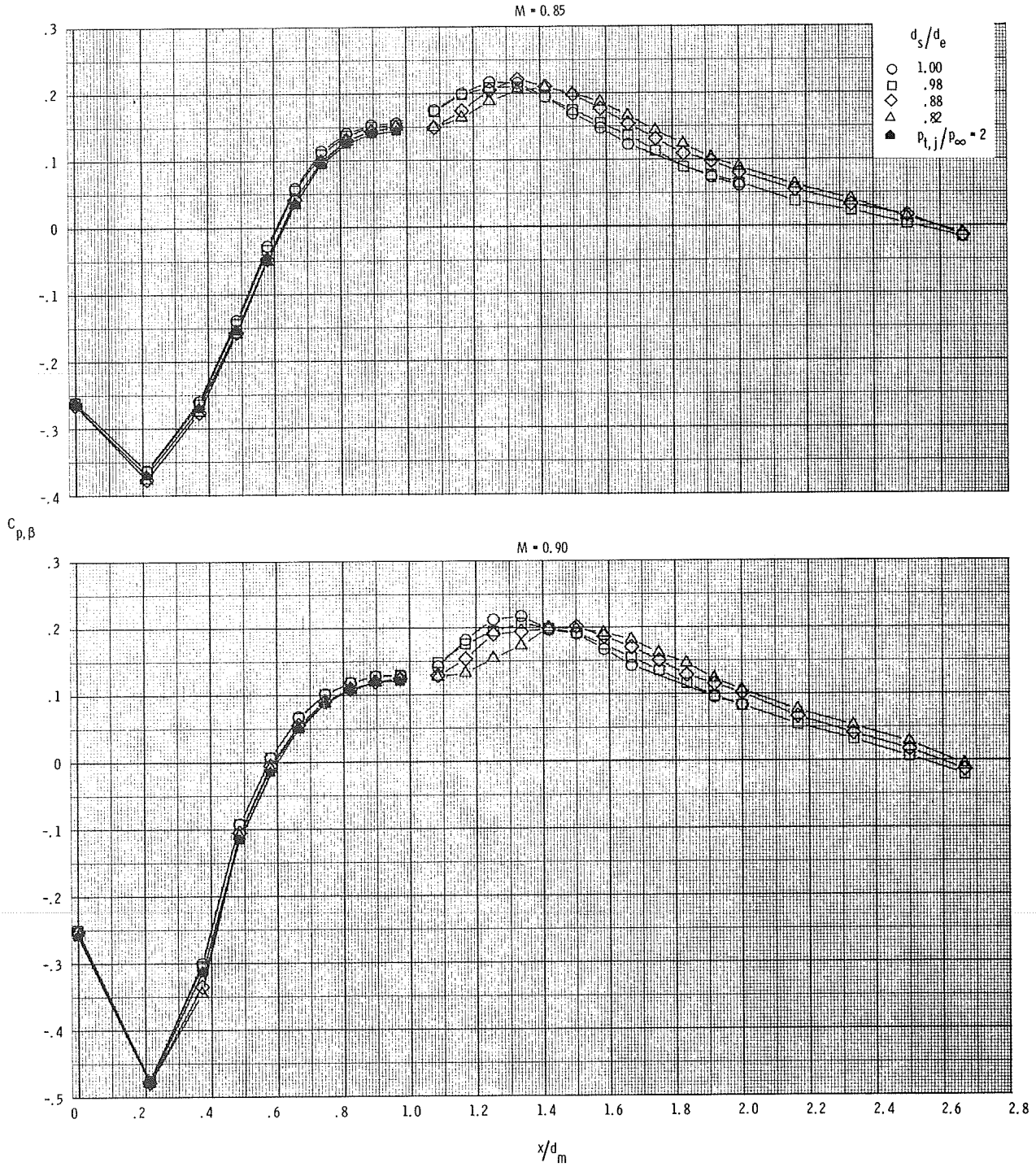

(c) M = 0.85 and 0.90.

Figure 9.- Continued.

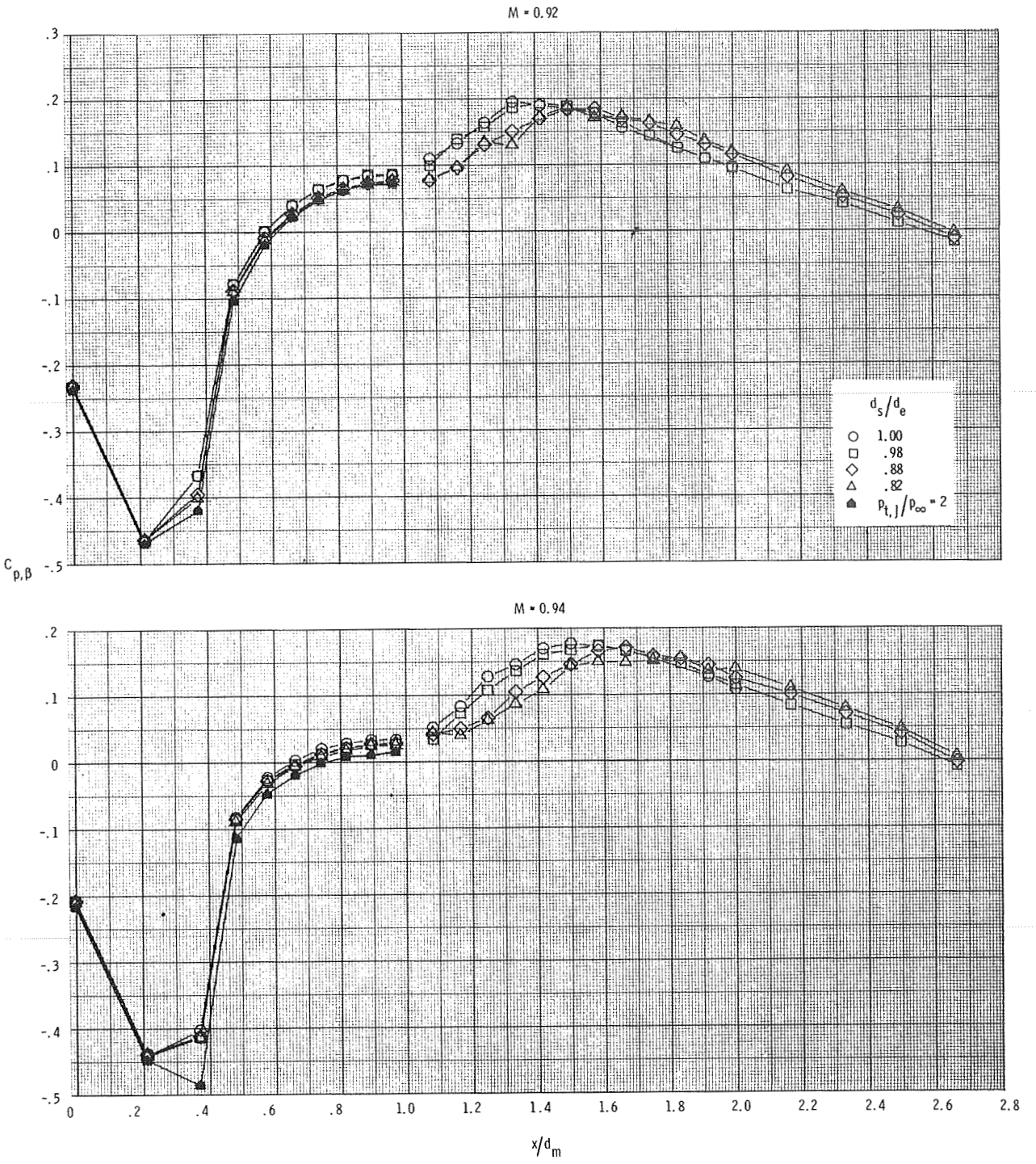

(d) M = 0.92 and 0.94.

Figure 9.- Continued.

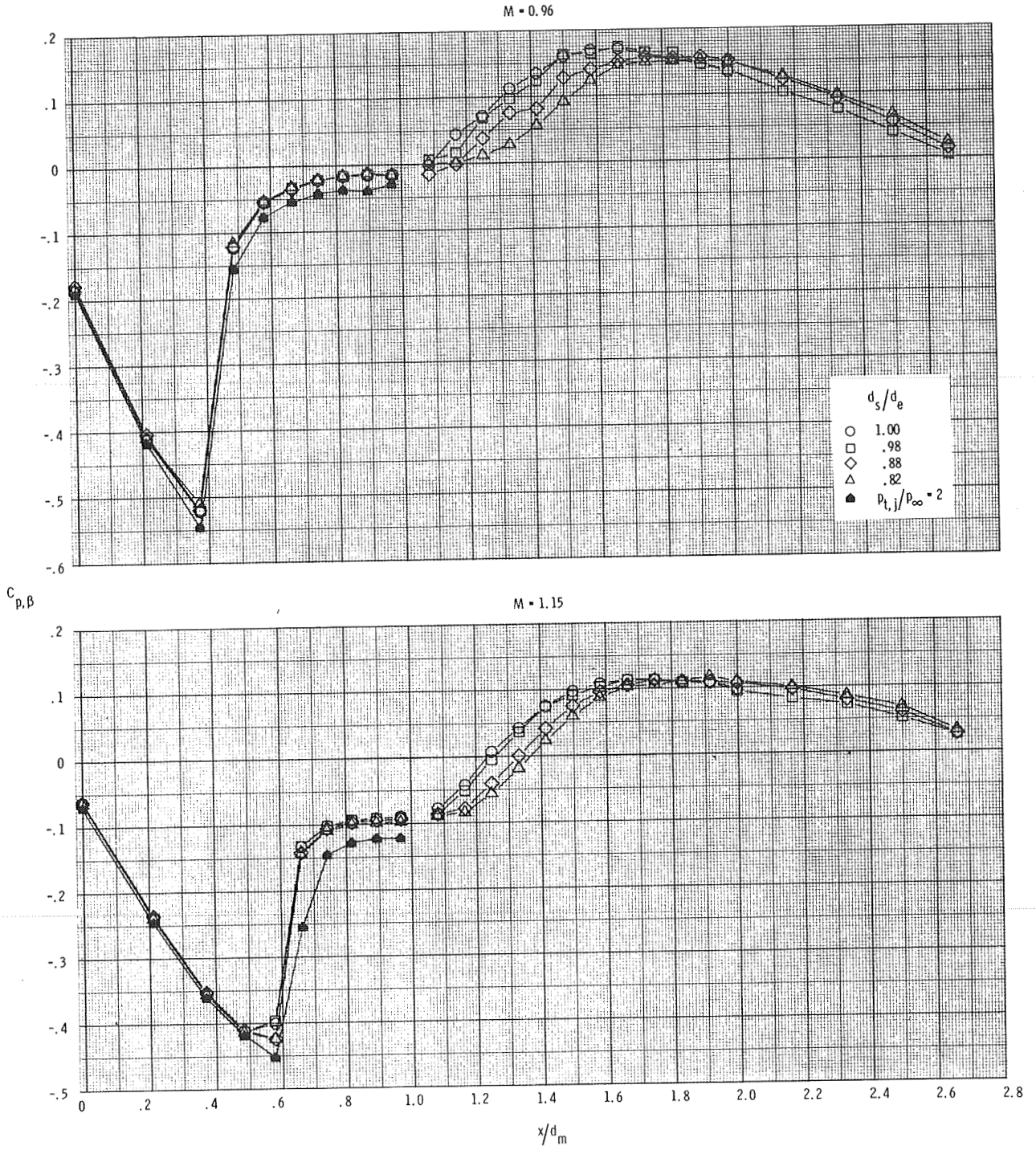

(e) M = 0.96 and 1.15.

Figure 9.- Continued.

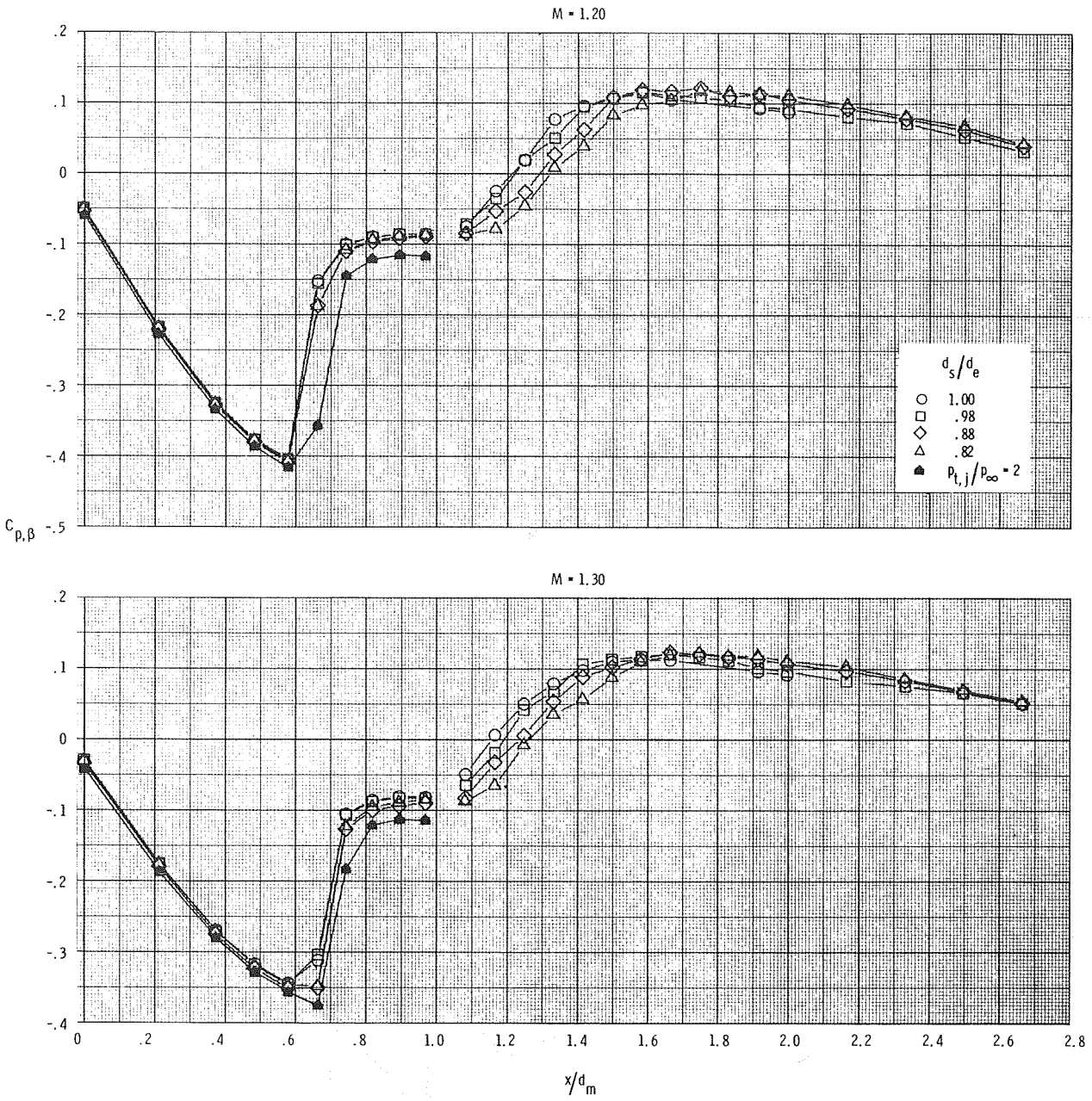

(f) M = 1.20 and 1.30.

Figure 9.- Concluded.

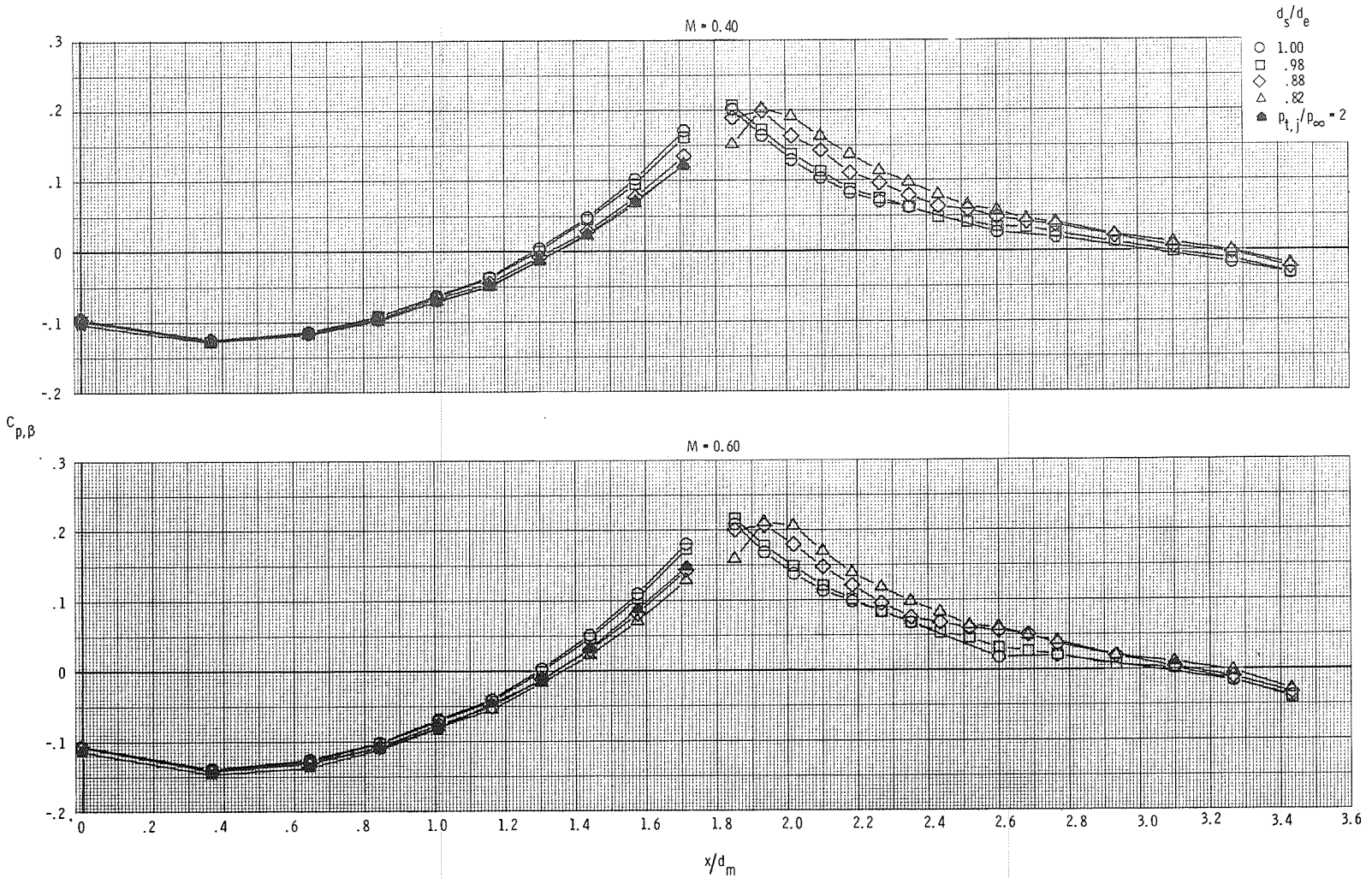

(a) M = 0.40 and 0.60.

Figure 10.- Comparison of pressure-coefficient distributions obtained through the use of plume simulators with those obtained from jet operation at $p_{t,j}/p_\infty = 2$ for configuration 3 ($l/d_m = 1.77$, $d_e/d_m = 0.50$).

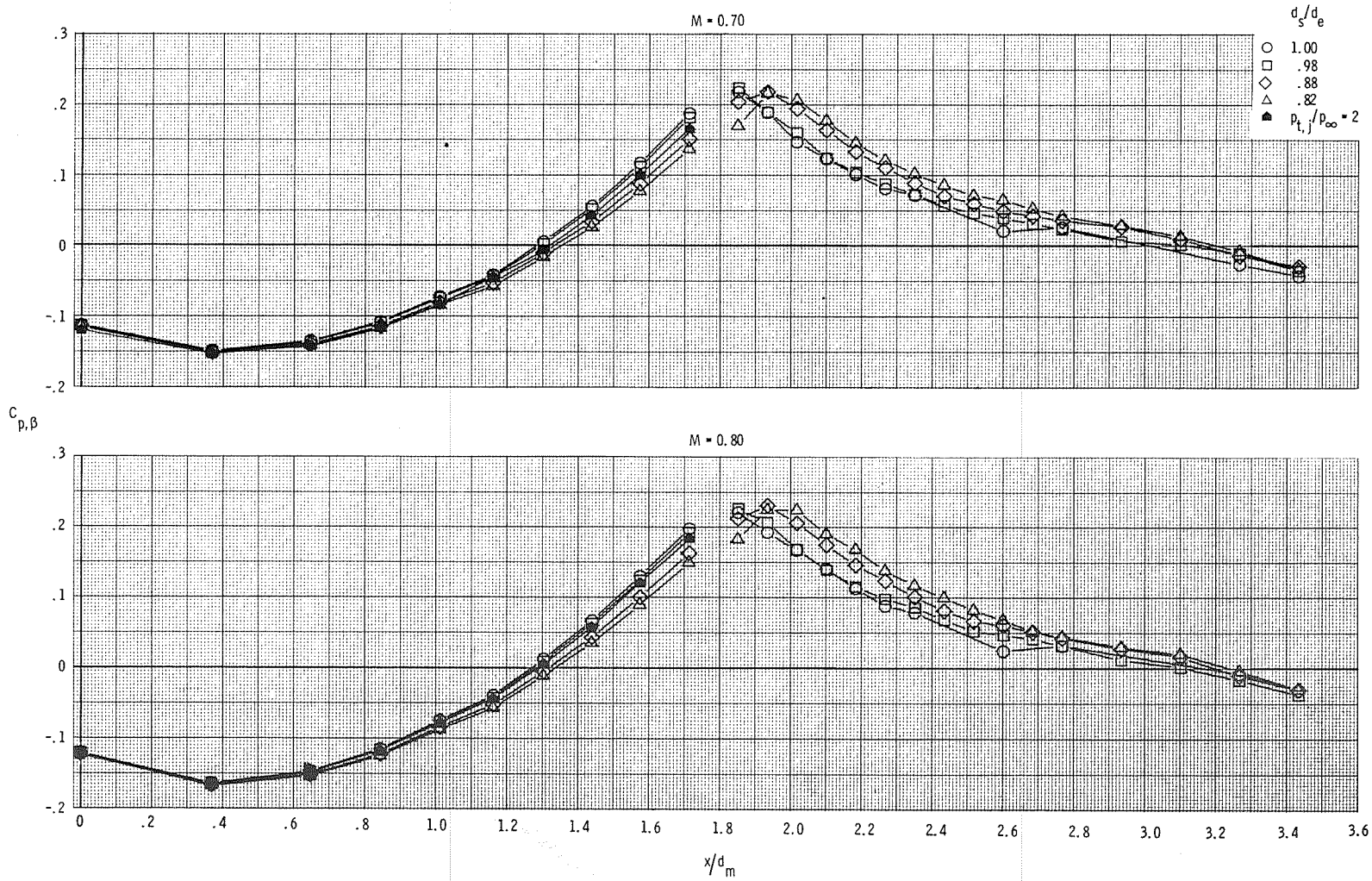

(b) M = 0.70 and 0.80.

Figure 10.- Continued.

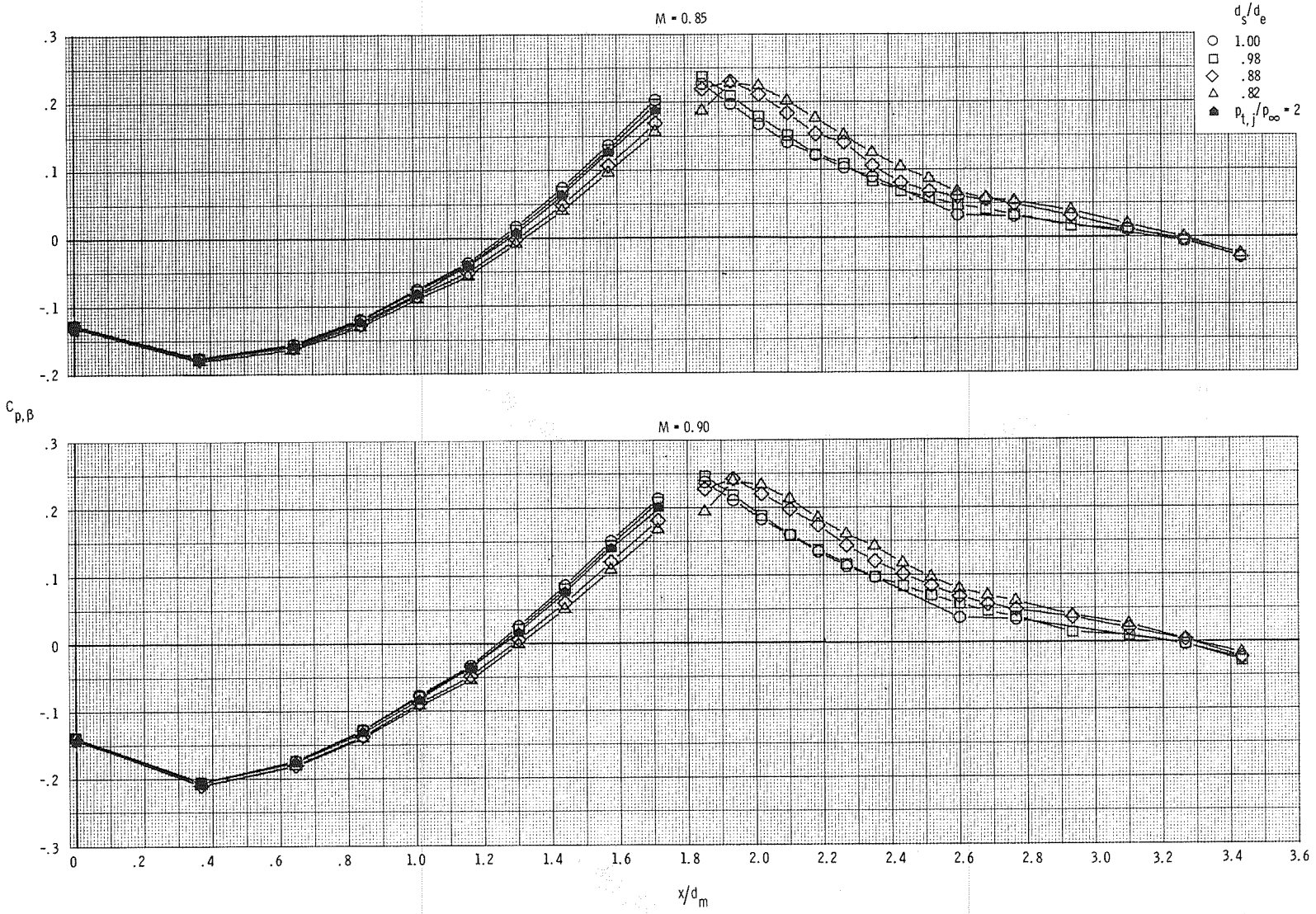

(c) M = 0.85 and 0.90.

Figure 10.- Continued.

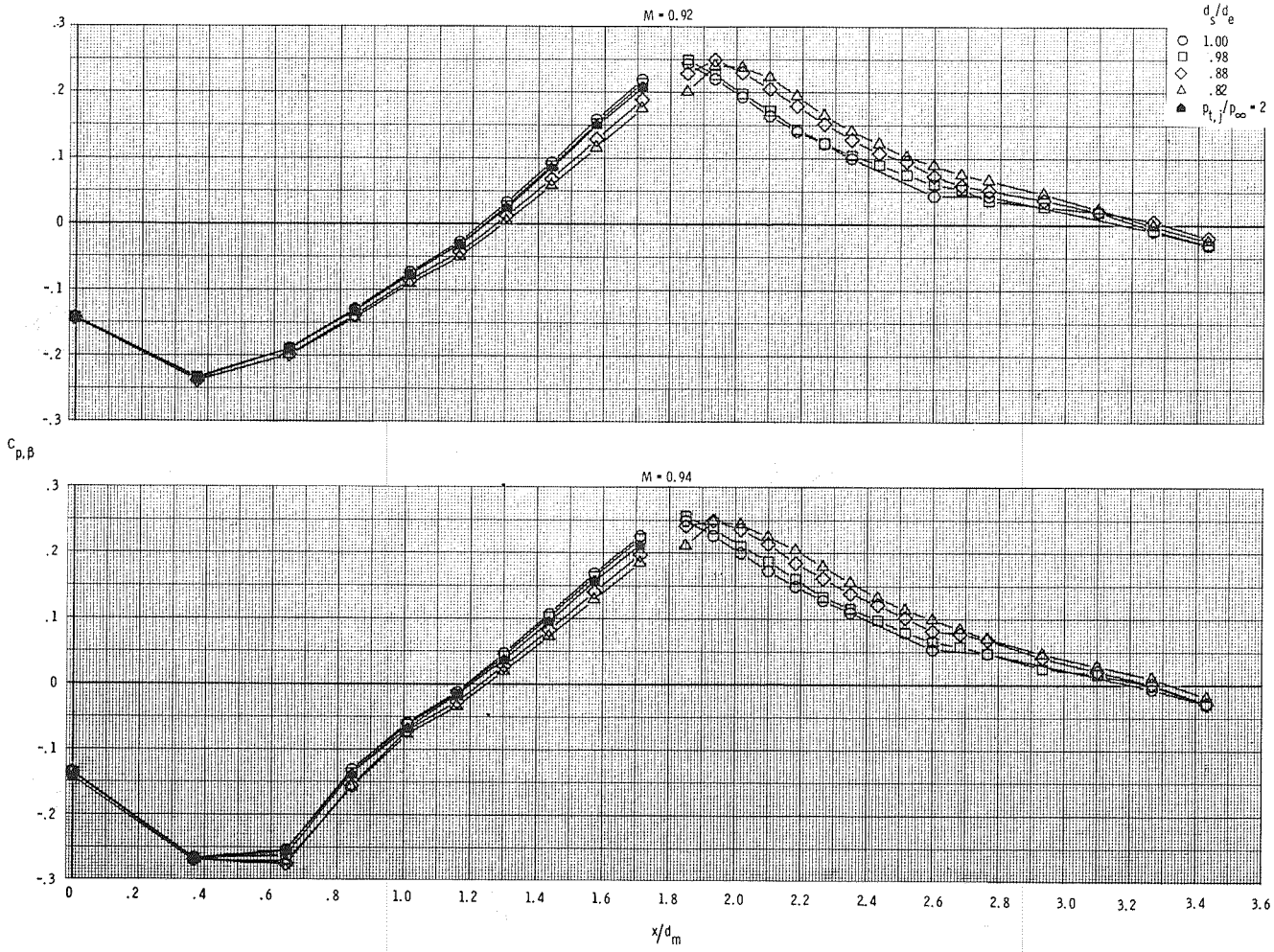

(d) M = 0.92 and 0.94.

Figure 10.- Continued.

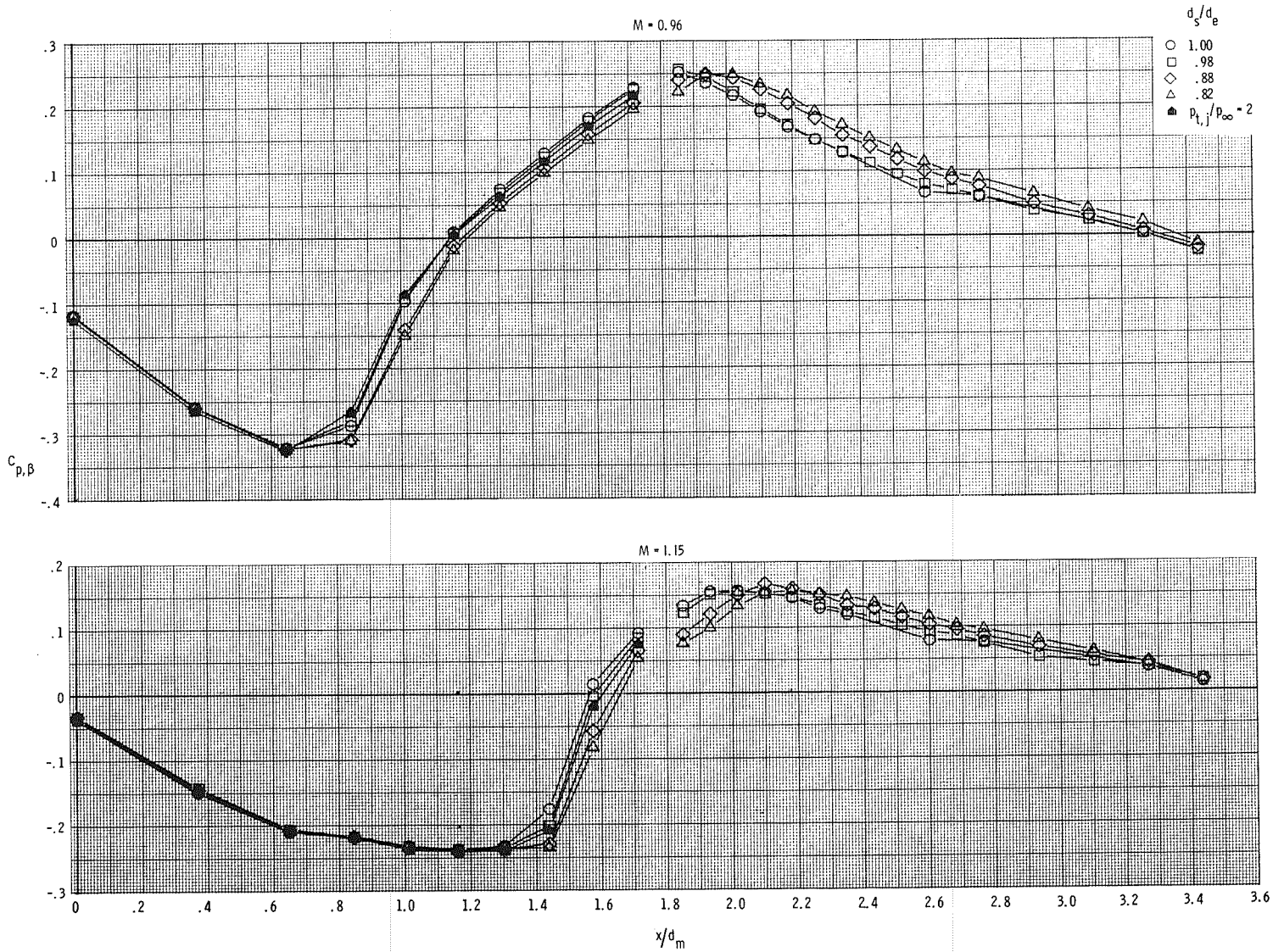

(e) M = 0.96 and 1.15.

Figure 10.- Continued.

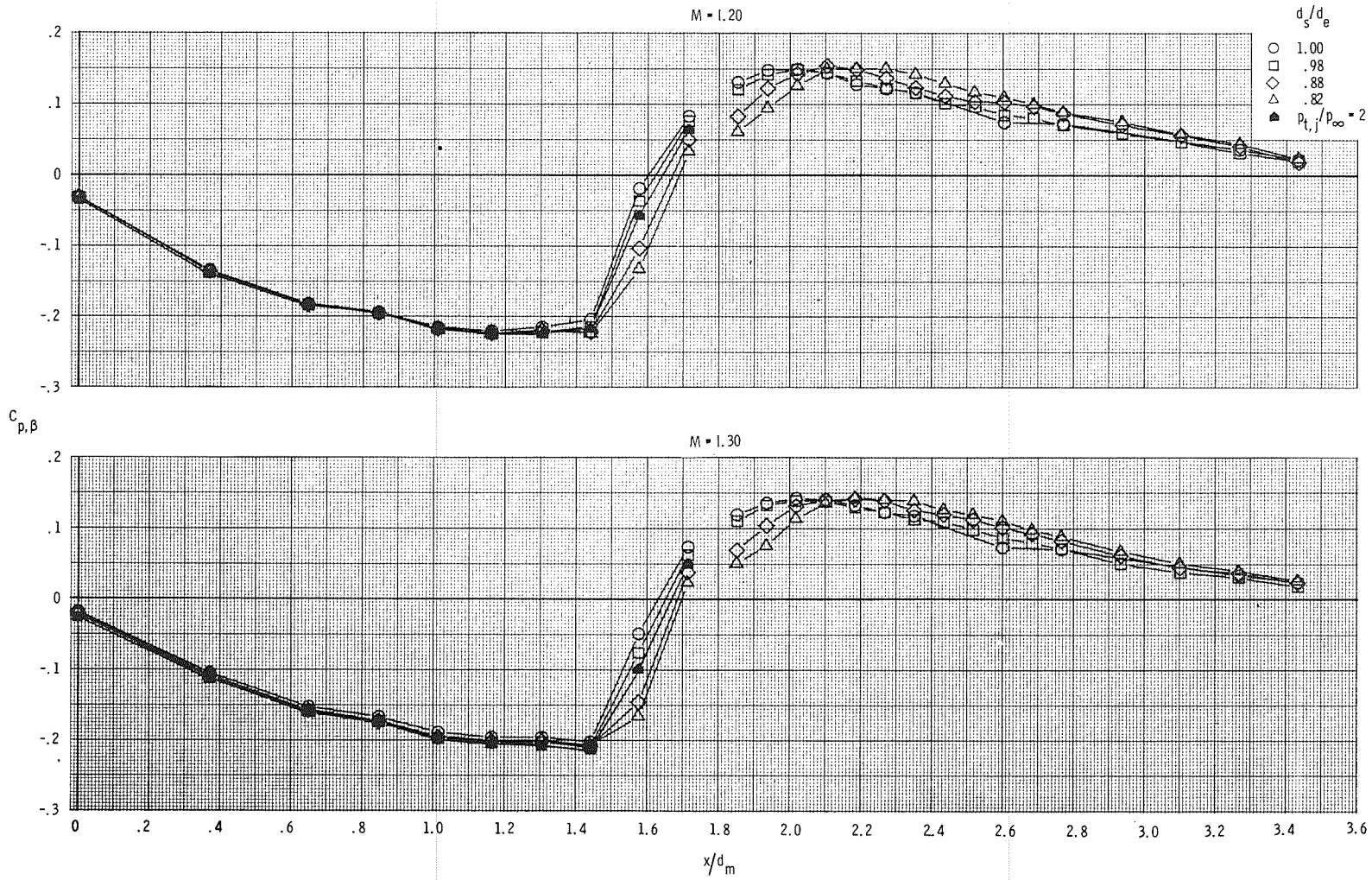

(f) M = 1.20 and 1.30.

Figure 10.- Concluded.

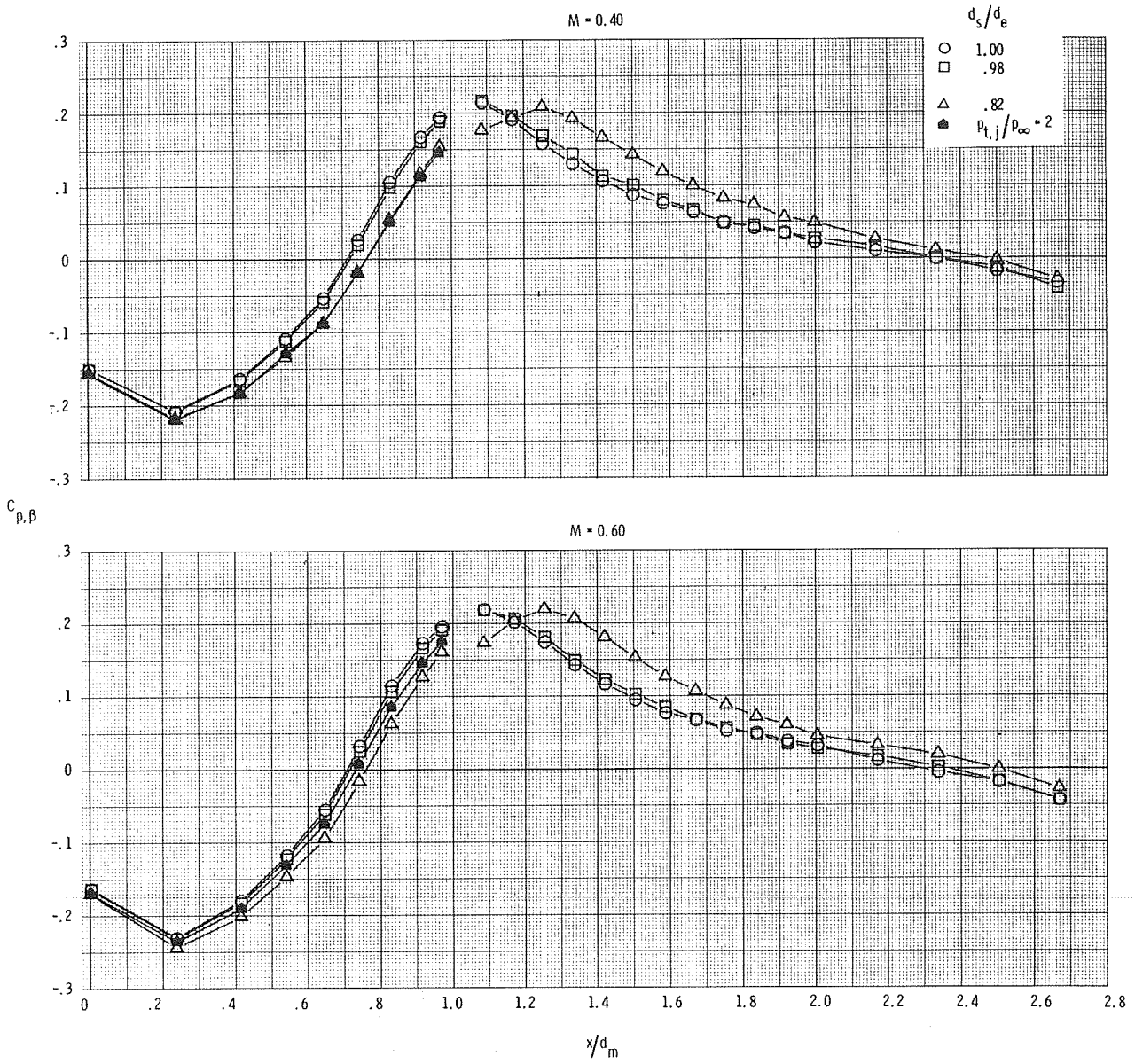

(a) M = 0.40 and 0.60.

Figure 11.- Comparison of pressure-coefficient distributions obtained through use of plume simulators with those obtained from jet operation at $p_{t,j}/p_\infty = 2$ for configuration 4 ($l/d_m = 1.00$, $d_e/d_m = 0.60$).

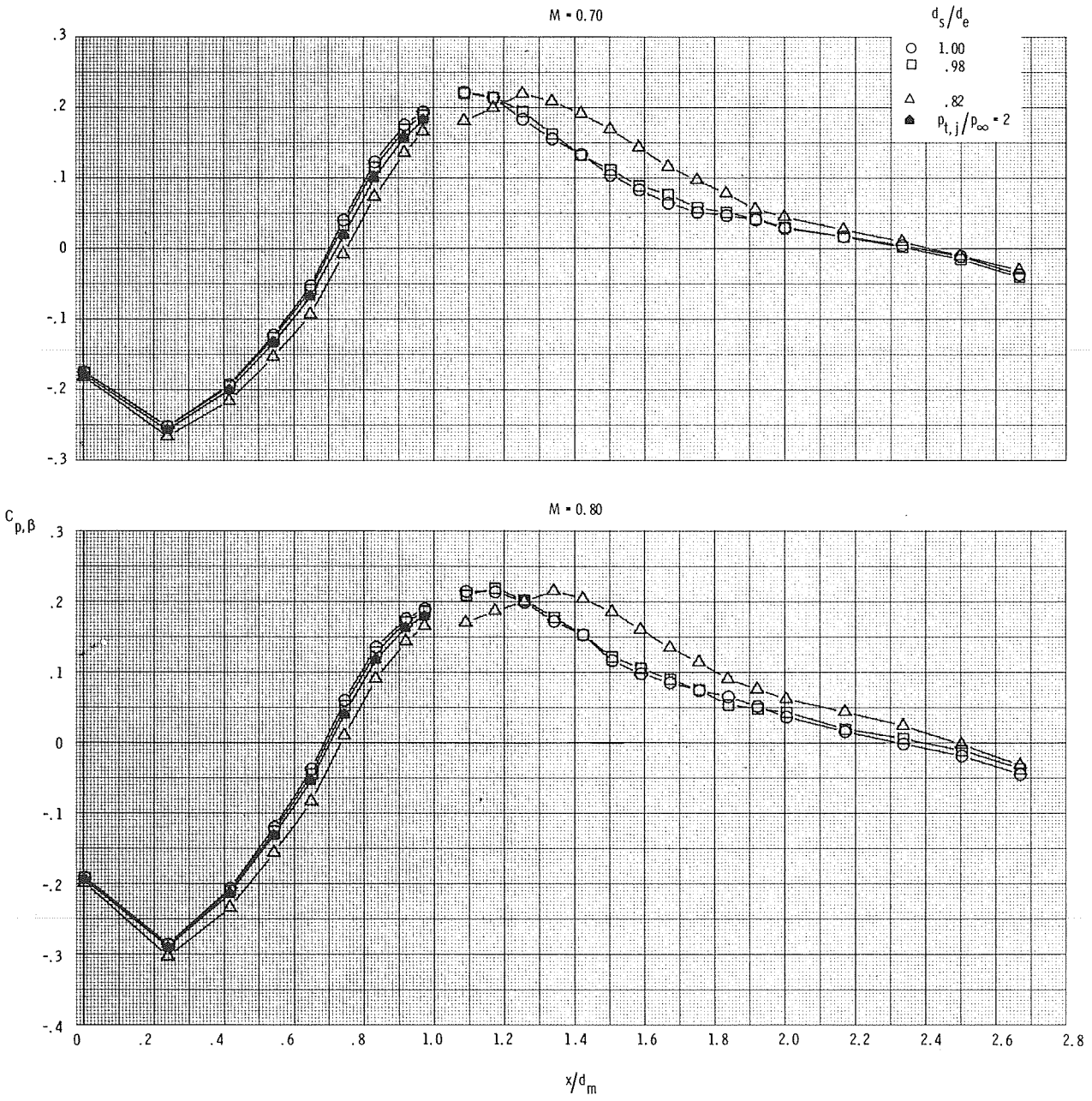

(b) M = 0.70 and 0.80.

Figure 11.- Continued.

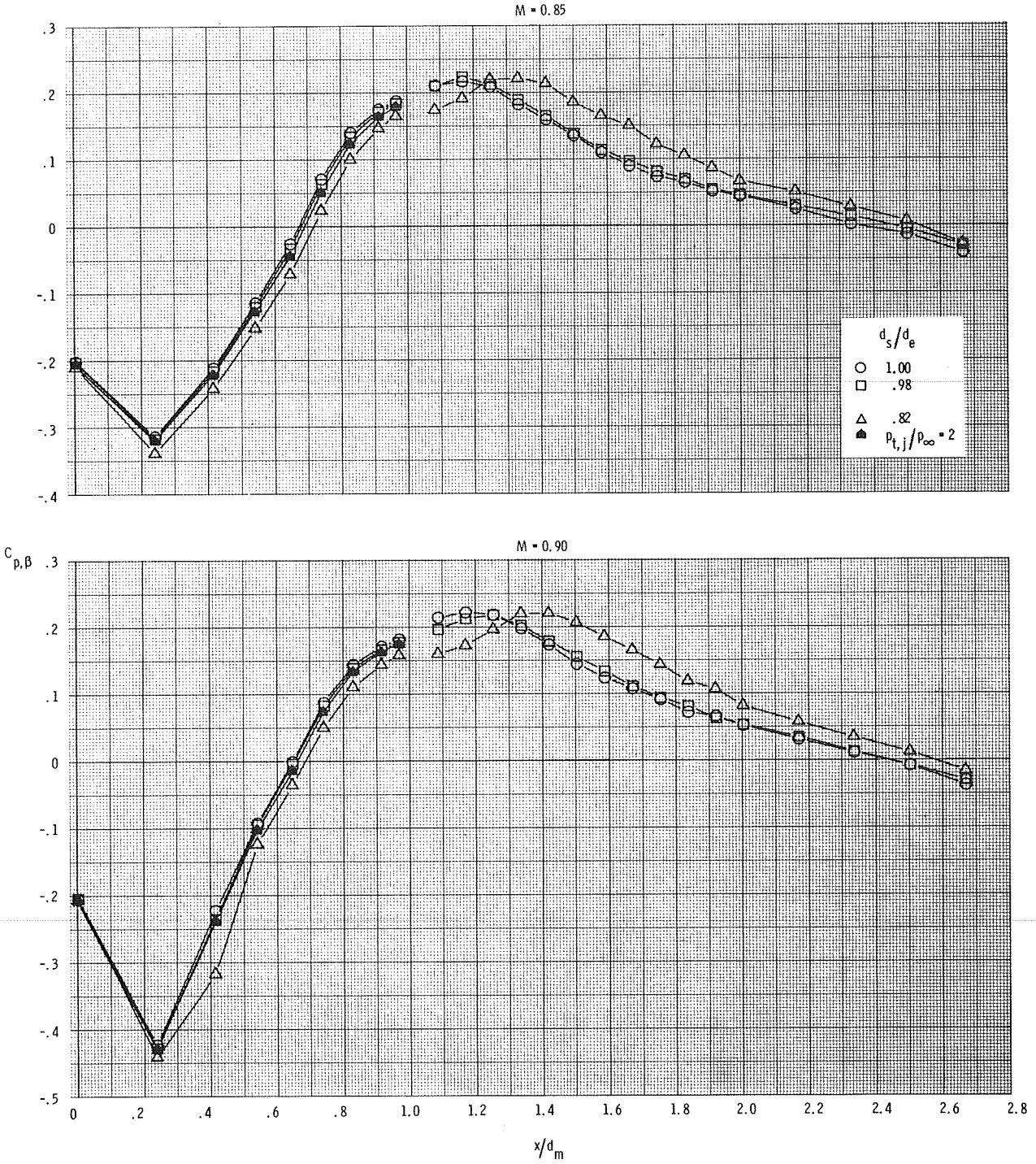

(c) M = 0.85 and 0.90.

Figure 11.- Continued.

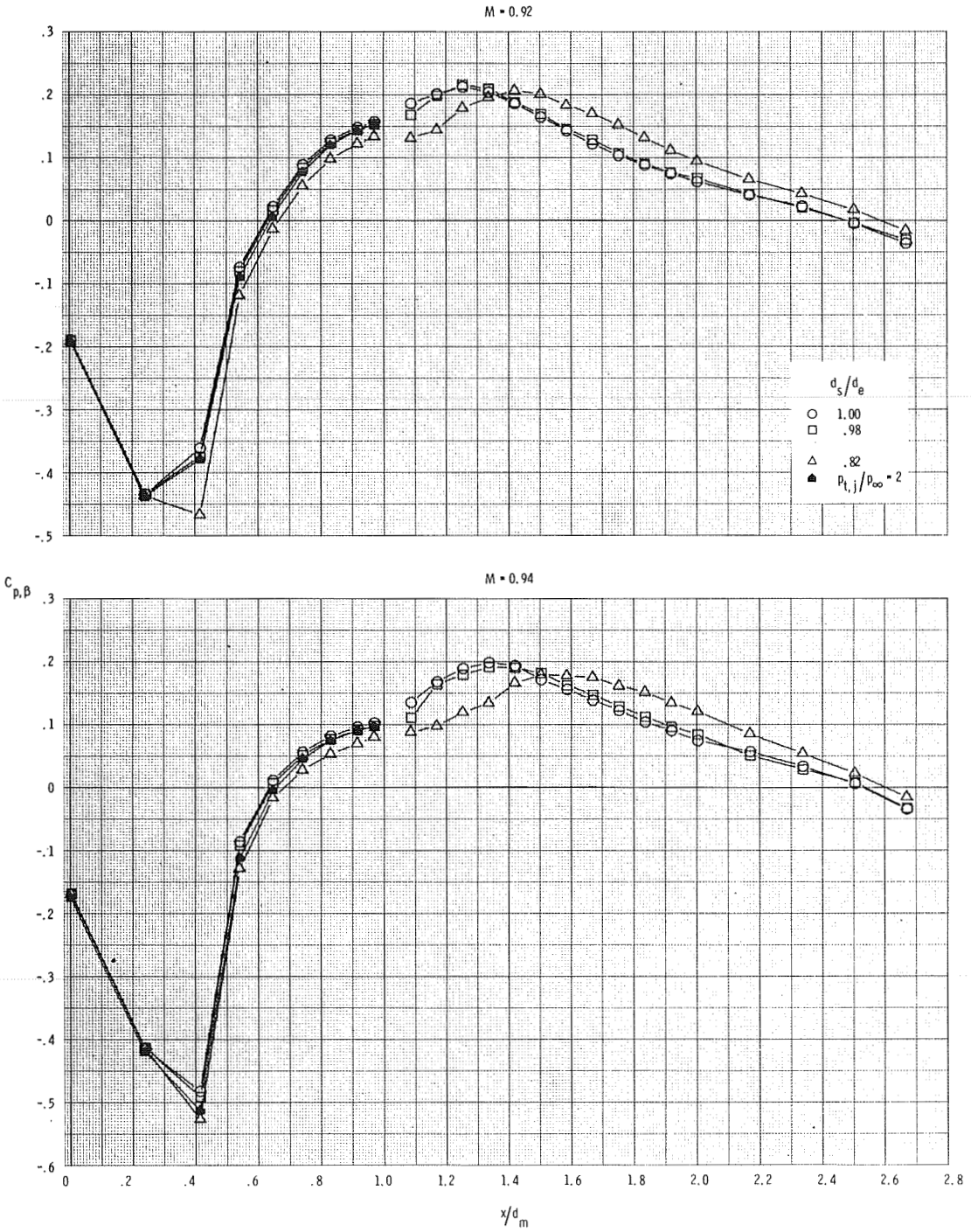

(d) M = 0.92 and 0.94.

Figure 11.- Continued.

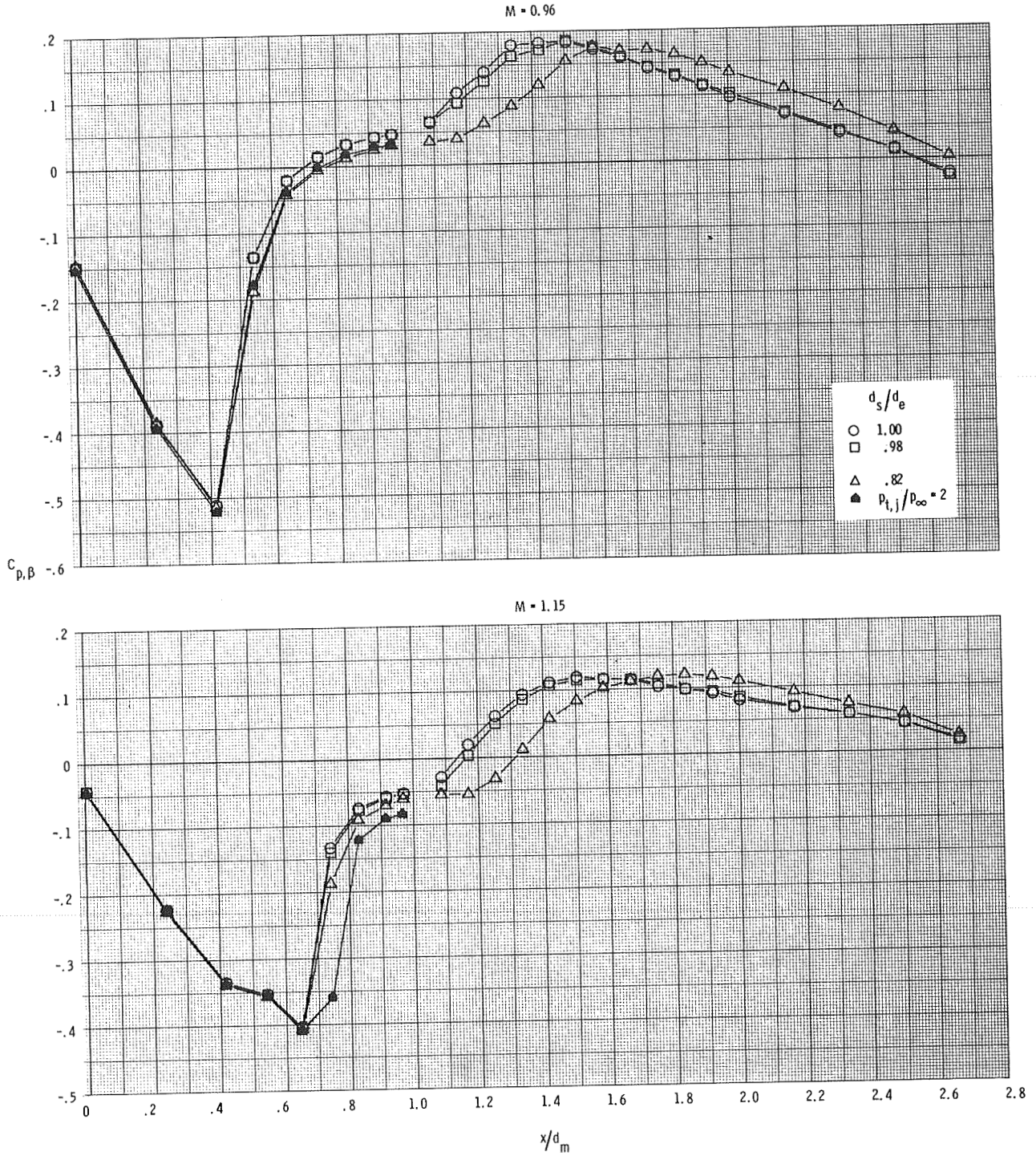

(e) M = 0.96 and 1.15.

Figure 11.- Continued.

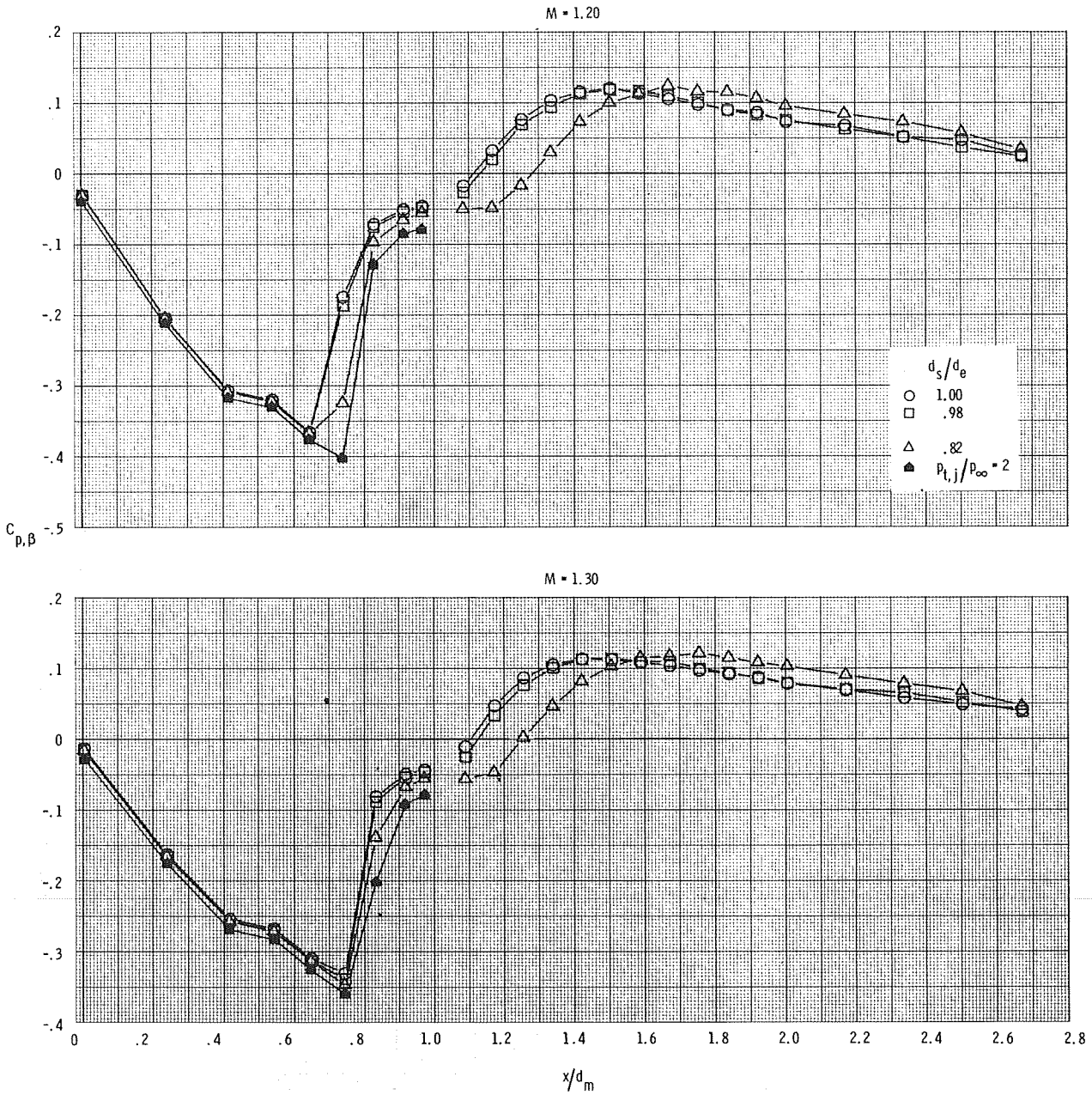

(f) M = 1.20 and 1.30.

Figure 11.- Concluded.

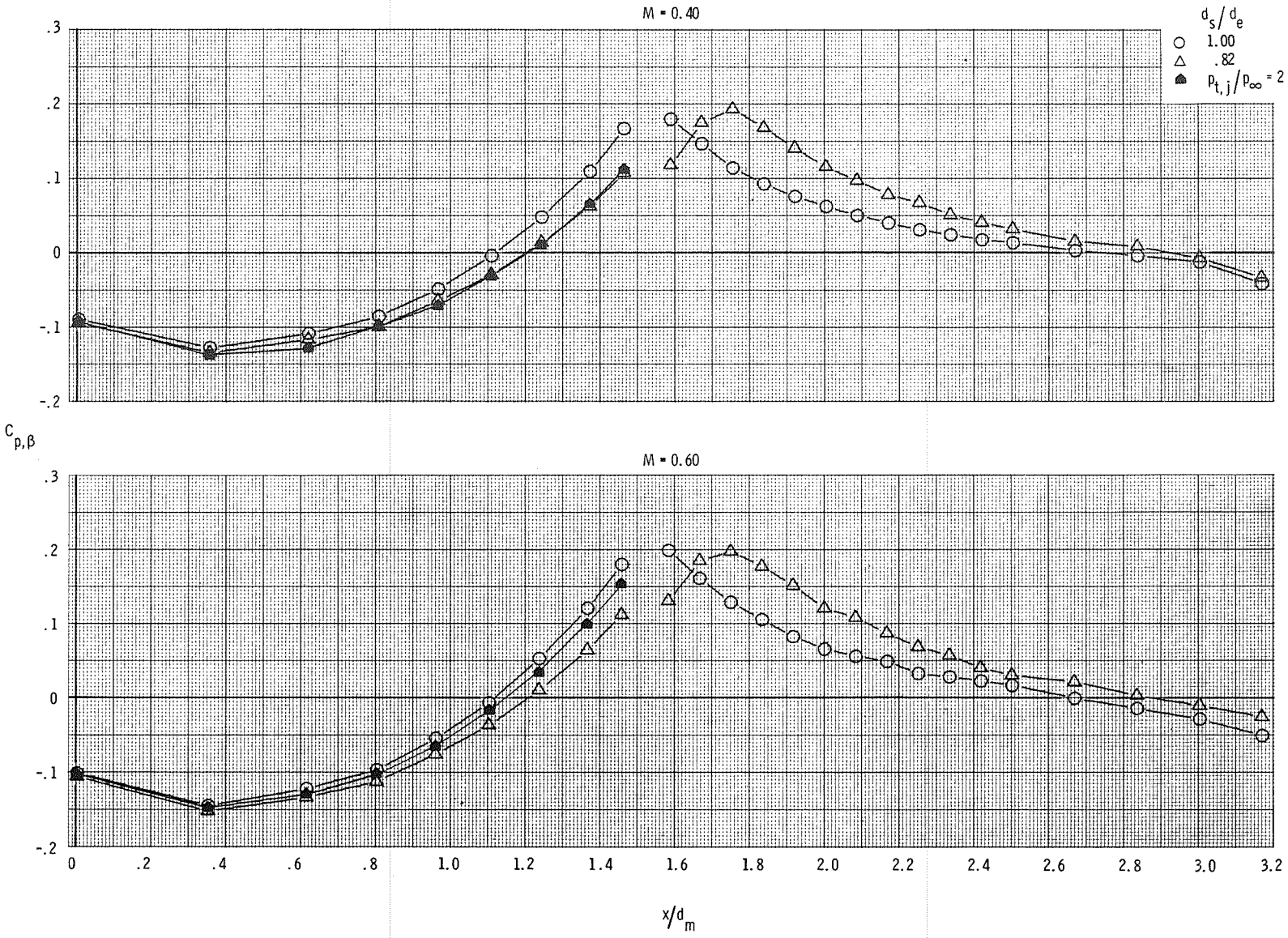

(a) M = 0.40 and 0.60.

Figure 12.- Comparison of pressure-coefficient distributions obtained through the use of plume simulators with those obtained from jet operation at $p_{t,j}/p_\infty = 2$ for configuration 5 ($l/d_m = 1.50$, $d_e/d_m = 0.60$).

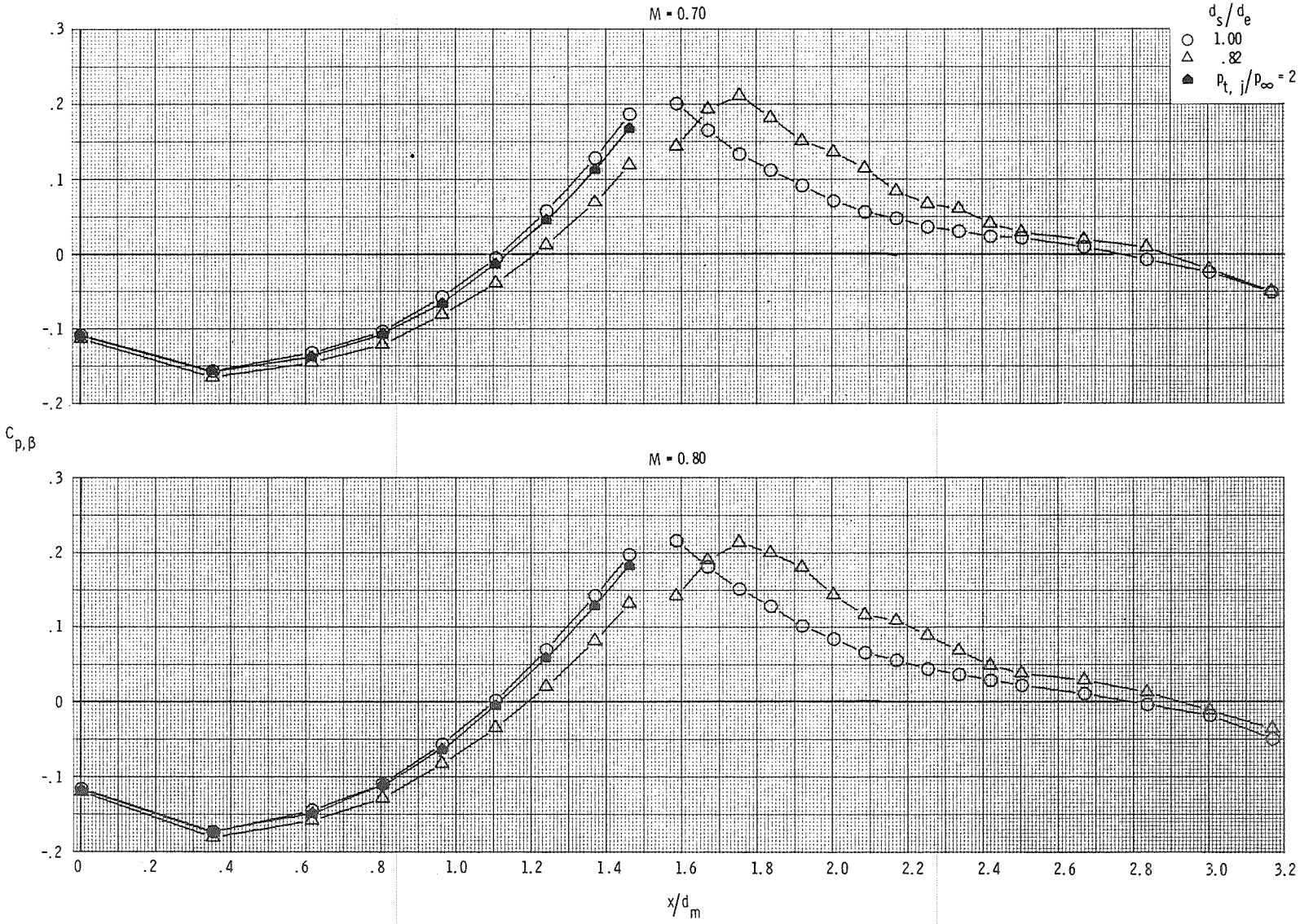

(b) M = 0.70 and 0.80.

Figure 12.- Continued.

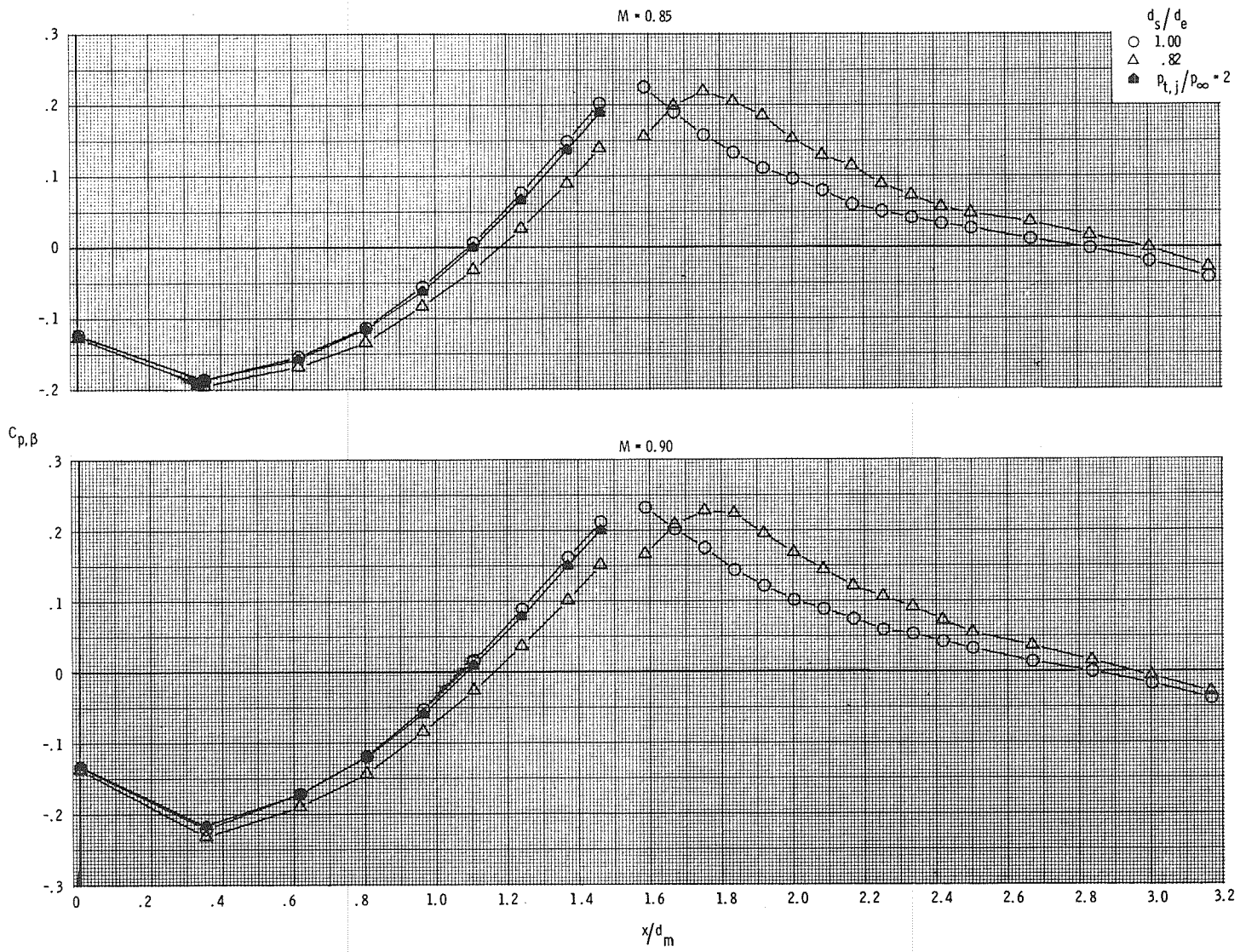

(c) M = 0.85 and 0.90.

Figure 12.- Continued.

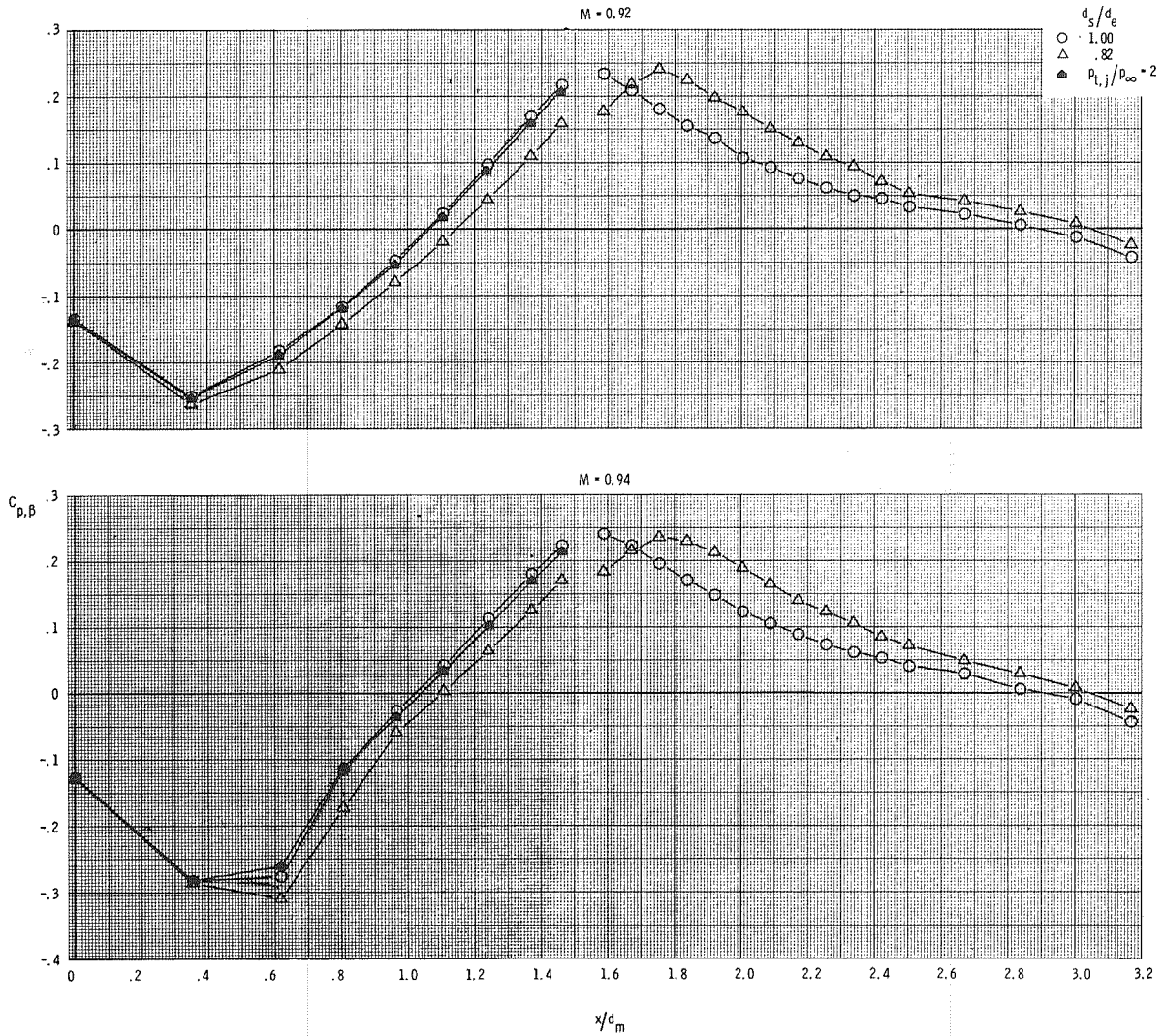

(d) M = 0.92 and 0.94.

Figure 12.- Continued.

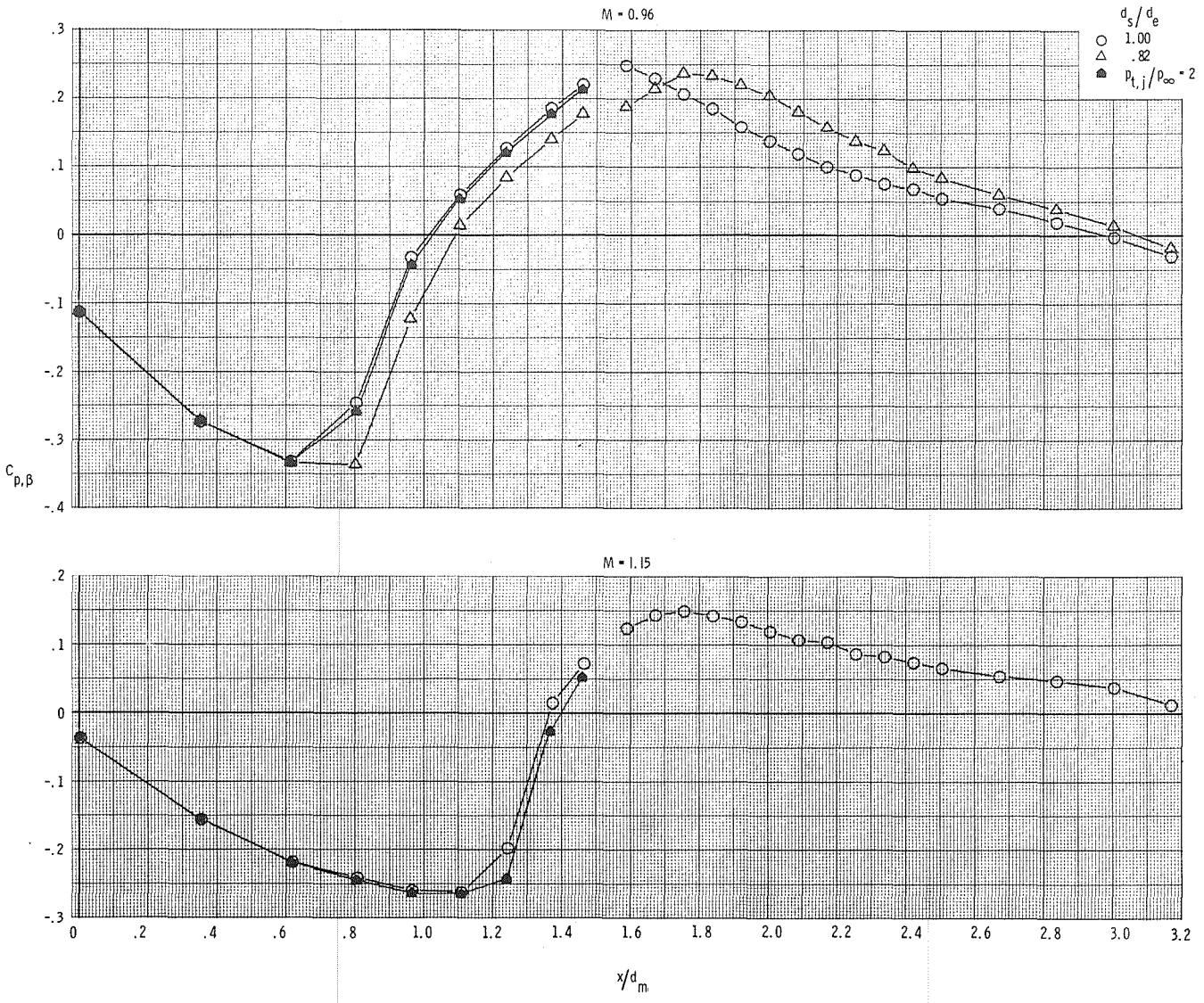

(e) M = 0.96 and 1.15.

Figure 12.- Continued.

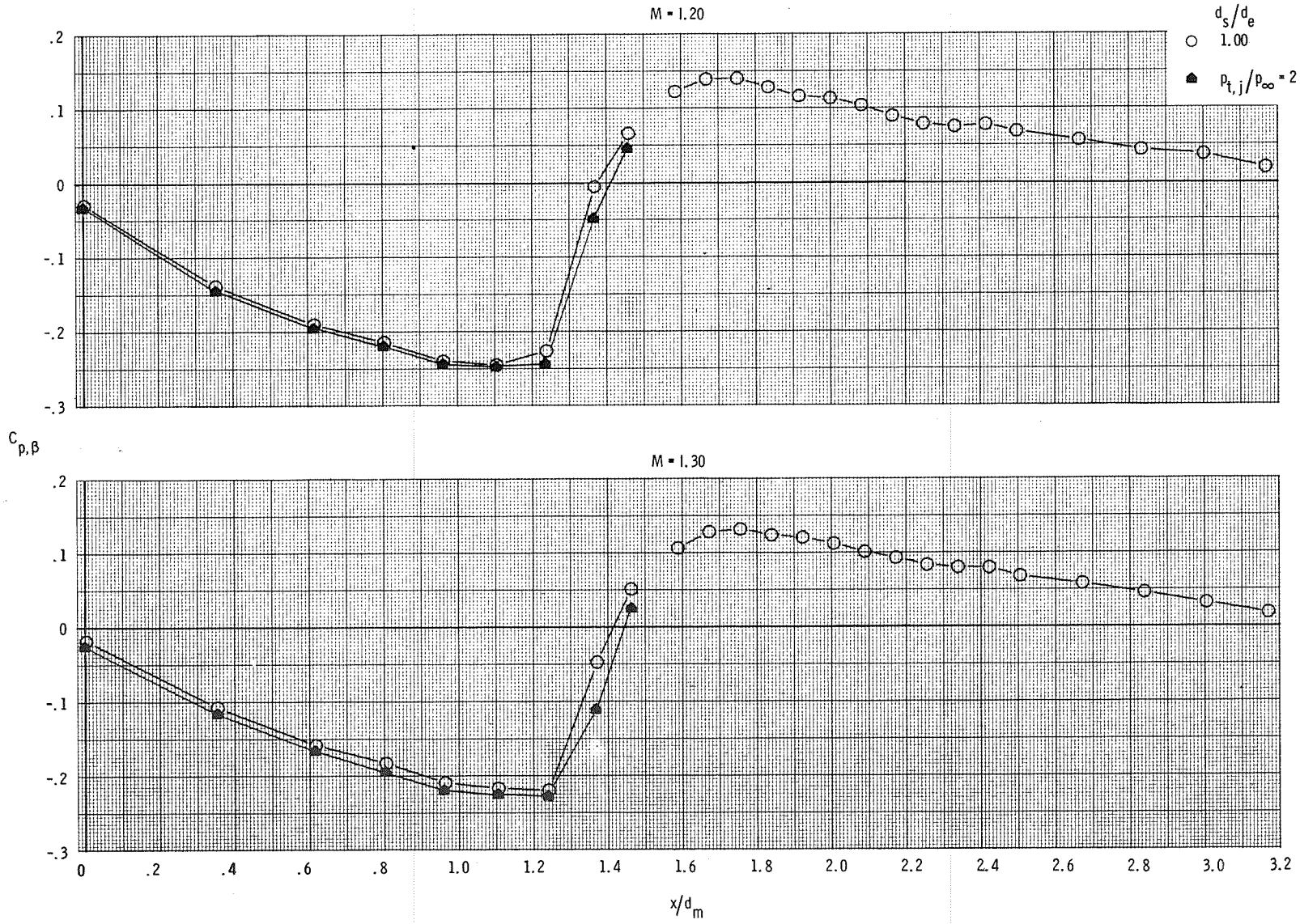

(f) M = 1.20 and 1.30.

Figure 12.- Concluded.

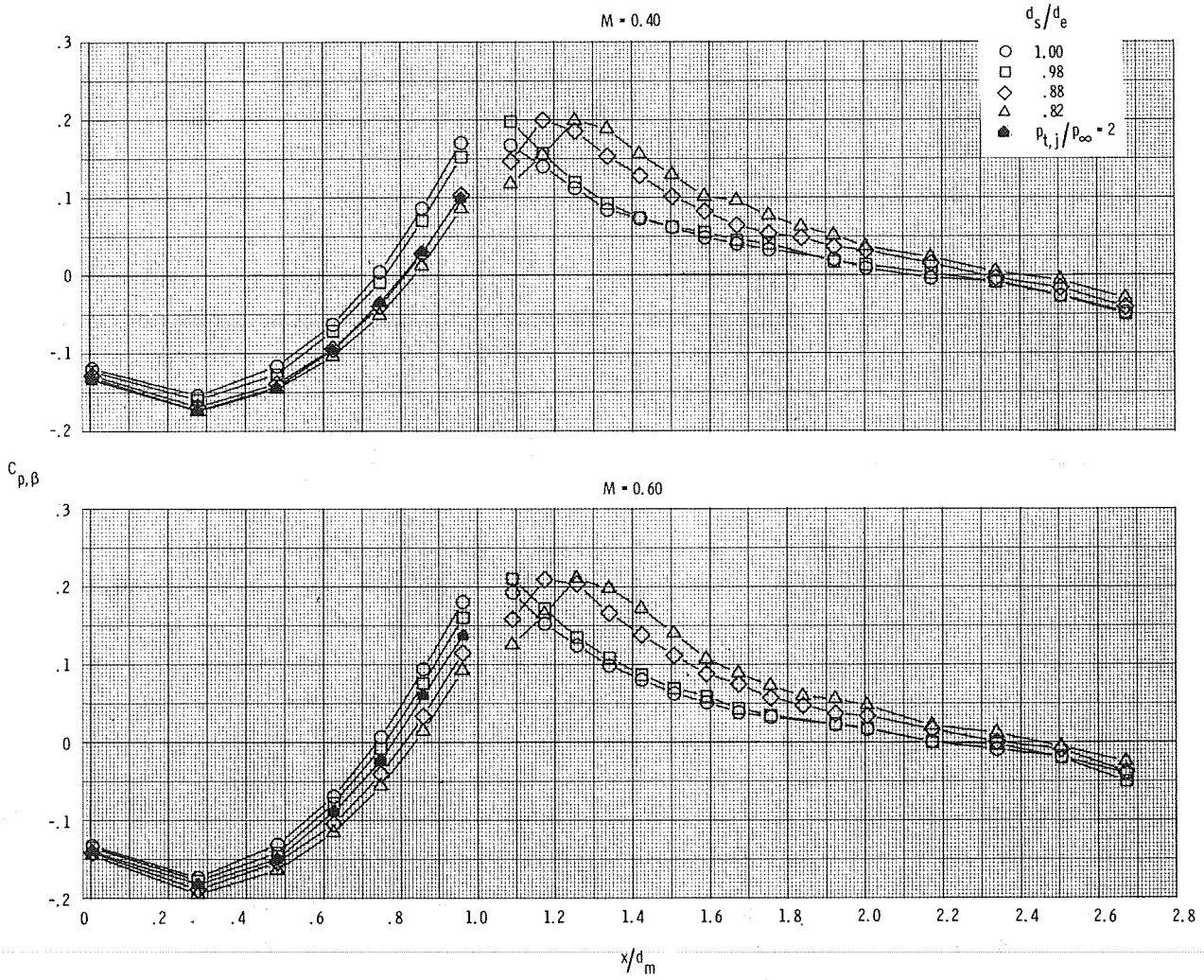

(a) M = 0.40 and 0.60.

Figure 13.- Comparison of pressure-coefficient distributions obtained through use of plume simulators with those obtained from jet operation at $p_{t,j}/p_\infty = 2$ for configuration 6 ($\ell/d_m = 1.00$, $d_e/d_m = 0.70$).

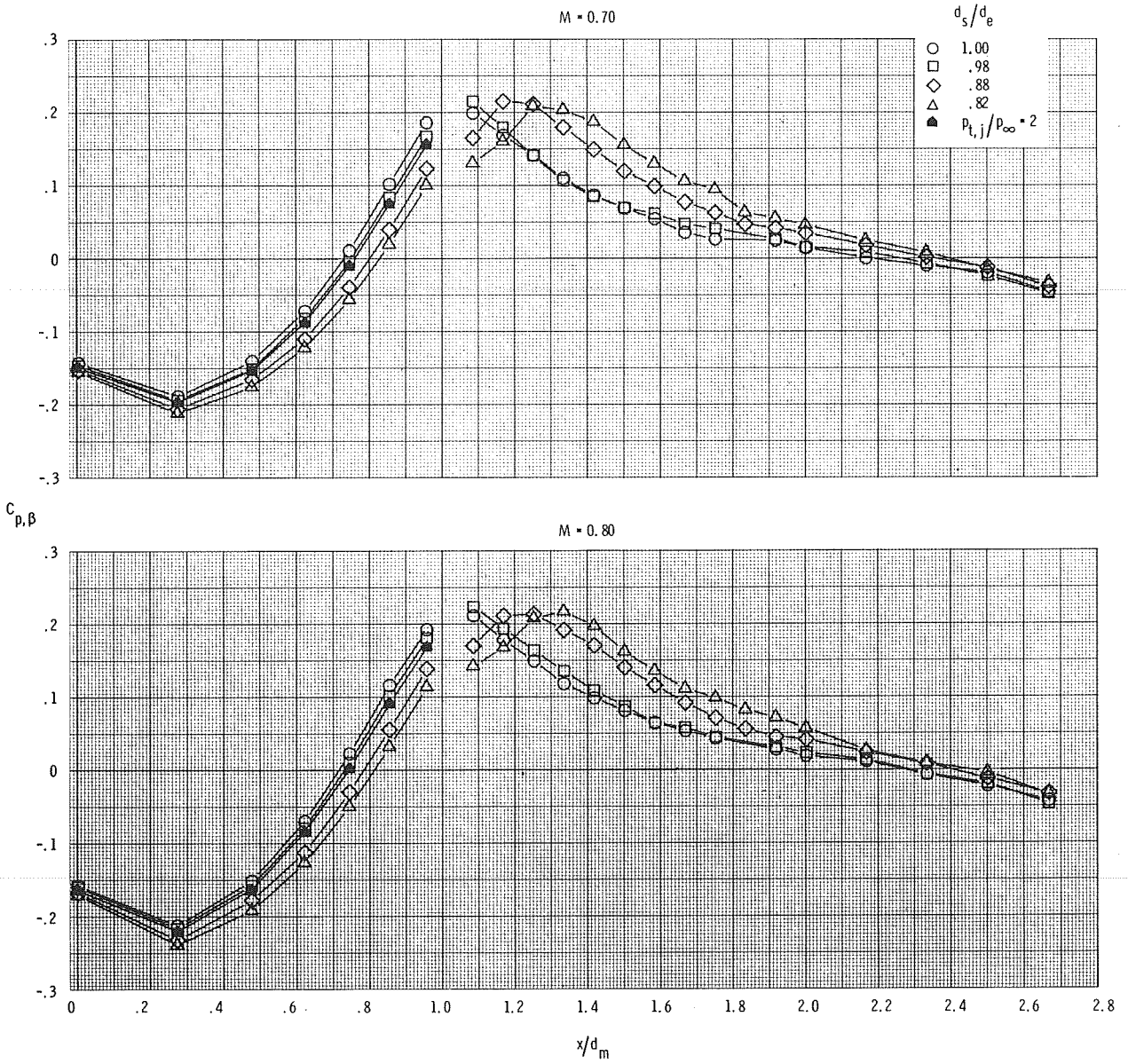

(b) M = 0.70 and 0.80.

Figure 13.- Continued.

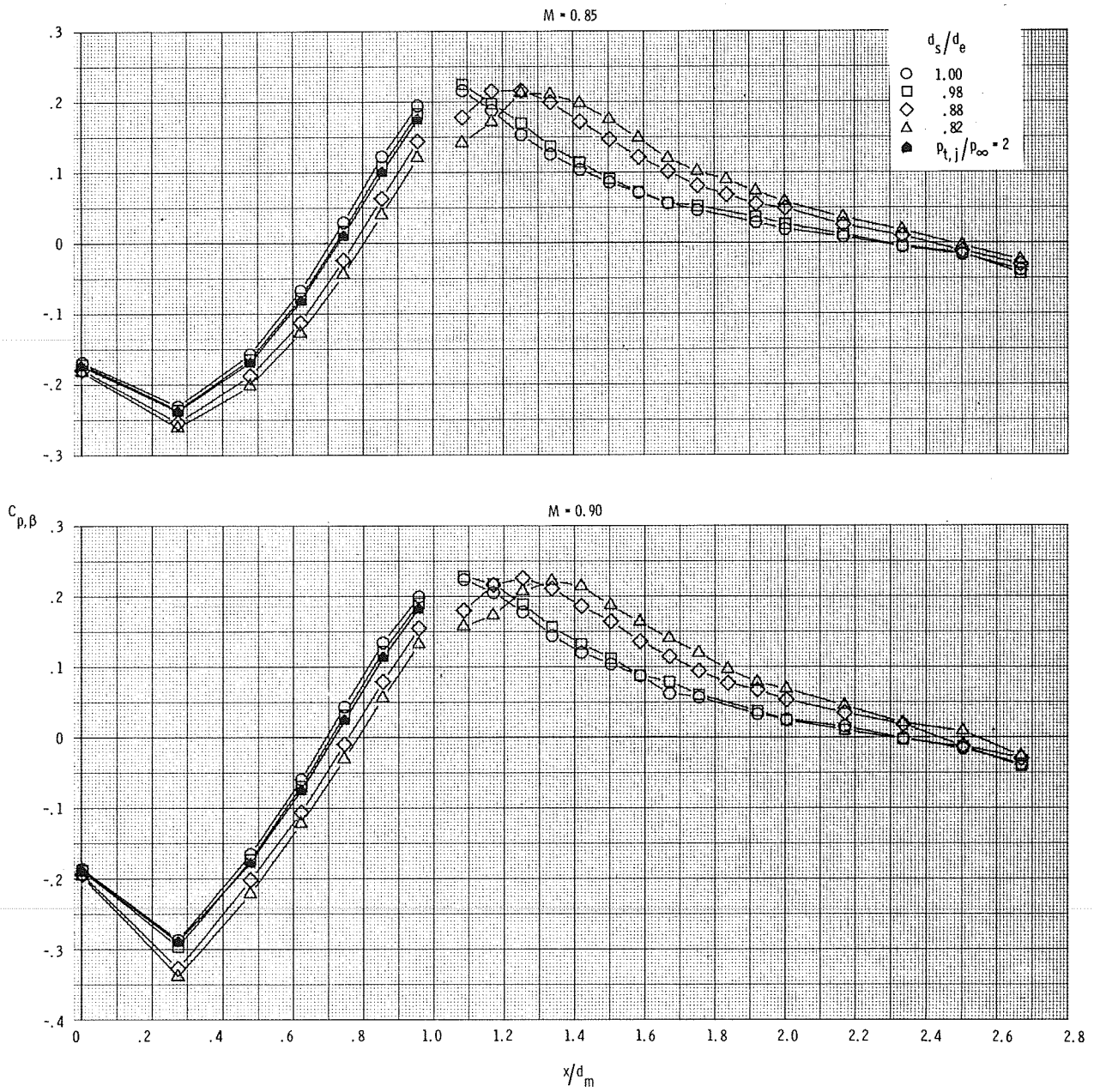

(c) M = 0.85 and 0.90.

Figure 13.- Continued.

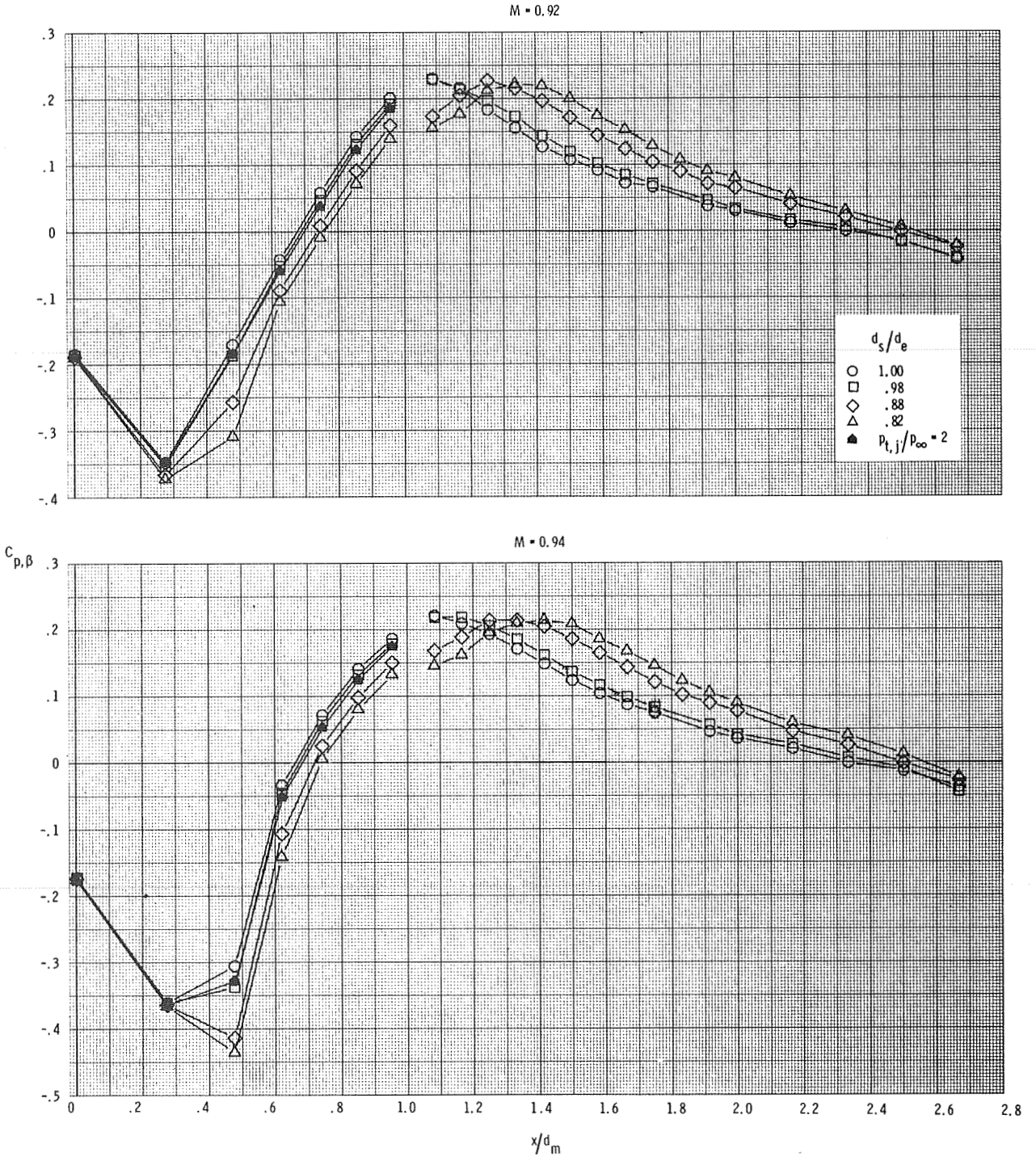

(d) M = 0.92 and 0.94.

Figure 13.- Continued.

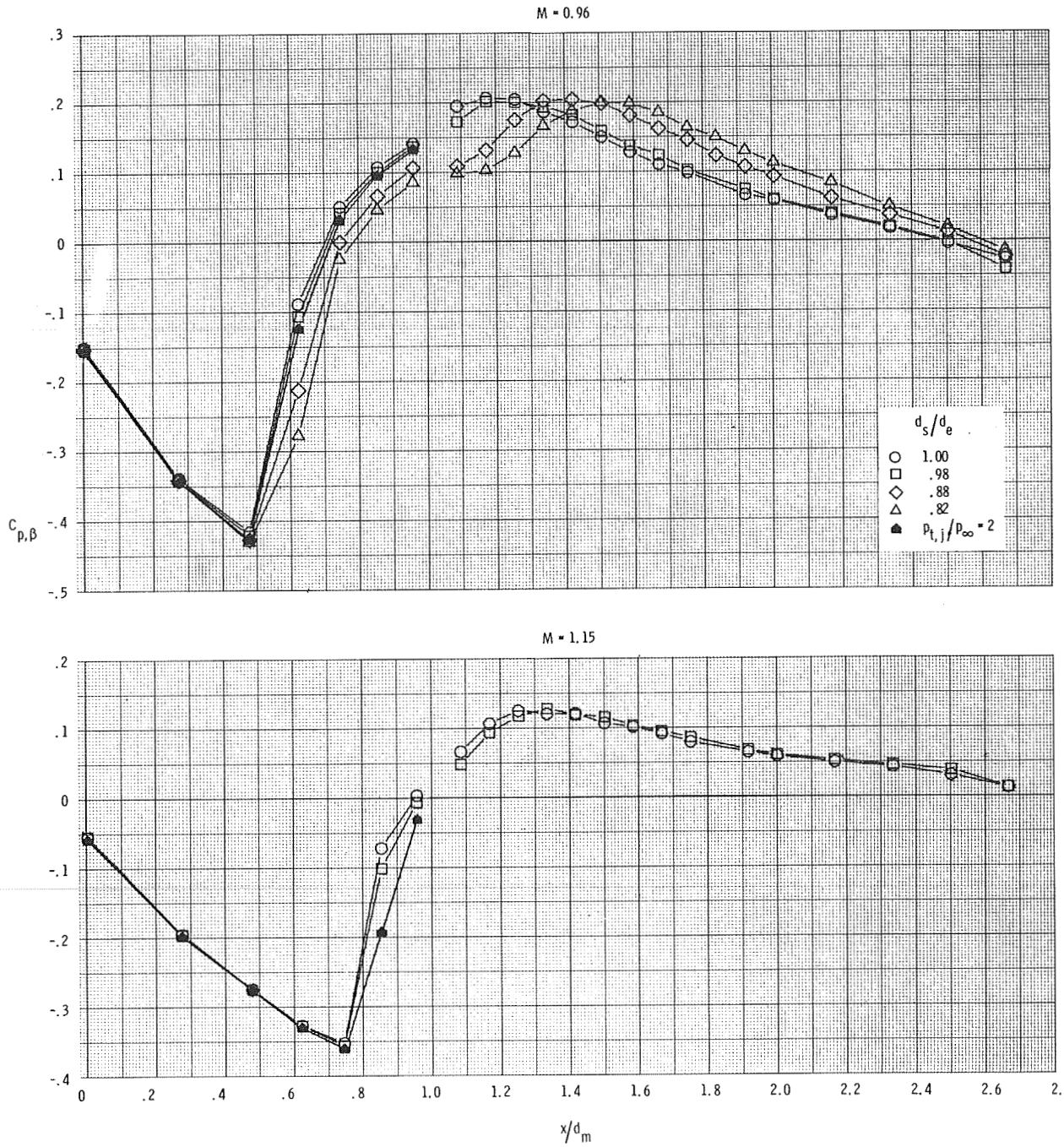

(e) M = 0.96 and 1.15.

Figure 13.- Continued.

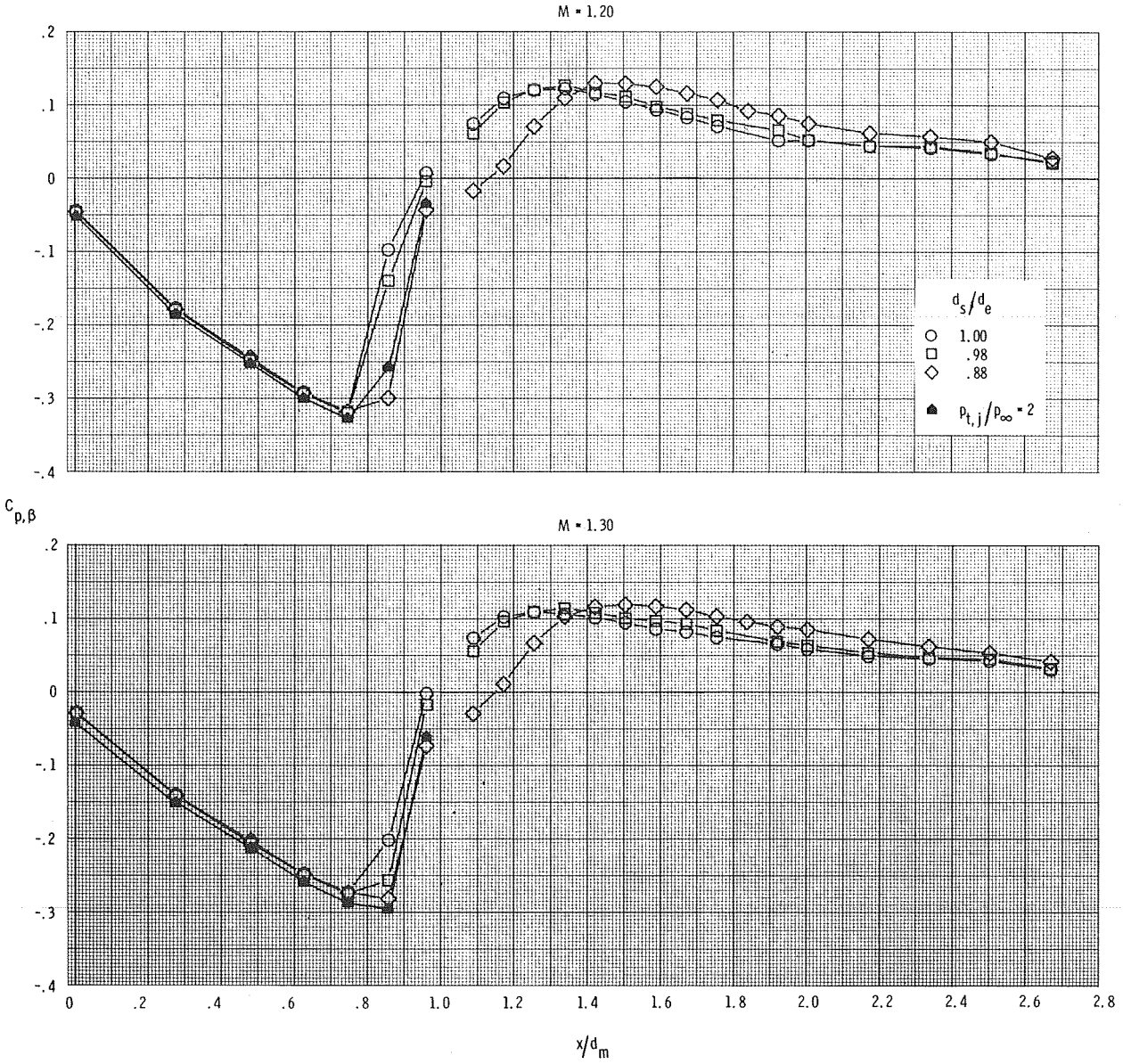

(f) M = 1.20 and 1.30.

Figure 13.- Concluded.

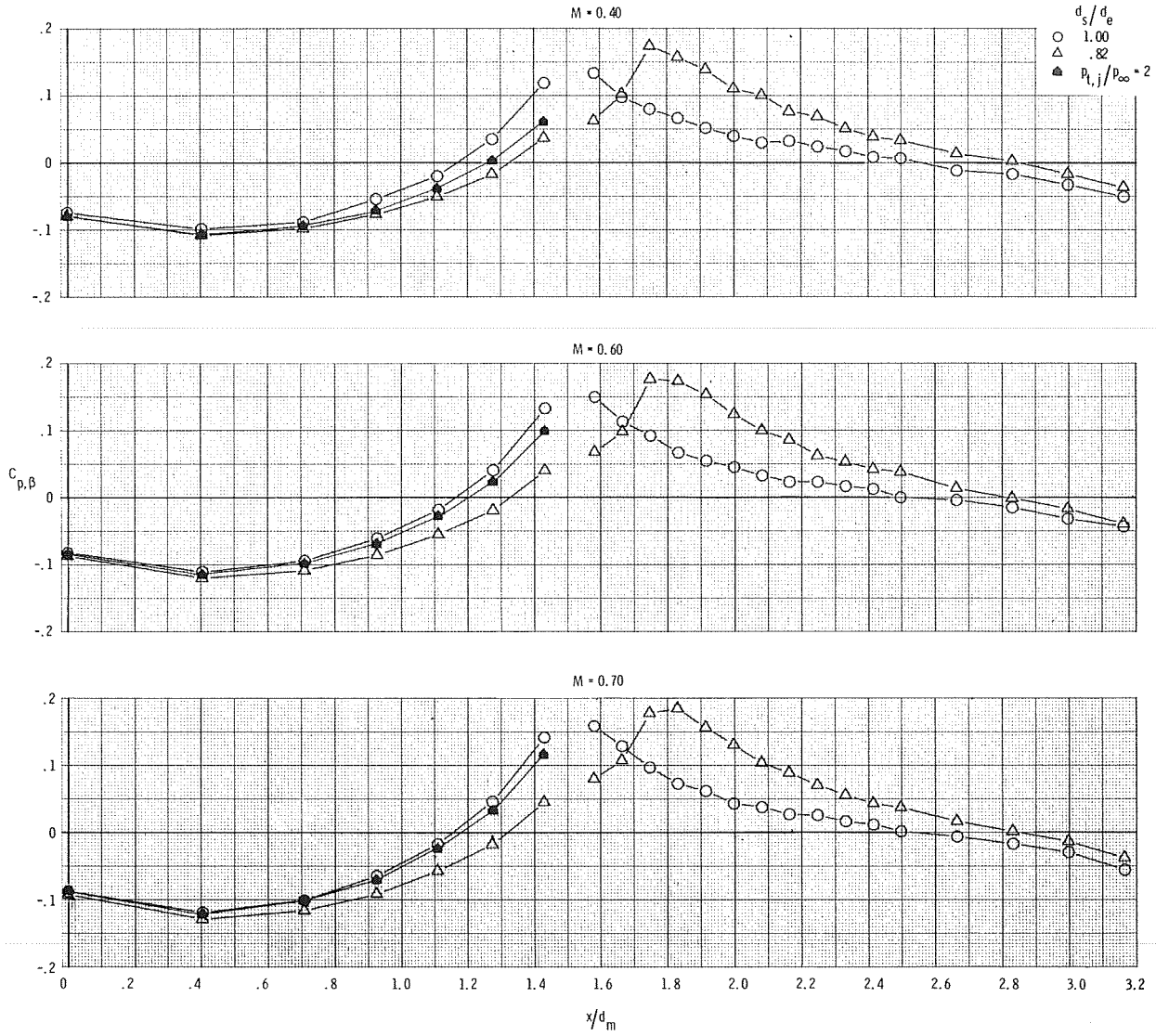

(a) M = 0.40, 0.60, and 0.70.

Figure 14.- Comparison of pressure-coefficient distributions obtained through the use of plume simulators with those obtained from jet operation at $p_{t,j}/p_\infty = 2$ for configuration 7 ($\ell/d_m = 1.50$, $d_e/d_m = 0.70$).

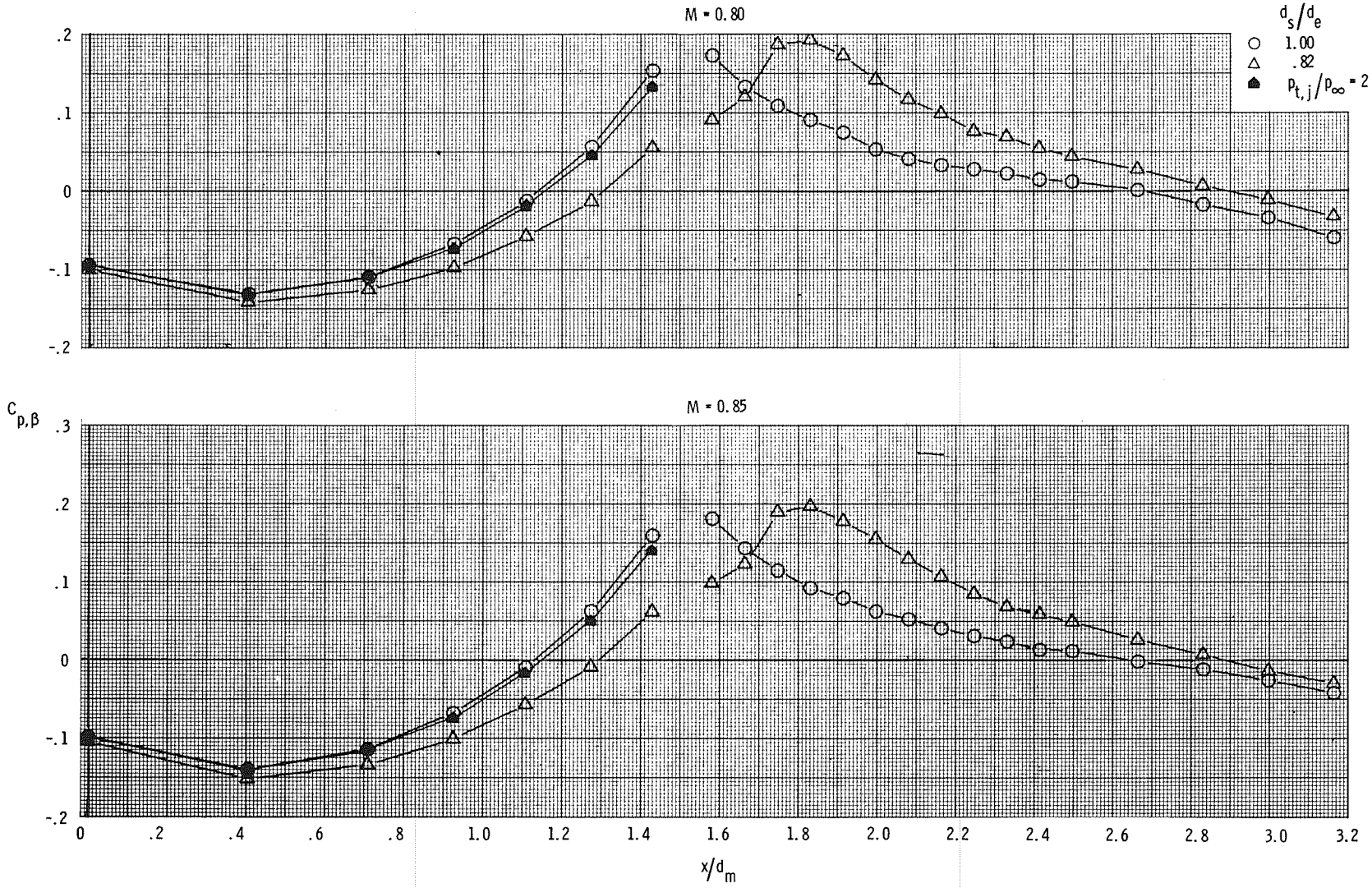

(b) M = 0.80 and 0.85.

Figure 14.- Continued.

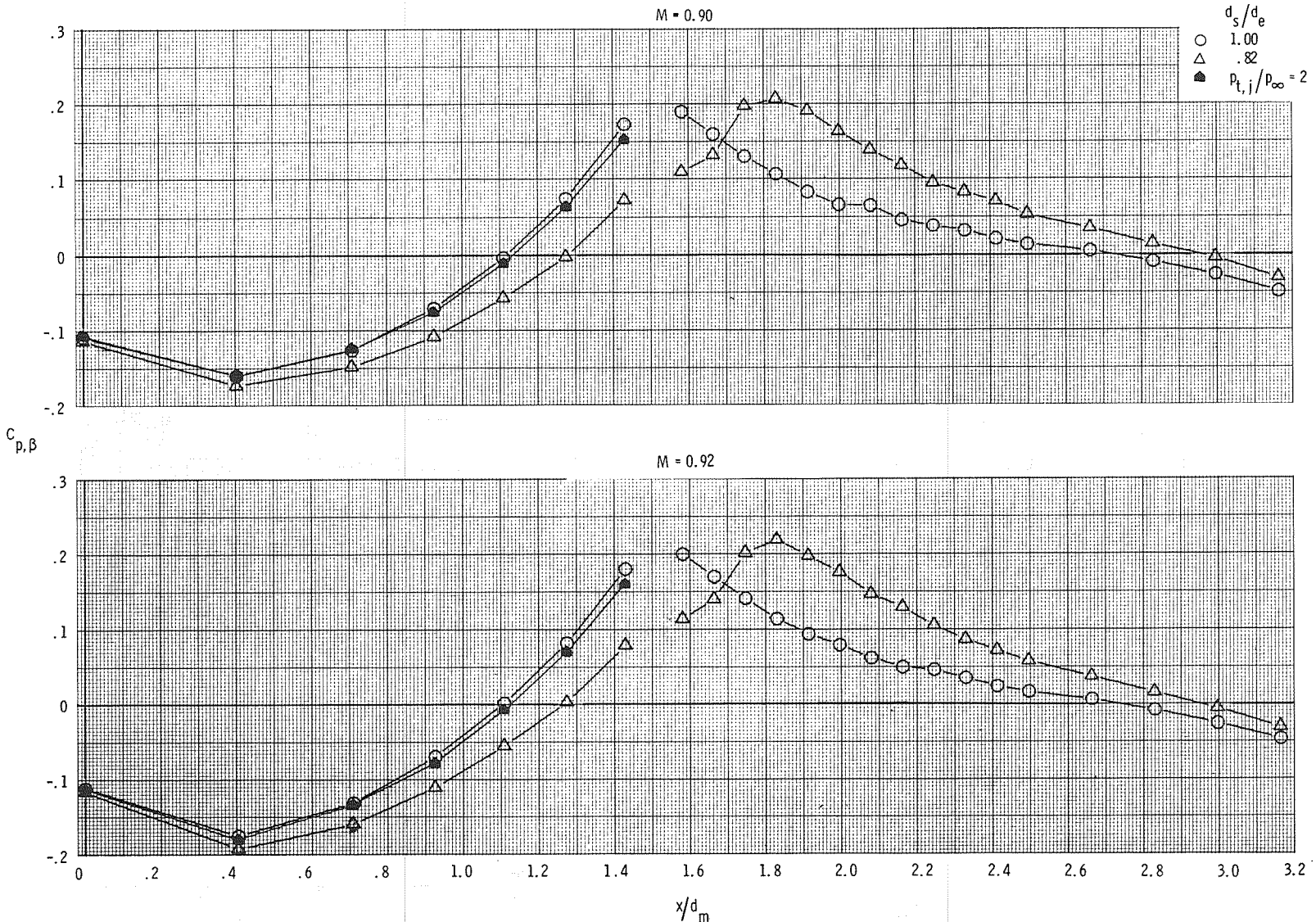

(c) M = 0.90 and 0.92.

Figure 14.- Continued.

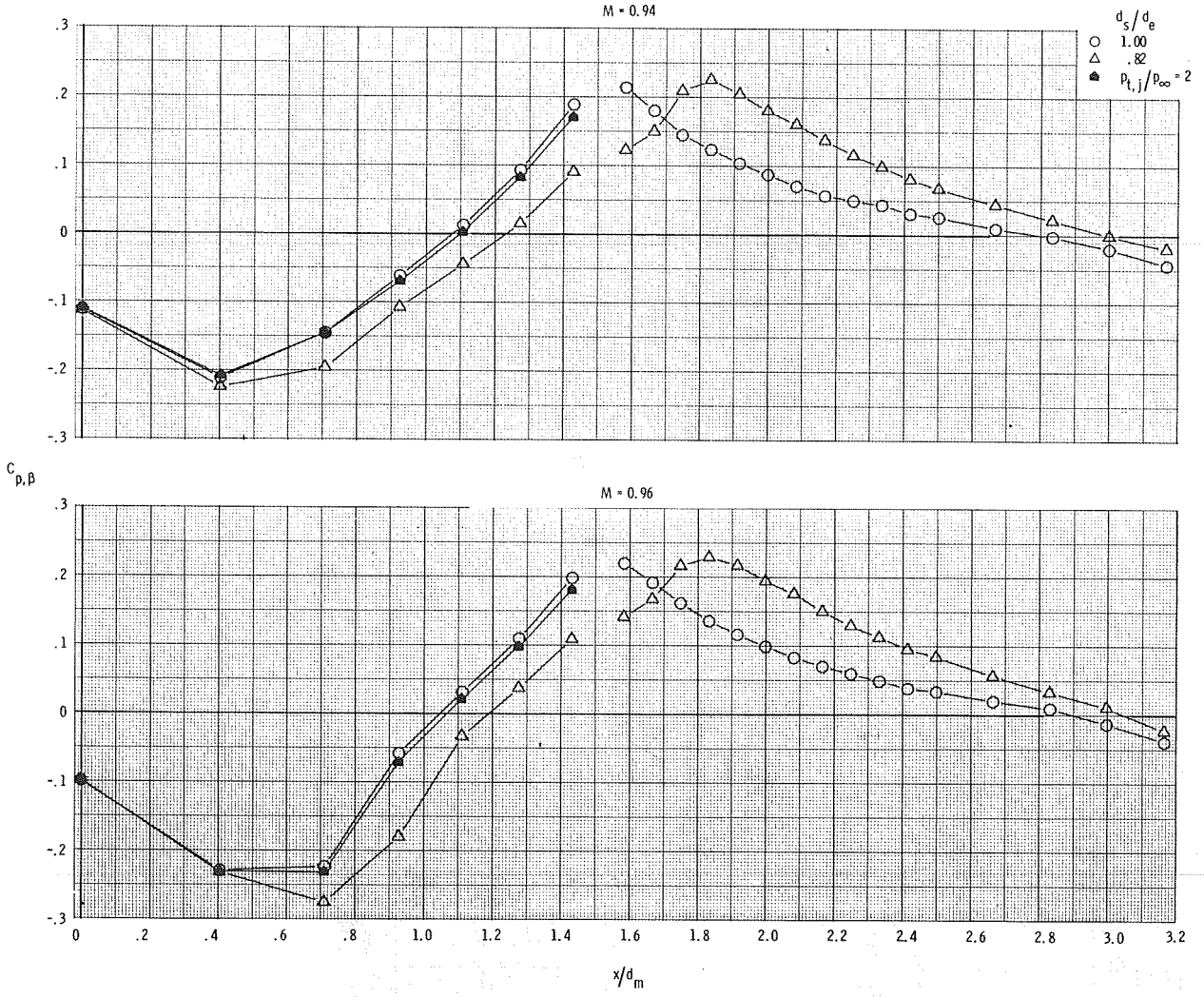

(d) M = 0.94 and 0.96.

Figure 14.- Continued.

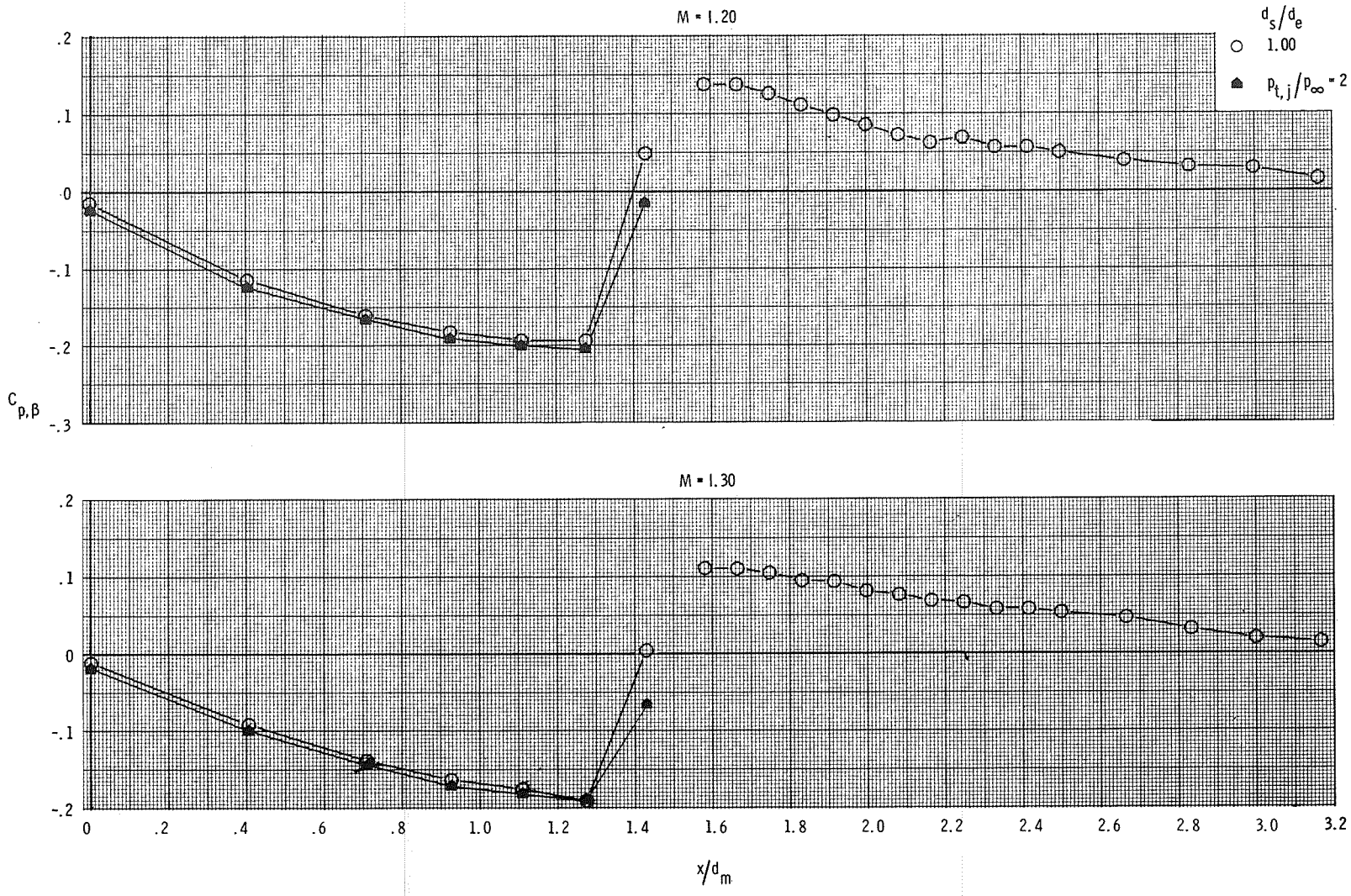

(e) M = 1.20 and 1.30.

Figure 14.- Concluded.

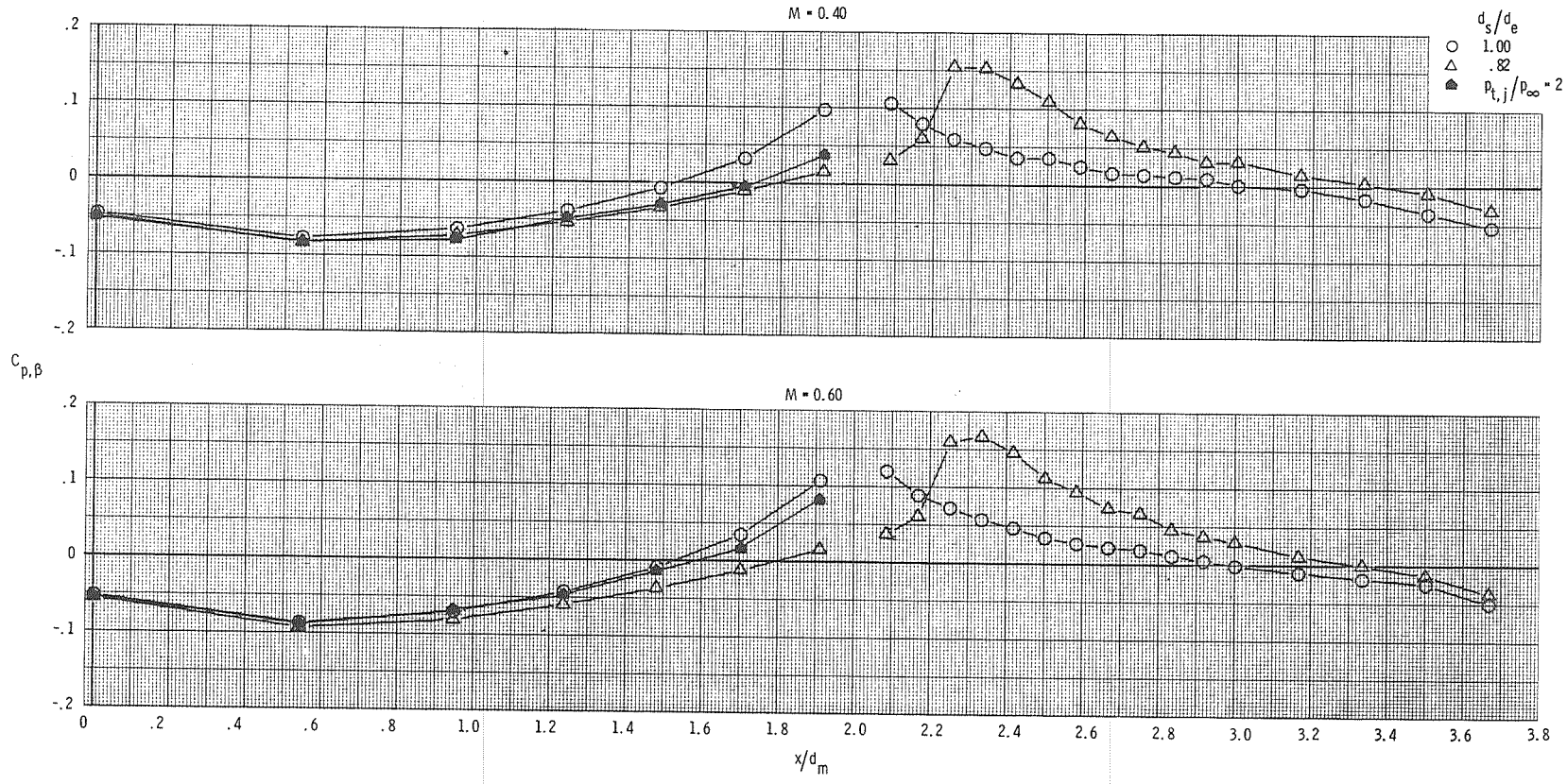

(a) M = 0.40 and 0.60.

Figure 15.- Comparison of pressure-coefficient distributions obtained through the use of plume simulators with those obtained from jet operation at $p_{t,j}/p_\infty = 2$ for configuration 8 ($\ell/d_m = 2.00$, $d_e/d_m = 0.70$).

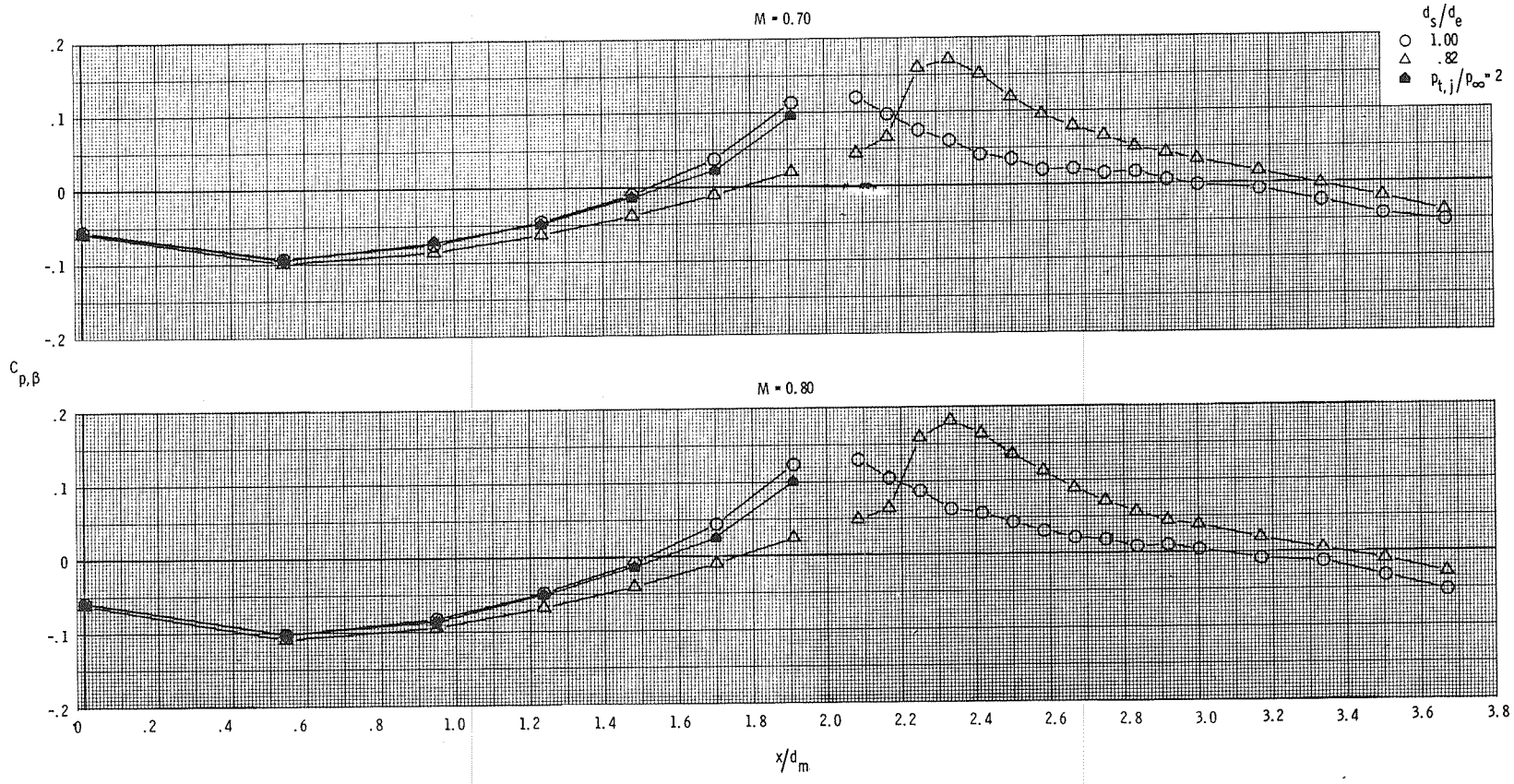

(b) M = 0.70 and 0.80.

Figure 15.- Continued.

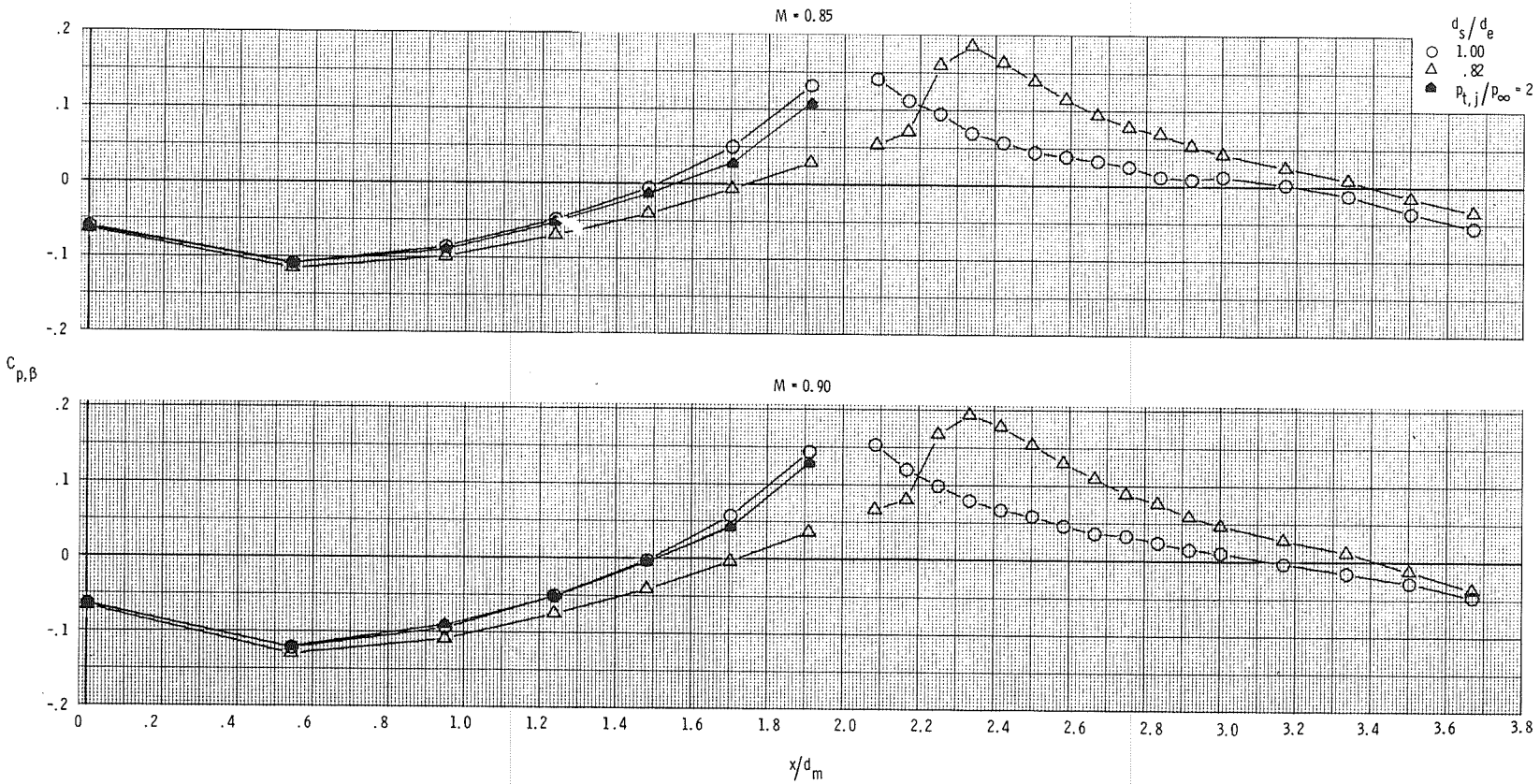

(c) M = 0.85 and 0.90.

Figure 15.- Continued.

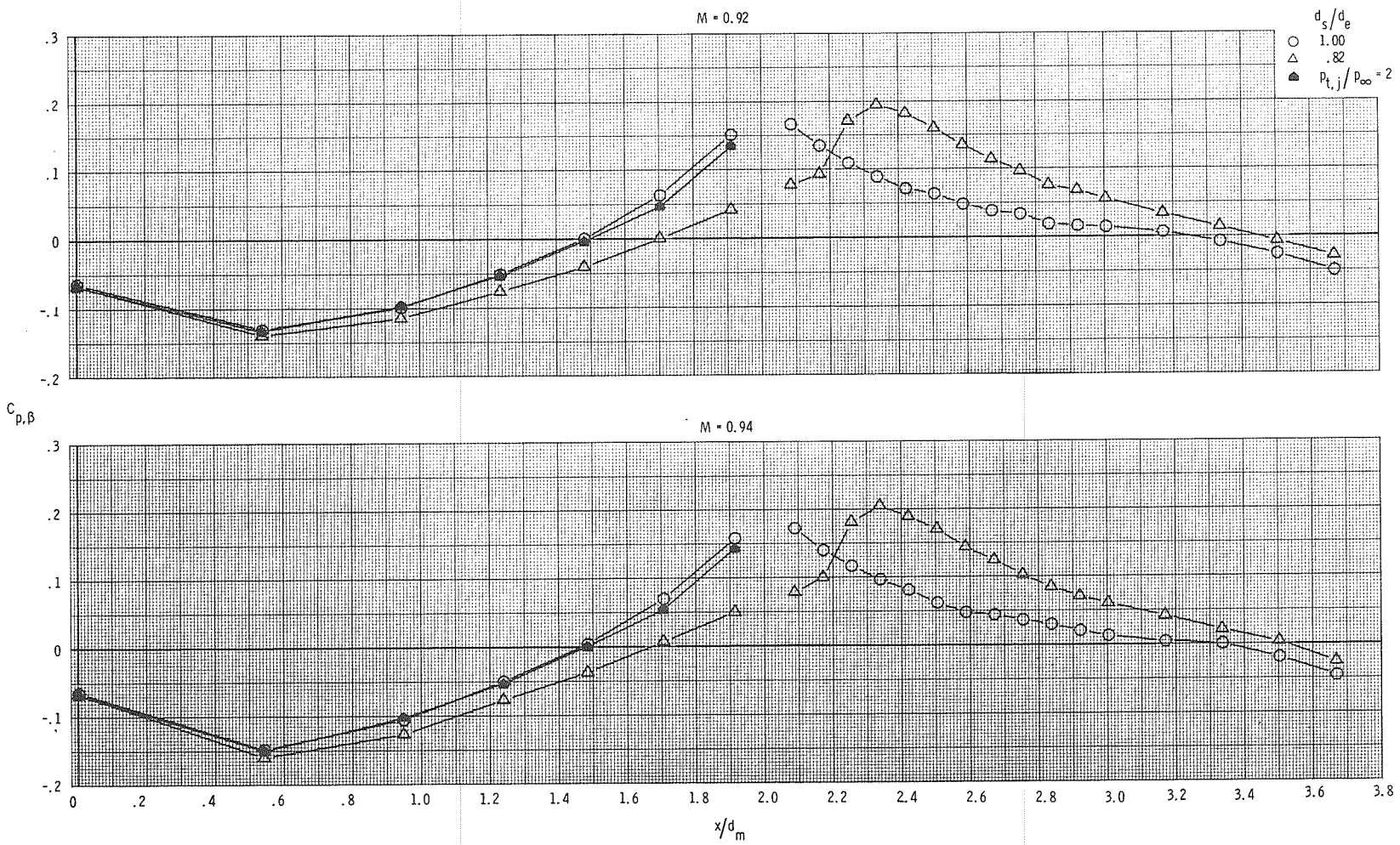

(d) M = 0.92 and 0.94.

Figure 15.- Continued.

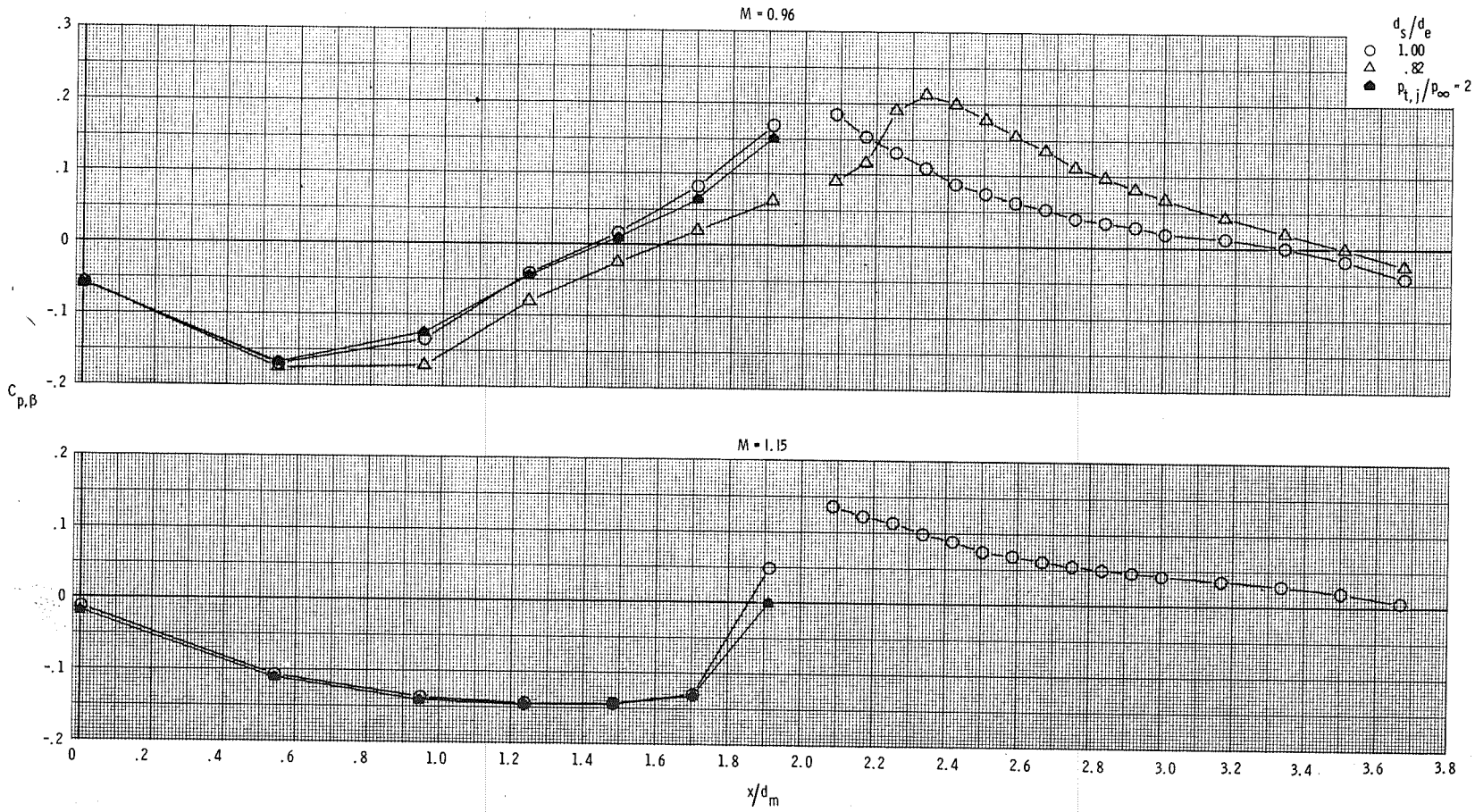

(e) M = 0.96 and 1.15.

Figure 15.- Continued.

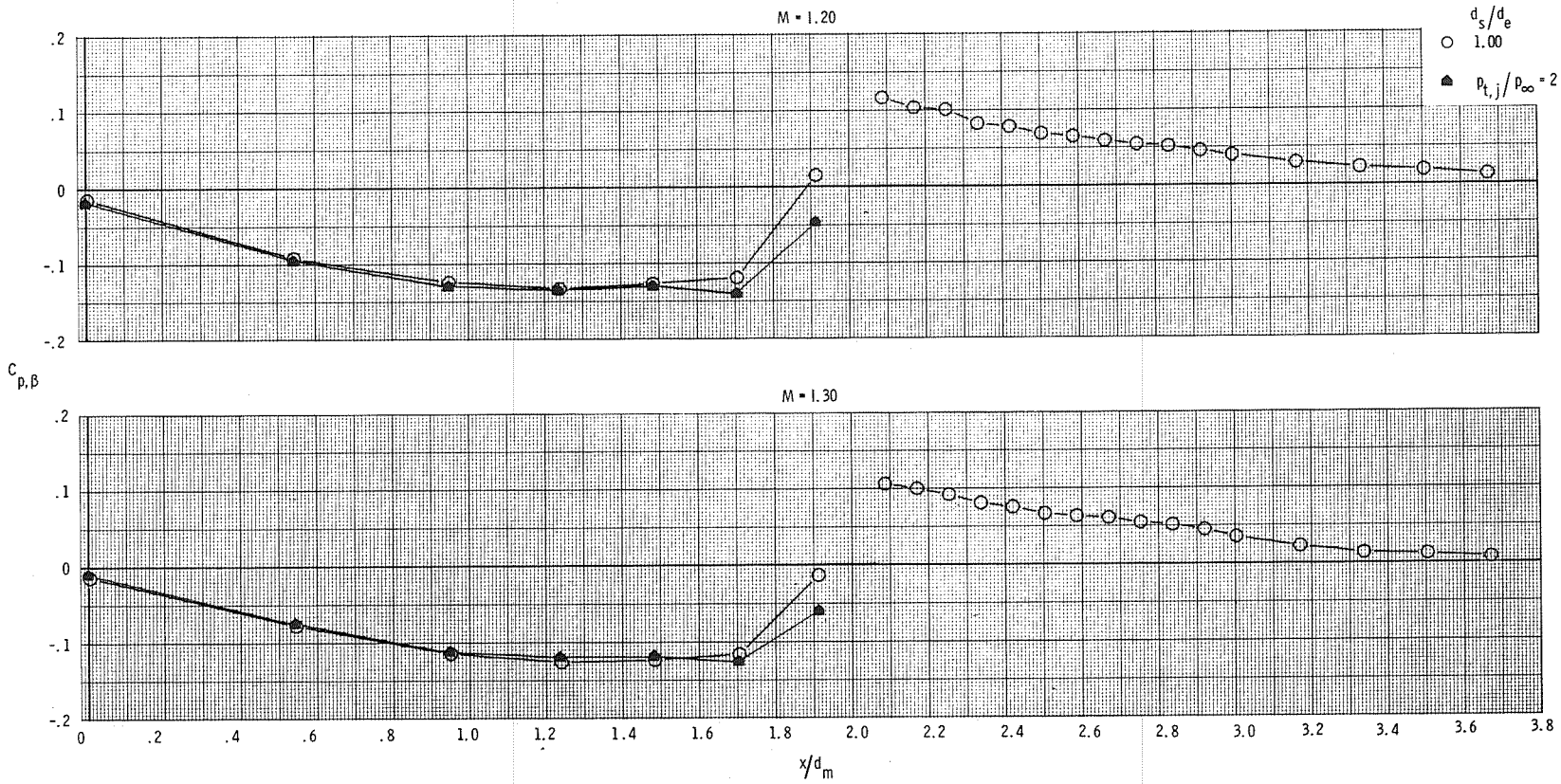

(f) M = 1.20 and 1.30.

Figure 15.- Concluded.

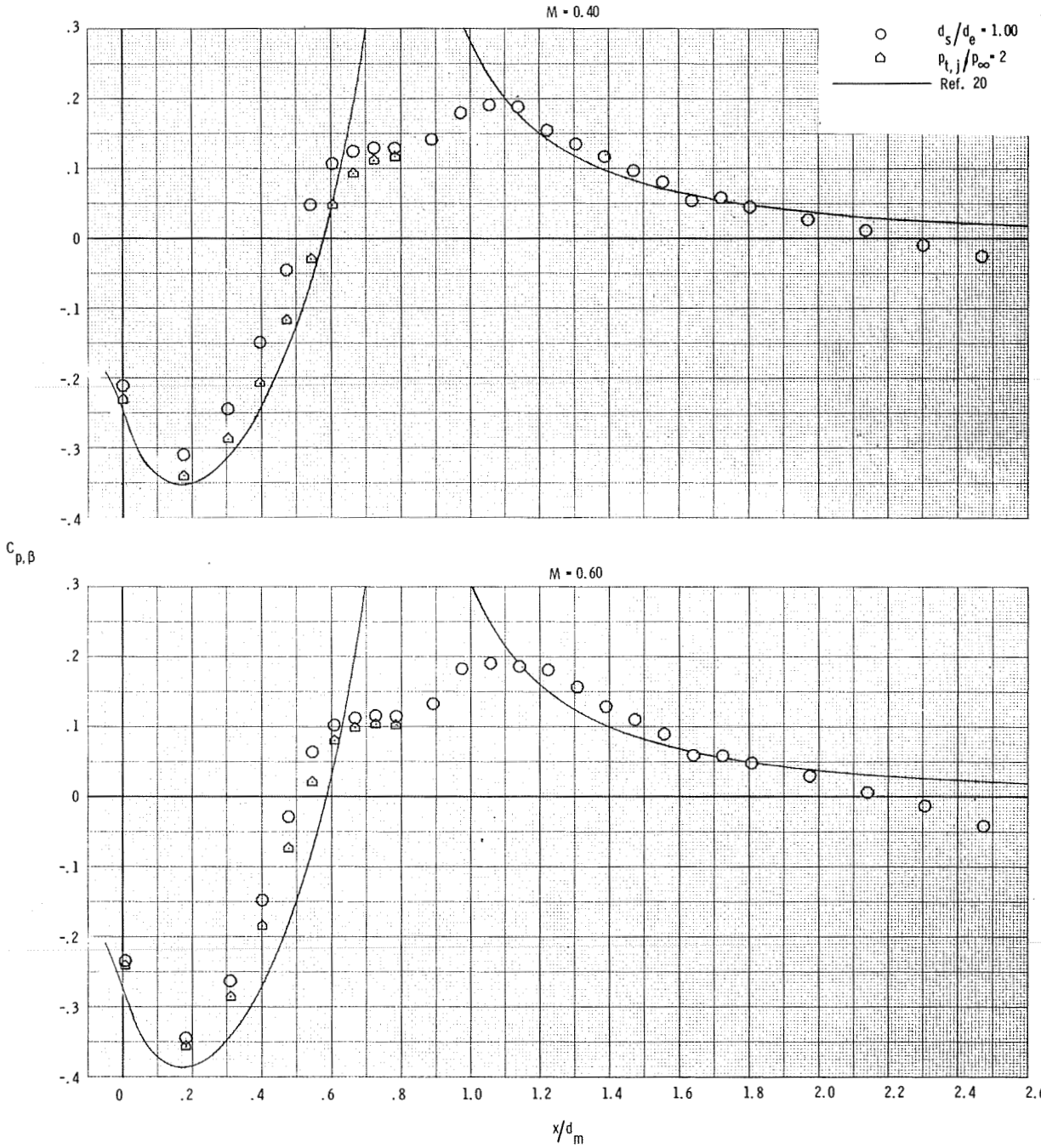

(a) M = 0.40 and 0.60.

Figure 16.- Comparison of pressure-coefficient distributions obtained by use of the theoretical technique of reference 20 with those obtained from jet operation at $p_{t,j}/p_\infty = 2$ and for use of the $d_s/d_e = 1.00$ simulator for configuration 1 ($l/d_m = 0.80$, $d_e/d_m = 0.50$). (Solution of ref. 21 would not converge for this configuration.)

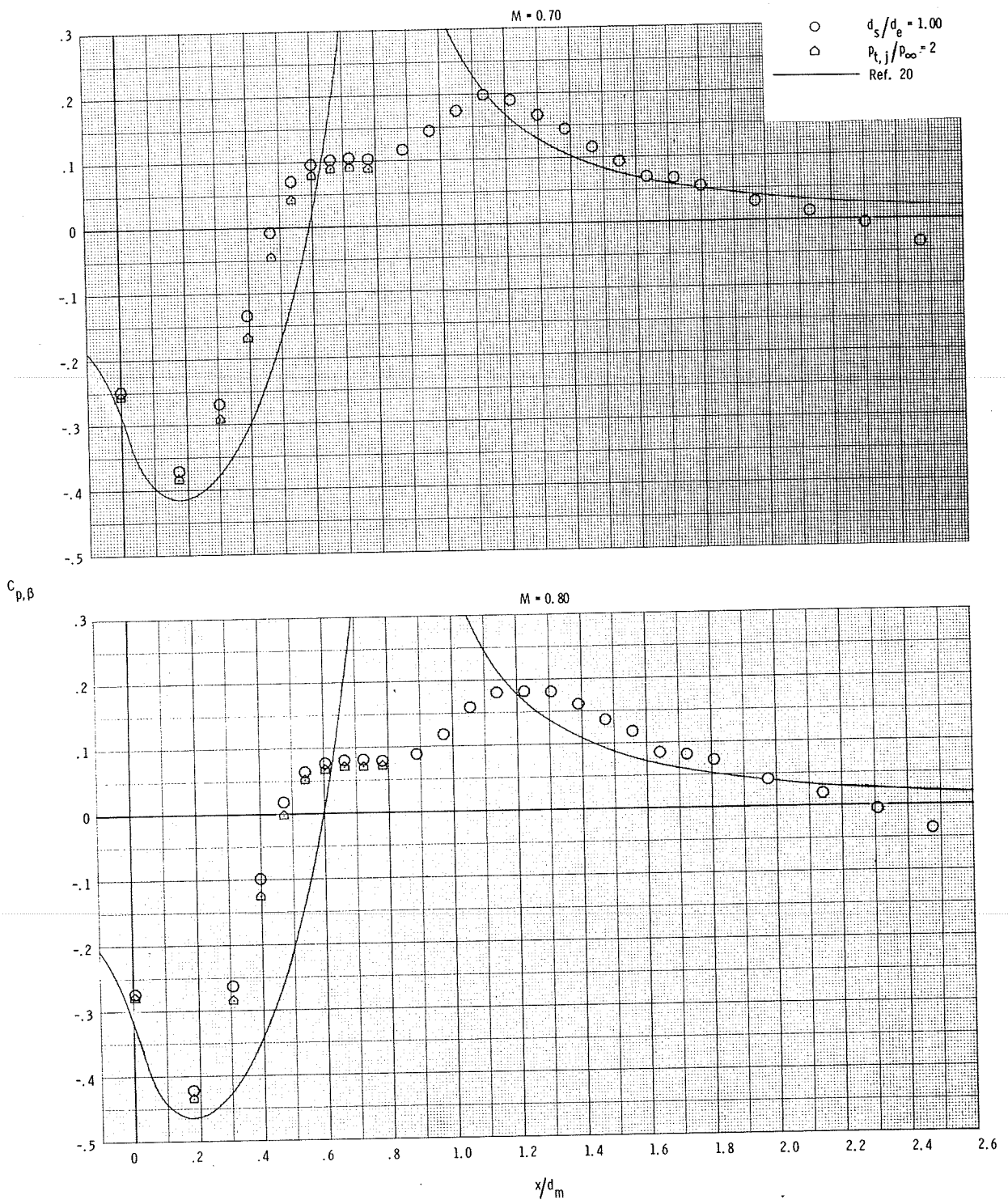

(b) M = 0.70 and 0.80.

Figure 16.- Continued.

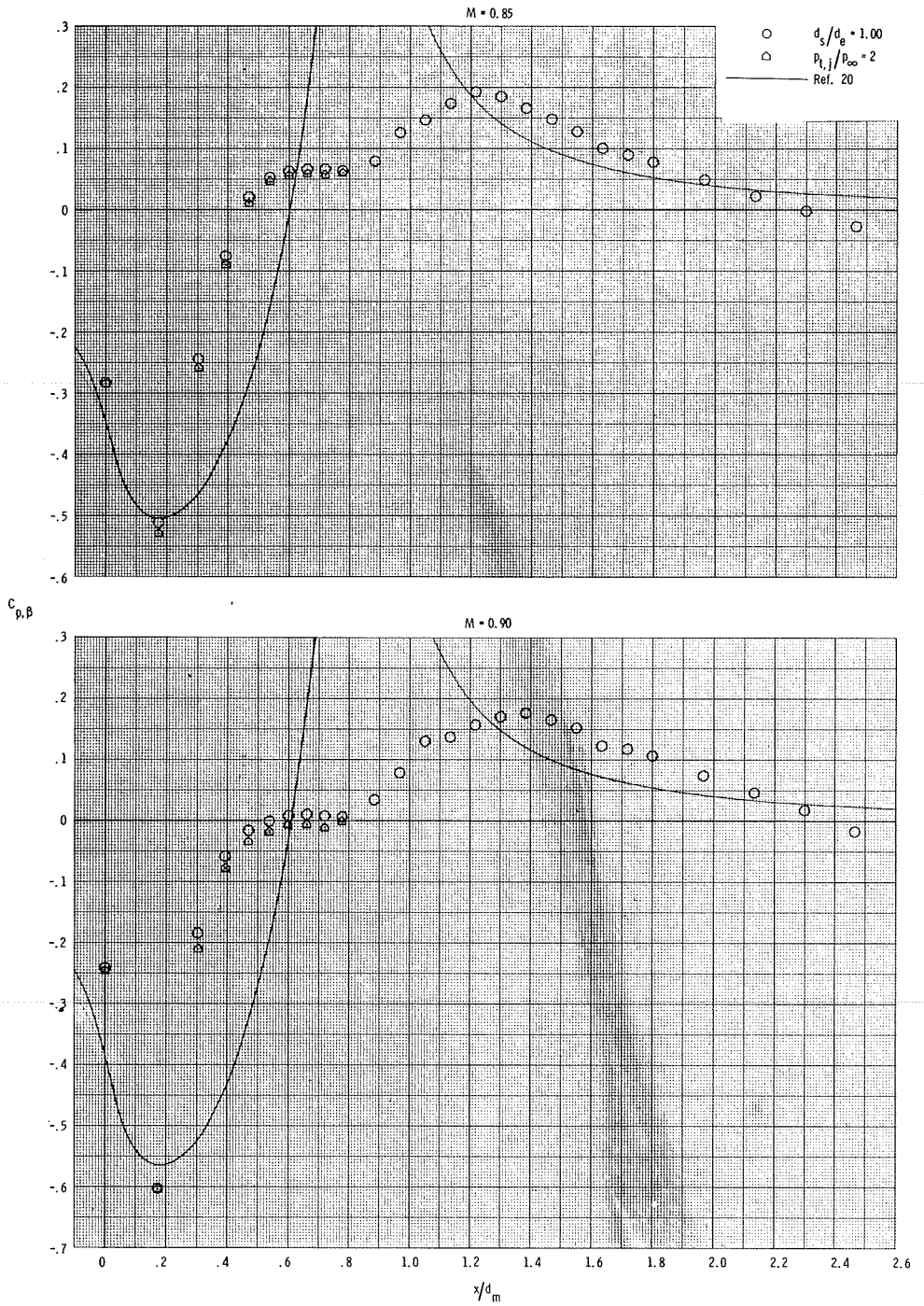

(c) M = 0.85 and 0.90.

Figure 16.- Concluded.

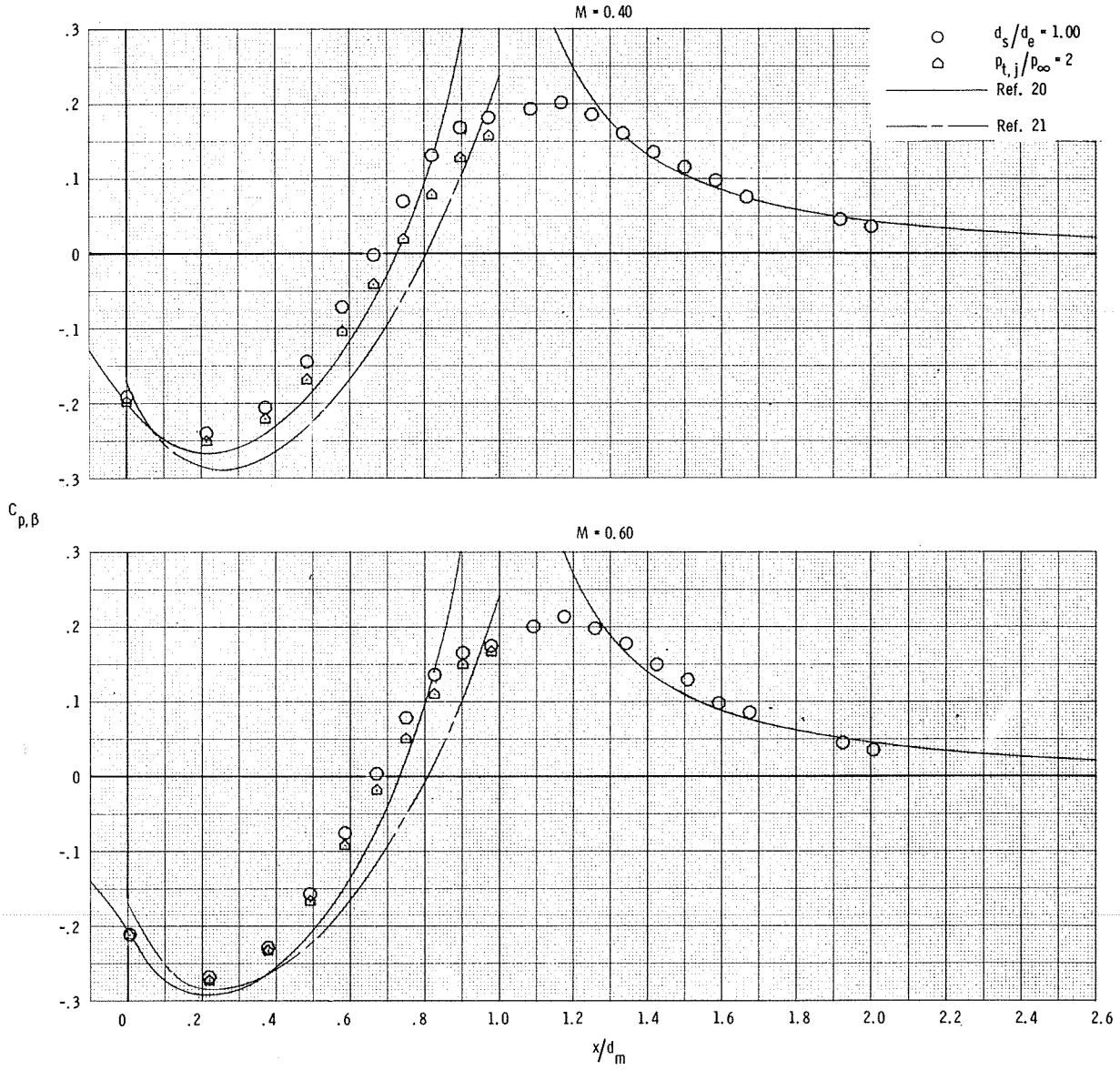

(a) M = 0.40 and 0.60.

Figure 17.- Comparison of pressure-coefficient distributions obtained by use of the theoretical techniques of references 20 and 21 with those obtained from jet operation at $p_{t,j}/p_\infty = 2$ and for use of the $d_s/d_e = 1.00$ simulator for configuration 2 ($l/d_m = 1.00$, $d_e/d_m = 0.50$).

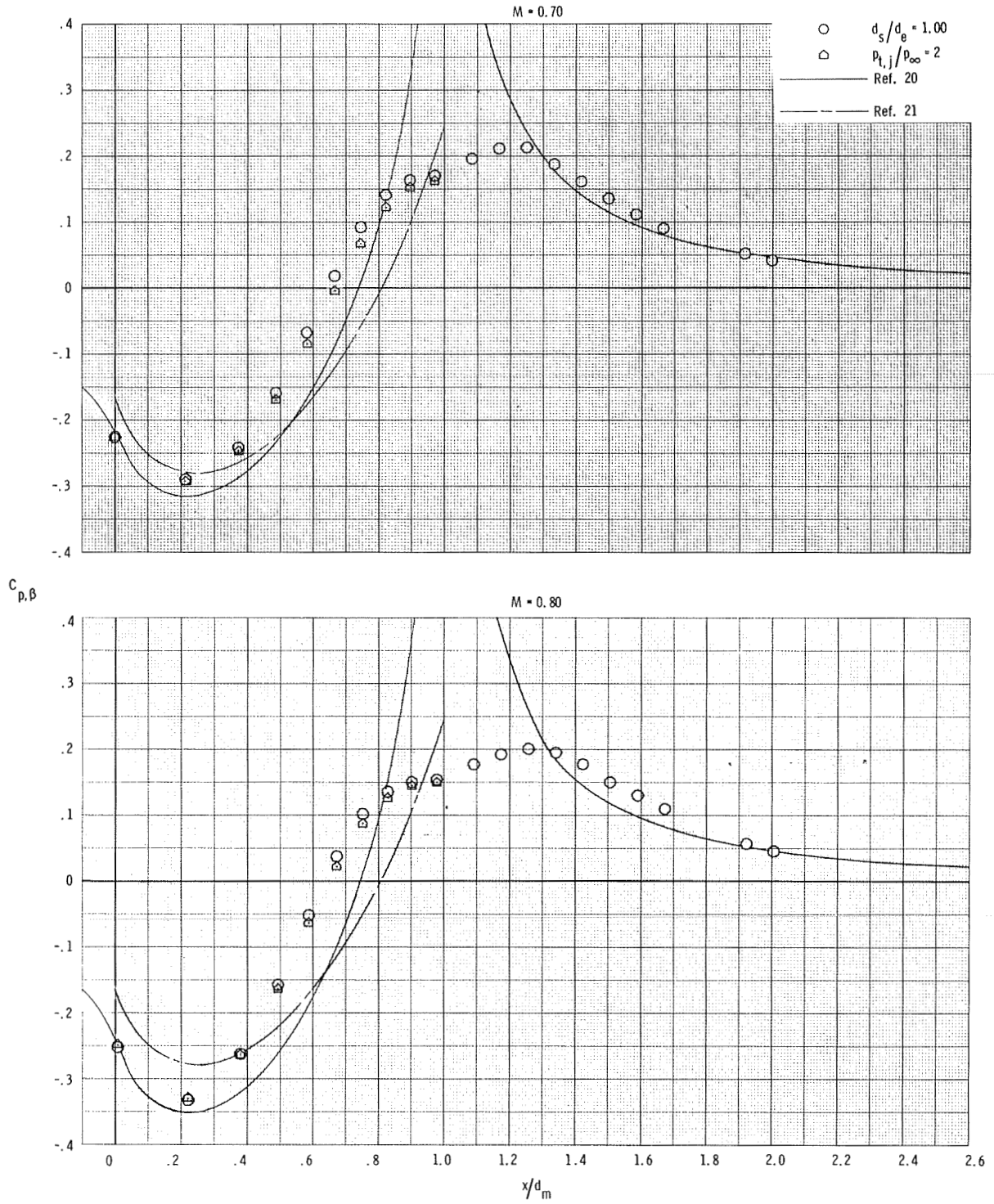

(b) M = 0.70 and 0.80.

Figure 17.- Continued.

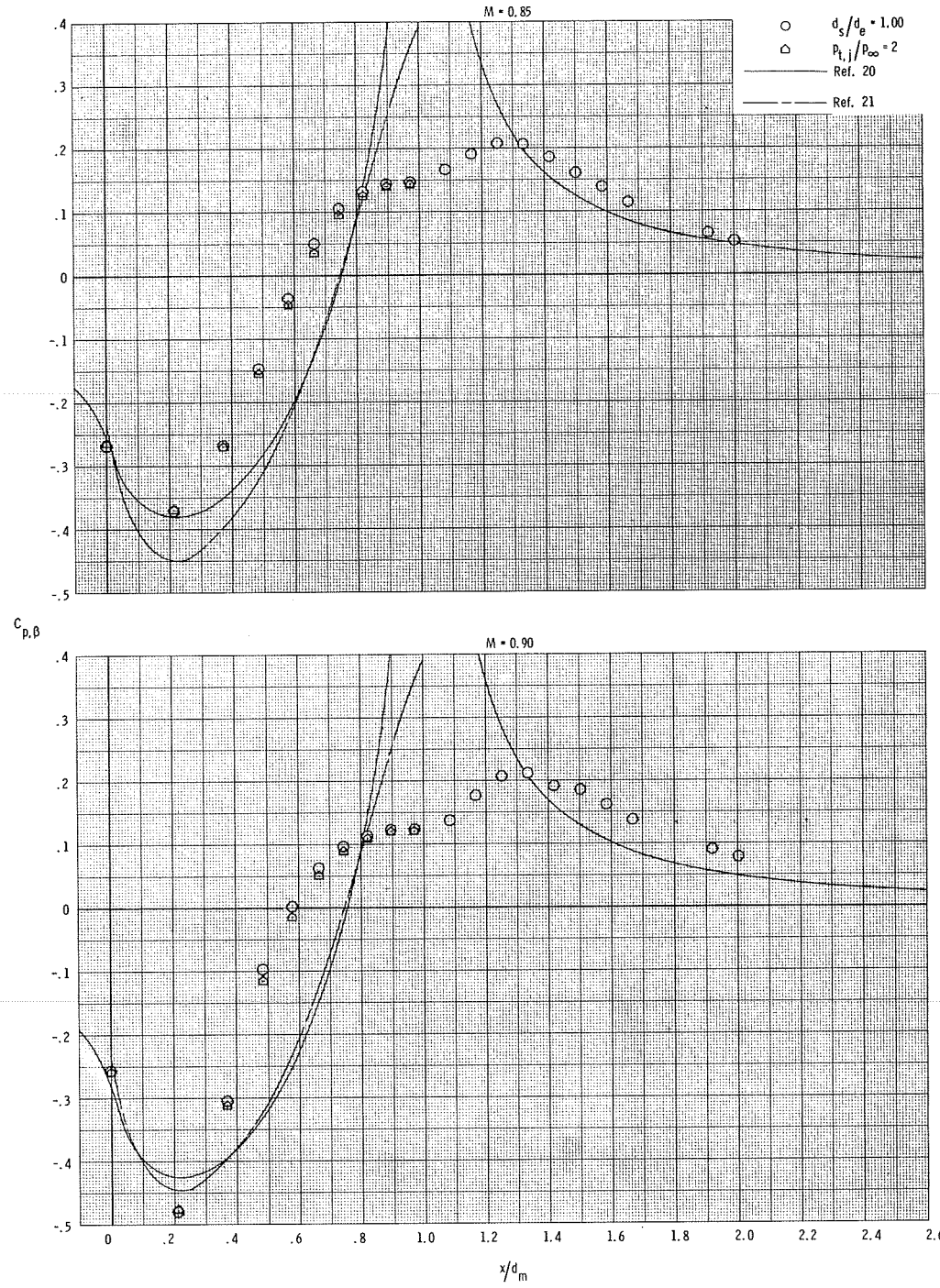

(c) M = 0.85 and 0.90.

Figure 17.- Concluded.

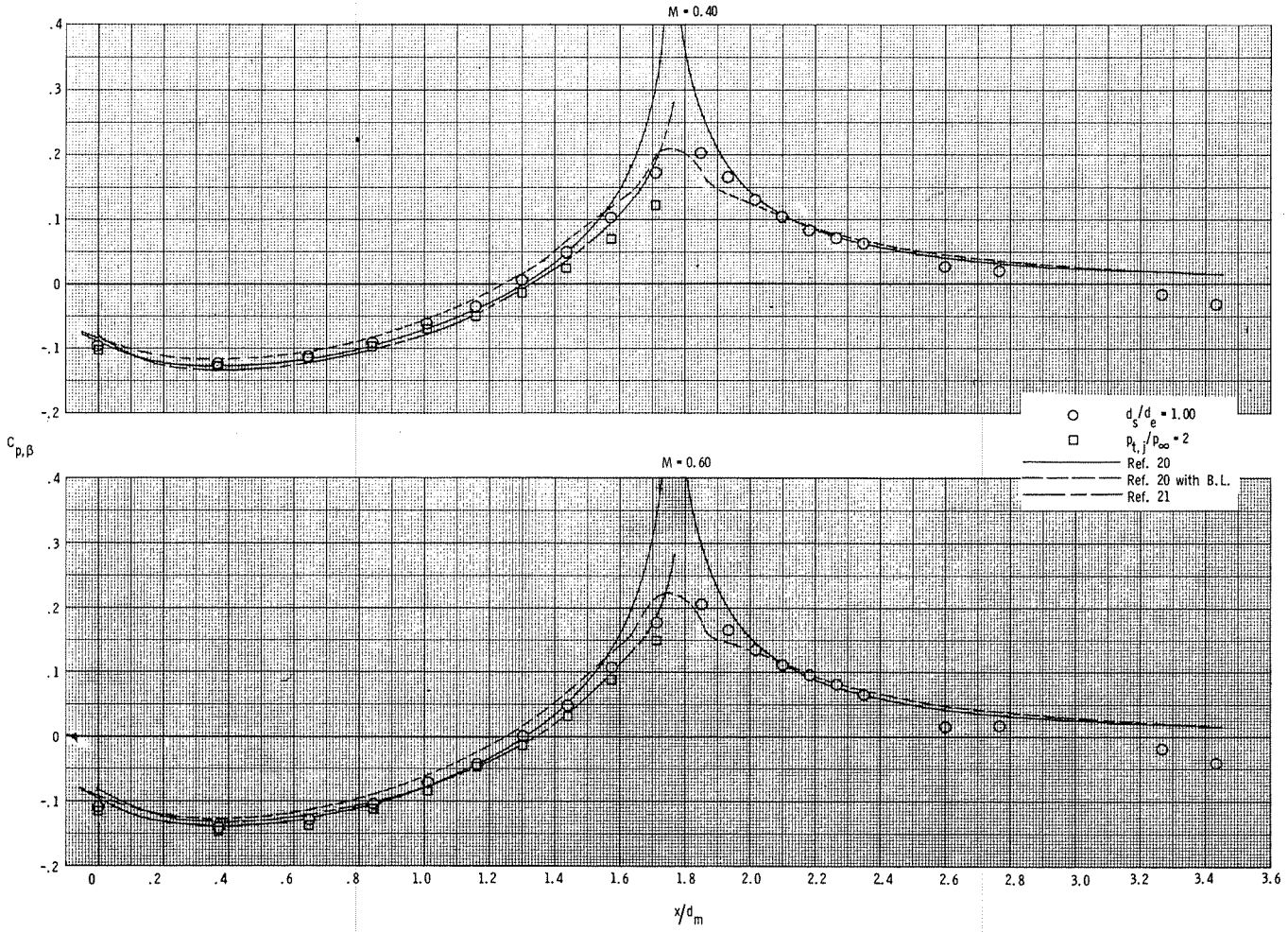

(a) M = 0.40 and 0.60.

Figure 18.- Comparison of pressure-coefficient distributions obtained by use of the theoretical techniques of references 20 and 21 with those obtained from jet operation at $p_{t,j}/p_\infty = 2$ and from use of the $d_s/d_e = 1.00$ simulator for configuration 3 ($l/d_m = 1.77$, $d_e/d_m = 0.50$). (B.L. indicates boundary layer.)

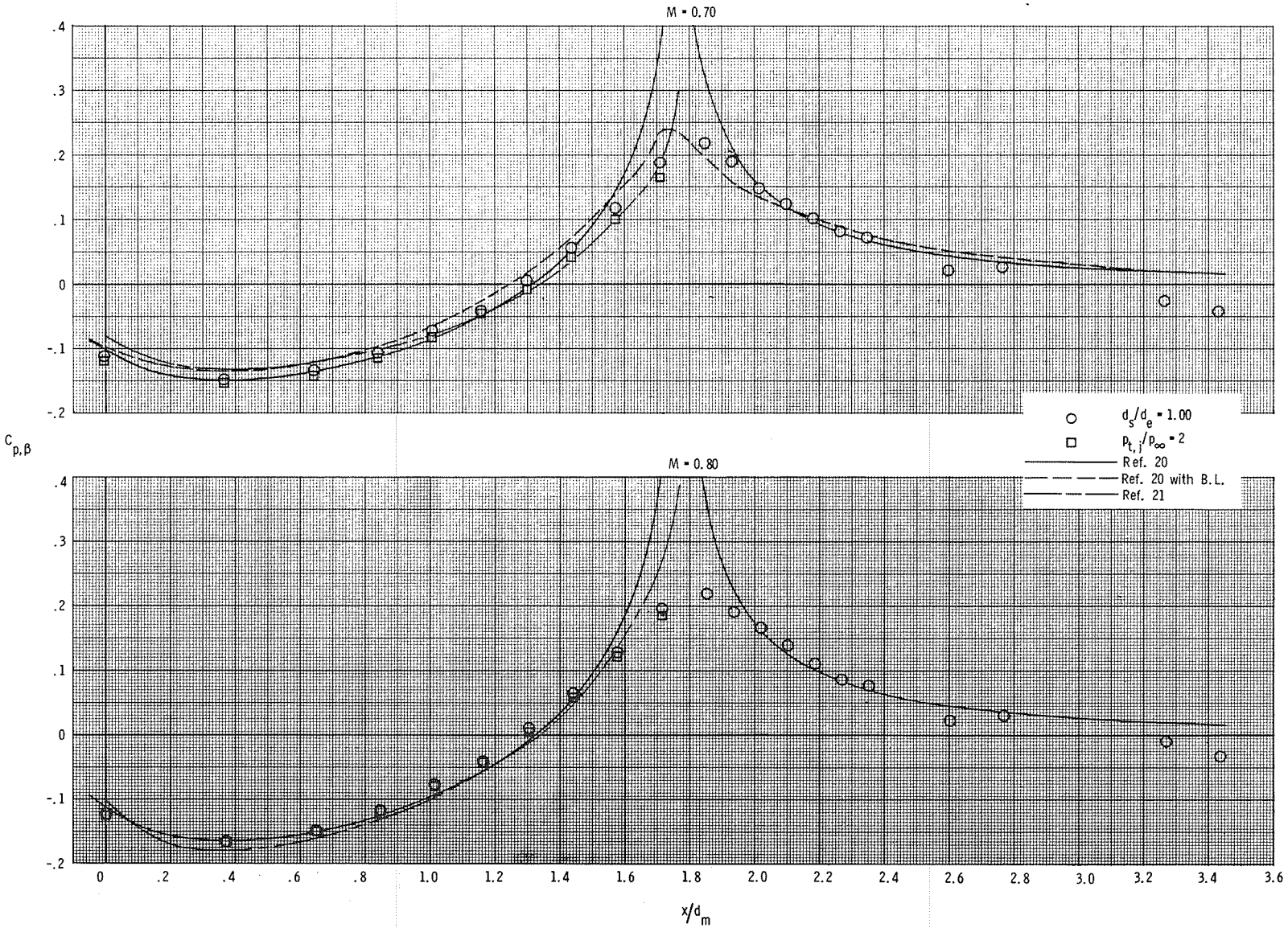

(b) M = 0.70 and 0.80.

Figure 18.- Continued.

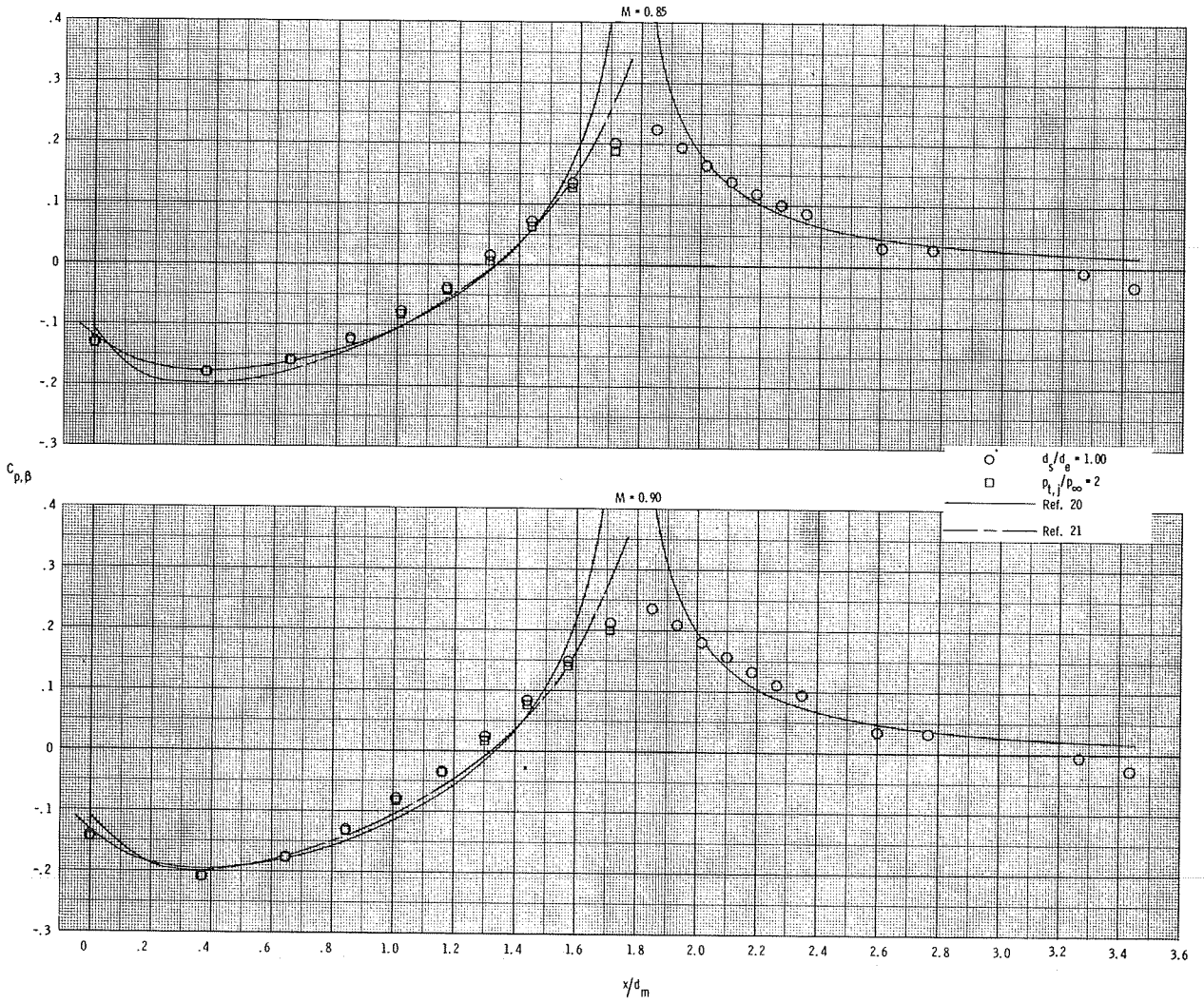

(c) M = 0.85 and 0.90.

Figure 18.- Concluded.

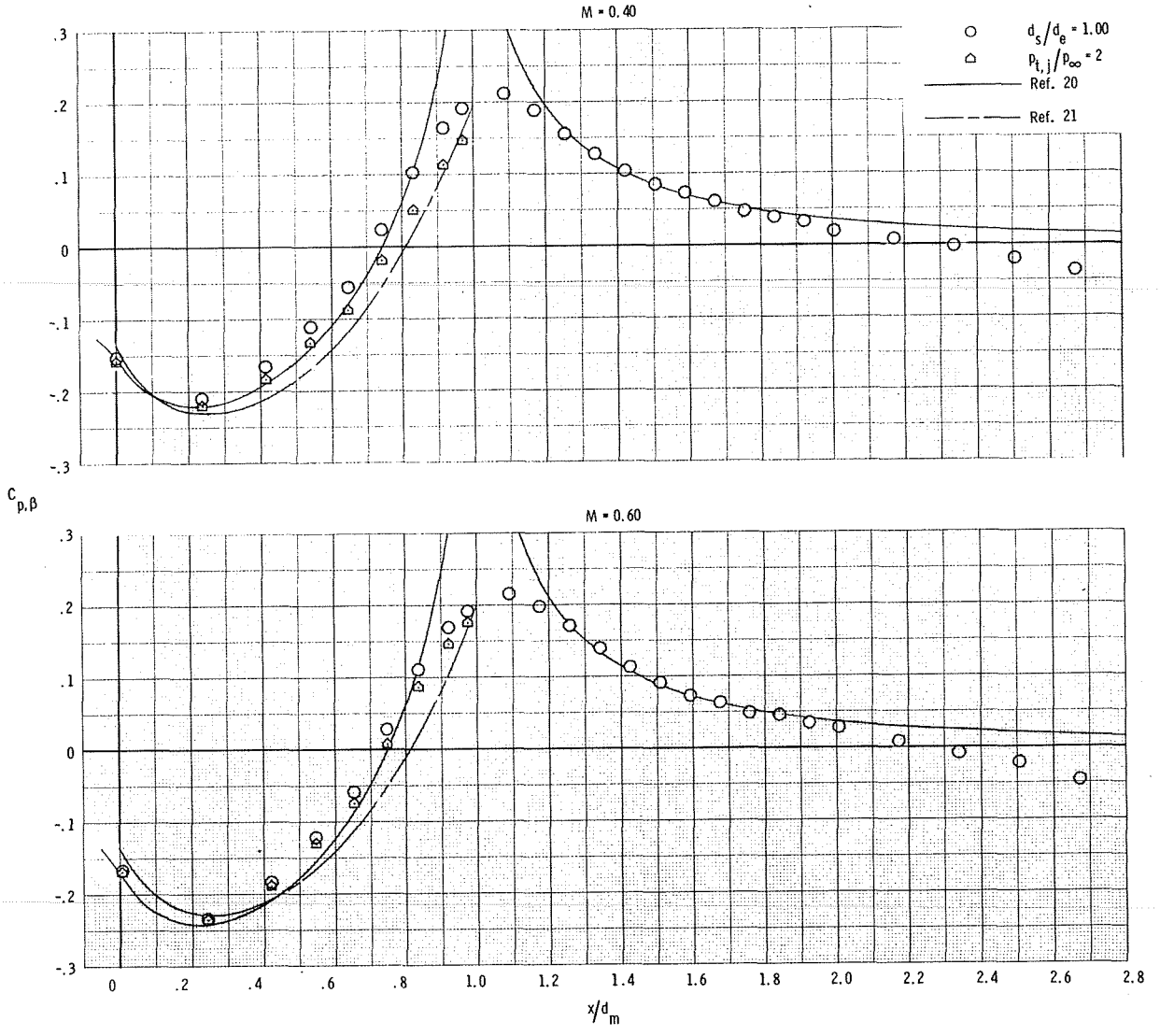

(a) M = 0.40 and 0.60.

Figure 19.- Comparison of pressure-coefficient distributions obtained by use of the theoretical techniques of references 20 and 21 with those obtained from jet operation at $p_{t,j}/p_\infty = 2$ and from use of the $d_s/d_e = 1.00$ simulator for configuration 4 ($l/d_m = 1.00$, $d_e/d_m = 0.60$).

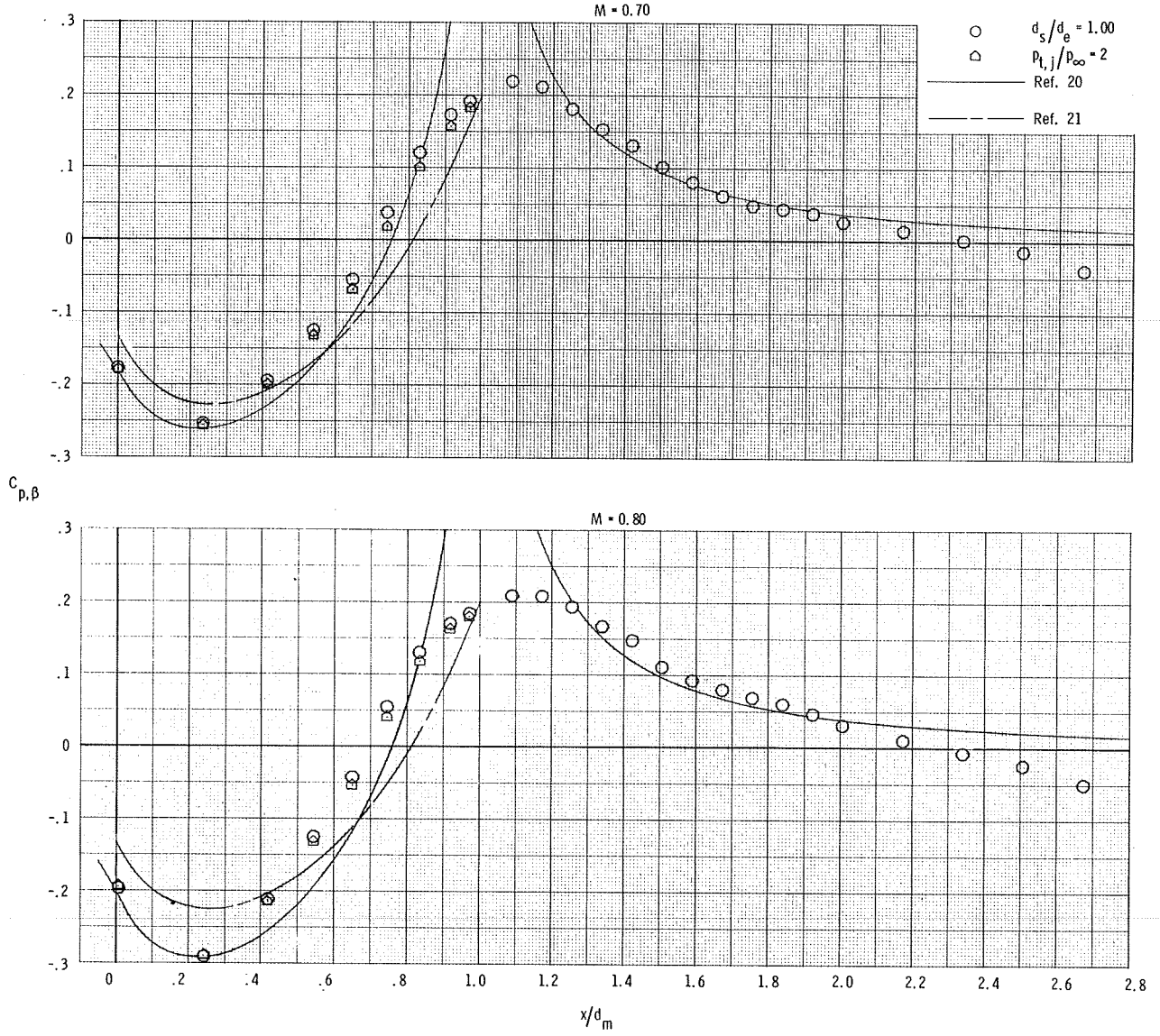

(b) M = 0.70 and 0.80.

Figure 19.- Continued.

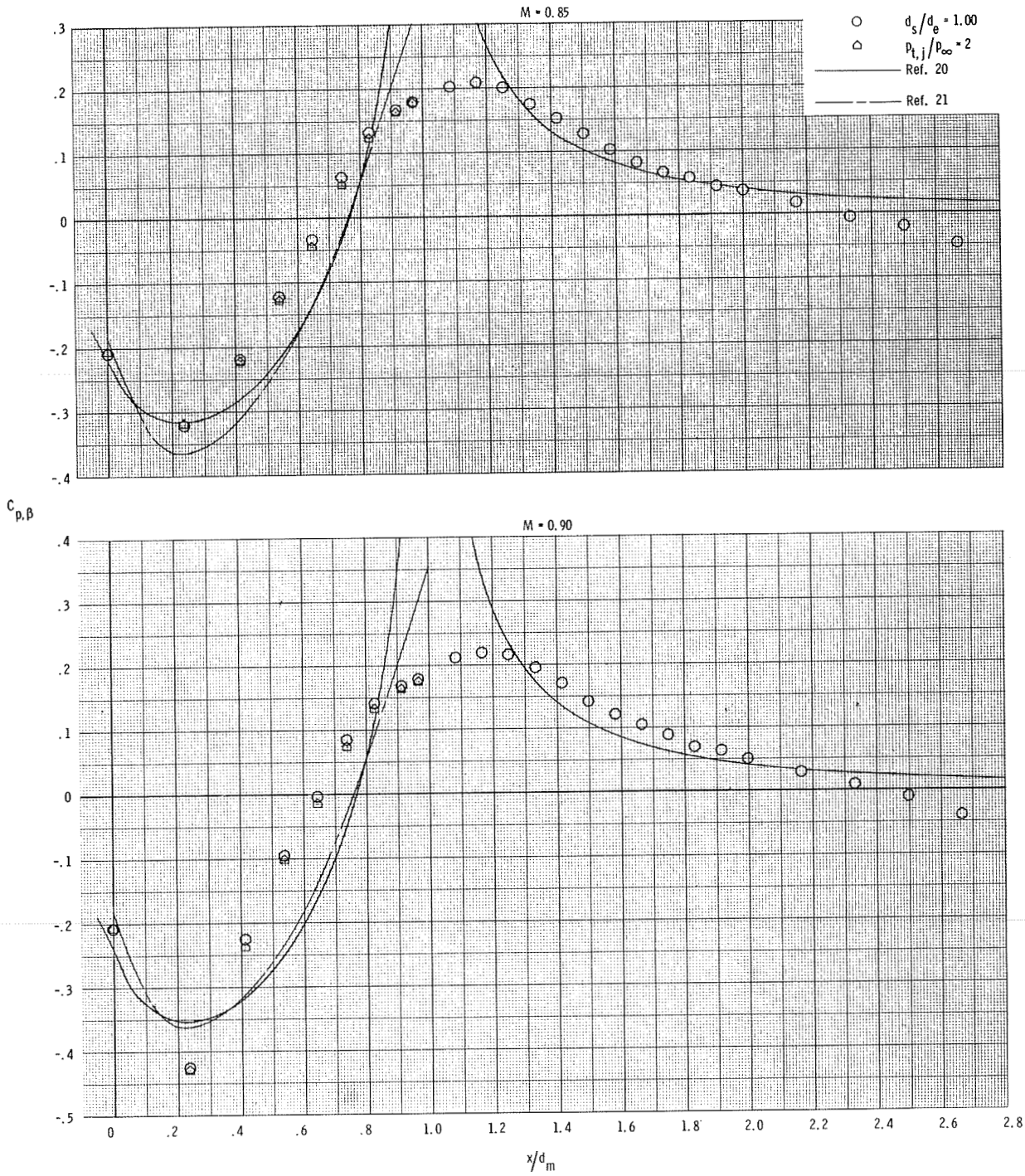

(c) M = 0.85 and 0.90.

Figure 19.- Concluded.

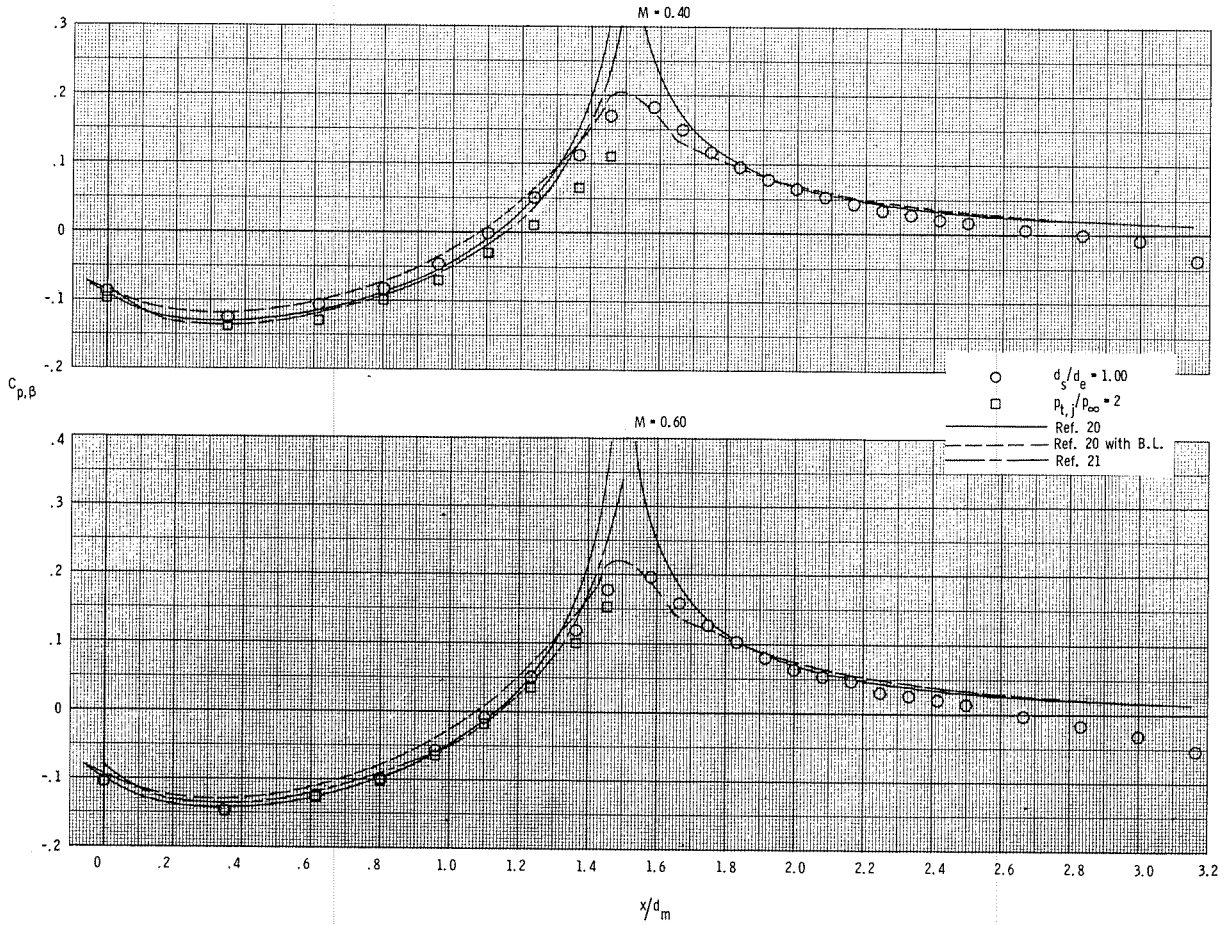

(a) M = 0.40 and 0.60.

Figure 20.- Comparison of pressure-coefficient distributions obtained by use of the theoretical techniques of references 20 and 21 with those obtained from jet operation at $p_{t,j}/p_\infty = 2$ and from use of the $d_s/d_e = 1.00$ simulator for configuration 5 ($l/d_m = 1.50$, $d_e/d_m = 0.60$). (B.L. indicates boundary layer.)

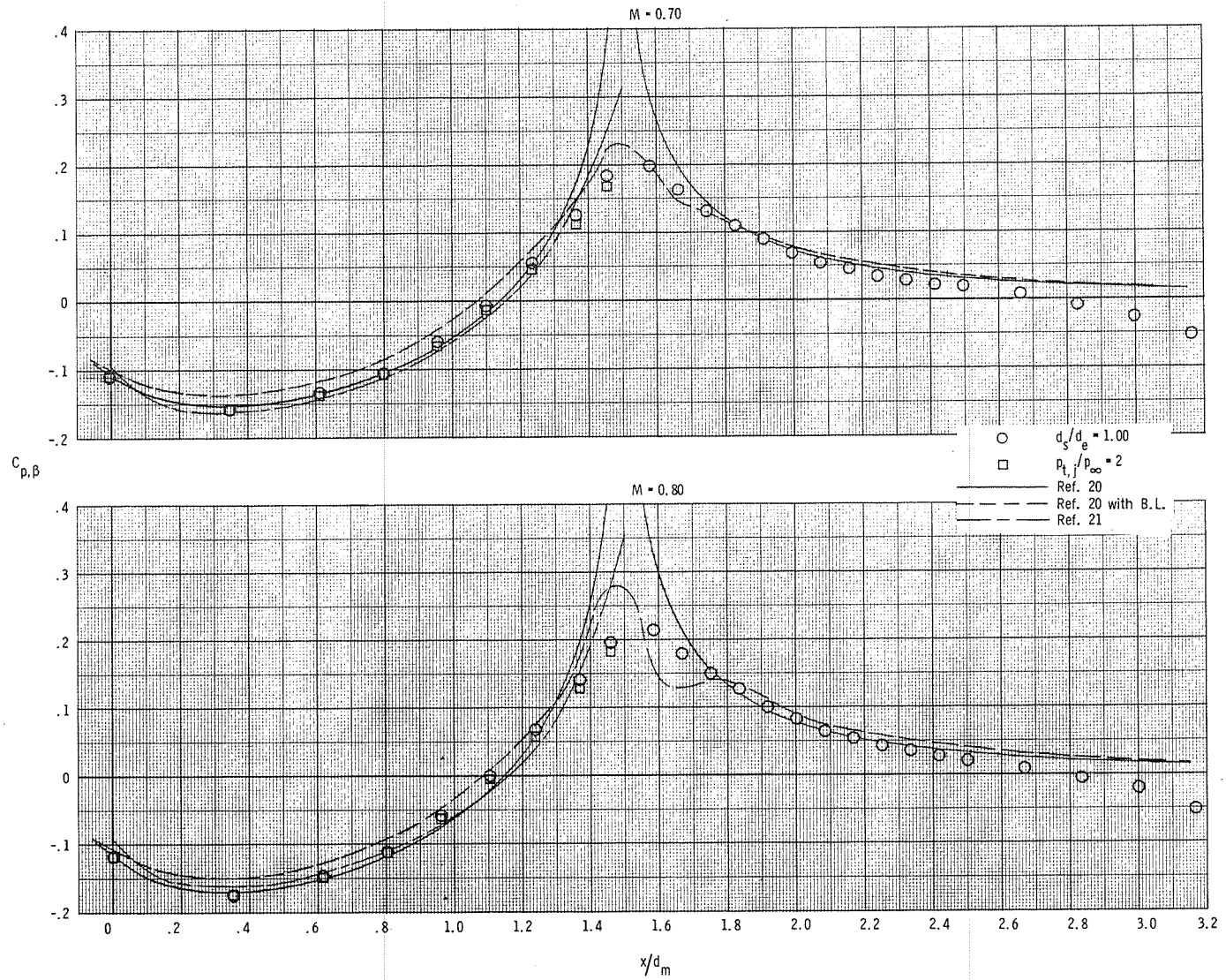

(b) M = 0.70 and 0.80.

Figure 20.- Continued.

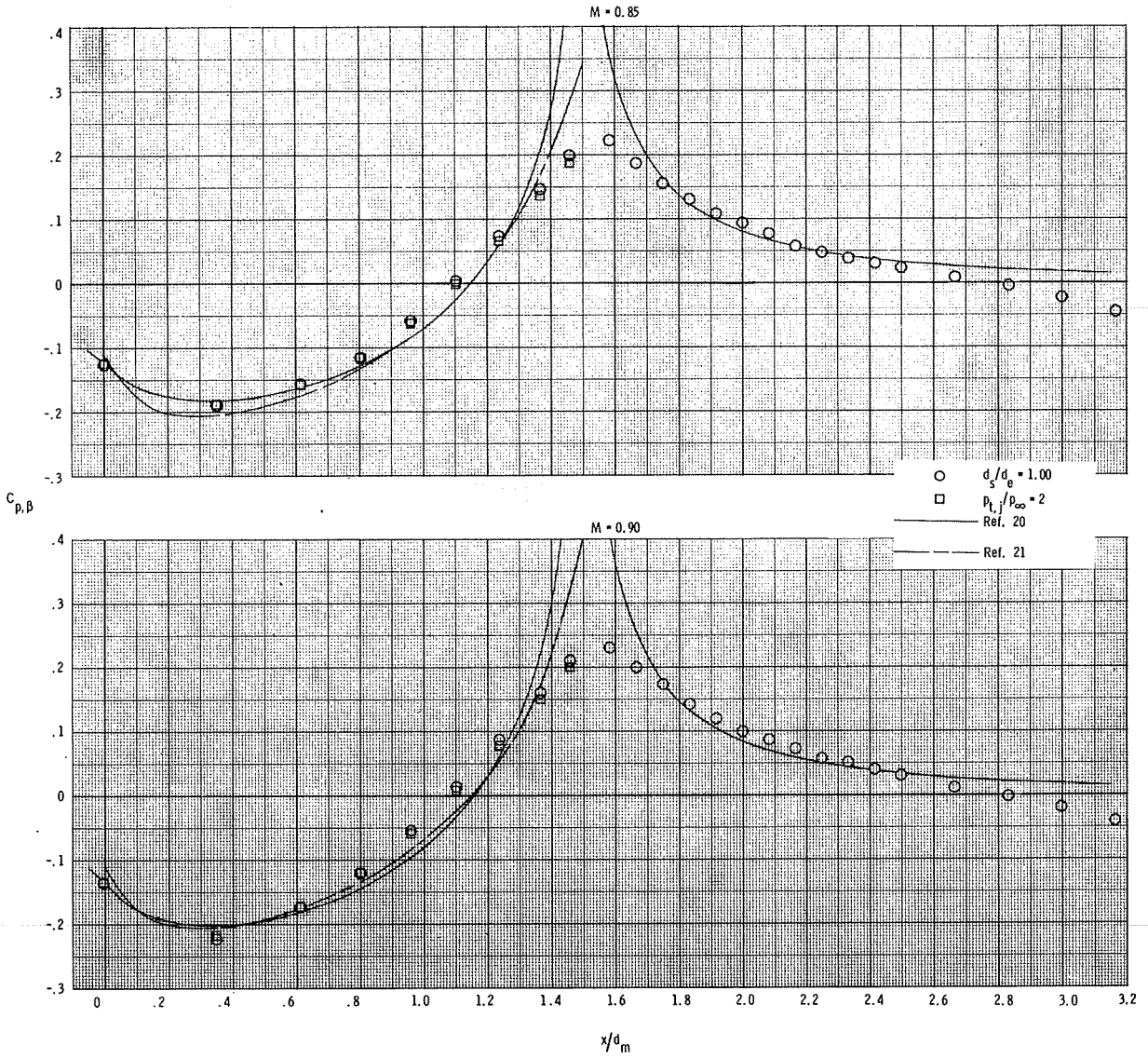

(c) M = 0.85 and 0.90.

Figure 20.- Concluded.

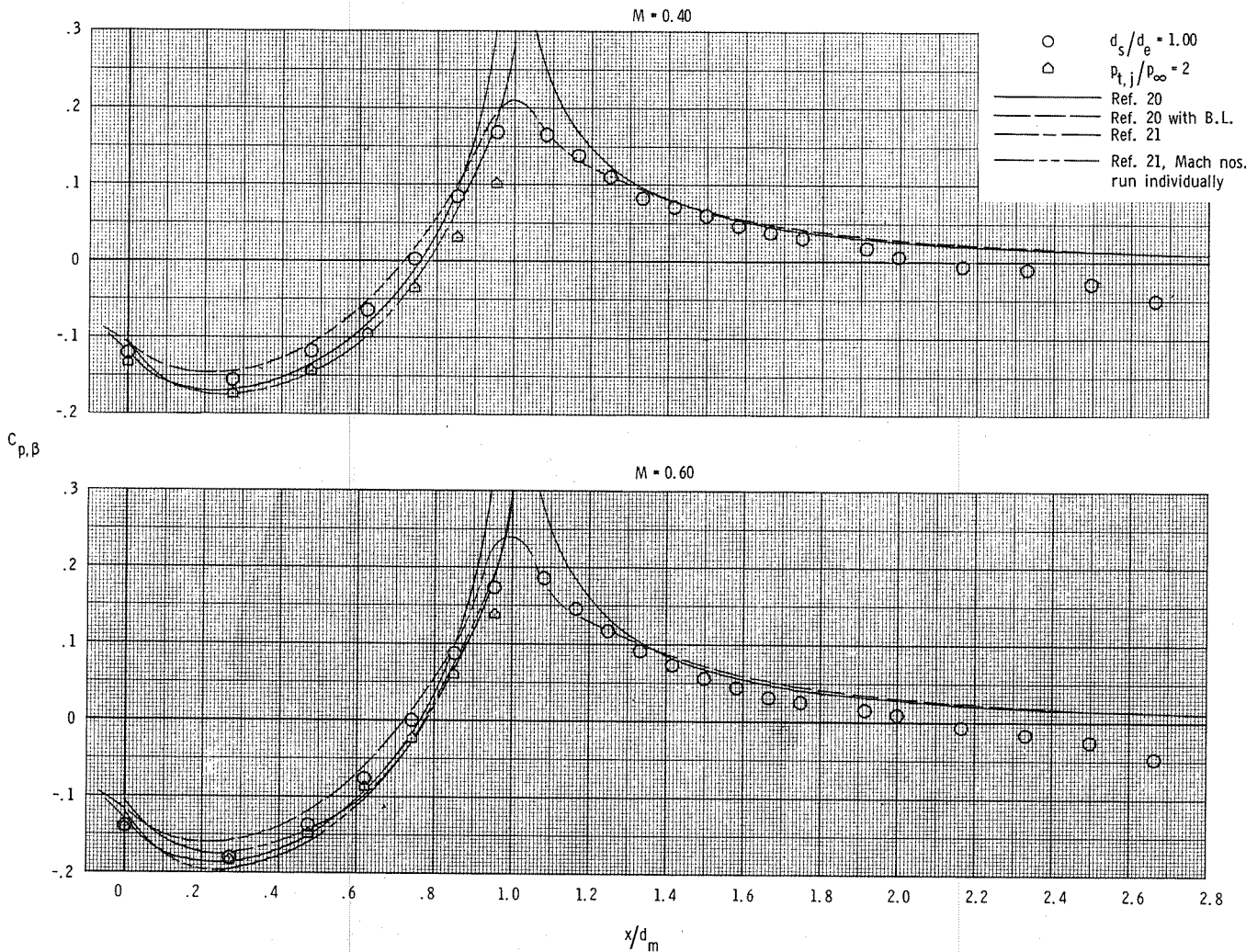

(a) M = 0.40 and 0.60.

Figure 21.- Comparison of pressure-coefficient distributions obtained by use of the theoretical techniques of references 20 and 21 with those obtained from jet operation at $p_{t,j}/p_\infty = 2$ and from use of the $d_S/d_e = 1.00$ simulator for configuration 6 ($l/d_m = 1.00$, $d_e/d_m = 0.70$). (B.L. indicates boundary layer.)

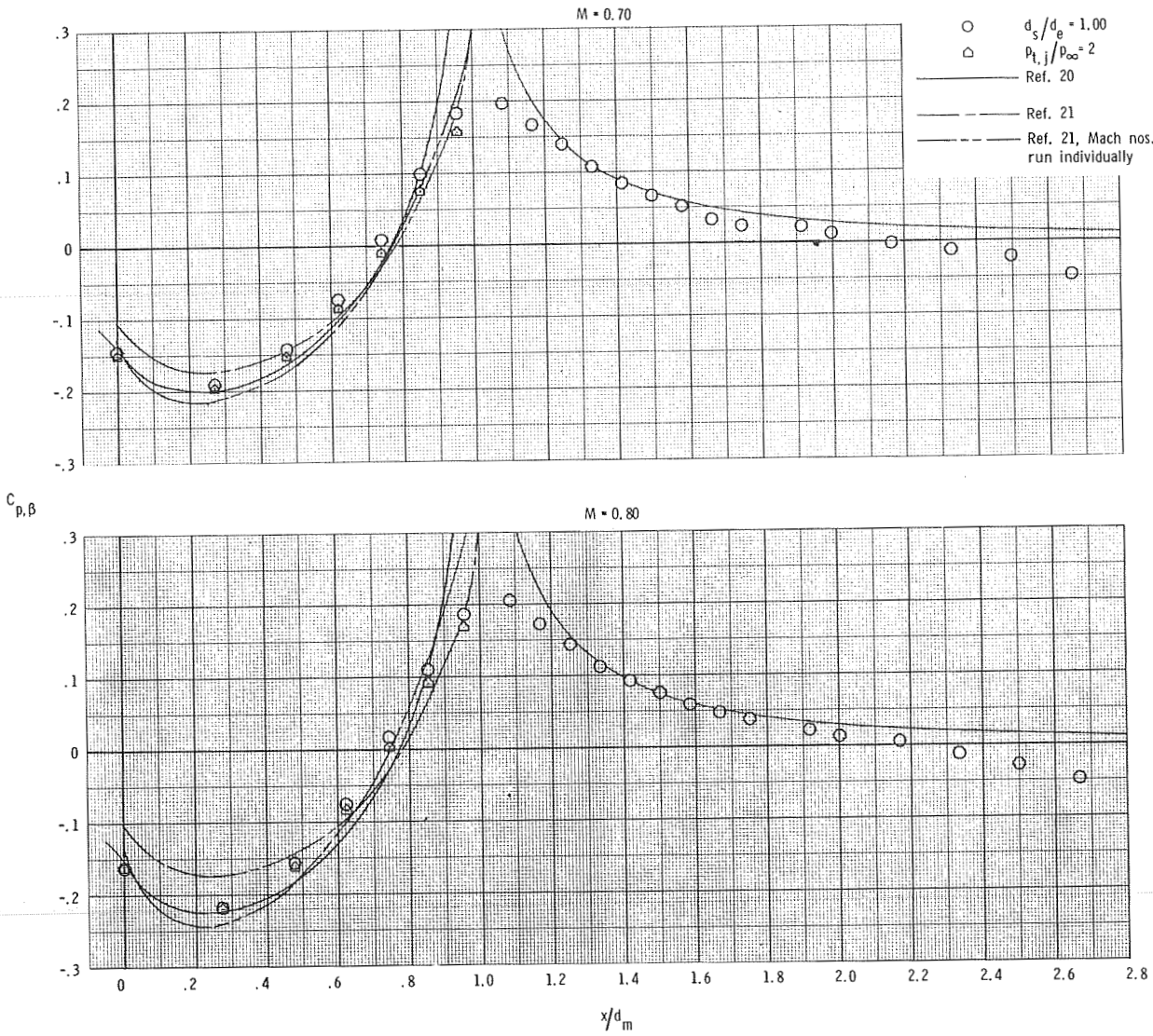

(b) M = 0.70 and 0.80.

Figure 21.- Continued.

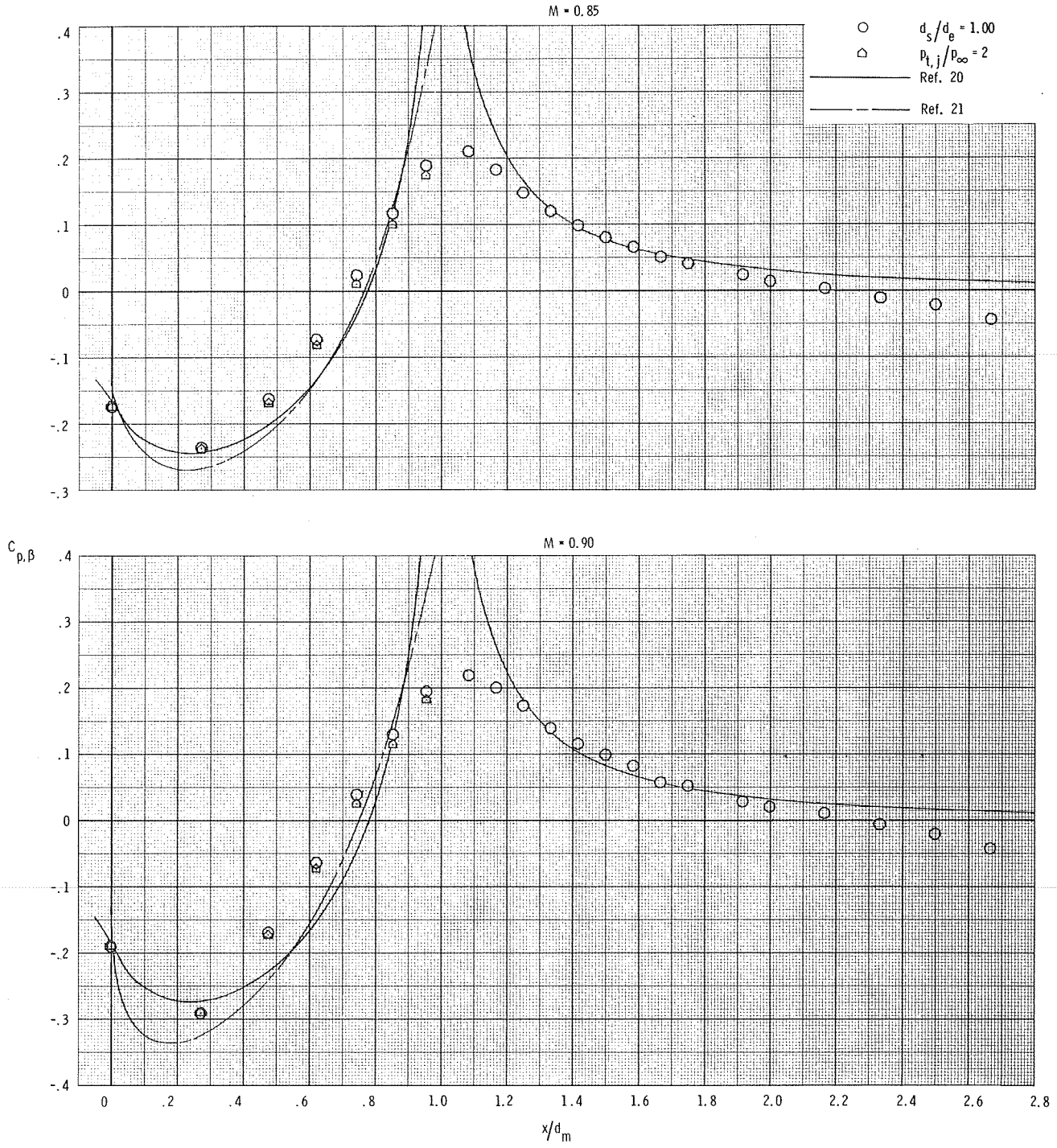

(c) M = 0.85 and 0.90.

Figure 21.- Concluded.

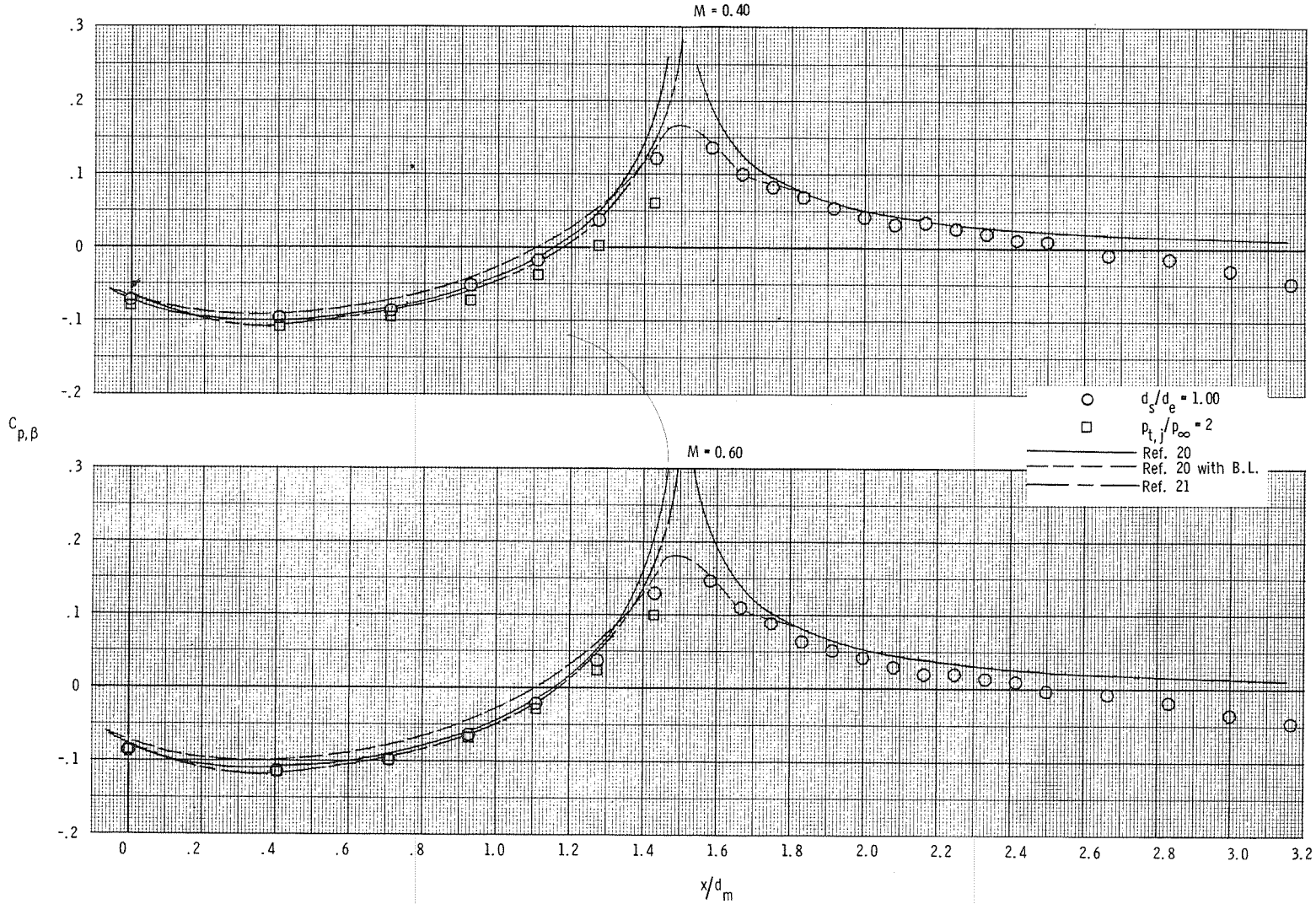

(a) M = 0.40 and 0.60.

Figure 22.- Comparison of pressure-coefficient distributions obtained by use of the theoretical techniques of references 20 and 21 with those obtained from jet operation at $p_{t,j}/p_\infty = 2$ and from use of the $d_s/d_e = 1.00$ simulator for configuration 7 ($l/d_m = 1.50$, $d_e/d_m = 0.70$). (B.L. indicates boundary layer.)

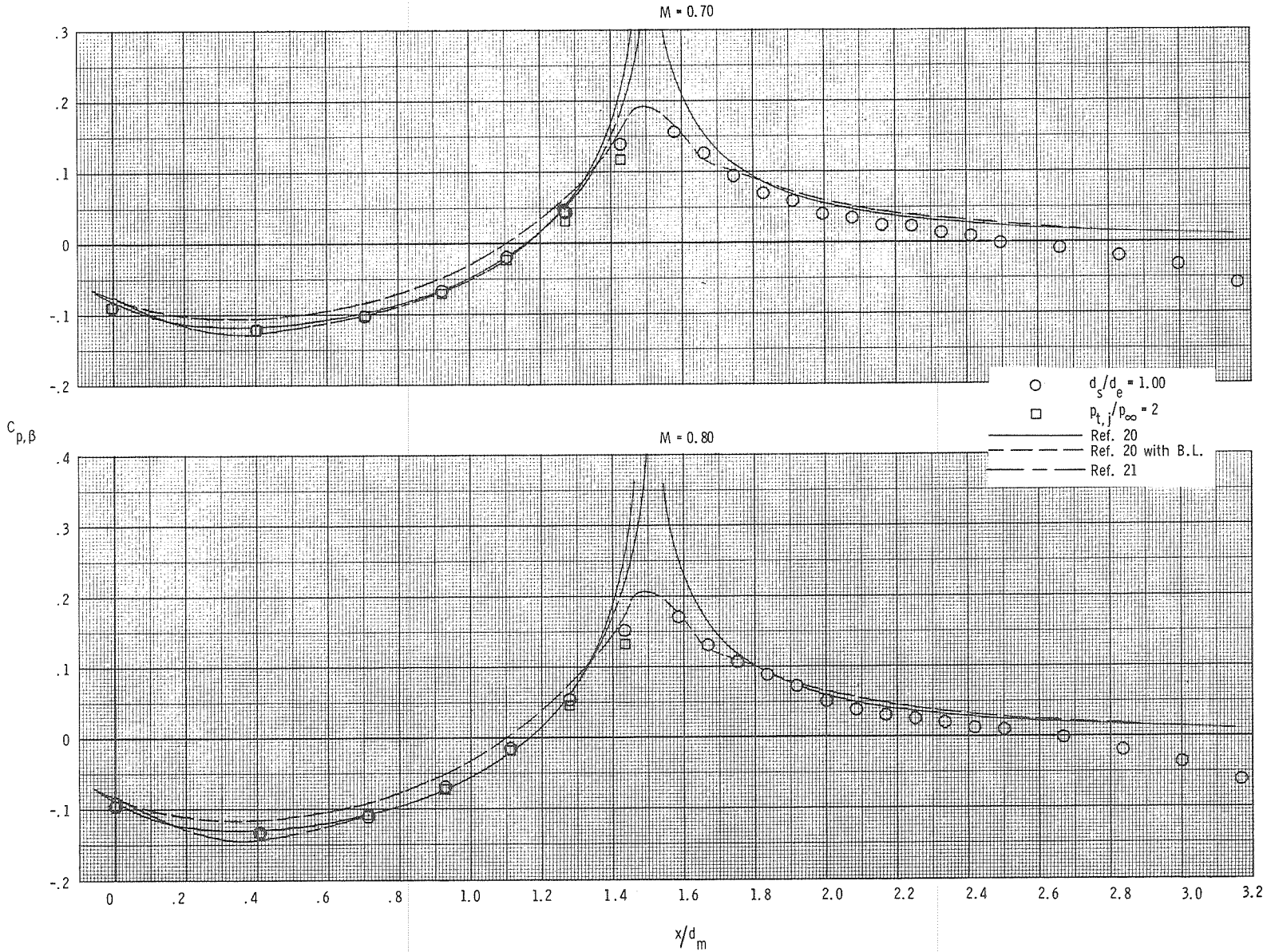

(b) M = 0.70 and 0.80.

Figure 22.- Continued.

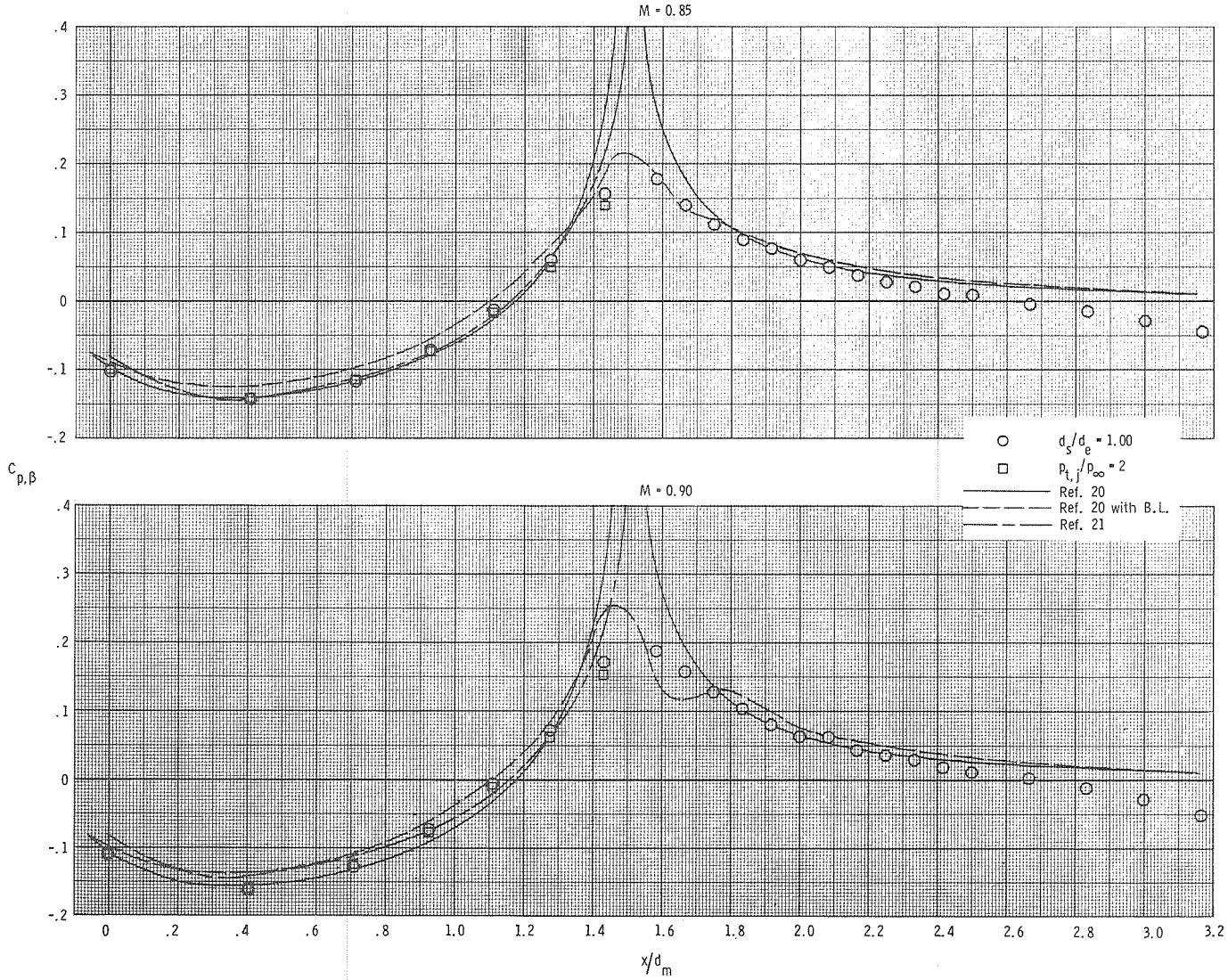

(c) M = 0.85 and 0.90.

Figure 22.- Concluded.

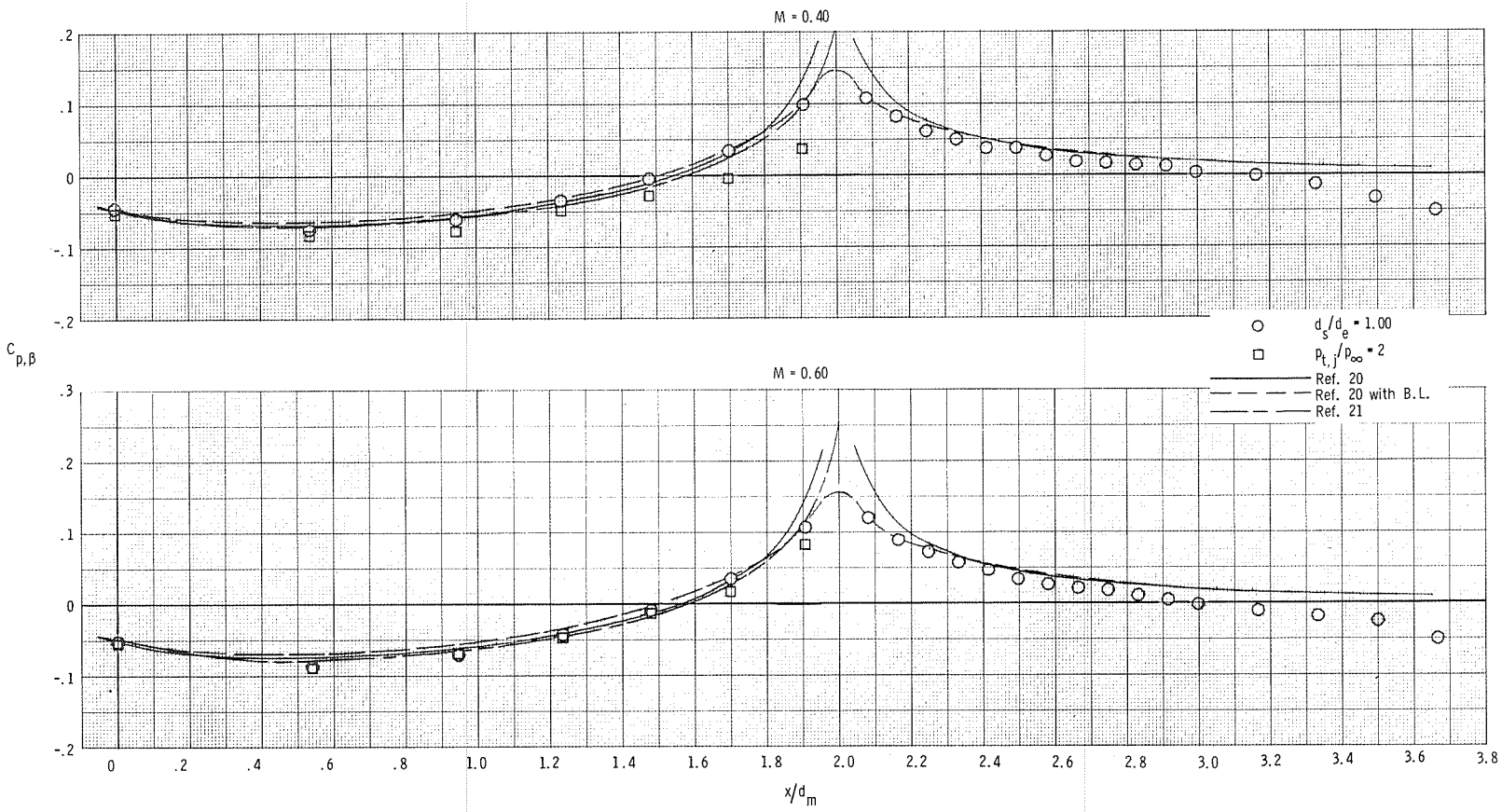

(a) M = 0.40 and 0.60.

Figure 23.- Comparison of pressure-coefficient distributions obtained by use of the theoretical techniques of references 20 and 21 with those obtained from jet operation at $p_{t,j}/p_\infty = 2$ and from use of the $d_s/d_e = 1.00$ simulator for configuration 8 ($l/d_m = 2.00$, $d_e/d_m = 0.70$). (B.L. indicates boundary layer.)

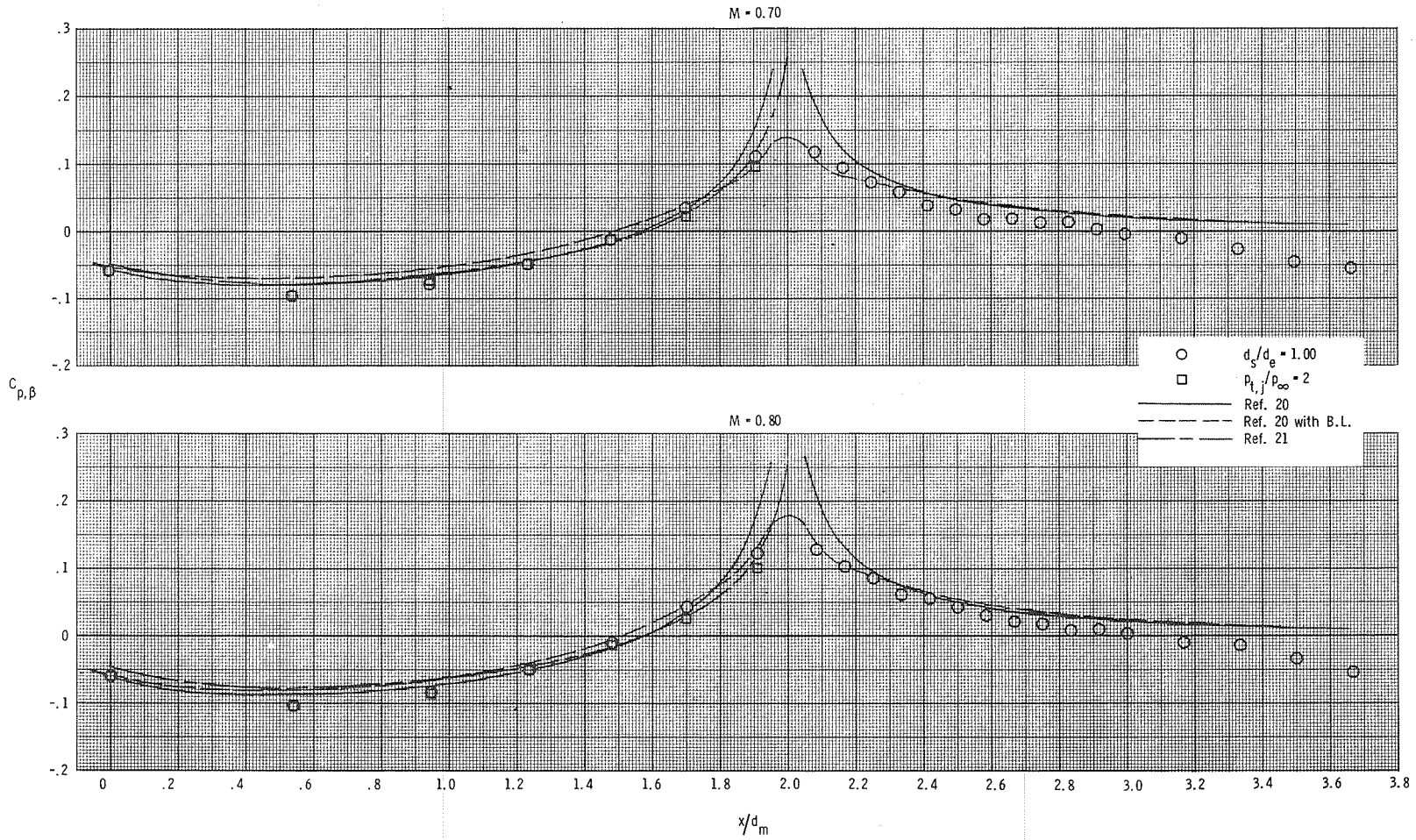

(b) M = 0.70 and 0.80.

Figure 23.- Continued.

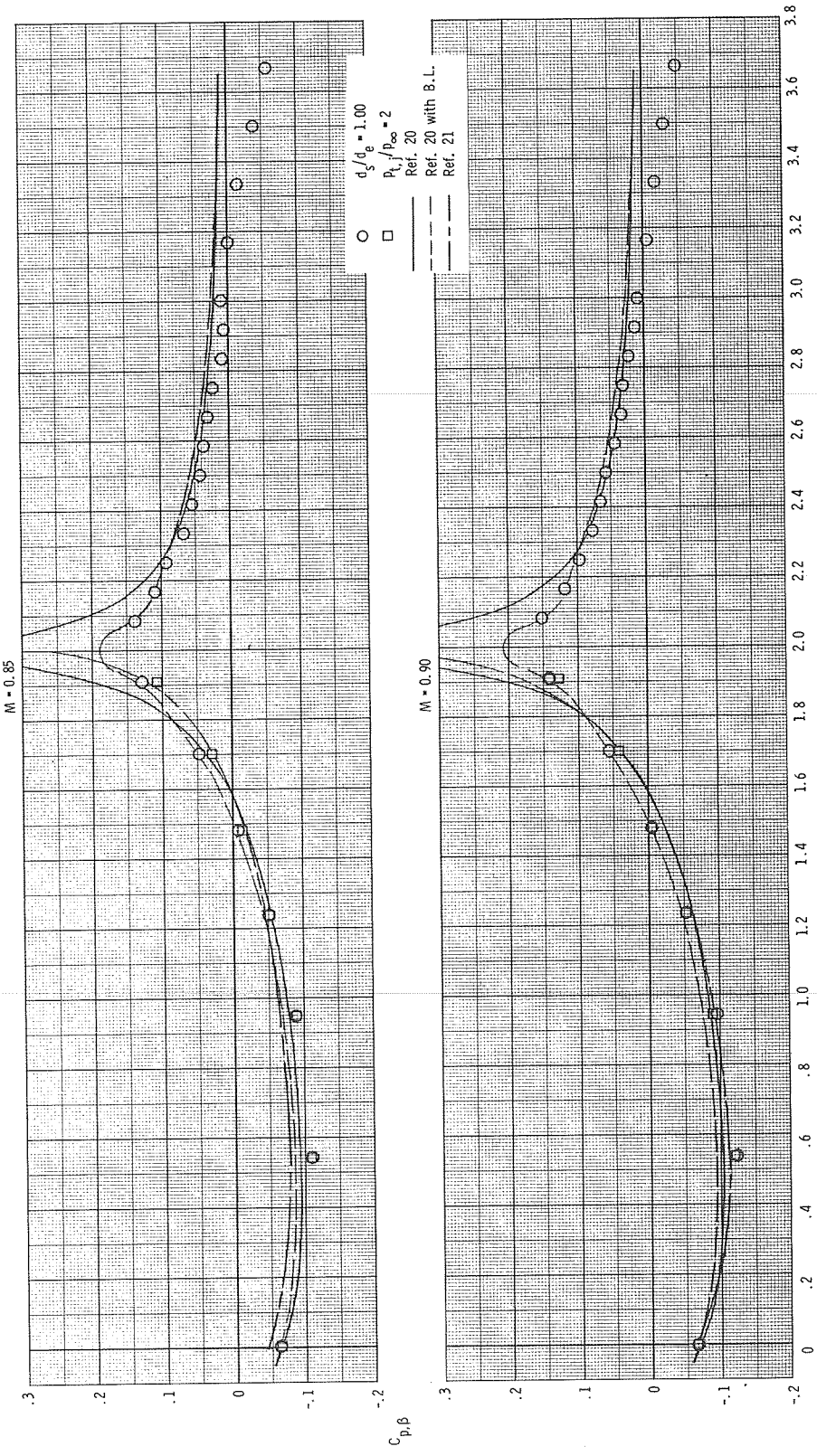

(c) M = 0.85 and 0.90.

Figure 23.- Concluded.

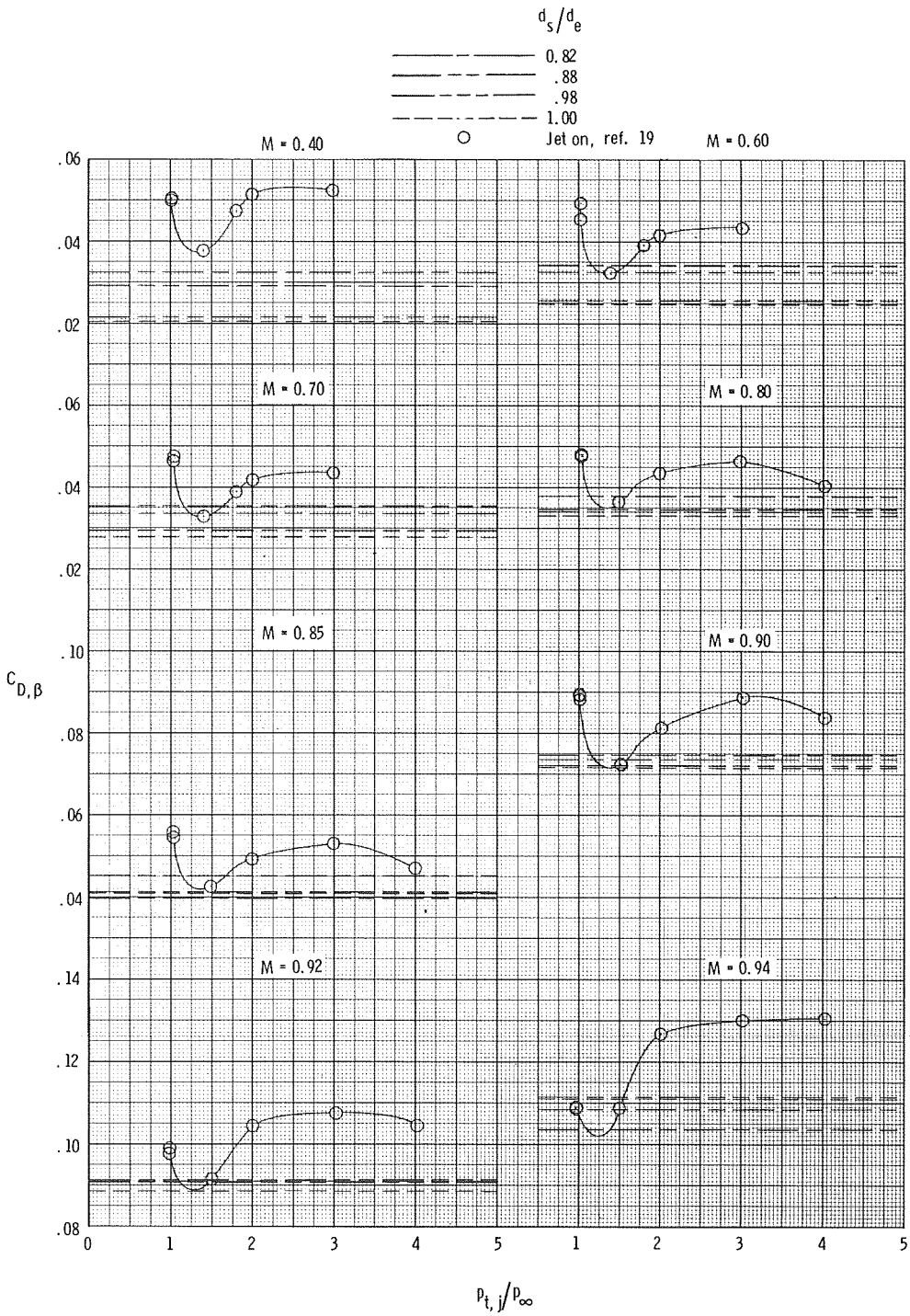

(a) M = 0.40 to 0.94.

Figure 24.- Comparison of integrated boattail pressure-drag coefficients obtained through use of the simulators with jet-on values for configuration 1 (ℓ/d_m = 0.80, d_e/d_m = 0.50).

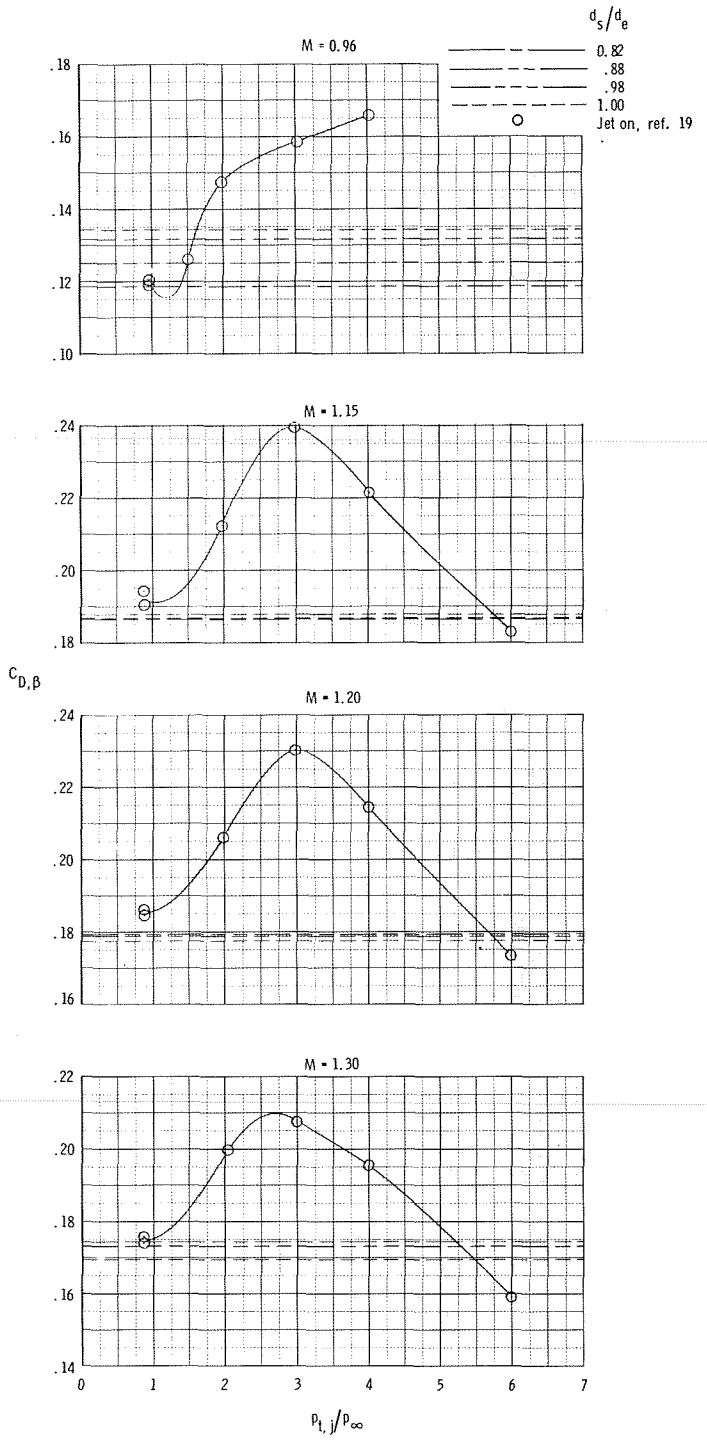

(b) M = 0.96 to 1.30.

Figure 24.- Concluded.

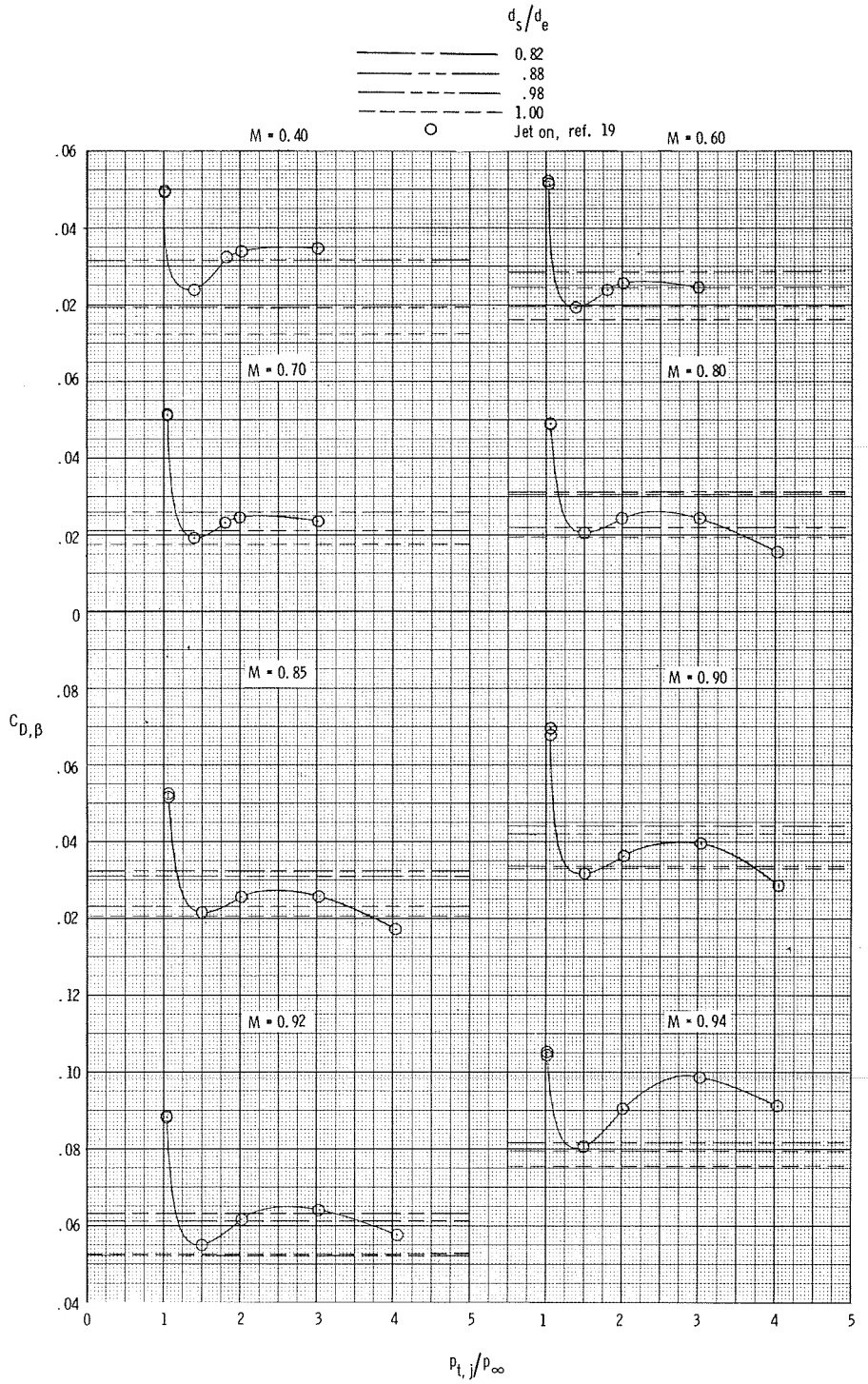

(a) M = 0.40 to 0.94.

Figure 25.- Comparison of integrated boattail pressure-drag coefficients obtained through use of the simulators with jet-on values for configuration 2 (ℓ/d_m = 1.00, d_e/d_m = 0.50).

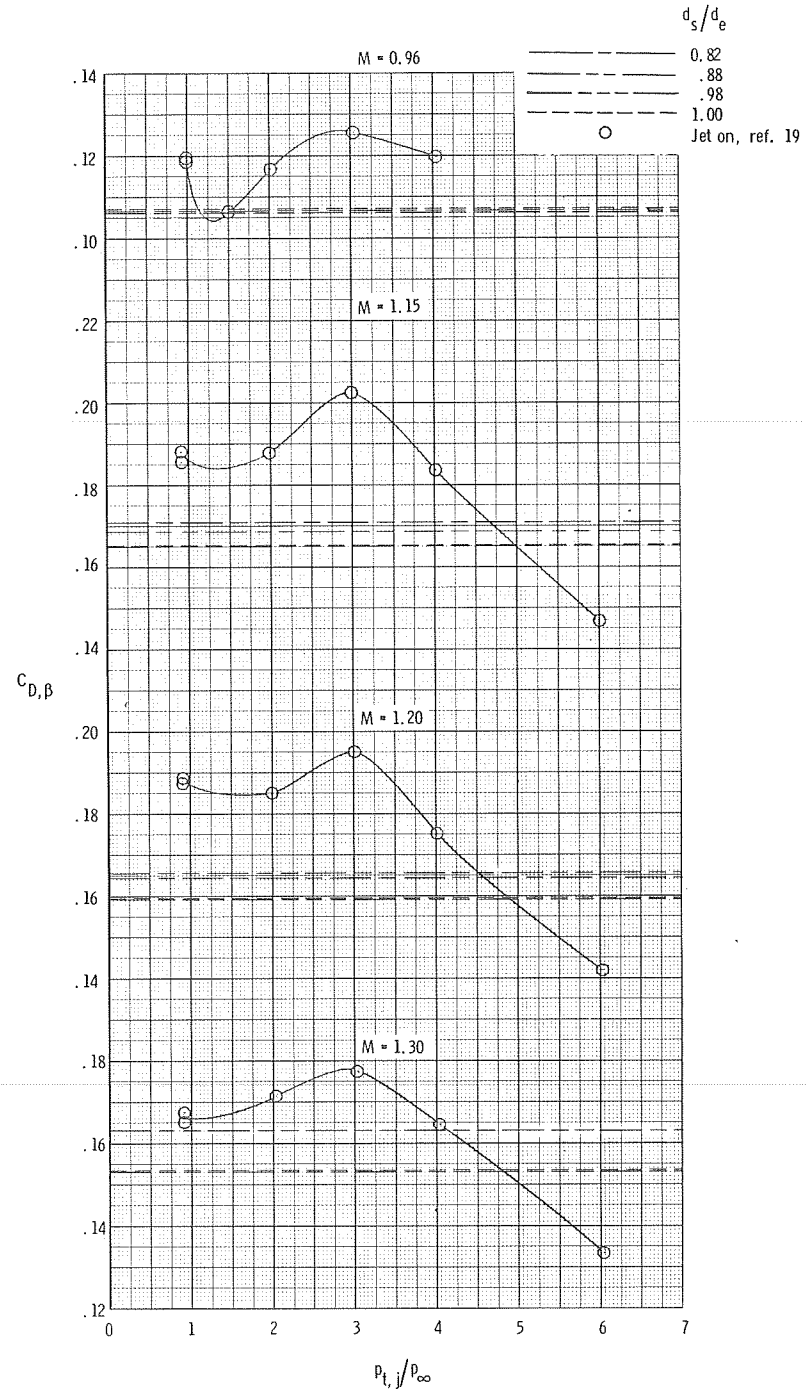

(b) M = 0.96 to 1.30.

Figure 25.- Concluded.

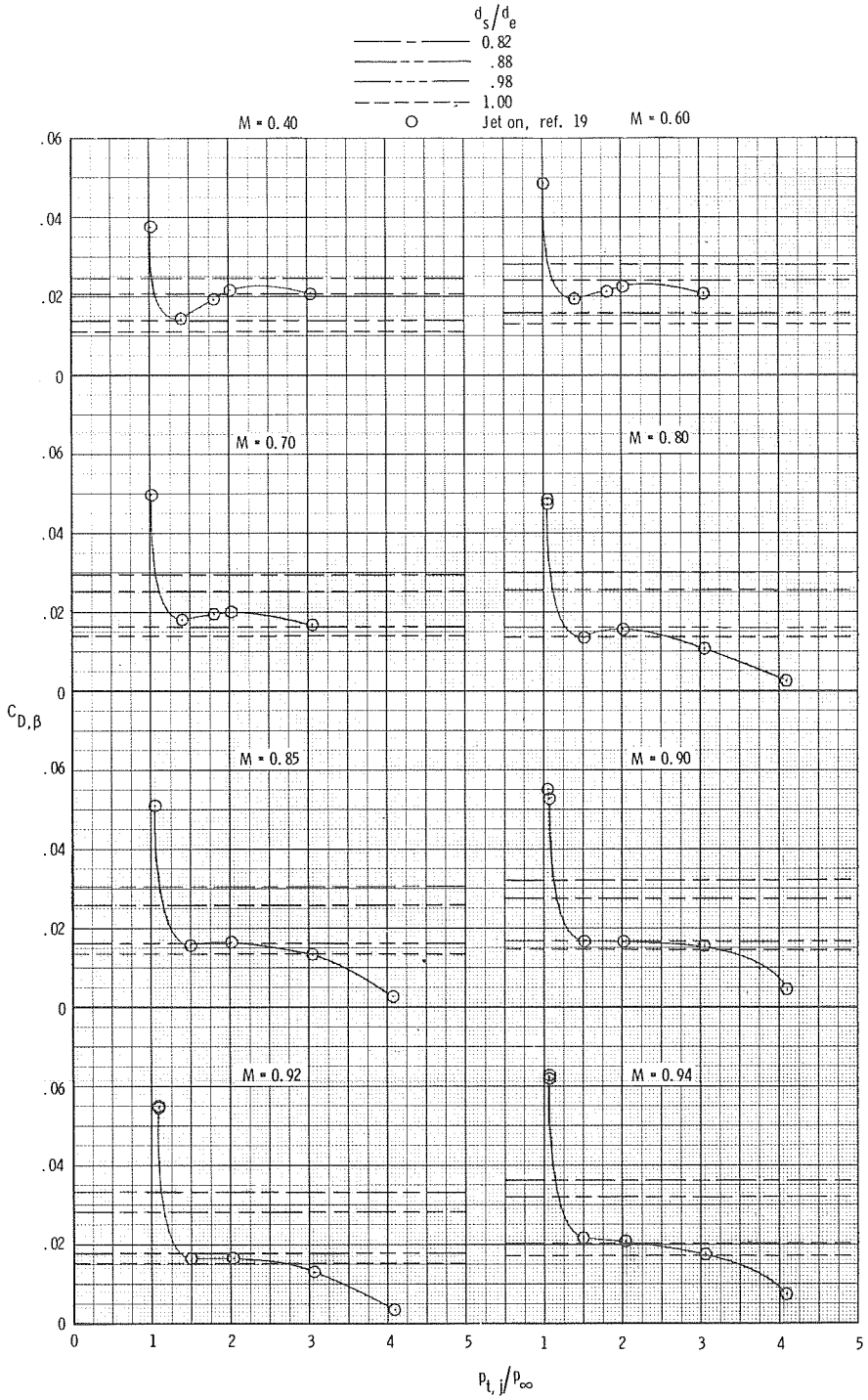

(a) M = 0.40 to 0.94.

Figure 26.- Comparison of integrated boattail pressure drag-coefficients obtained through use of the simulators with jet-on values for configuration 3 (ℓ/d_m = 1.77, d_e/d_m = 0.50).

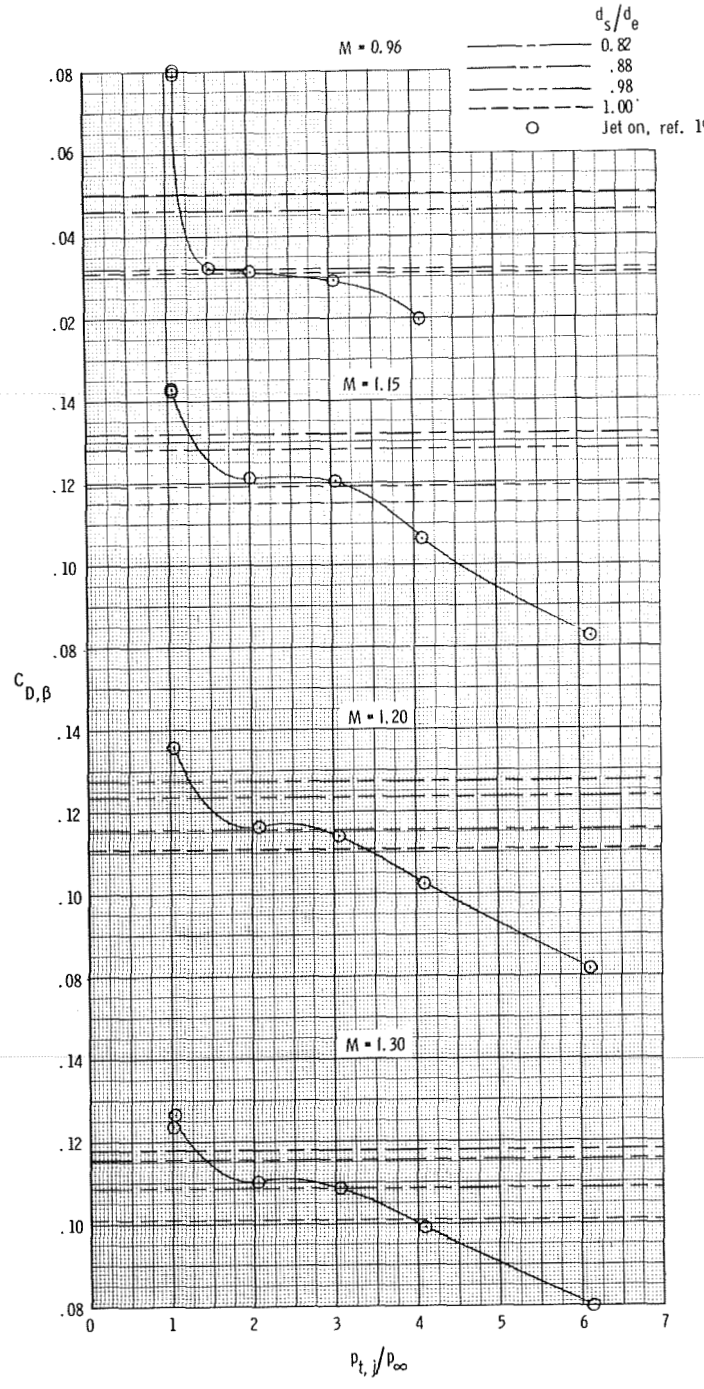

(b) M = 0.96 to 1.30.

Figure 26.- Concluded.

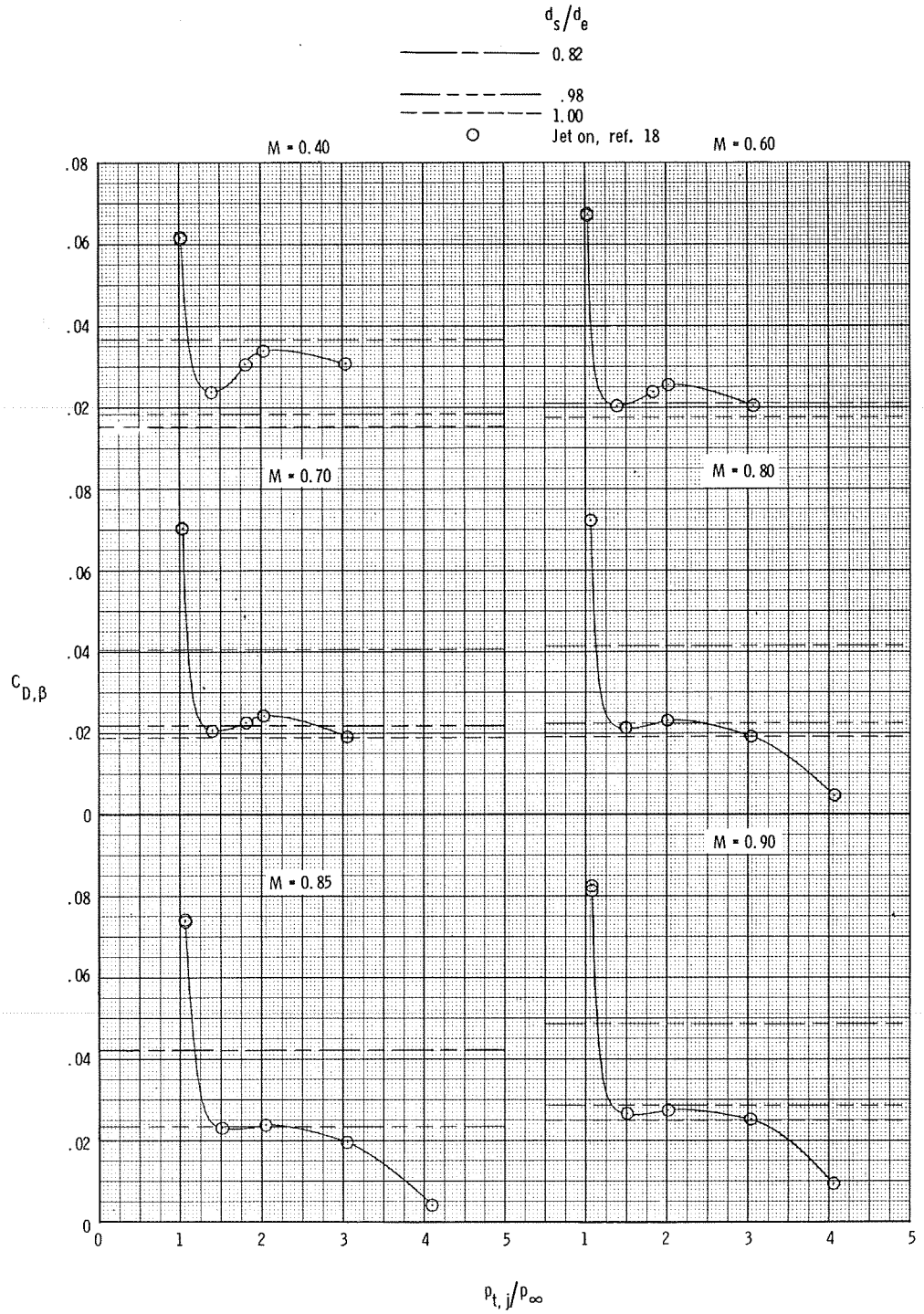

(a) M = 0.40 to 0.90.

Figure 27.- Comparison of integrated boattail pressure-drag coefficients obtained through use of the simulators with jet-on values for configuration 4 (l/d_m = 1.00, d_e/d_m = 0.60).

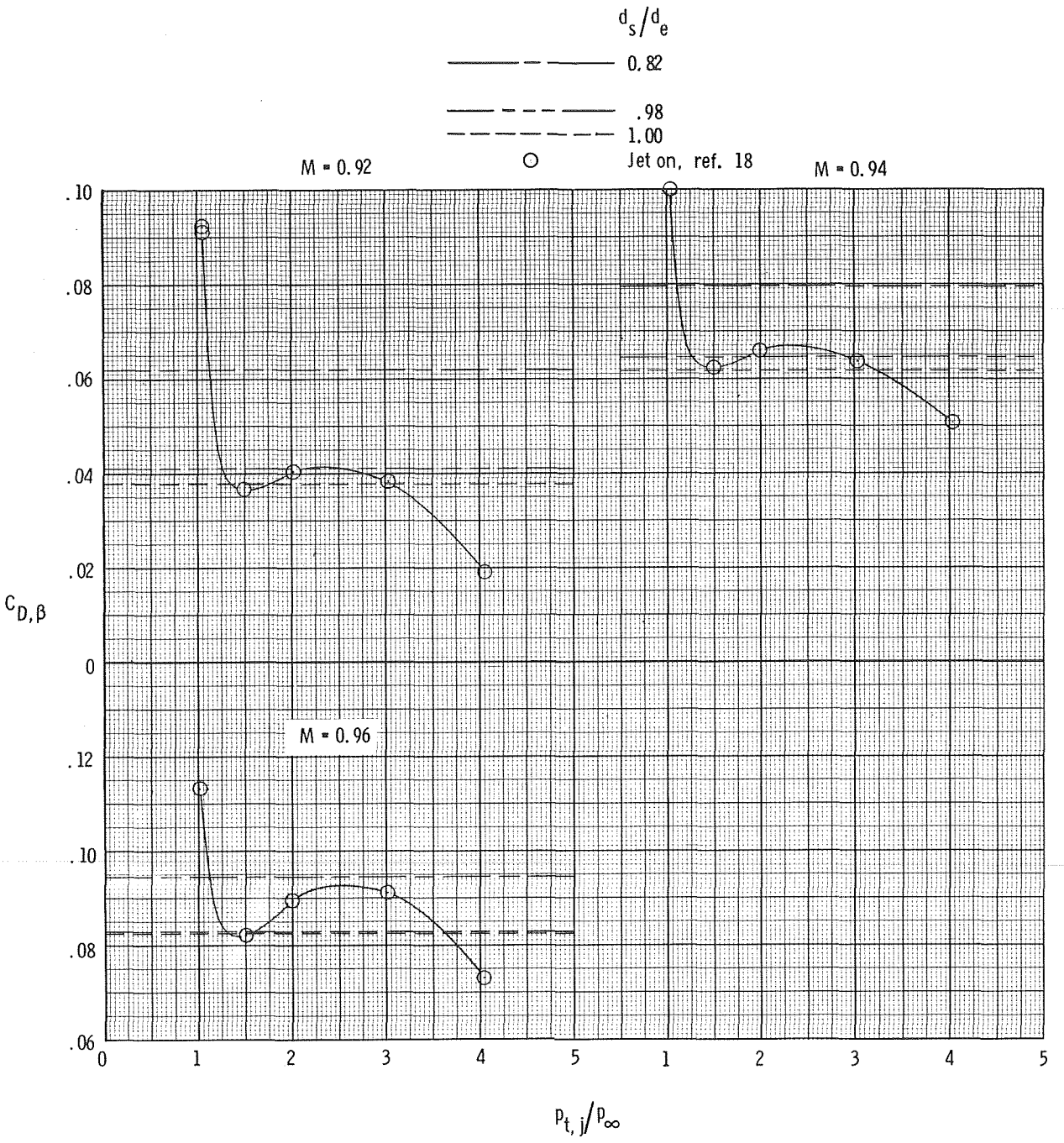

(b) M = 0.92 to 0.96.

Figure 27.- Continued.

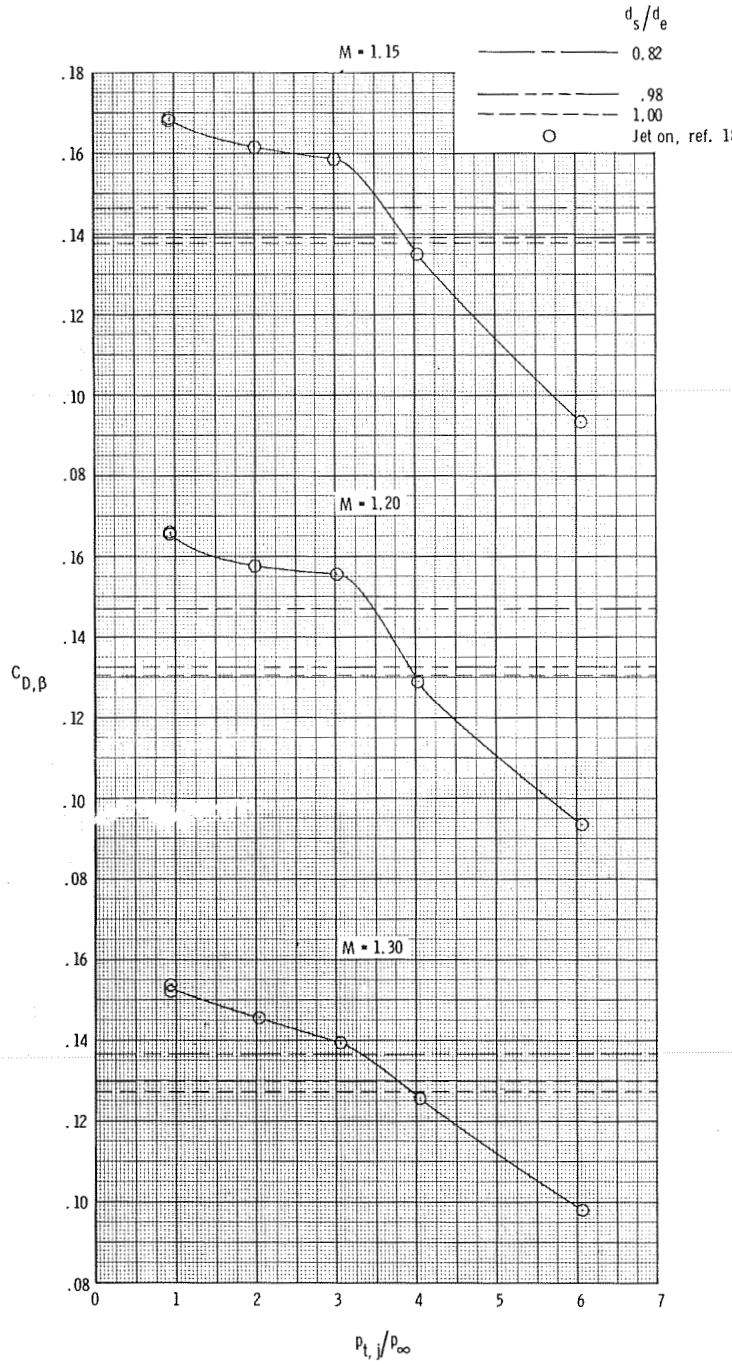

(c) M = 1.15 to 1.30.

Figure 27.- Concluded.

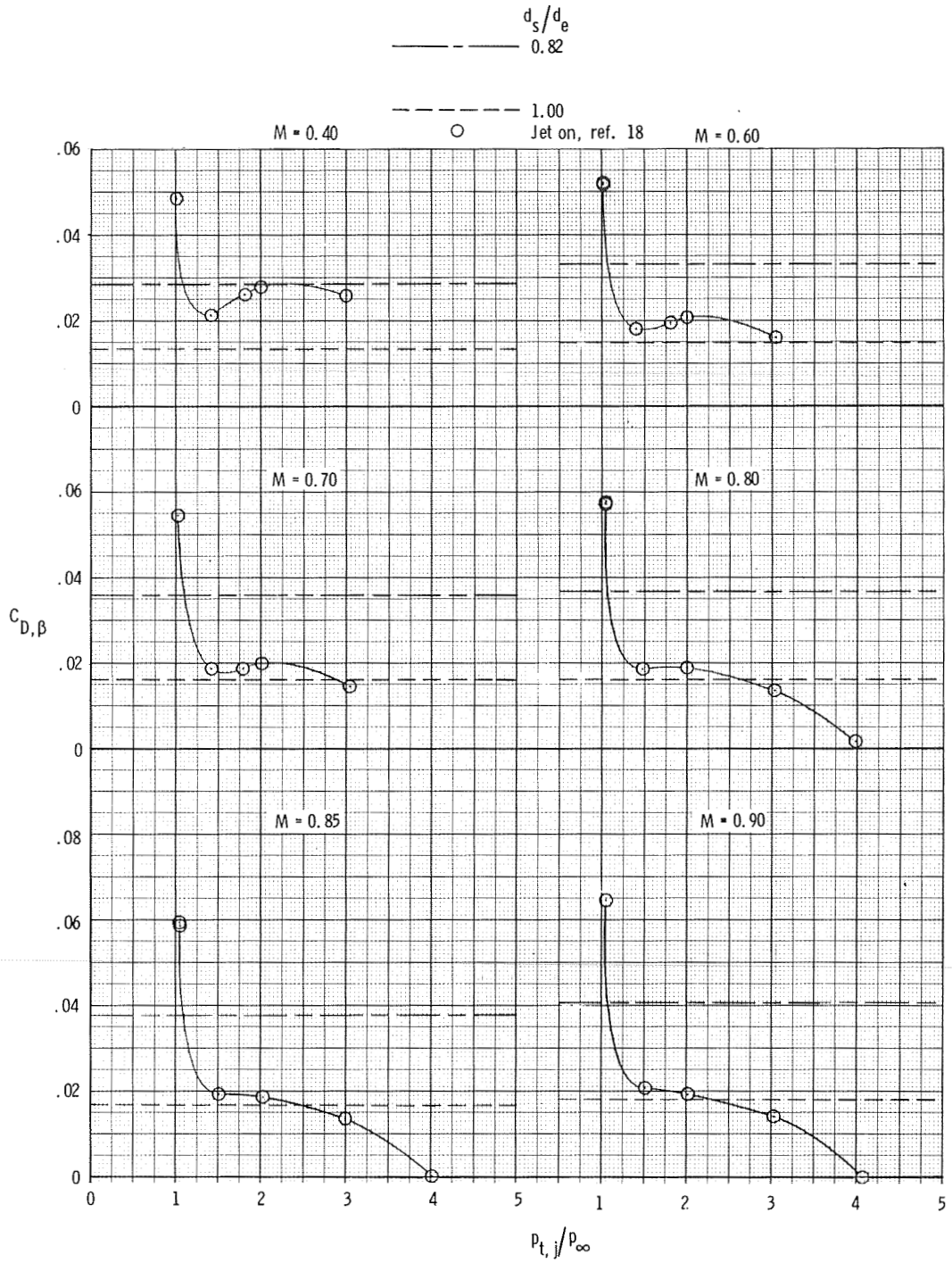

(a) M = 0.40 to 0.90.

Figure 28.- Comparison of integrated boattail pressure-drag coefficients obtained through use of the simulators with jet-on values for configuration 5 (ℓ/d_m = 1.50, d_e/d_m = 0.60).

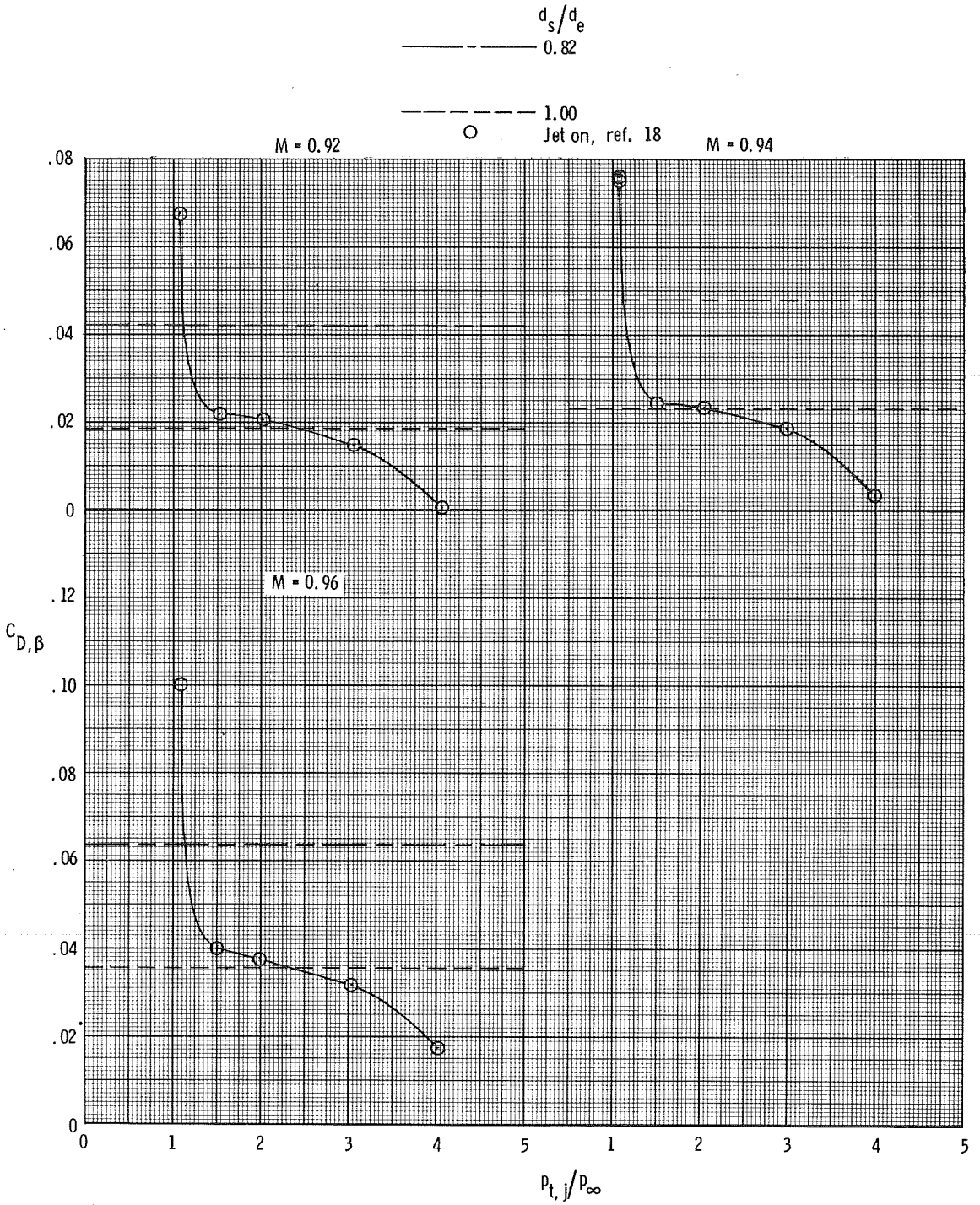

(b) M = 0.92 to 0.96.

Figure 28.- Continued.

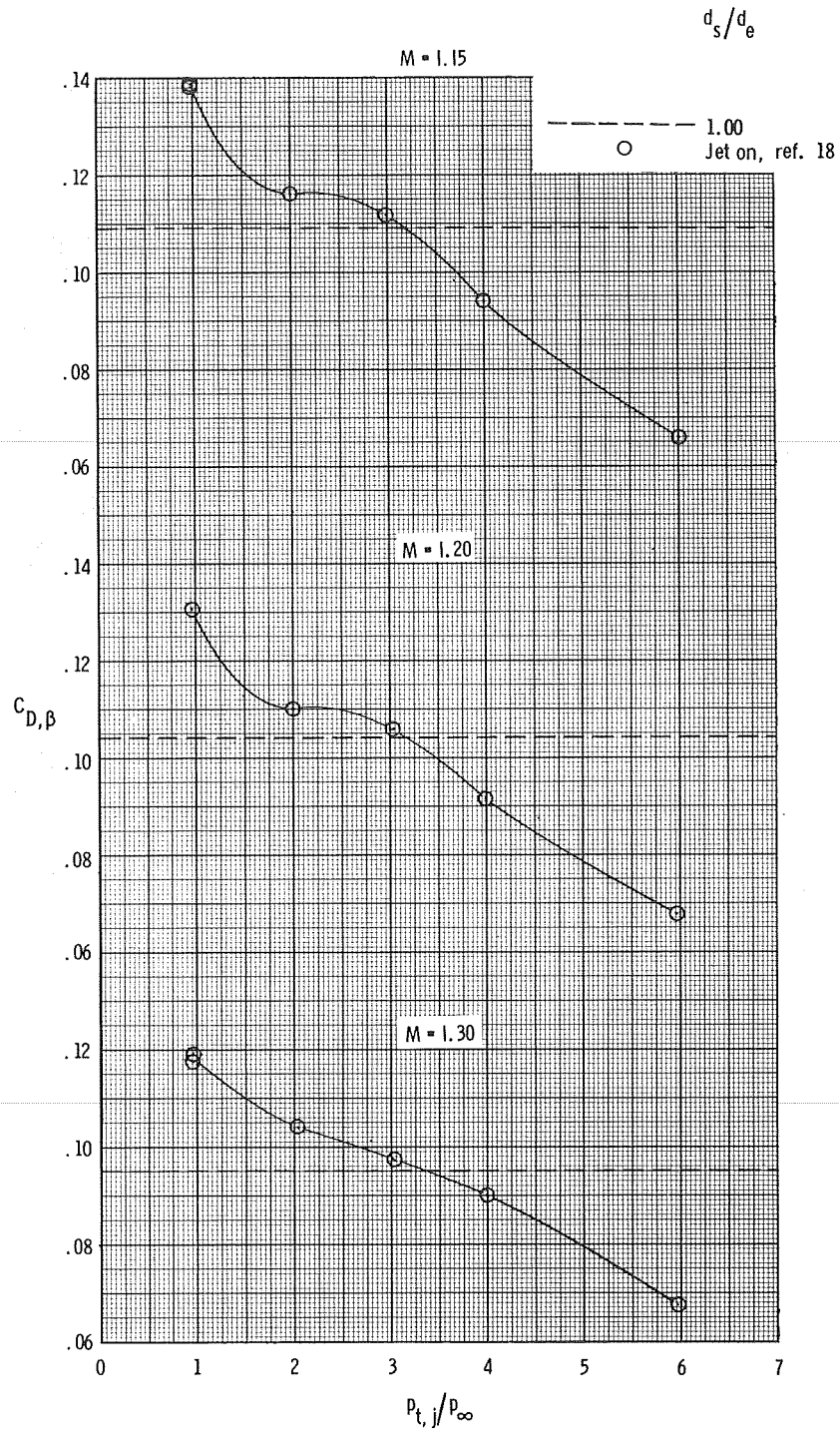

(c) M = 1.15 to 1.30.

Figure 28.- Concluded.

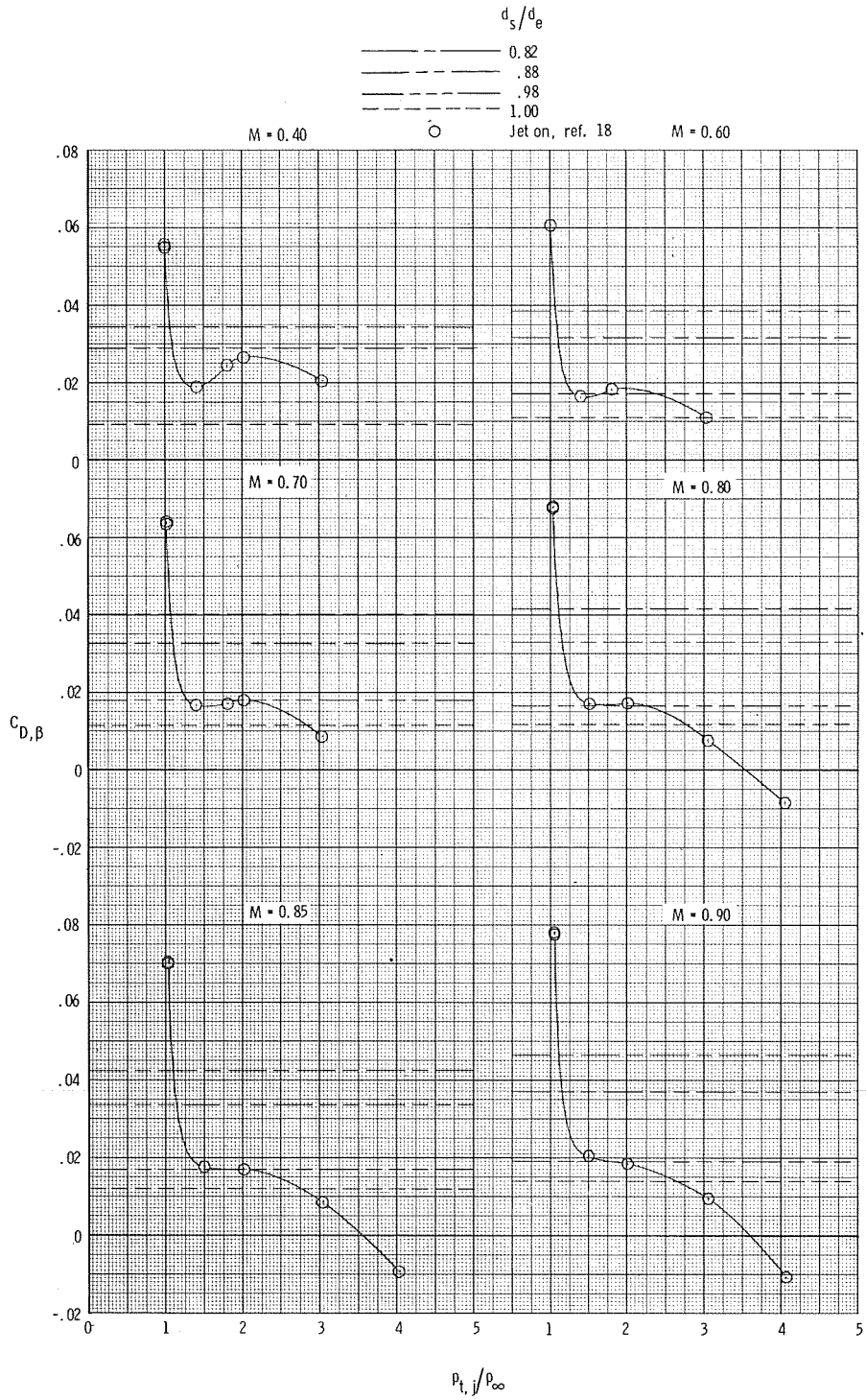

(a) M = 0.40 to 0.90.

Figure 29.- Comparison of integrated boattail pressure-drag coefficients obtained through use of the simulators with jet-on values for configuration 6 (ℓ/d_m = 1.00, d_e/d_m = 0.70).

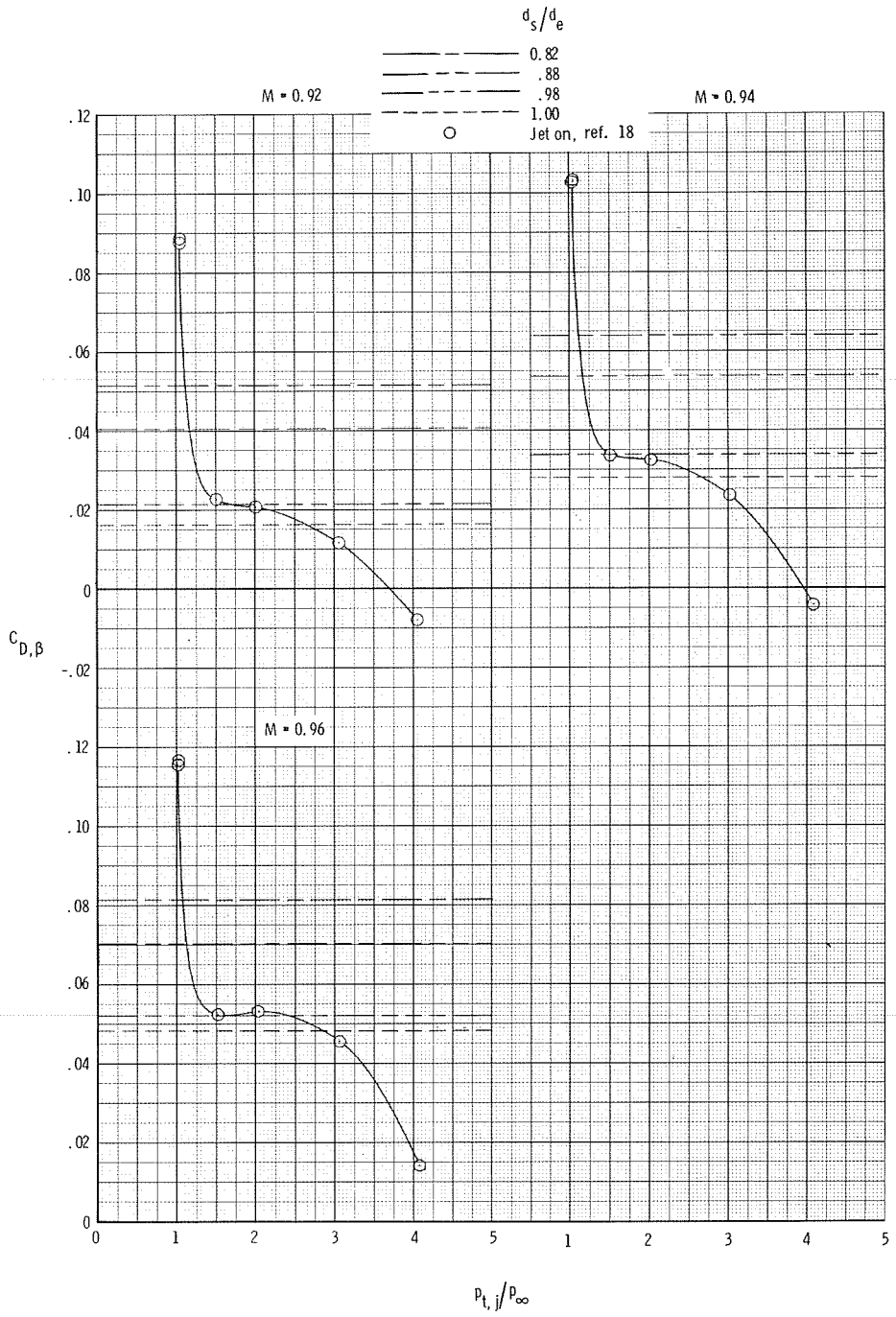

(b) M = 0.92 to 0.96.

Figure 29.- Continued.

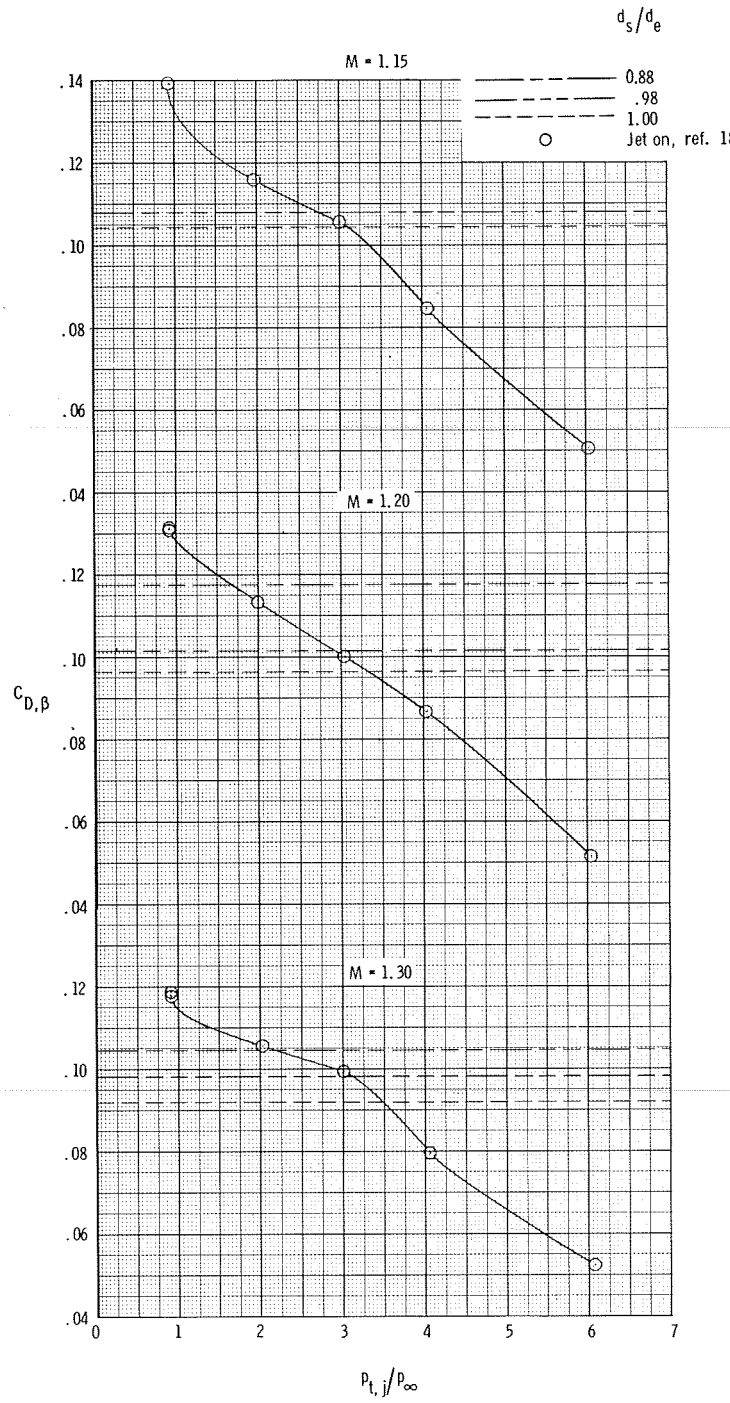

(c) M = 1.15 to 1.30.

Figure 29.- Concluded.

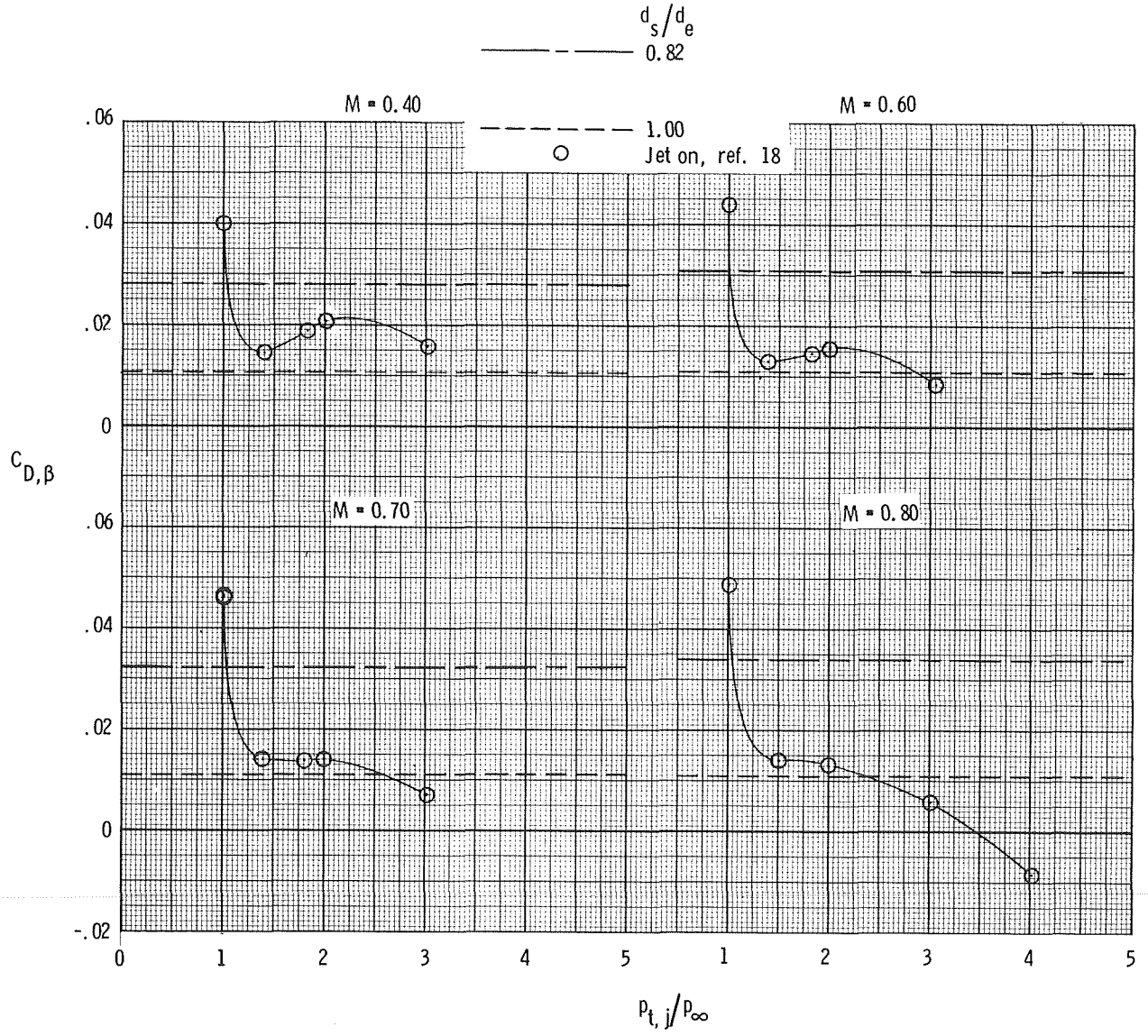

(a) M = 0.40 to 0.80.

Figure 30.- Comparison of integrated boattail pressure-drag coefficients obtained through use of the simulators with jet-on values for configuration 7 (l/d_m = 1.50, d_e/d_m = 0.70).

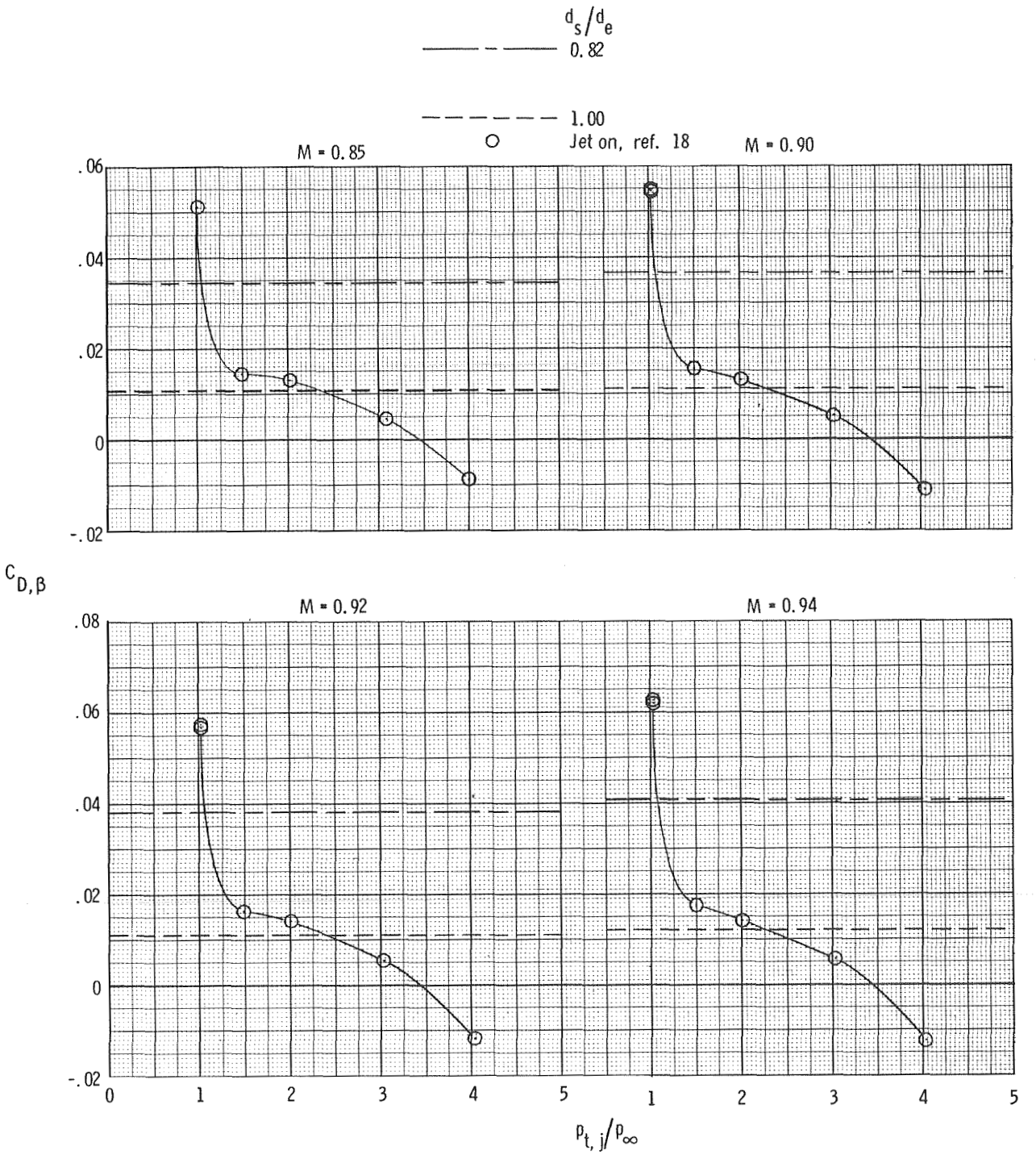

(b) M = 0.85 to 0.94.

Figure 30.- Continued.

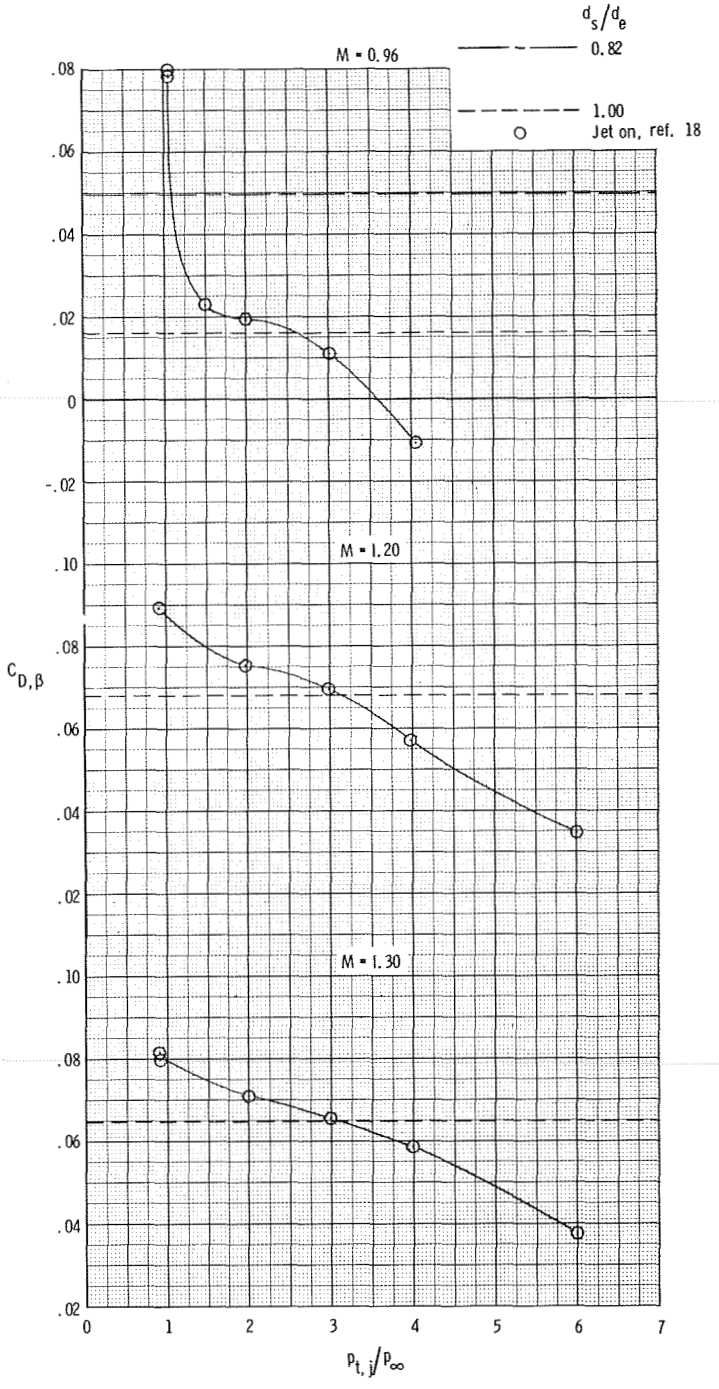

(c) M = 0.96 to 1.30.

Figure 30.- Concluded.

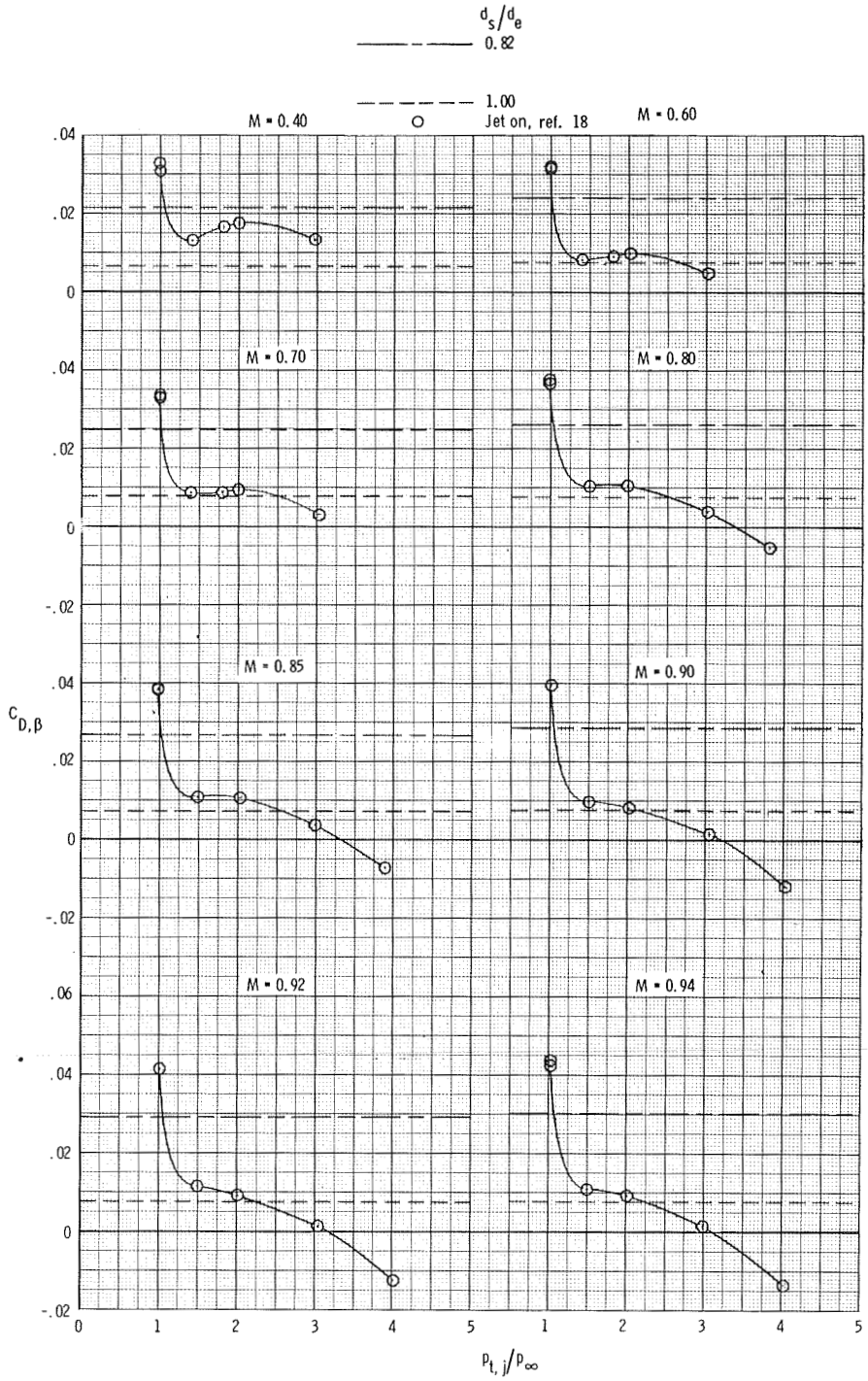

(a) M = 0.40 to 0.94.

Figure 31.- Comparison of integrated boattail pressure-drag coefficients obtained through use of the simulators with jet-on values for configuration 8 (l/d_m = 2.00, d_e/d_m = 0.70).

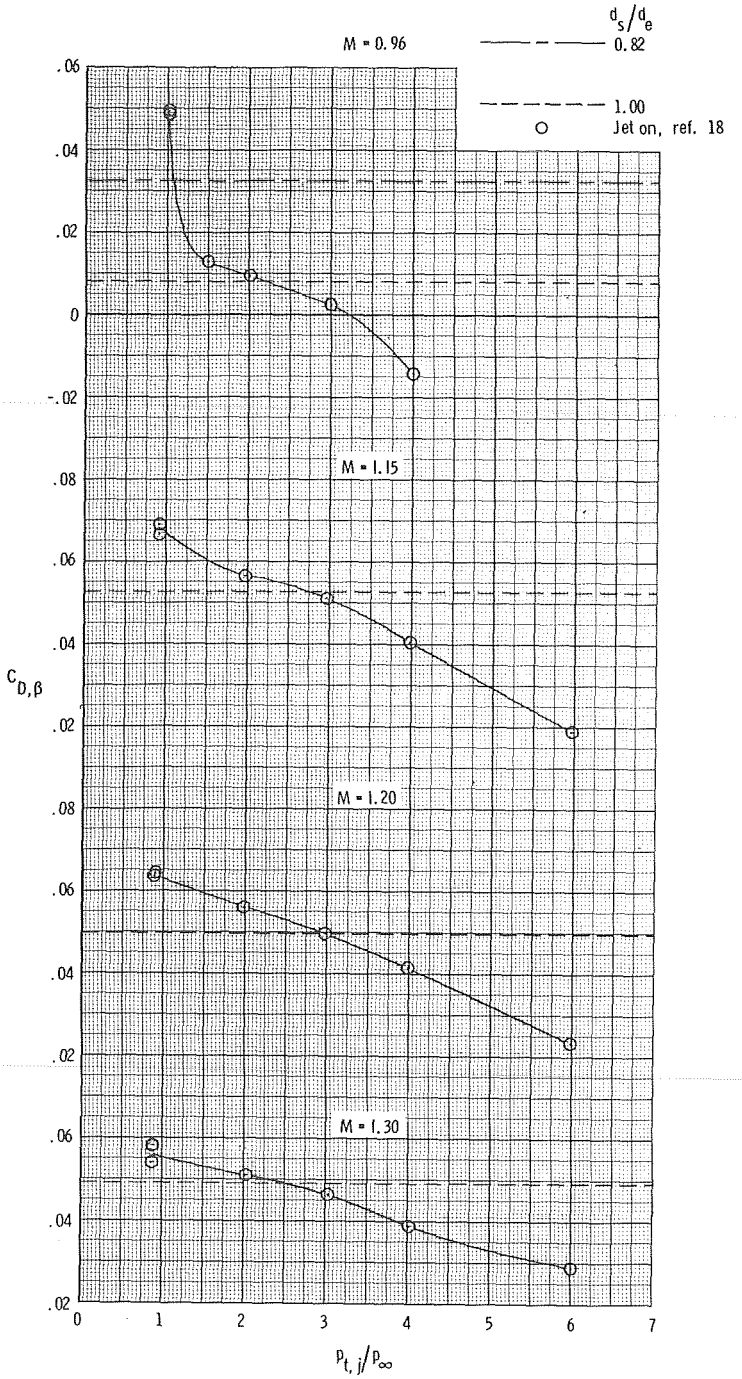

(b) M = 0.96 to 1.30.

Figure 31.- Concluded.

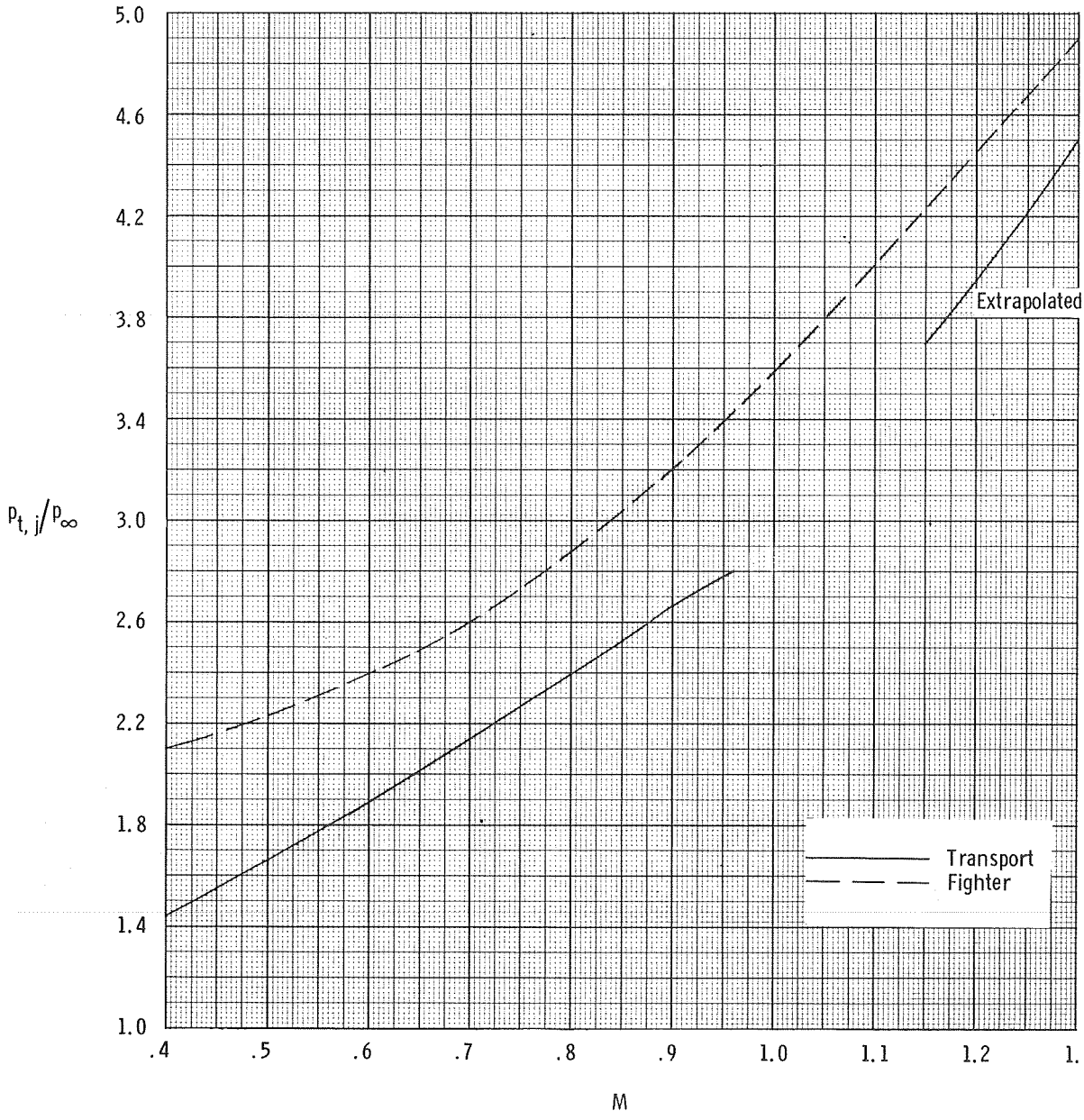

Figure 32.- Jet total-pressure ratio variation with Mach number for typical transport and fighter turbofan engines.

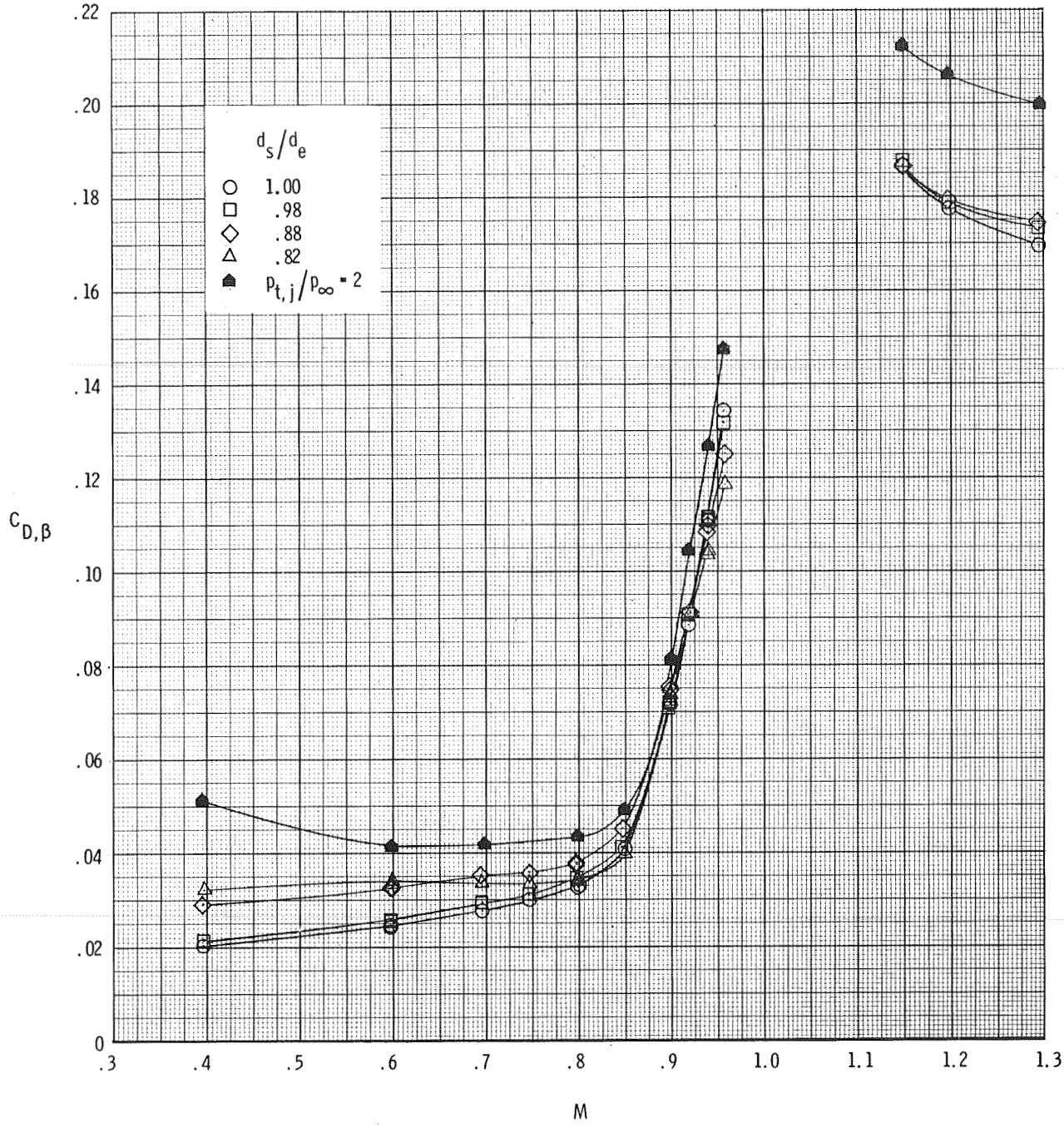

(a) Configuration 1.

Figure 33.- Comparison of integrated boattail pressure-drag coefficients obtained through use of the simulators with jet-on, $p_{t,j}/p_\infty = 2$ values as a function of Mach number.

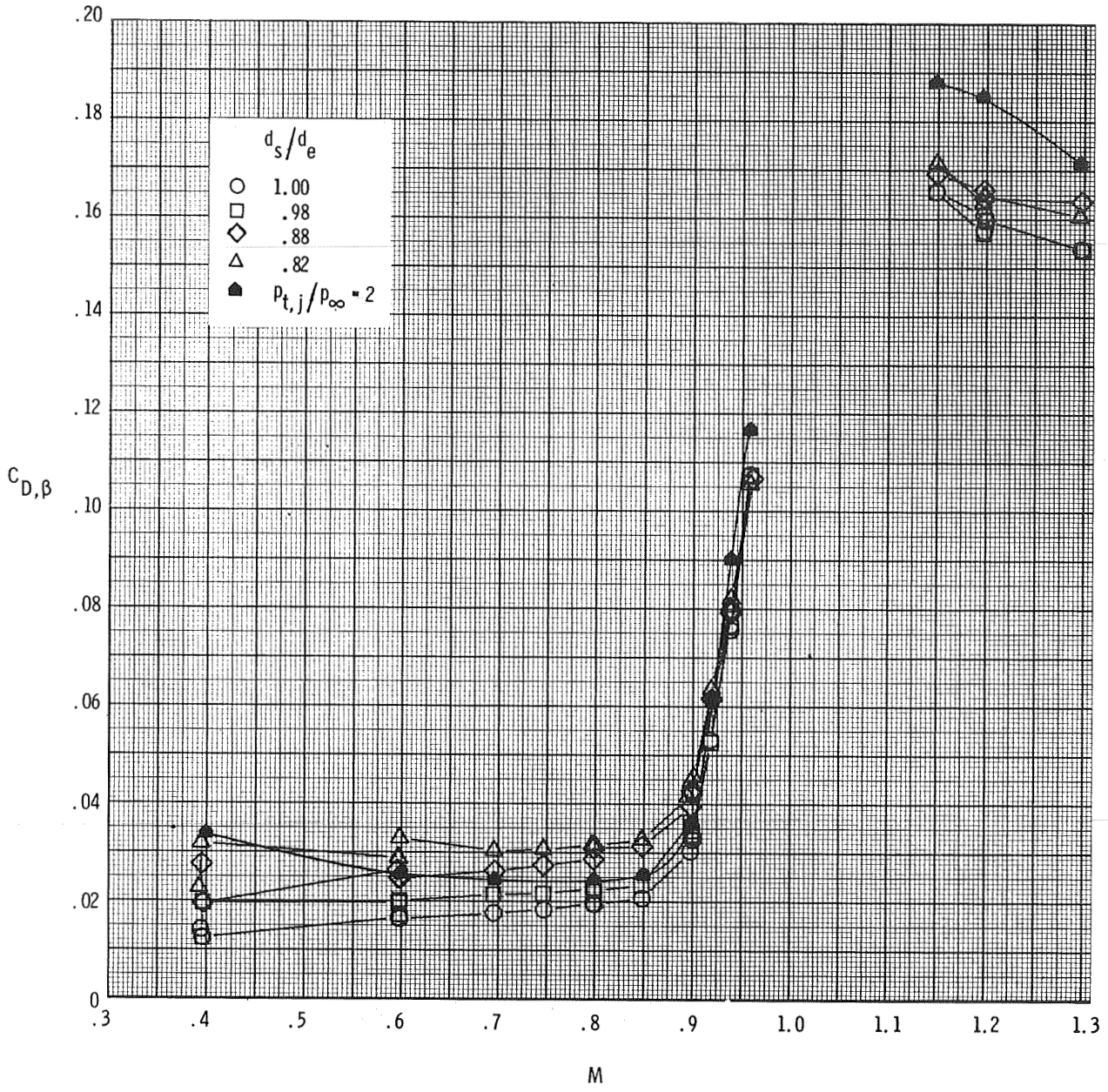

(b) Configuration 2.

Figure 33.- Continued.

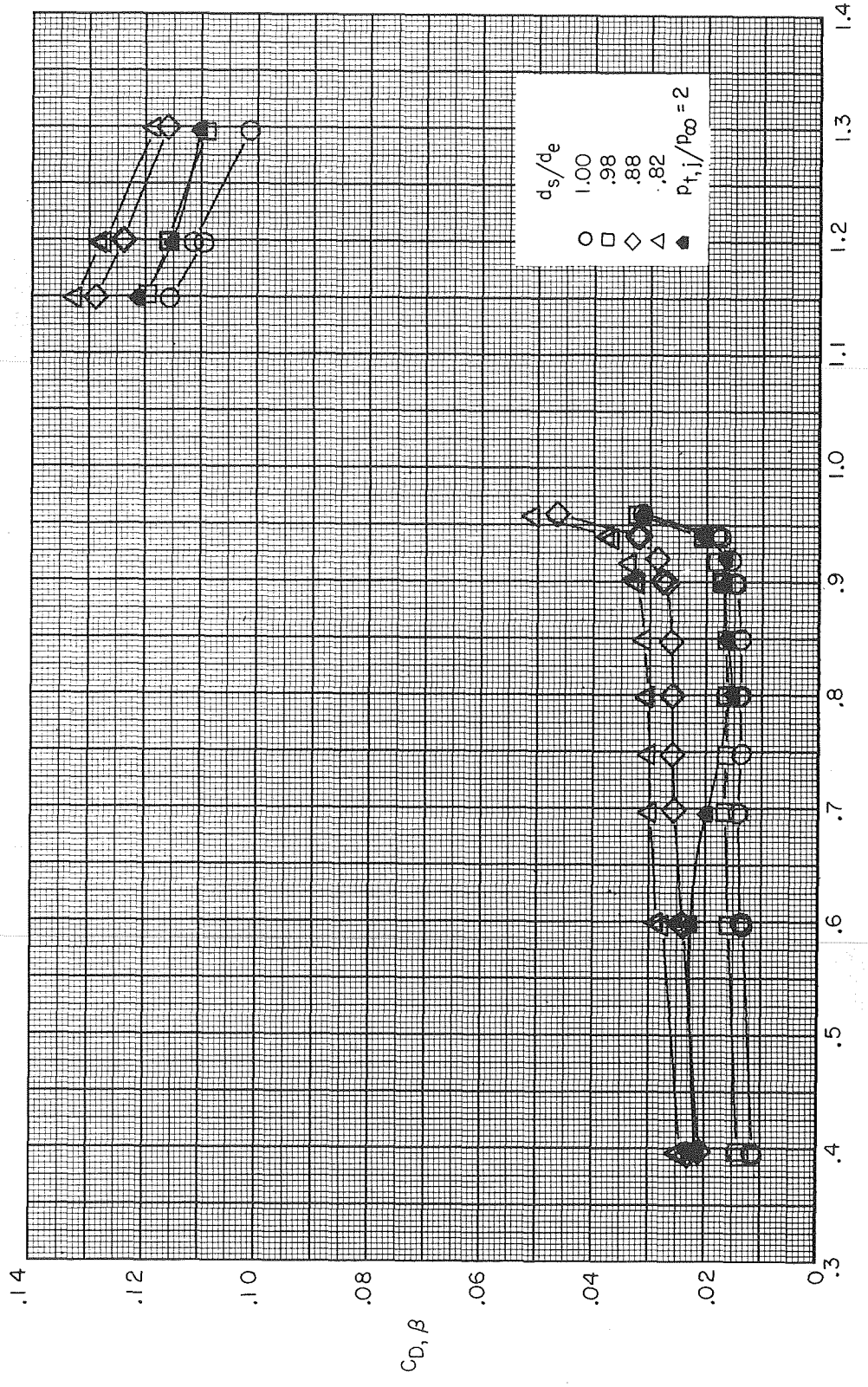

(c) Configuration 3.

Figure 33.- Continued.

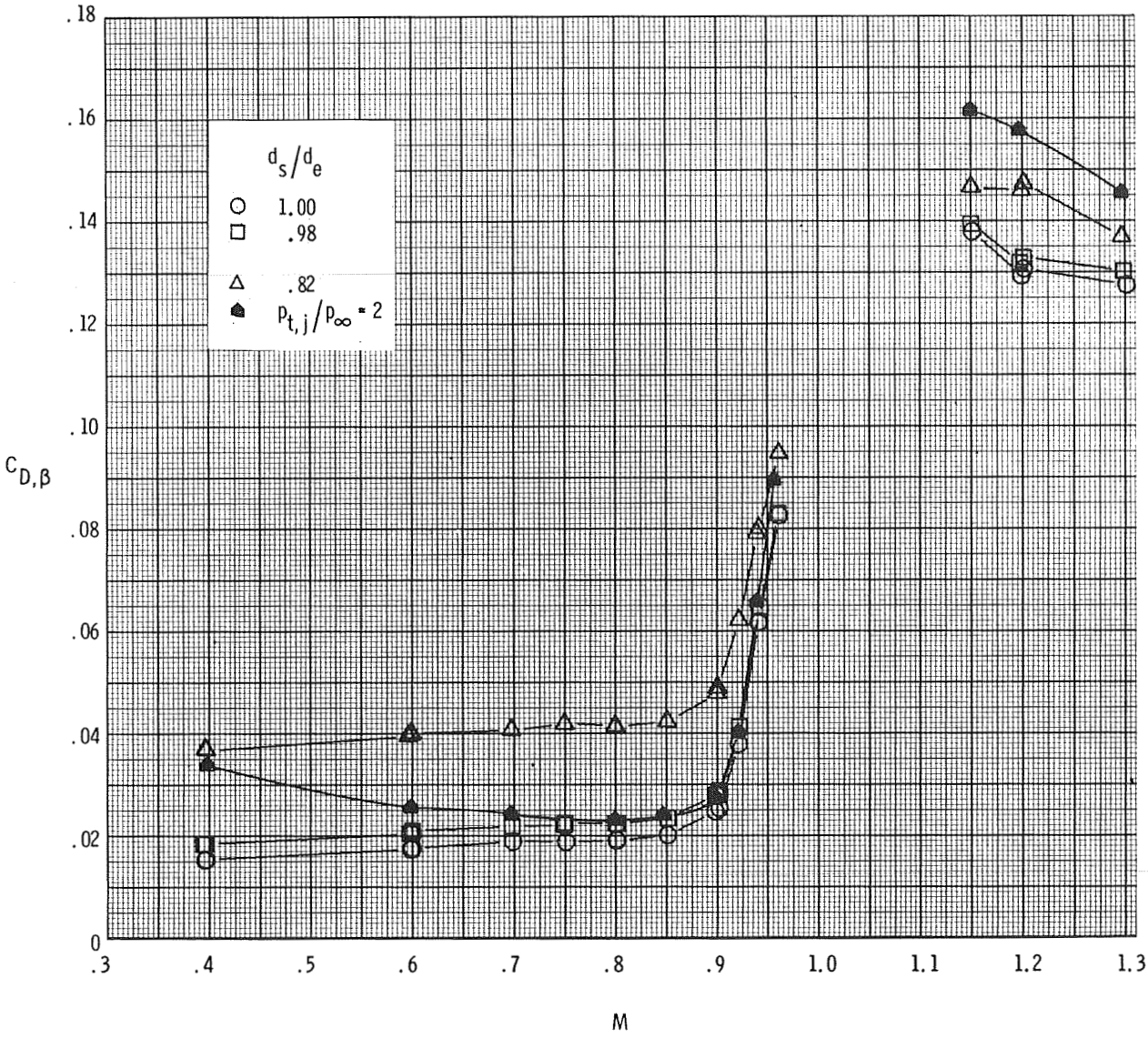

(d) Configuration 4.

Figure 33.- Continued.

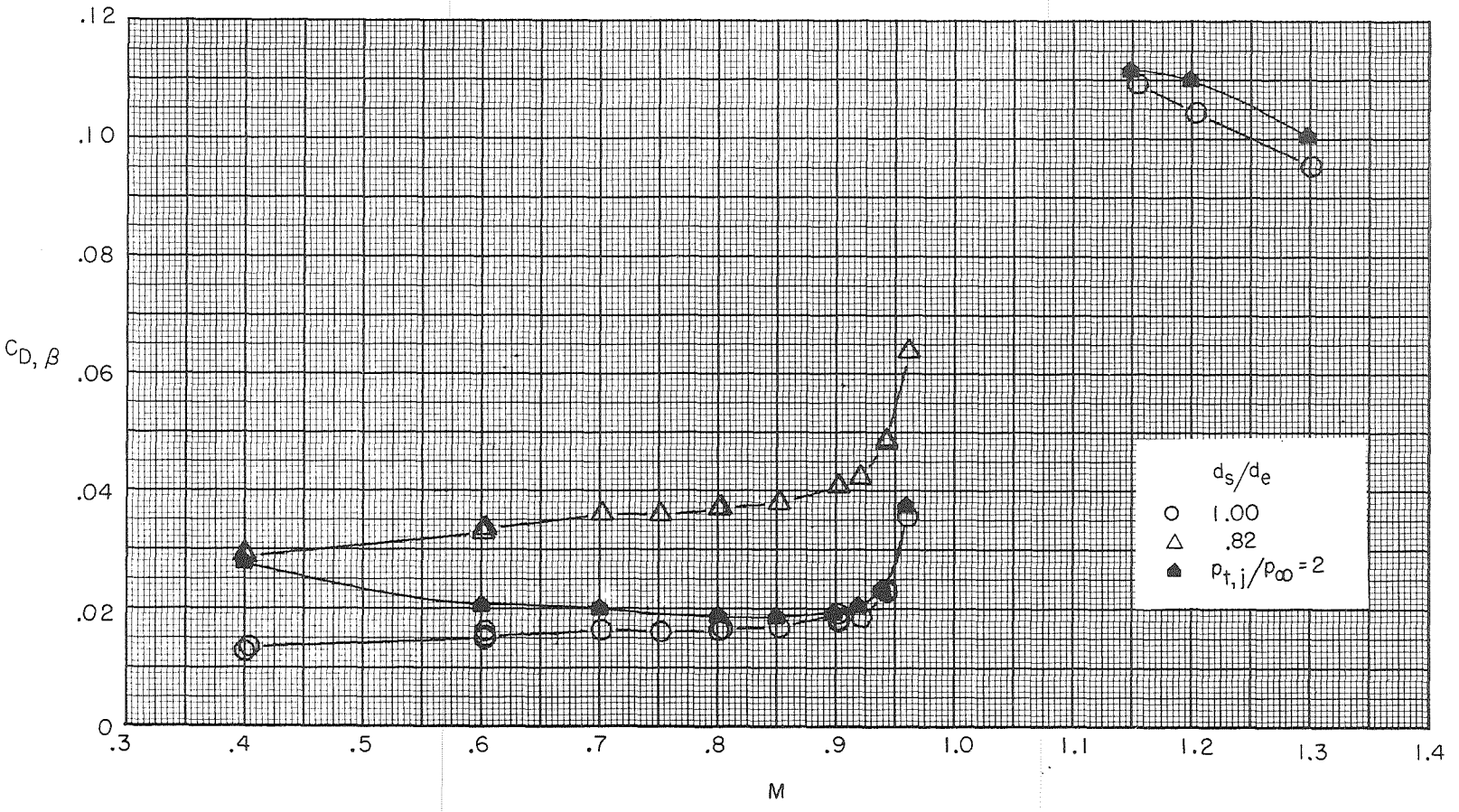

(e) Configuration 5.

Figure 33.- Continued.

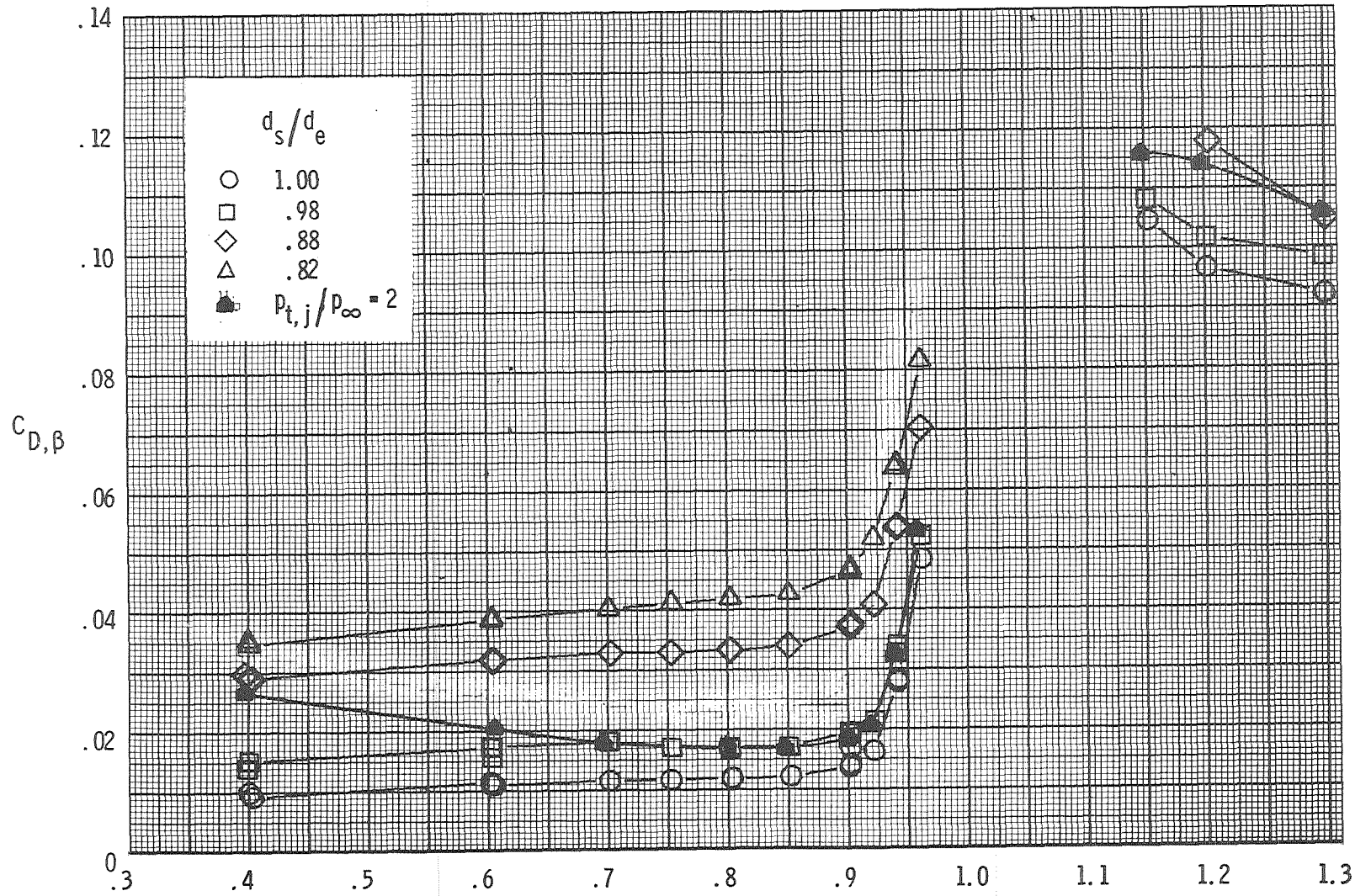

(f) Configuration 6.

Figure 33.- Continued.

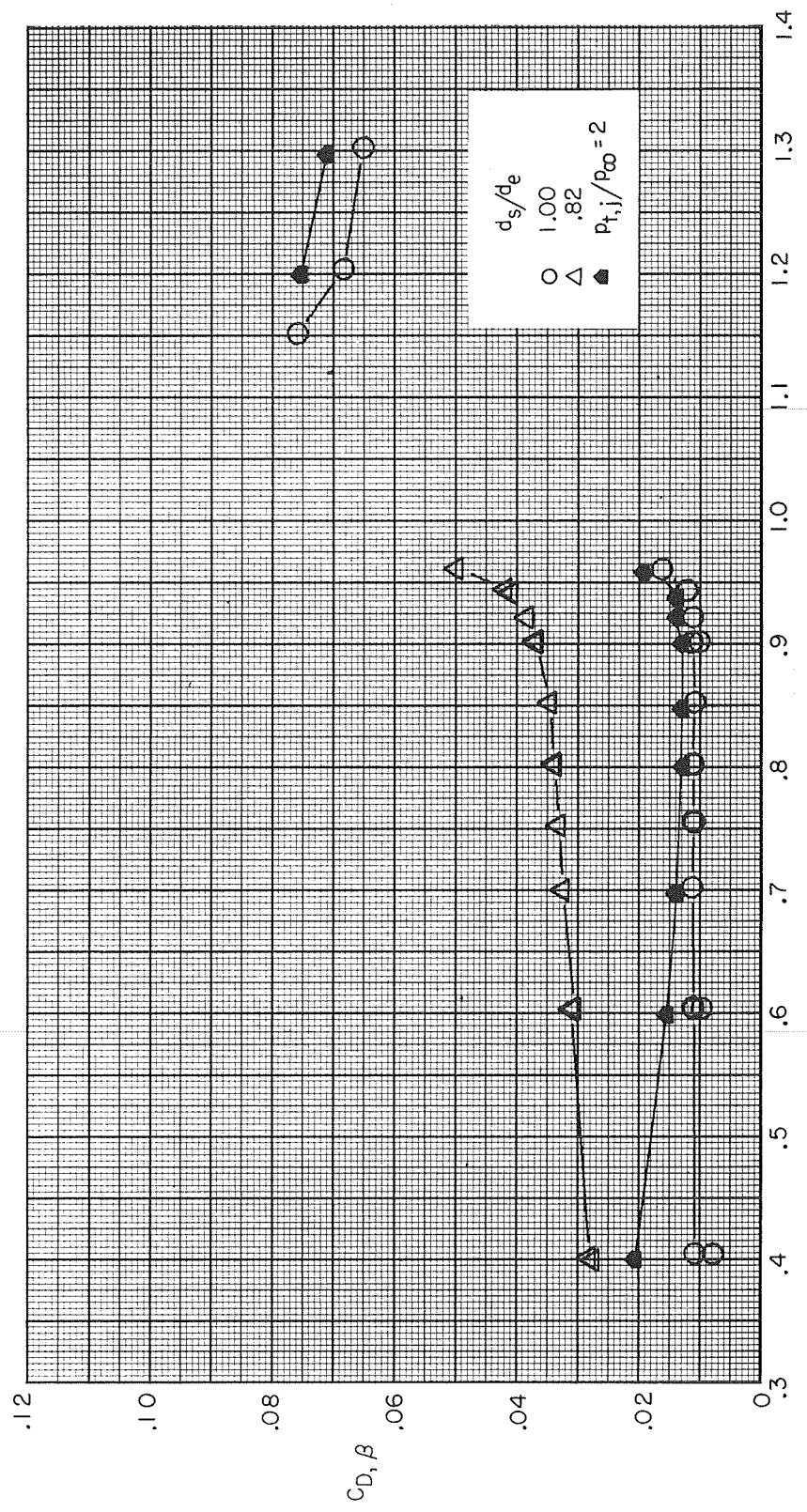

(g) Configuration 7.

Figure 33.- Continued.

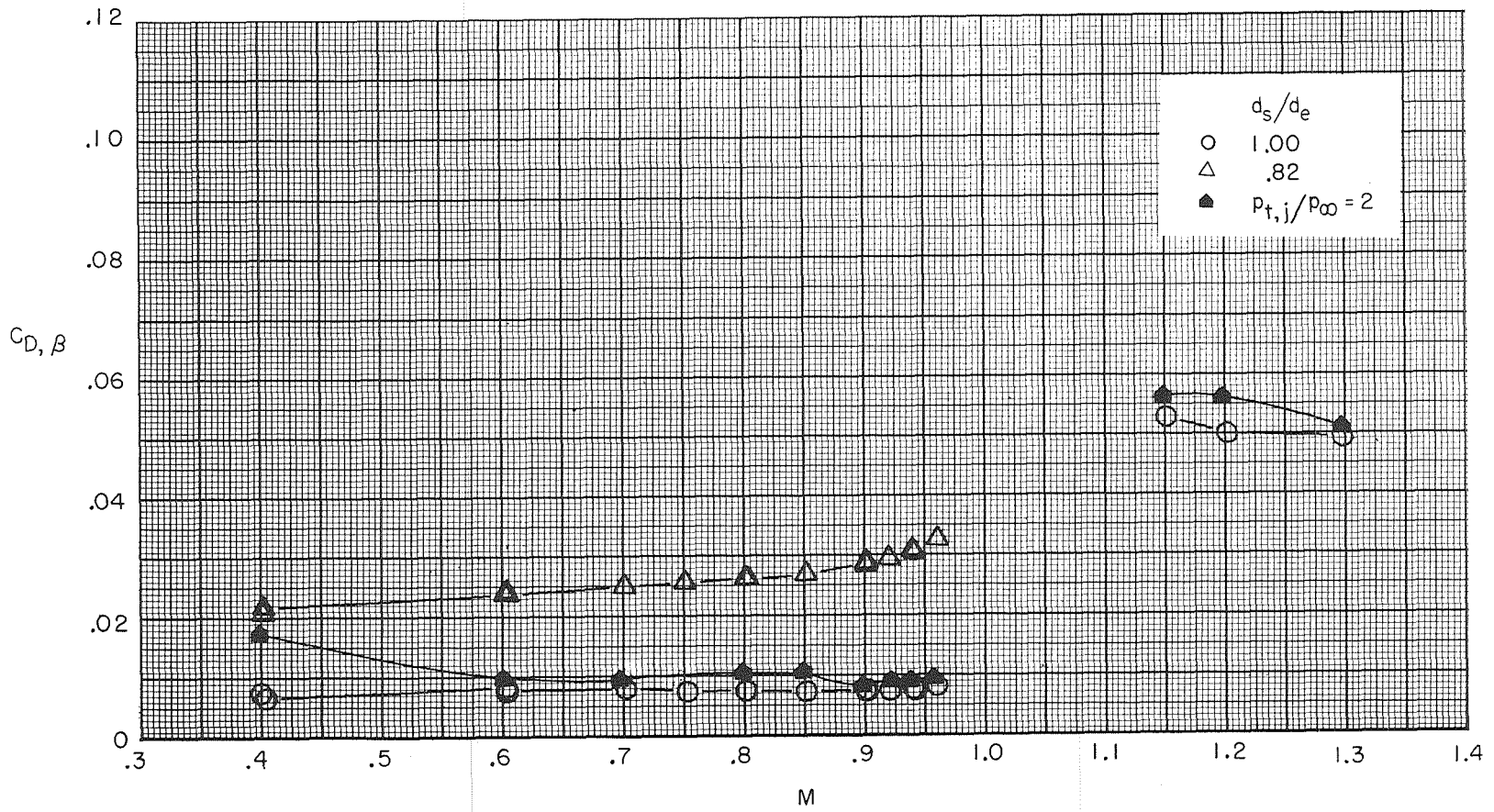

(h) Configuration 8.

Figure 33.- Concluded.

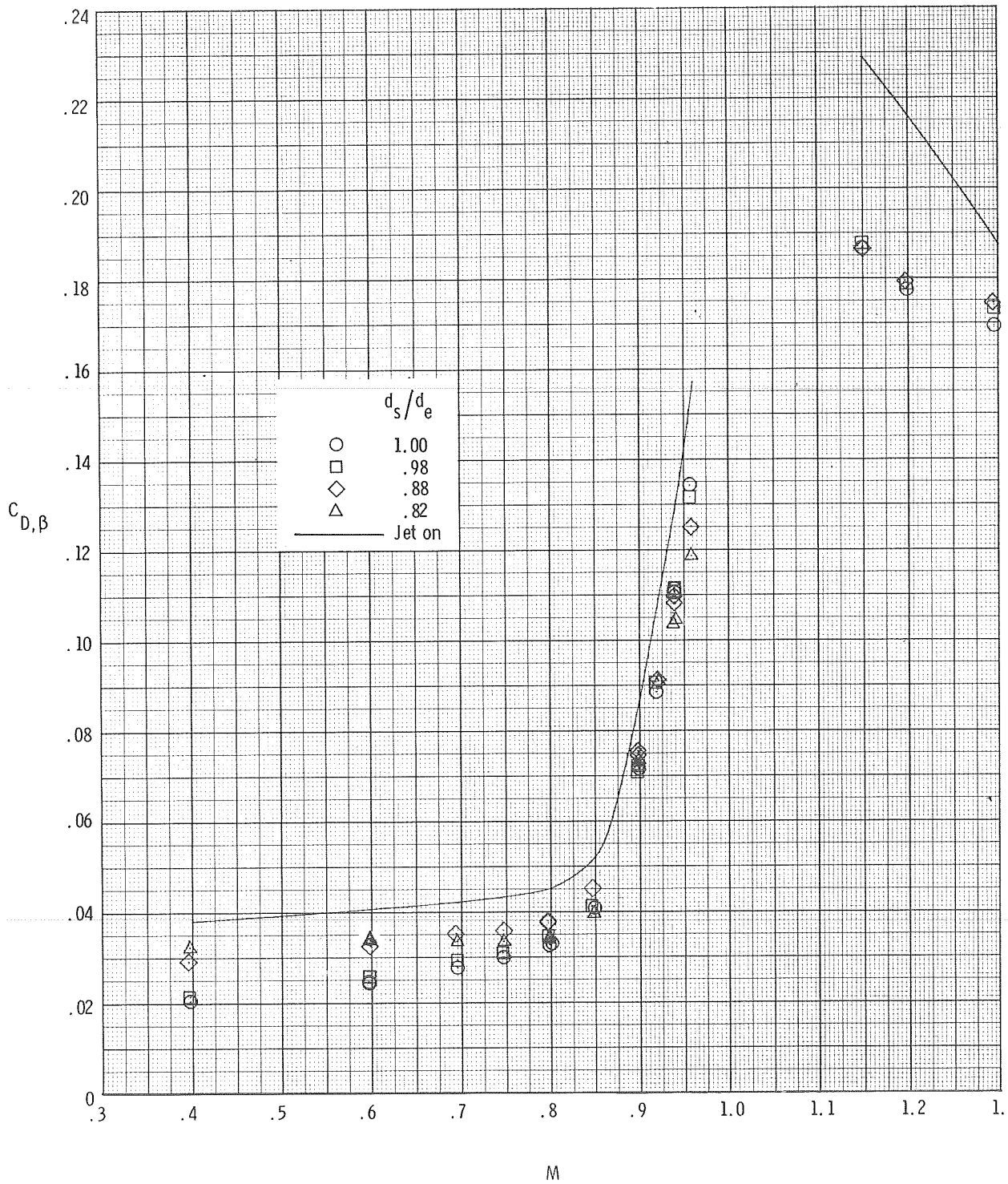

(a) Configuration 1.

Figure 34.- Comparison of integrated boattail pressure-drag coefficients obtained through use of the simulators with jet-on values at the transport jet total-pressure ratio schedule of figure 32.

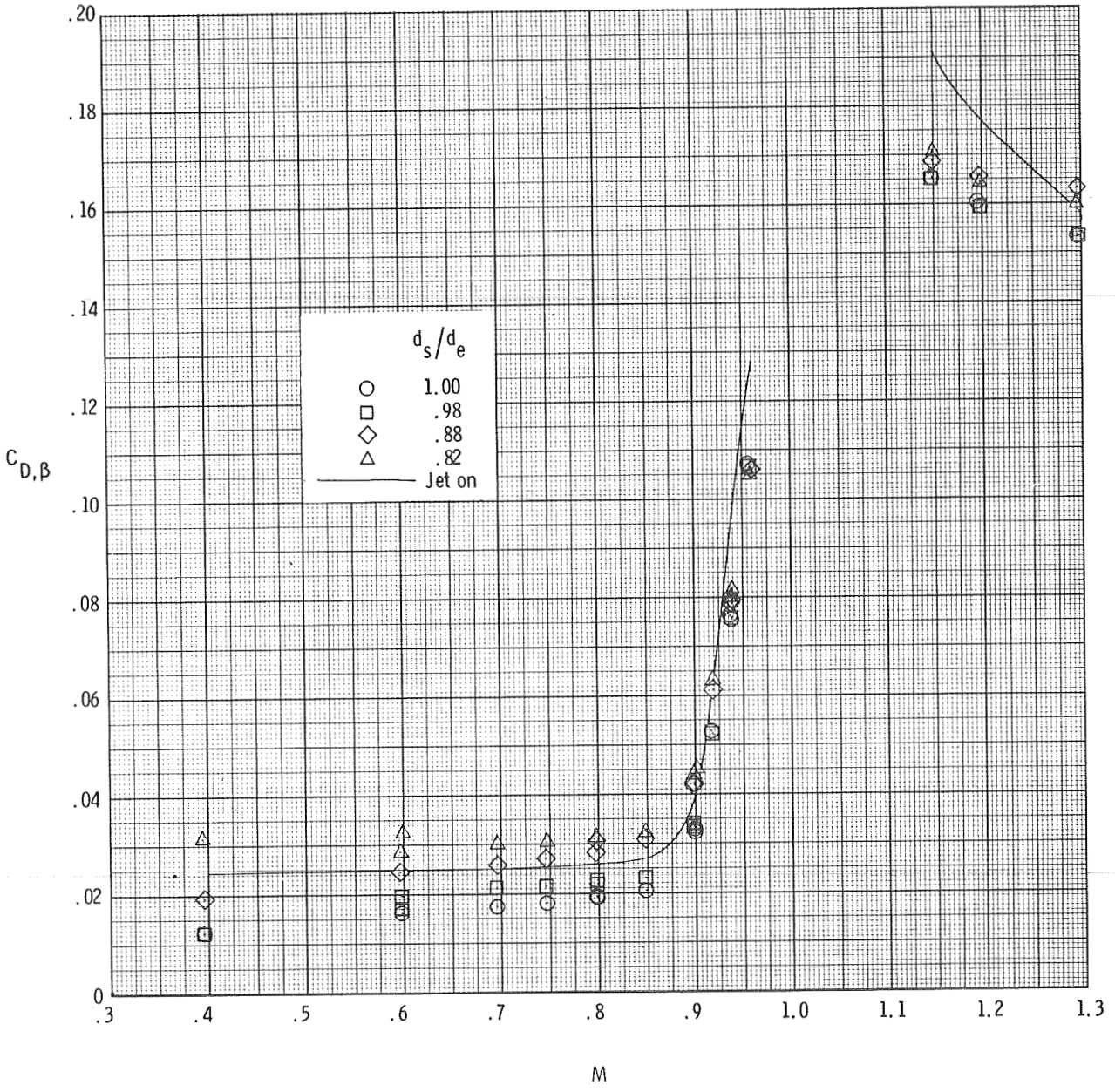

(b) Configuration 2.

Figure 34.- Continued.

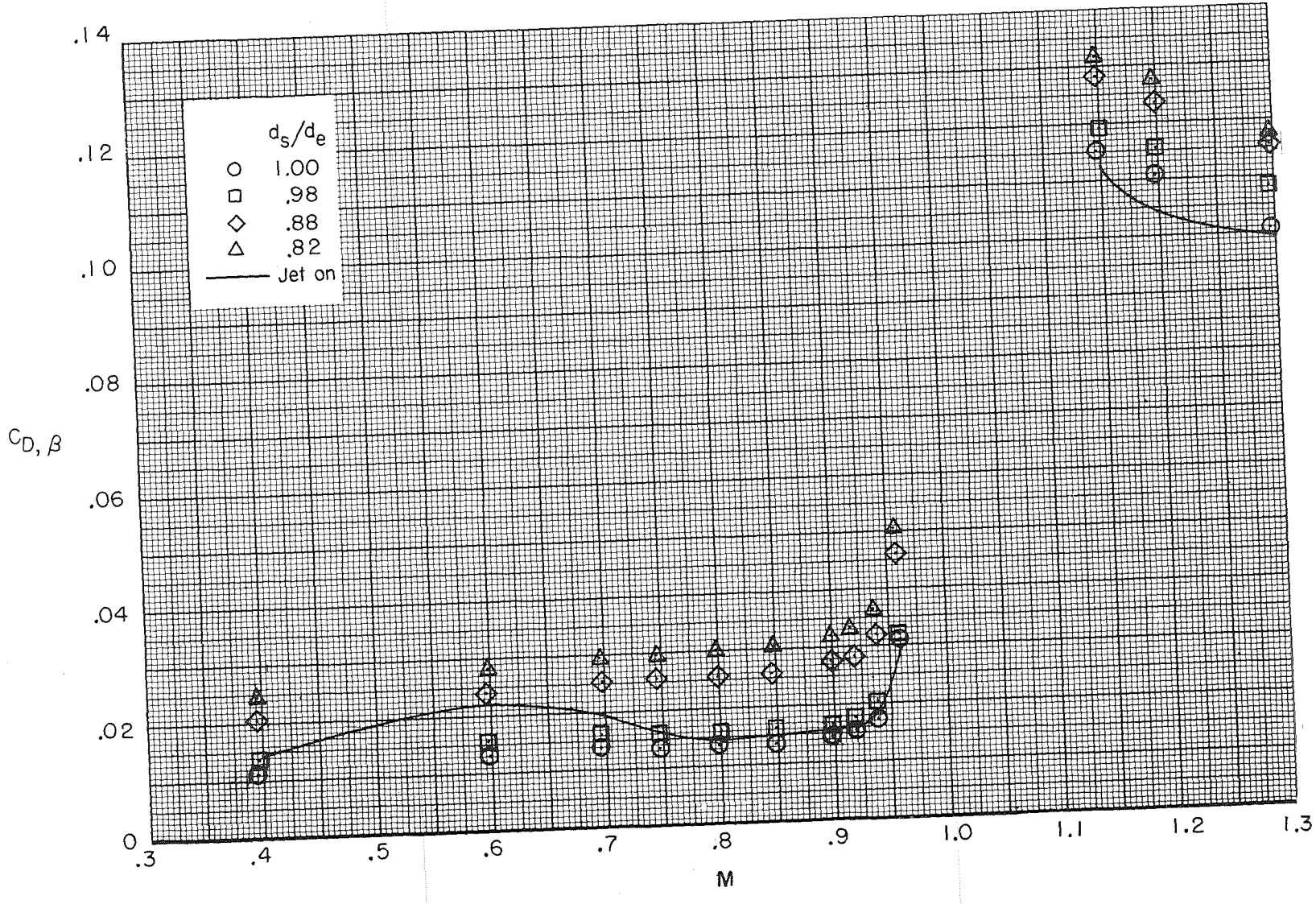

(c) Configuration 3.

Figure 34.- Continued.

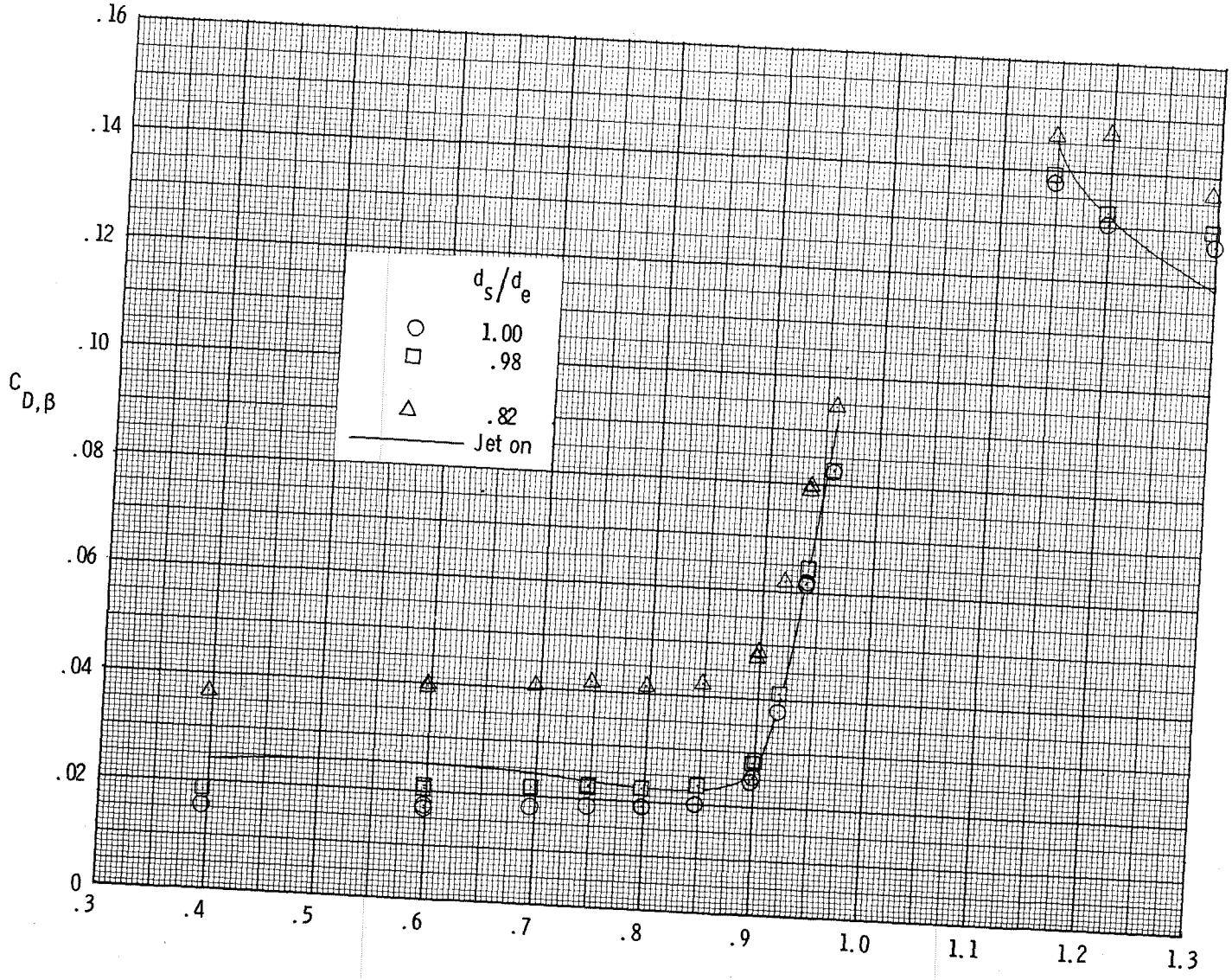

(d) Configuration 4.

Figure 34.- Continued.

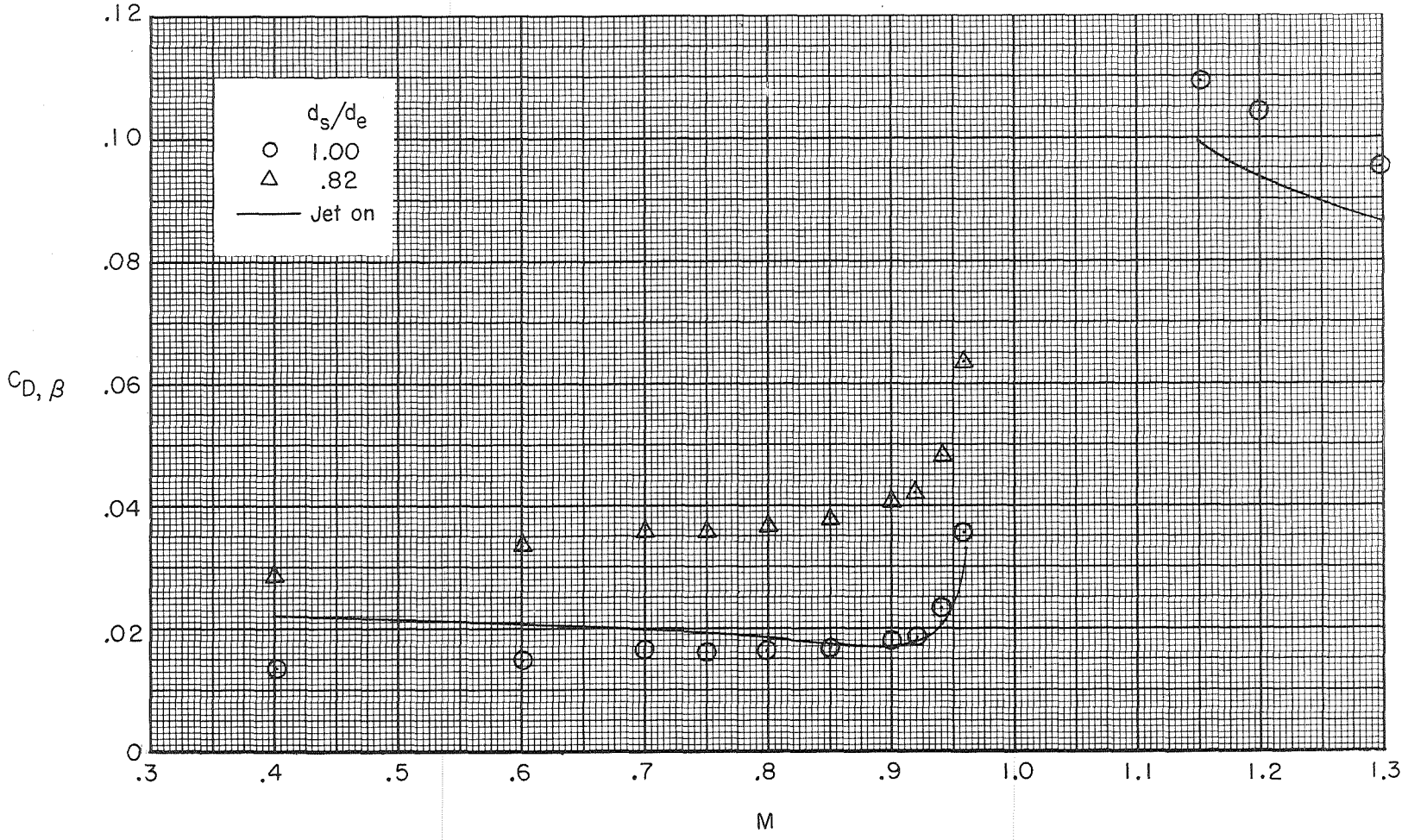

(e) Configuration 5.

Figure 34.- Continued.

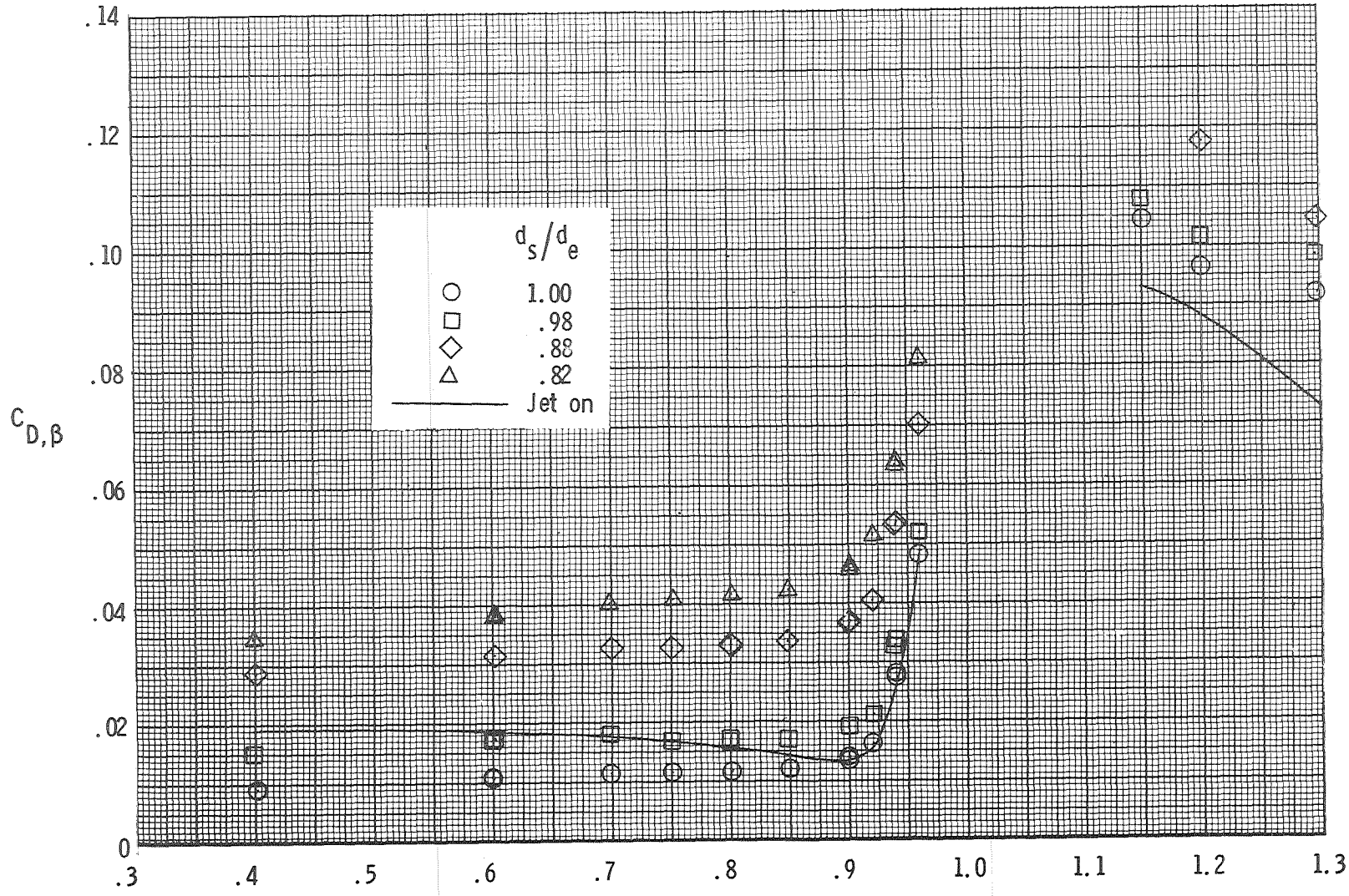

(f) Configuration 6.

Figure 34.- Continued.

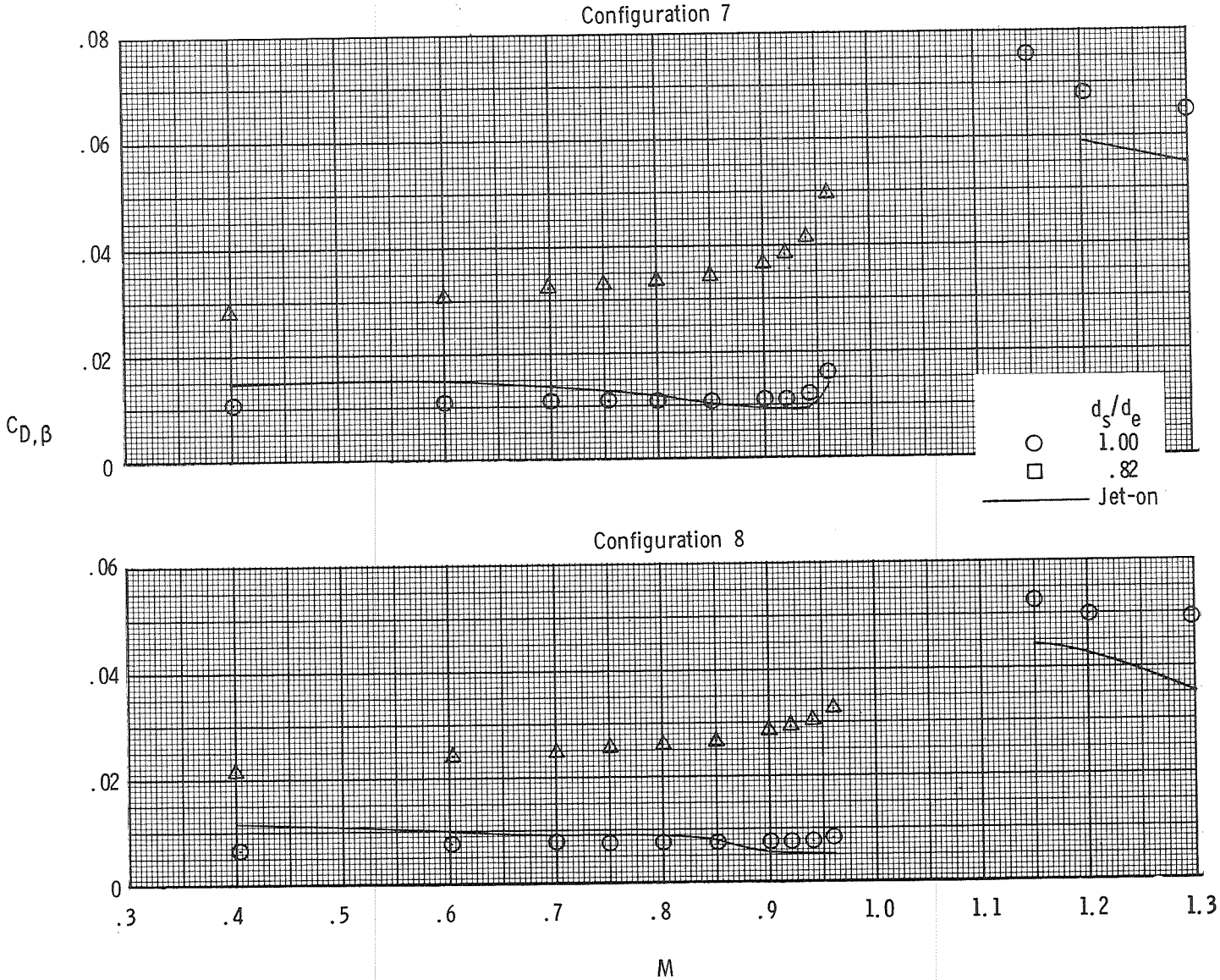

(g) Configurations 7 and 8.

Figure 34.- Concluded.

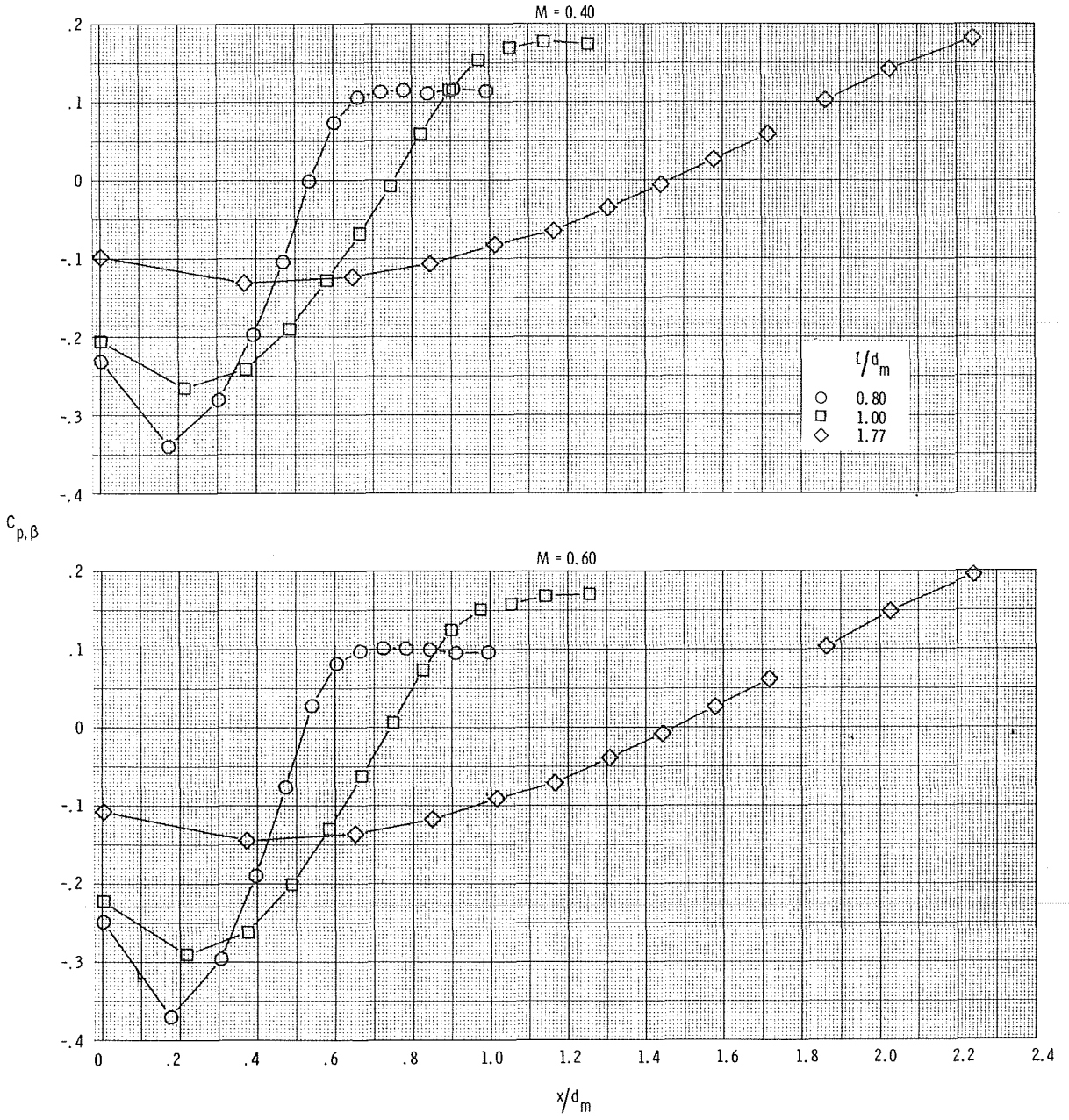

(a) M = 0.40 and 0.60.

Figure 35.- Boattail pressure-coefficient distributions for the $d_e/d_m = 0.50$ boattails with the circular-arc contour continued to a point.

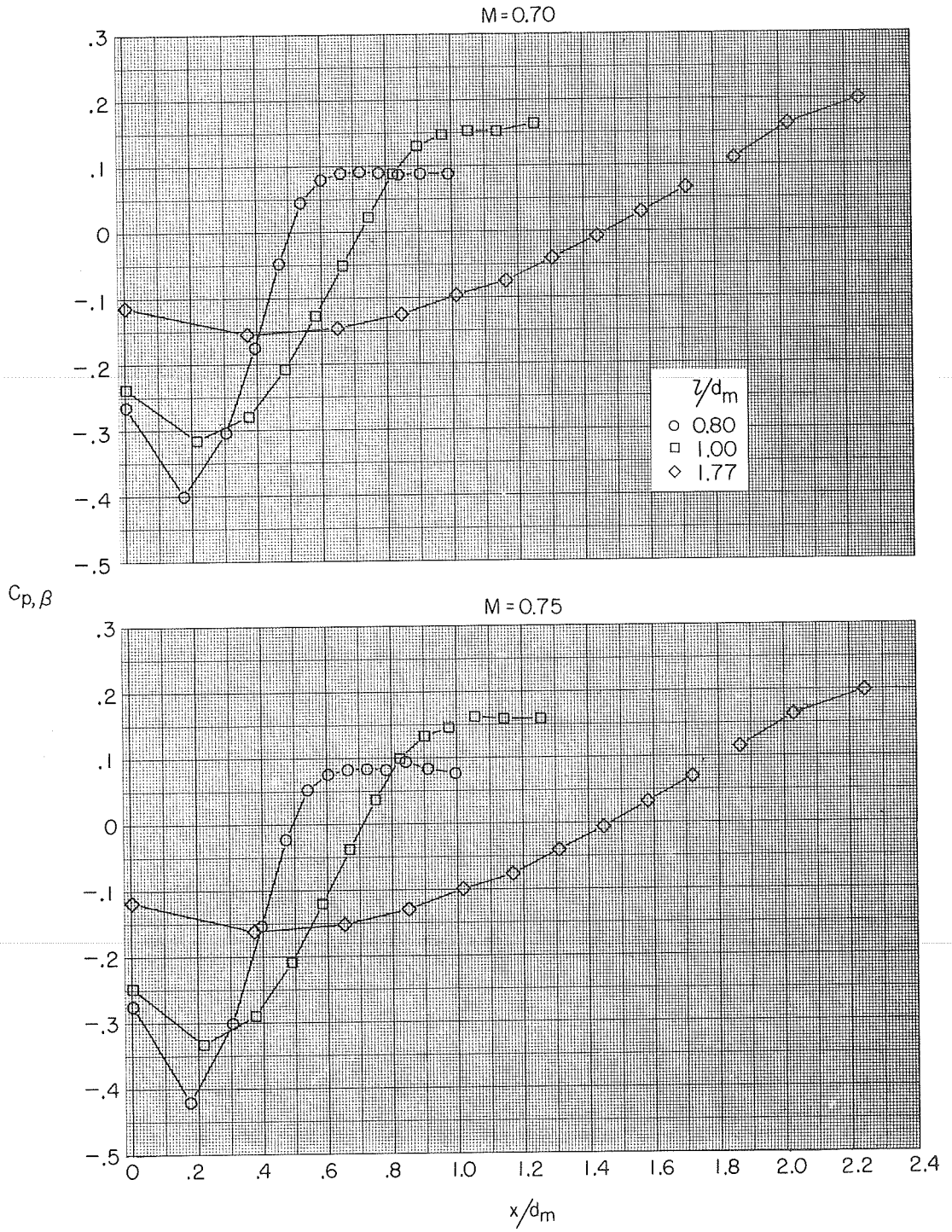

(b) M = 0.70 and 0.75.

Figure 35.- Continued.

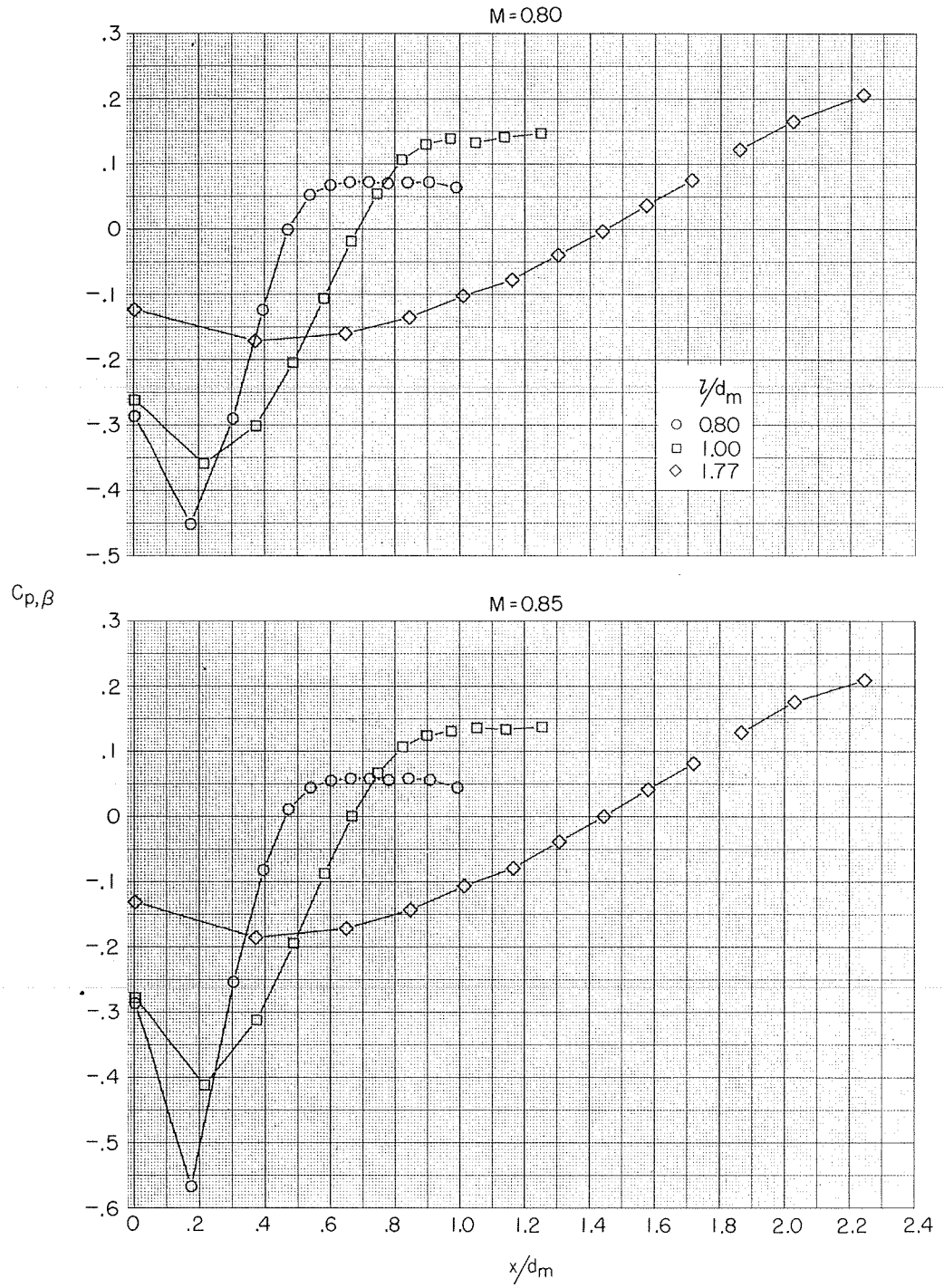

(c) M = 0.80 and 0.85.

Figure 35.- Continued.

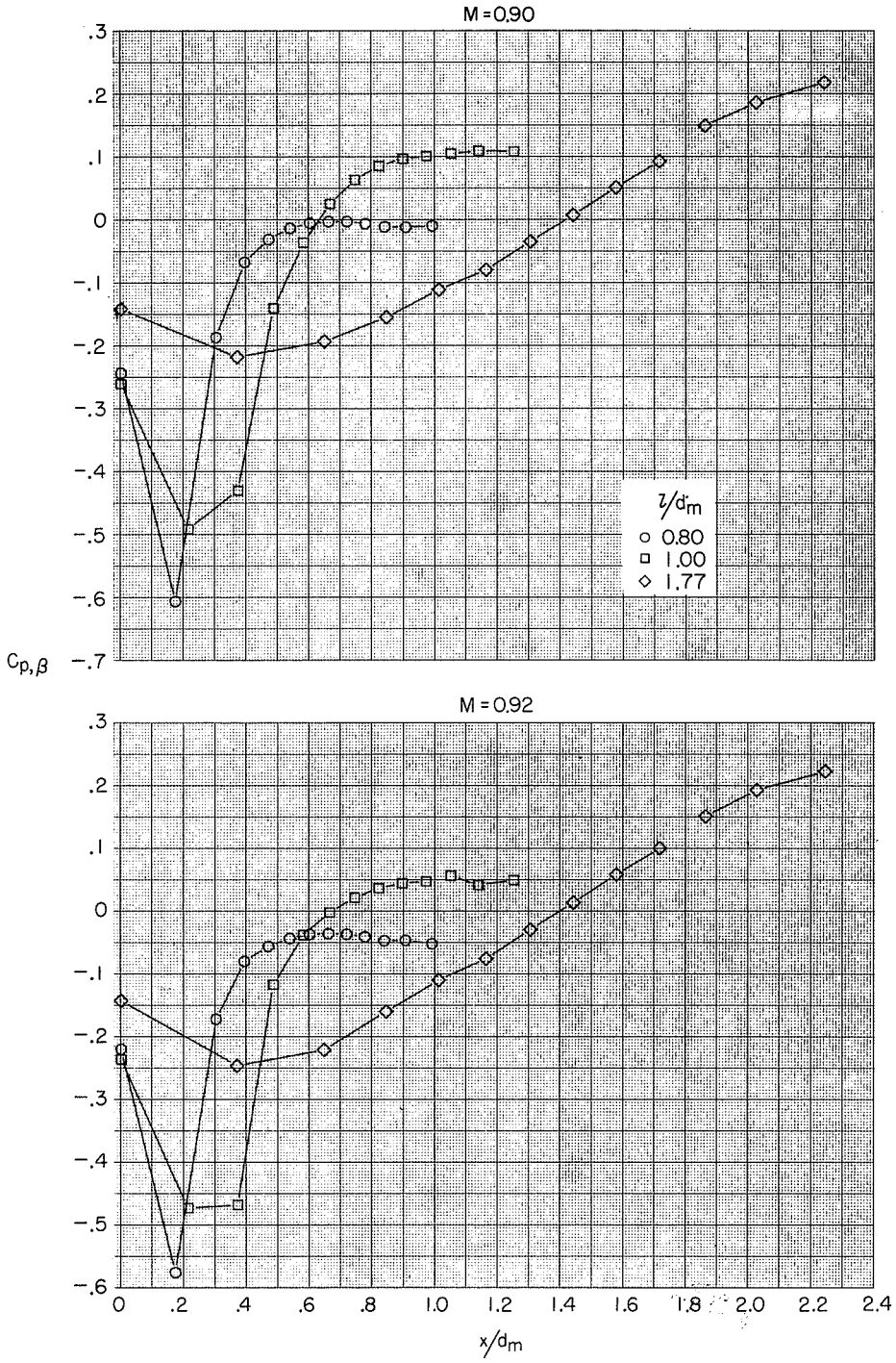

(d) M = 0.90 and 0.92.

Figure 35.- Continued.

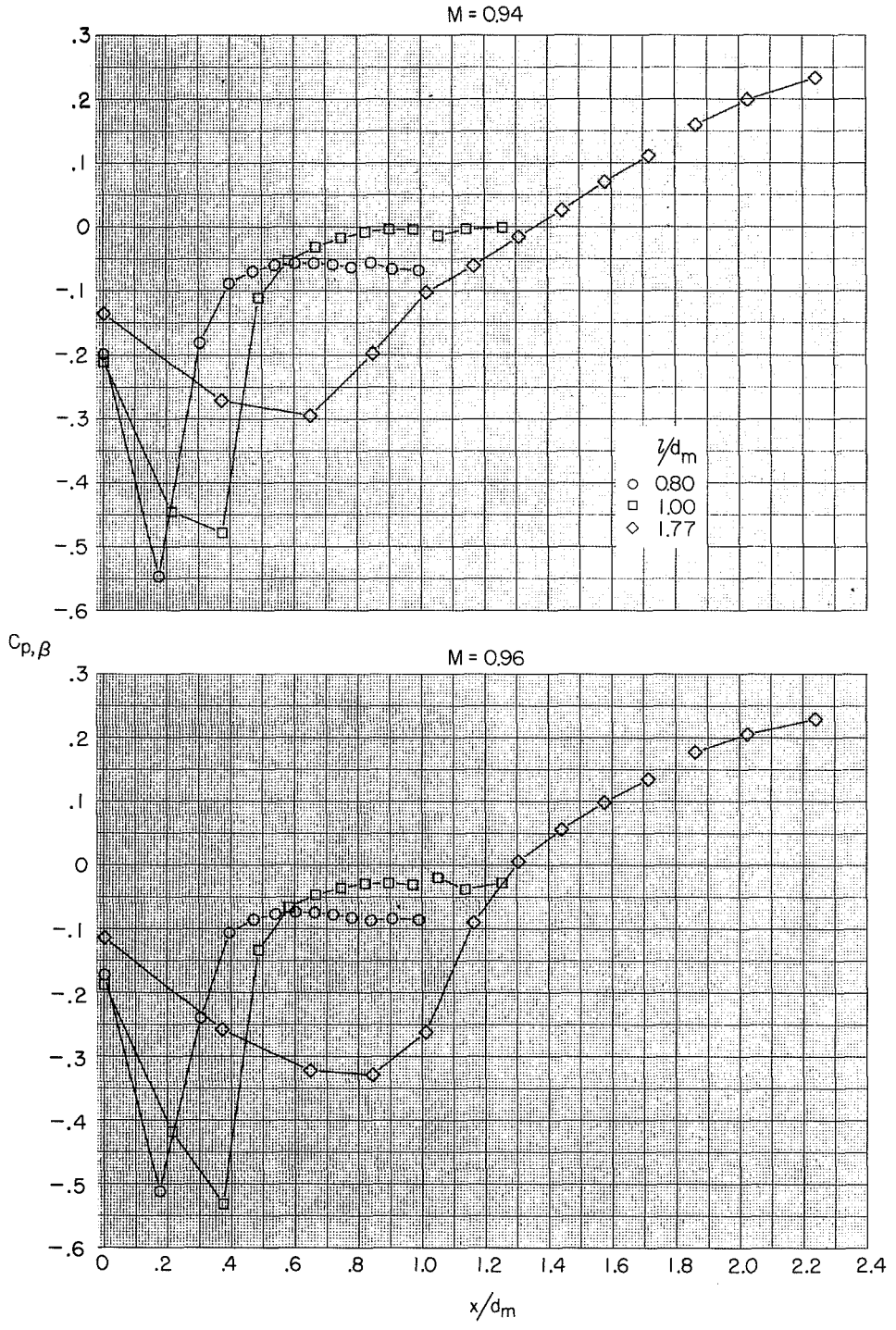

(e) M = 0.94 and 0.96.

Figure 35.- Continued.

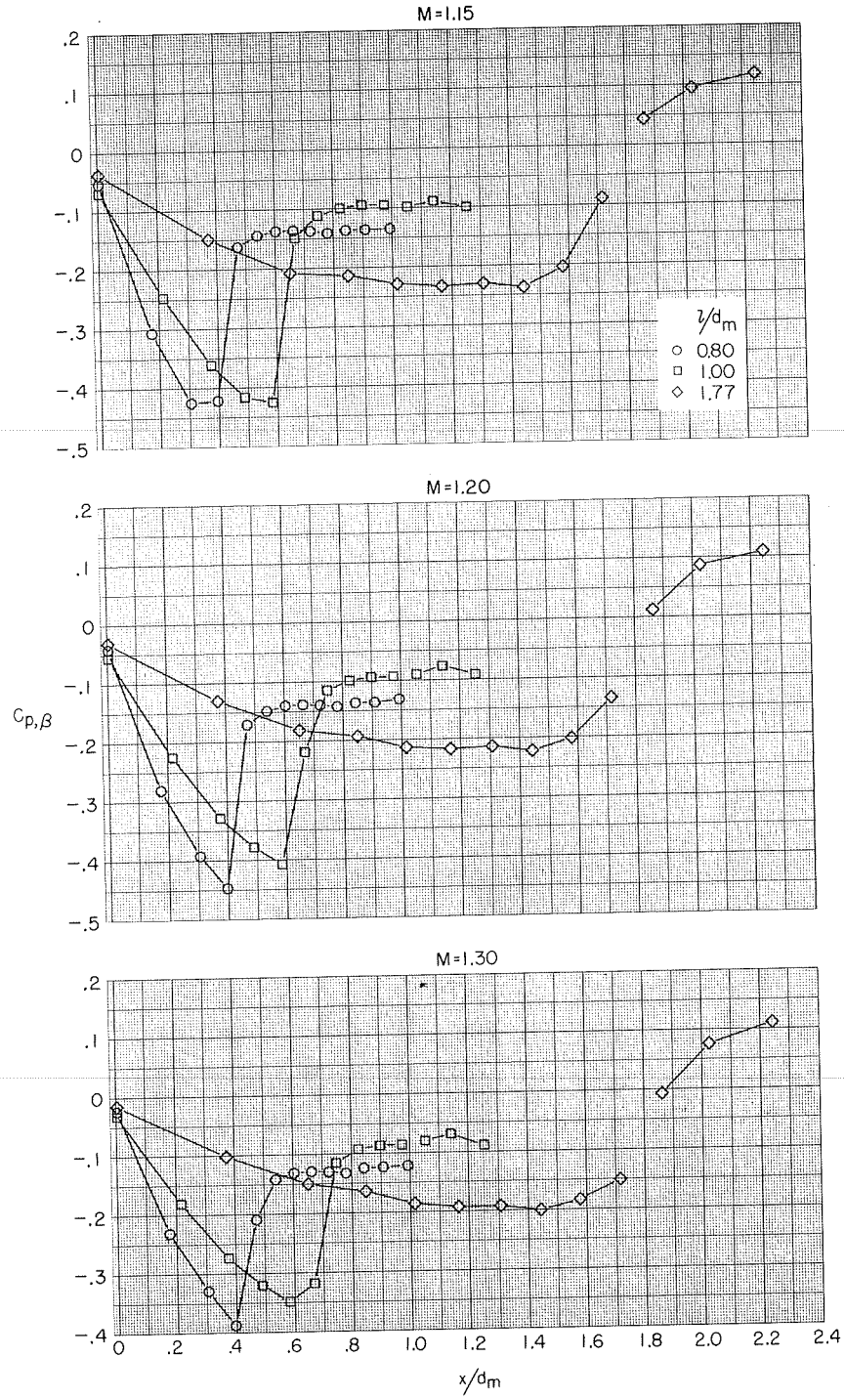

(f) M = 1.15 to 1.30.

Figure 35.- Concluded.

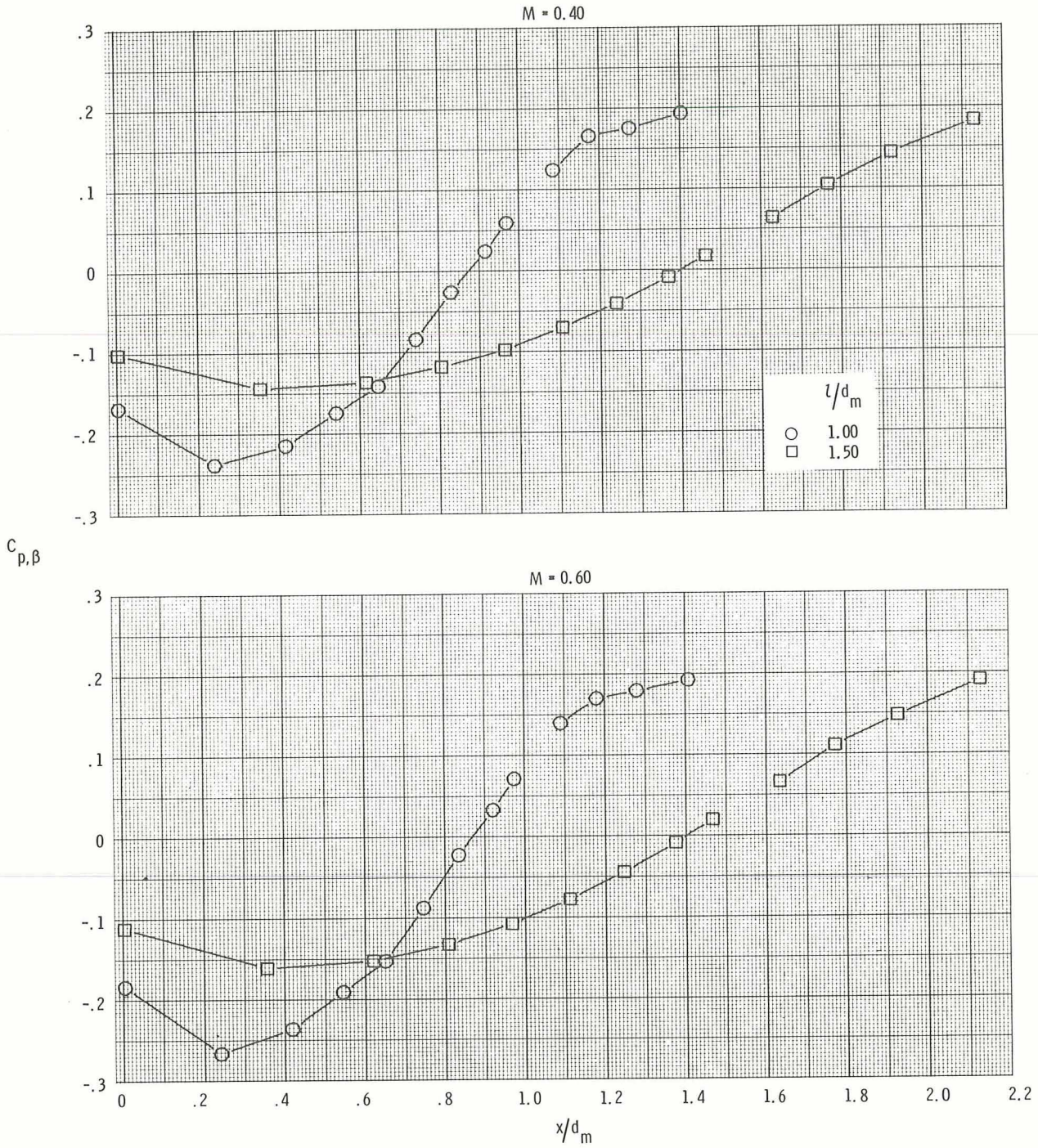

(a) M = 0.40 and 0.60.

Figure 36.- Boattail pressure-coefficient distributions for the $d_e/d_m = 0.60$ boattails with the circular-arc contour continued to a point.

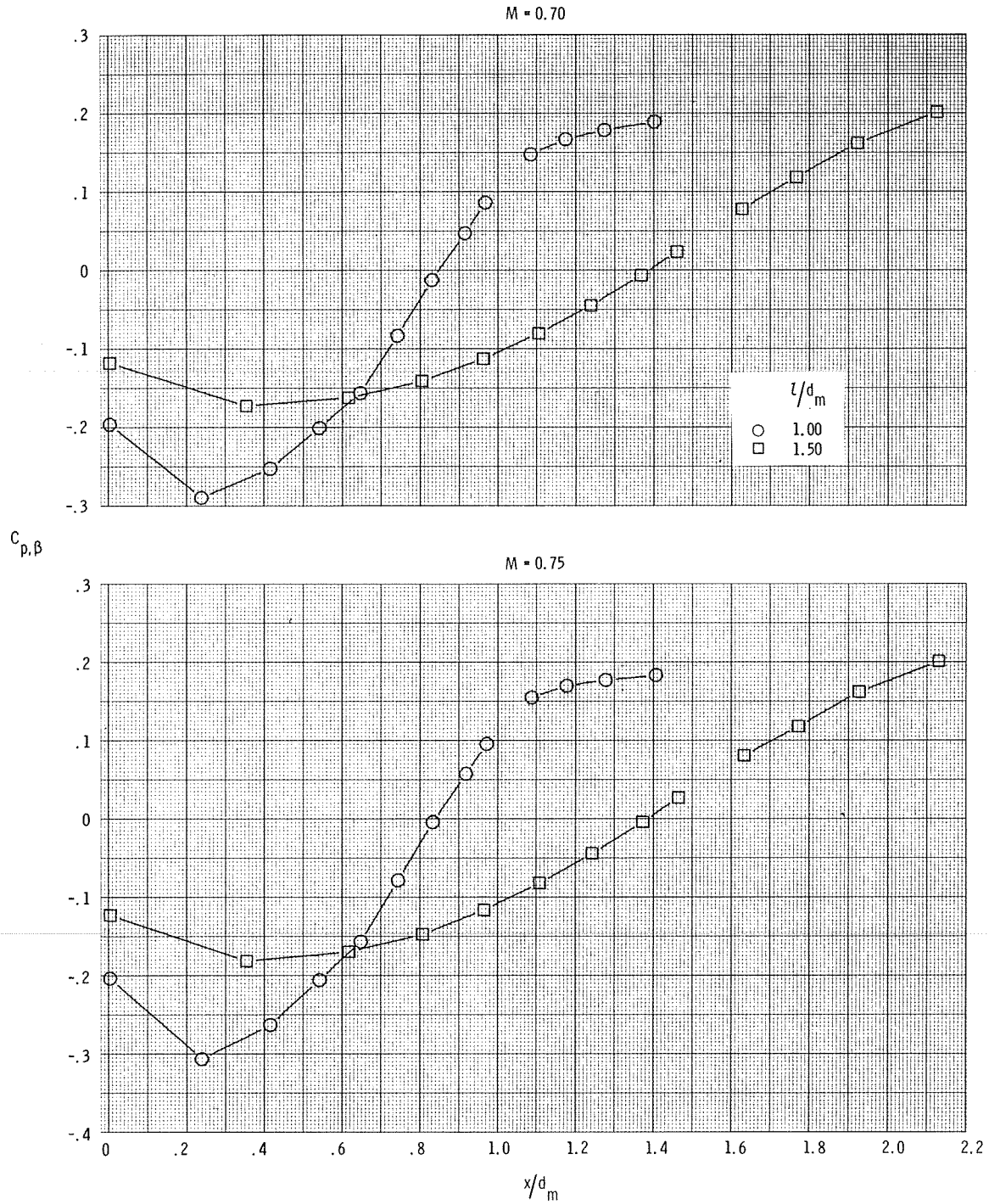

(b) M = 0.70 and 0.75.

Figure 36.- Continued.

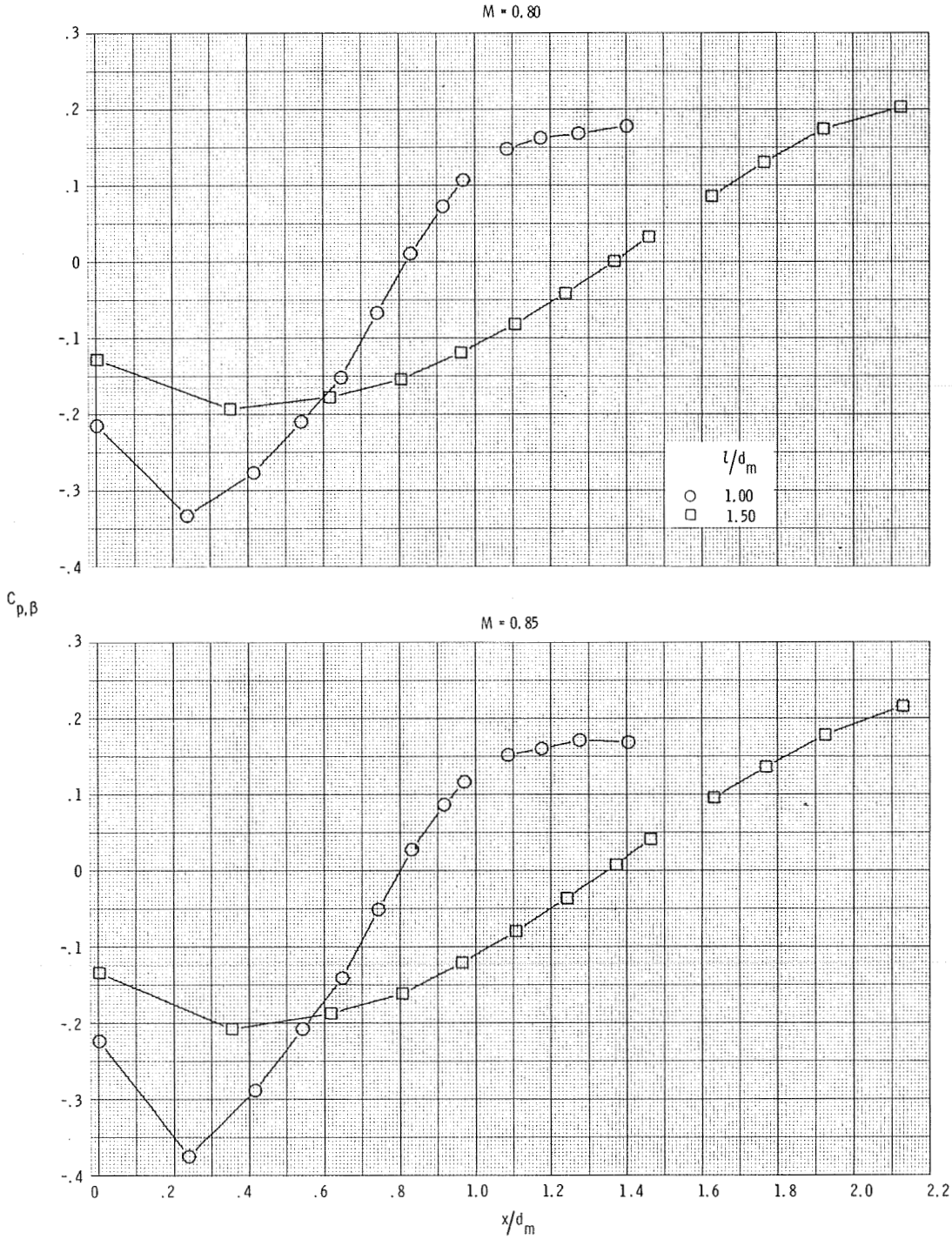

(c) M = 0.80 and 0.85.

Figure 36.- Continued.

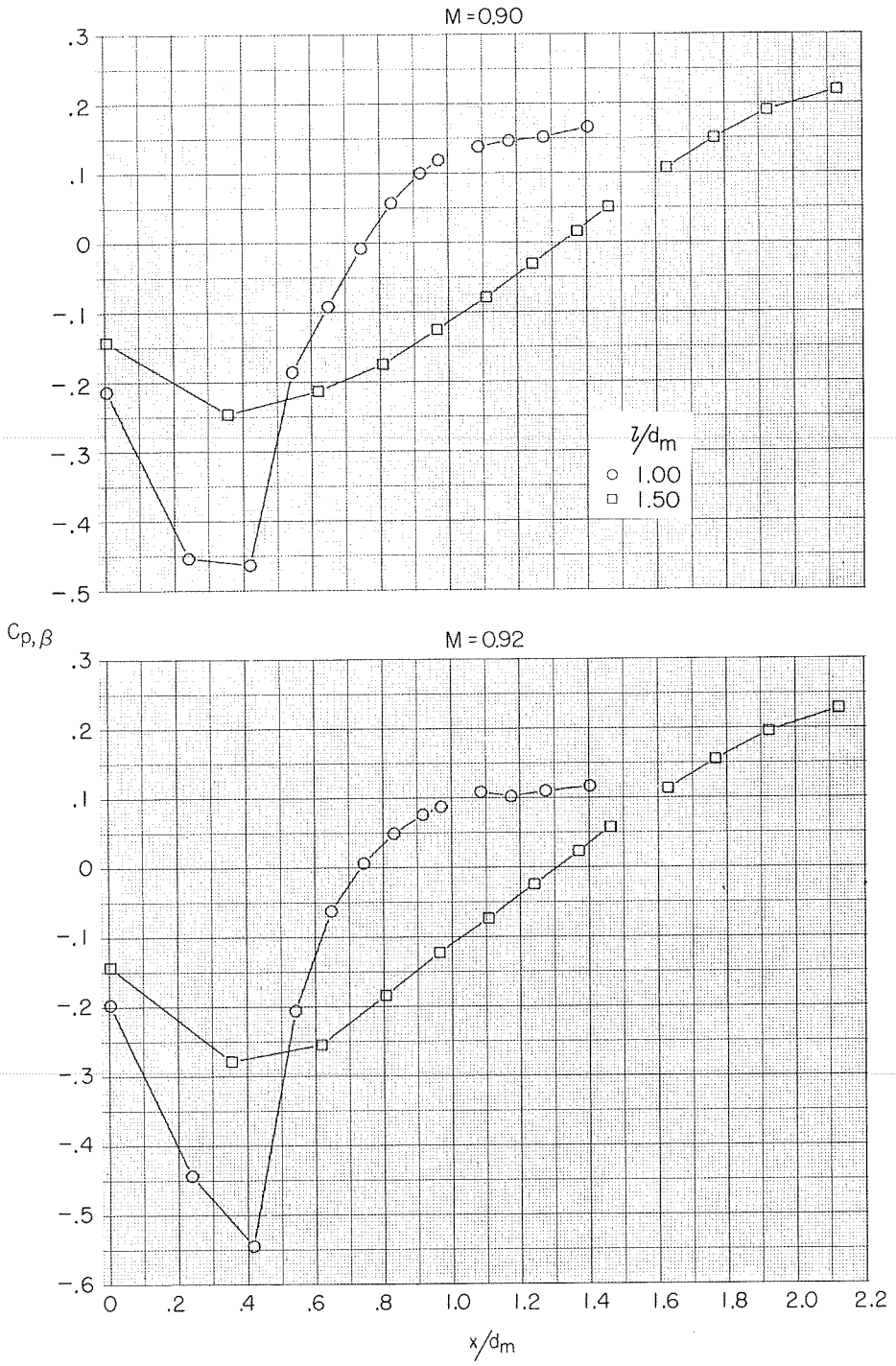

(d) M = 0.90 and 0.92.

Figure 36.- Continued.

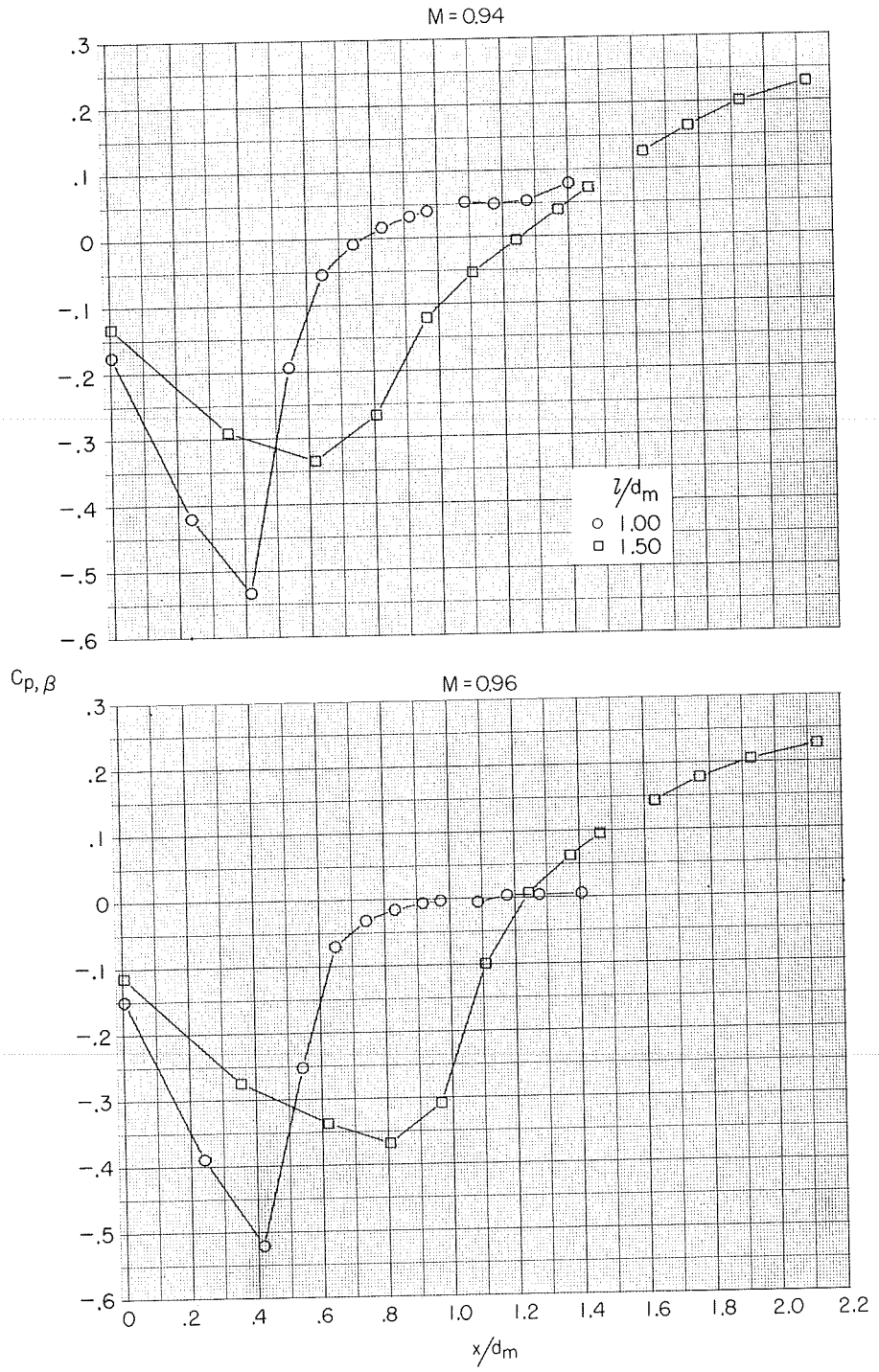

(e) M = 0.94 and 0.96.

Figure 36.- Continued.

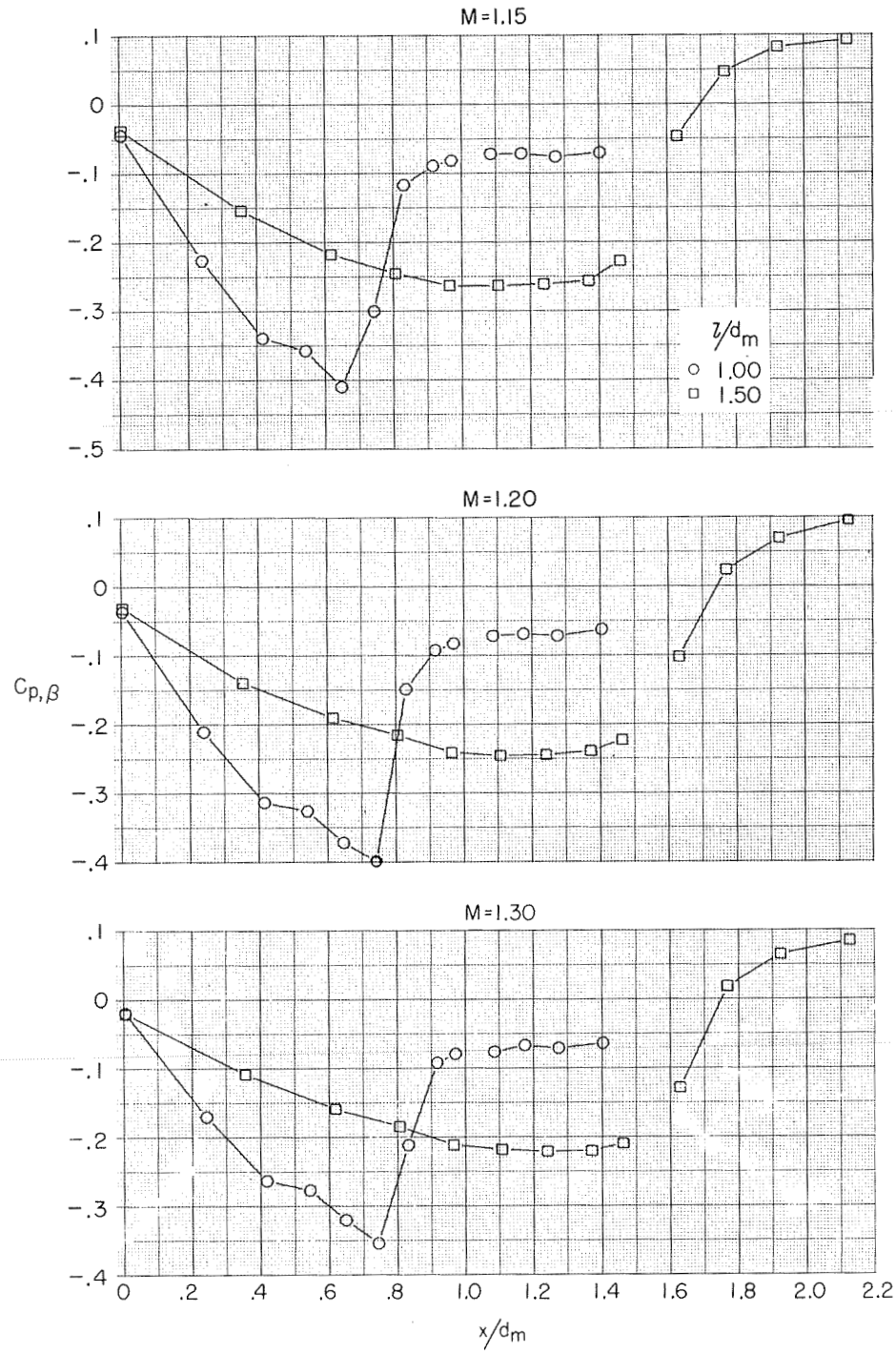

(f) M = 1.15 to 1.30.

Figure 36.- Concluded.

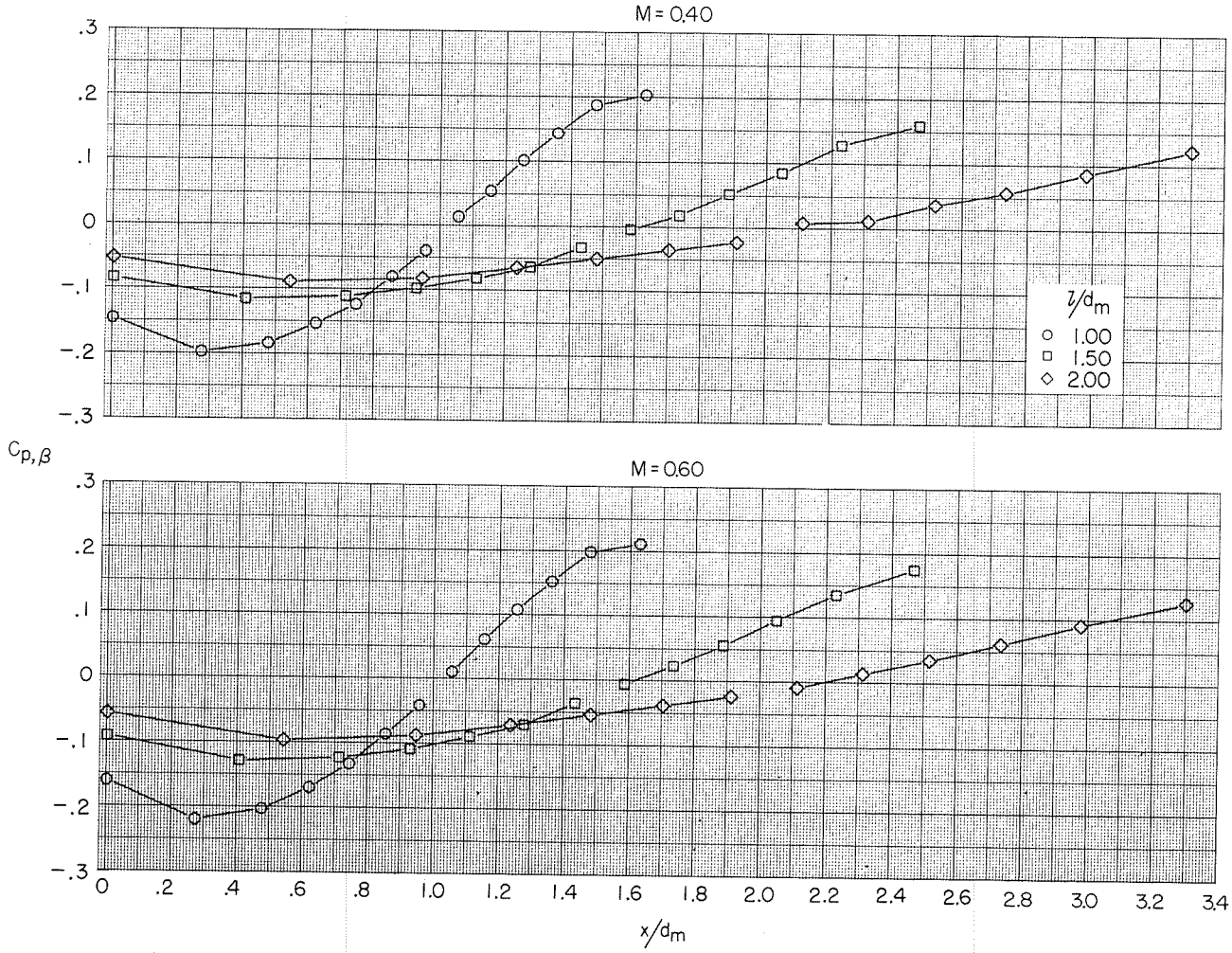

(a) M = 0.40 and 0.60.

Figure 37.- Boattail pressure-coefficient distributions for the $d_e/d_m = 0.70$ boattails with the circular-arc contour continued to a point.

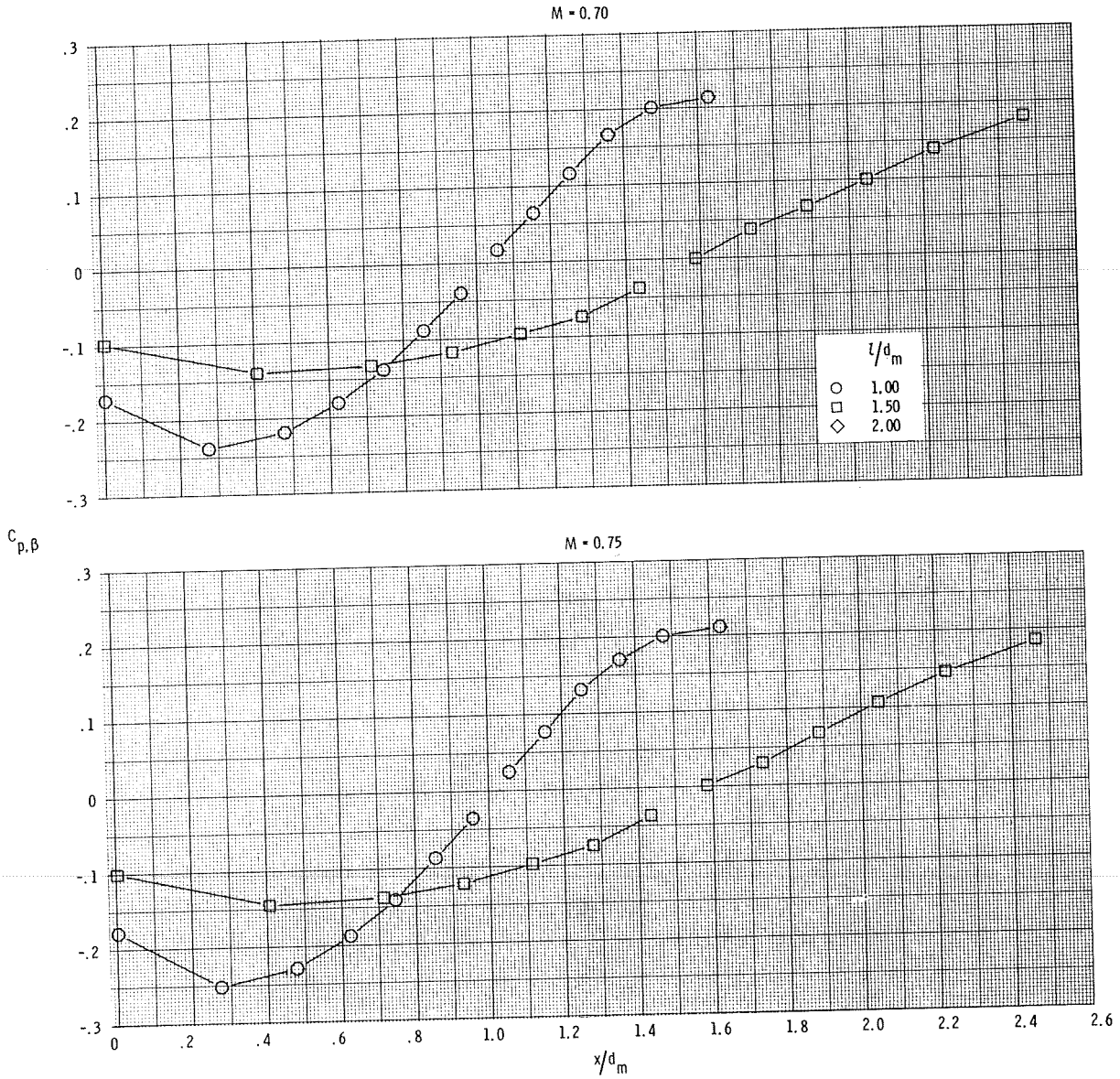

(b) M = 0.70 and 0.75.

Figure 37.- Continued.

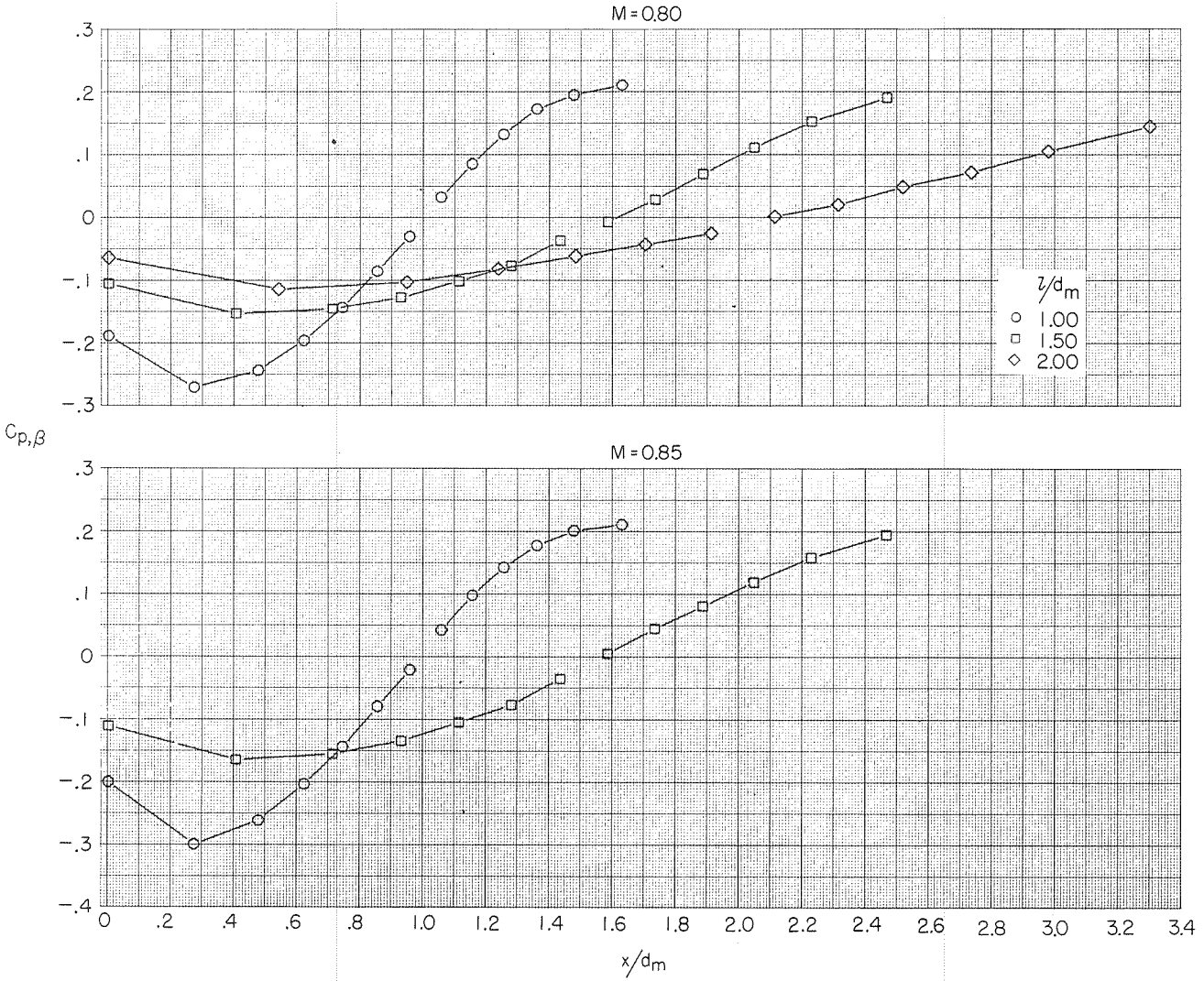

(c) M = 0.80 and 0.85.

Figure 37.- Continued.

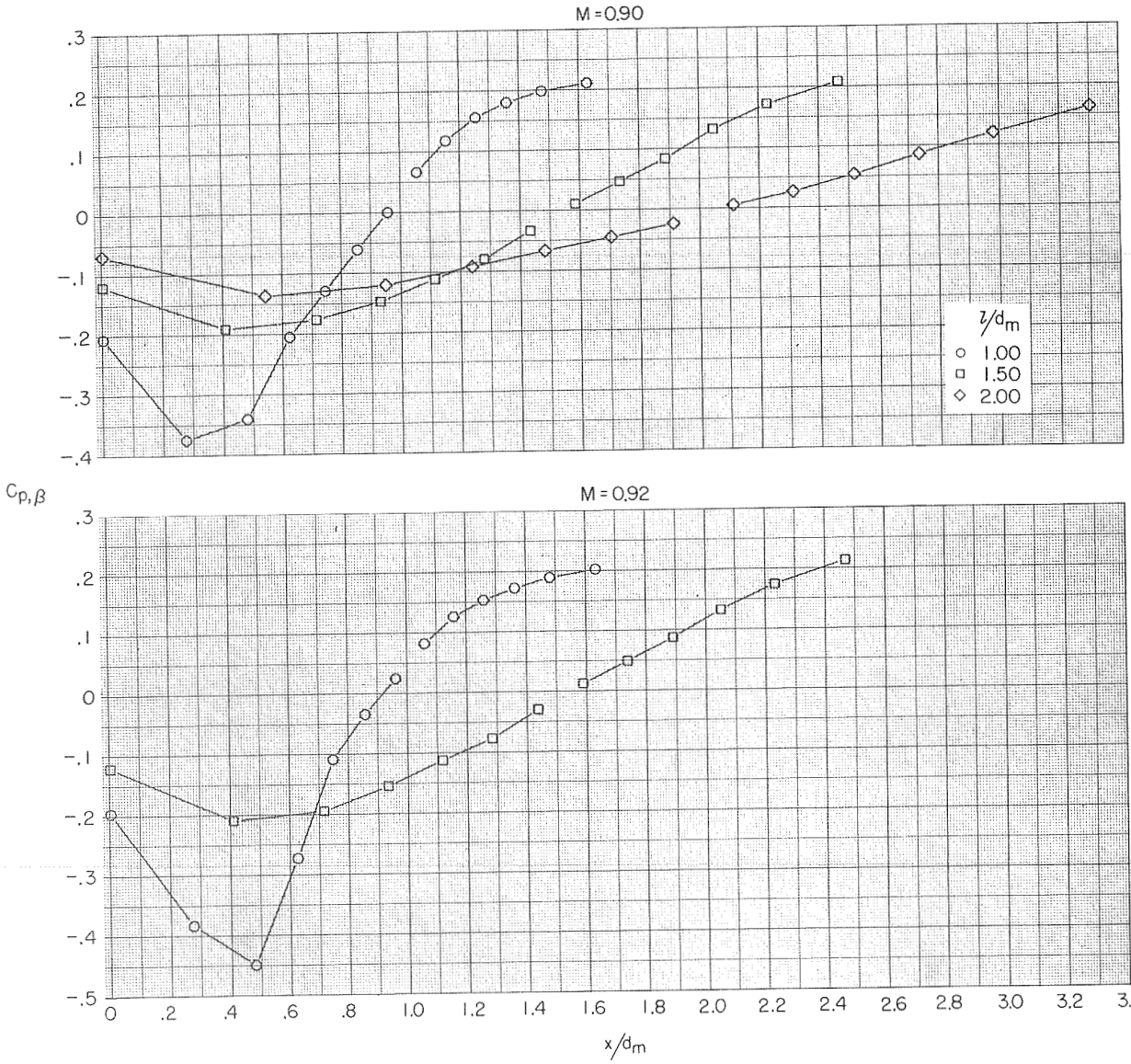

(d) M = 0.90 and 0.92.

Figure 37.- Continued.

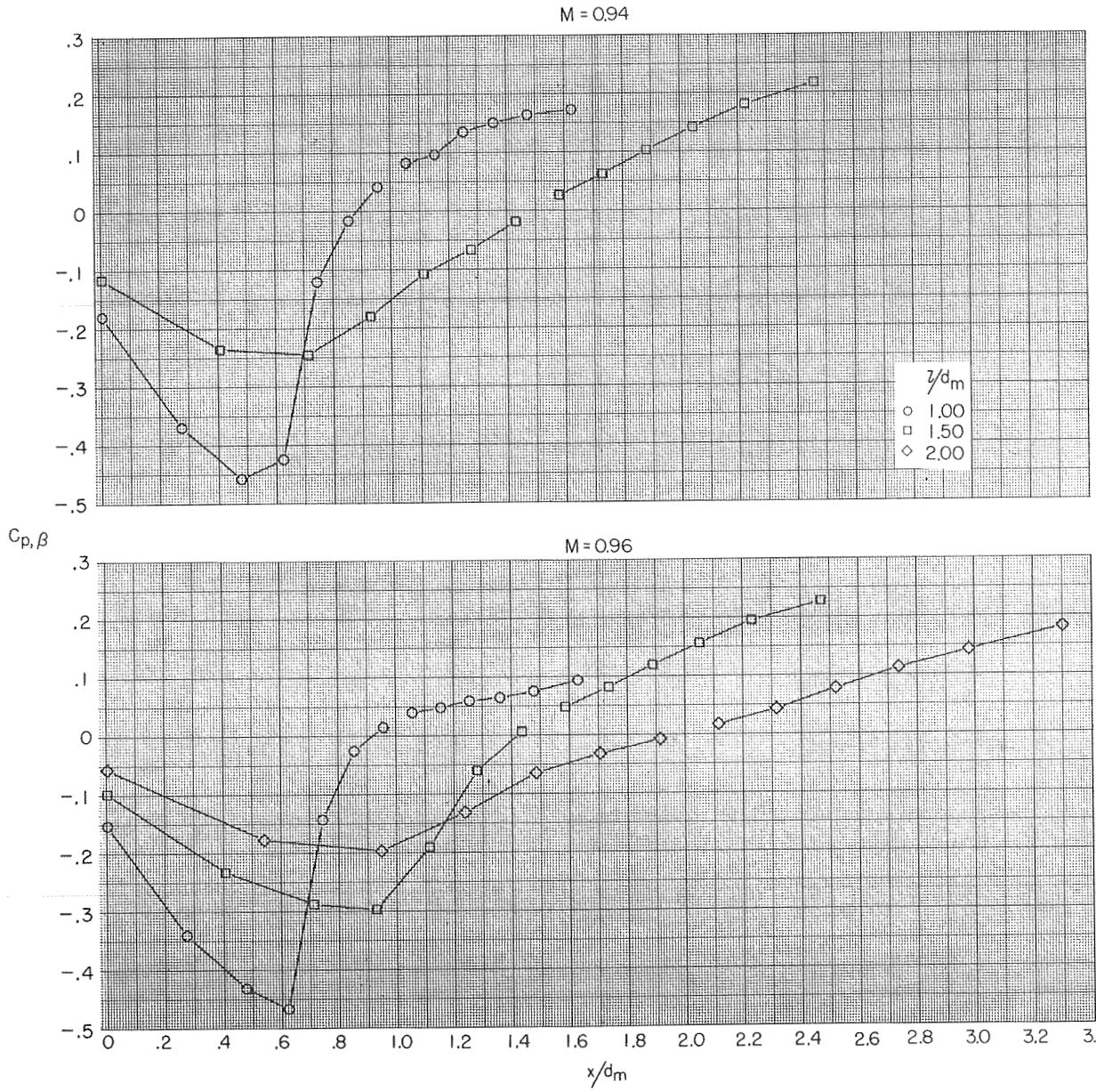

(e) M = 0.94 and 0.96.

Figure 37.- Continued.

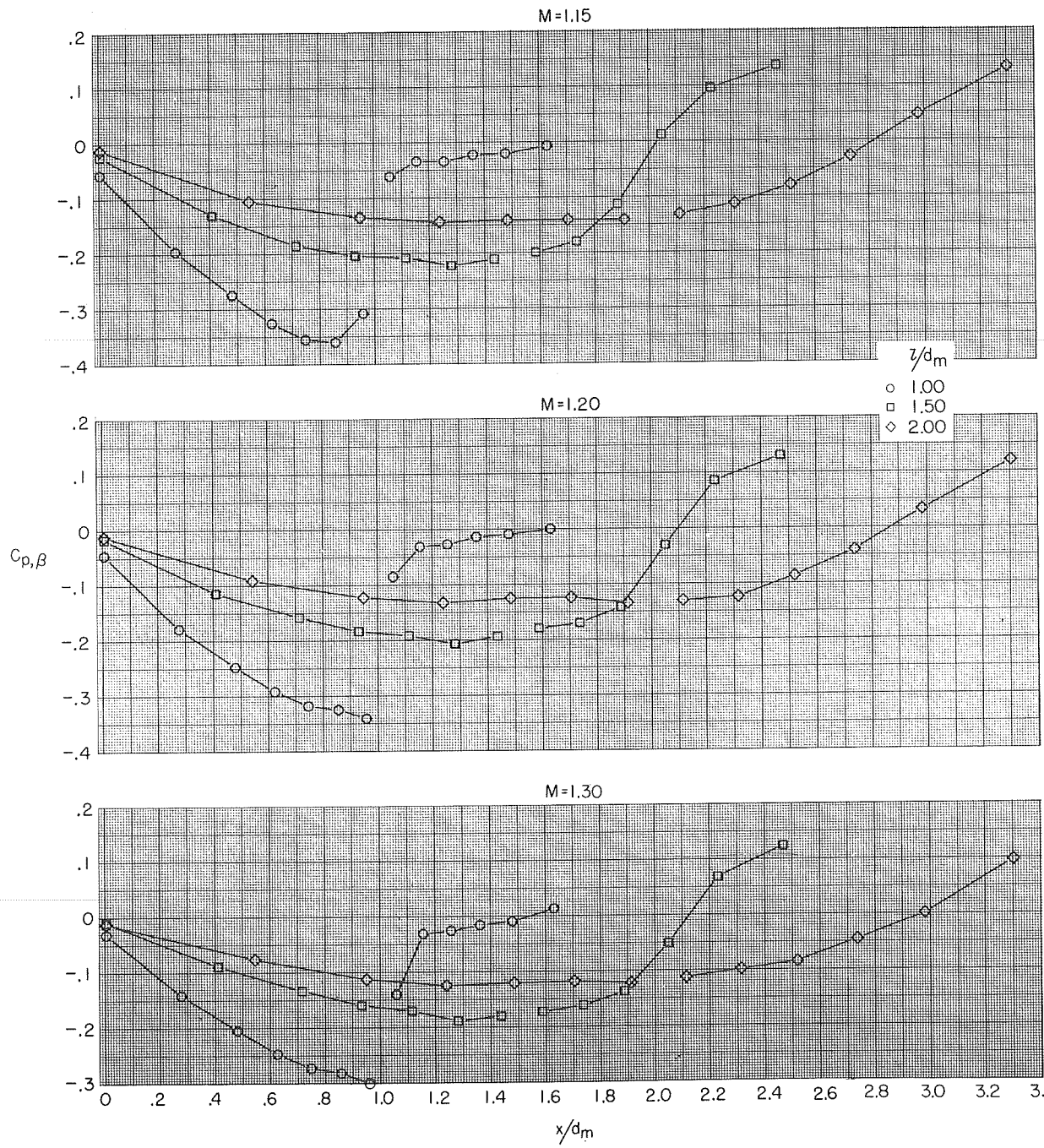

(f) M = 1.15 to 1.30.

Figure 37.- Concluded.

NATIONAL AERONAUTICS AND SPACE ADMINISTRATION
WASHINGTON, D.C. 20546

OFFICIAL BUSINESS
PENALTY FOR PRIVATE USE $300

SPECIAL FOURTH-CLASS RATE BOOK

POSTAGE AND FEES PAID
NATIONAL AERONAUTICS AND SPACE ADMINISTRATION
451

U.S.MAIL

941 001 C1 U 01 741101 S00120ES
PHILCO FORD CORP
AERONUTRONIC DIV
AEROSPACE & COMMUNICATIONS OPERATIONS
ATTN: TECHNICAL INFO SERVICES
JAMBOREE & FORD ROADS
NEWPORT BEACH CA 92663

POSTMASTER: If Undeliverable (Section 158 Postal Manual) Do Not Return

"The aeronautical and space activities of the United States shall be conducted so as to contribute . . . to the expansion of human knowledge of phenomena in the atmosphere and space. The Administration shall provide for the widest practicable and appropriate dissemination of information concerning its activities and the results thereof."

—NATIONAL AERONAUTICS AND SPACE ACT OF 1958

NASA SCIENTIFIC AND TECHNICAL PUBLICATIONS

TECHNICAL REPORTS: Scientific and technical information considered important, complete, and a lasting contribution to existing knowledge.

TECHNICAL NOTES: Information less broad in scope but nevertheless of importance as a contribution to existing knowledge.

TECHNICAL MEMORANDUMS: Information receiving limited distribution because of preliminary data, security classification, or other reasons. Also includes conference proceedings with either limited or unlimited distribution.

CONTRACTOR REPORTS: Scientific and technical information generated under a NASA contract or grant and considered an important contribution to existing knowledge.

TECHNICAL TRANSLATIONS: Information published in a foreign language considered to merit NASA distribution in English.

SPECIAL PUBLICATIONS: Information derived from or of value to NASA activities. Publications include final reports of major projects, monographs, data compilations, handbooks, sourcebooks, and special bibliographies.

TECHNOLOGY UTILIZATION PUBLICATIONS: Information on technology used by NASA that may be of particular interest in commercial and other non-aerospace applications. Publications include Tech Briefs, Technology Utilization Reports and Technology Surveys.

Details on the availability of these publications may be obtained from:

SCIENTIFIC AND TECHNICAL INFORMATION OFFICE

NATIONAL AERONAUTICS AND SPACE ADMINISTRATION

Washington, D.C. 20546